國立臺灣大學工學院土木工程學系

碩士論文

Department of Civil Engineering

College of Engineering

National Taiwan University

Master's Thesis

RC 構架含開口填充磚牆之側力位移曲線預測

Prediction of Lateral Load-Deflection Curves for Brick Infill Walls with Openings in RC Frames

張榮光

William Christopher Chandra

指導教授：黃世建 博士

Advisor: Shyh-Jiann Hwang, Ph.D.

中華民國 114 年 7 月

July, 2025

doi:10.6342/NTU202502280

國立臺灣大學碩士學位論文
口試委員會審定書

NATIONAL TAIWAN UNIVERSITY
MASTER'S THESIS ACCEPTANCE CERTIFICATE

RC構架含開口填充磚牆之側力位移曲線預測

Prediction of Lateral Load-Deflection Curves for Brick Infill Walls with Openings in RC Frames

本論文係 張榮光 (R12521251) 在國立臺灣大學土木工程學系結構工程組完成之碩士學位論文，於民國114年07月01日承下列考試委員審查通過及口試及格，特此證明。

The undersigned, appointed by the Department of Civil Engineering Structural Engineering on 07/01,2025 have examined a Master's Thesis entitled above presented by William Christopher Chandra (R12521251) candidate and hereby certify that it is worthy of acceptance.

口試委員 Oral examination committee:

黃世建 黃世建
（指導教授 Advisor）

李宏仁 李宏仁

邱聰智 邱聰智

系主管Director： 葛宇甯 葛宇甯

doi:10.6342/NTU202502280

ACKNOWLEDGEMENT

First of all, I would like to thank my advisor, Prof. Shyh-Jiann Hwang for guiding me throughout my master's research, which finally culminated in its completion. His patient and supportive guidance was invaluable and deeply appreciated.

I would also like to thank Prof. Hung-Jen Lee and Prof. Tsung-Chih Chiou for their willingness to serve as the oral defense committee and for giving valuable insights and suggestions for this research.

I would like to also thank my fellow labmates, 翰佑, 承鑫, and 宋羽. Their dedication and support during my Master's study significantly inspired my work. I wish them all the best in their future endeavors. For my junior labmates 翰維, 冠穎, 梓佑, 俊儒, and 語喬, I thank you for the companionship and support throughout my Master's study. I wish you a smooth journey through your research courses and study, and the ability to overcome any challenges along the way. I also extend my gratitude to my senior labmates, 黃強, 家瑋, 奕承, 于哲, 樸文, and 文成, for the advice and support during my Master's study.

Last but not least, I would like to thank my family for allowing and supporting me throughout this Master's study. Their unwavering support has tremendously helped me throughout the journey.

摘要

過去的實驗研究表示，填充磚牆具有顯著的側向強度，而這一貢獻在結構耐震評估中常被保守地忽略。本研究提出了一種新的側力位移曲線公式，整合了先前的研究成果，適用於各種填充磚牆配置：包括四面圍束、三面圍束，以及開口牆（含補強與未補強）。研究採用曲線疊加法來獲得填充磚牆的整體側力位移曲線。結果顯示，先砌填充磚牆與後砌填充磚牆在強度和勁度方面存在顯著差異。雖然本文提出的側力位移曲線總體上能很好地預測填充磚牆試體的行為，但部分試體（尤其是後砌填充磚牆試體）的強度被高估了。本研究建議改進強度公式，以考慮後砌填充磚牆不同的破壞路徑，尤其是在負向側力作用下或側力先作用於磚牆時。

關鍵詞： 填充磚牆、側力位移曲線、破壞路徑、曲線疊加法。

doi:10.6342/NTU202502280

ABSTRACT

Past experimental studies have demonstrated that brick infill walls possess significant lateral strength, a contribution often conservatively neglected in seismic evaluation. This study proposes new formulations for lateral load-deflection curves, integrating findings from previous research, applicable to various brick infill configurations: four-sided confined, three-sided confined, and walls with openings (with and without retrofit). The method of curves superposition is used to obtain the overall lateral load-deflection curves for brick infill walls. The results reveal a notable difference in strength and stiffness between pre-laid and post-laid brick infill walls. While the proposed lateral load-deflection curve generally predicts the behavior of the brick infill specimens well, strengths of some specimens, particularly post-laid brick infill specimens are found to be overestimated. This study recommends refining the strength formulations to account for the distinct failure mechanisms observed in post-laid brick infill, particularly under negative loading conditions or when the load strikes the brick wall first.

Keywords: brick infill, lateral load-deflection curve, failure path, curves superposition method.

doi:10.6342/NTU202502280

TABLE OF CONTENTS

doi:10.6342/NTU202502280

doi:10.6342/NTU202502280

LIST OF TABLES

doi:10.6342/NTU202502280

doi:10.6342/NTU202502280

LIST OF FIGURES

doi:10.6342/NTU202502280

doi:10.6342/NTU202502280

doi:10.6342/NTU202502280

doi:10.6342/NTU202502280

doi:10.6342/NTU202502280

doi:10.6342/NTU202502280

doi:10.6342/NTU202502280

doi:10.6342/NTU202502280

CHAPTER 1 INTRODUCTION

1.1 Motivation and Objective

Brick infill wall is a popular partition wall used in Taiwan, especially used in old buildings. From the post-earthquake reconnaissance, it is shown that many cracks were formed on the brick wall. This led to the question on whether to consider the presence of brick wall on the load transfer path. Due to the lack of the understanding of the brick wall behavior, the engineers often neglect the contribution of the brick wall in resisting the earthquakes.

However, decades of researches and experiments have shown that the brick wall has a considerable amount of strength that should also be considered. This becomes crucial when it comes to the evaluation of the existing buildings. By considering the strength contribution from the brick wall, we can minimize the underestimation of the structure's strength. Eventually, this would lead to the decrease on the amount of cost needed to repair or to retrofit these buildings.

This motivates this research to provide a more accurate lateral load-deflection curve describing the behavior of the brick wall when it is loaded with lateral load, such as earthquake. This way, the behavior of the overall structure with brick infill wall can be modeled and simulated more accurately.

doi:10.6342/NTU202502280

1.2 Methodology

The way this research conducting the analysis is through collecting the experiments conducted in the past. As in reality the brick wall is perforated for architectural use as shown in Figure 1-1, the analysis of this research is not limited to four-sided confined brick wall, but also included the three-sided confined, and brick wall with opening specimens. Additionally, the analysis also includes the brick wall with openings and retrofit specimens to measure the post-retrofit behavior of specimens, evaluating its efficiency in increasing the strength and stiffness.

After the behaviors of the specimens through its lateral load-deflection curves are obtained, the analysis model is proposed and validated by the collected experiment results. The analysis model is created by the modified formulation for brick infills lateral load-deflection curve superposed with column lateral load-deflection curve to obtain the overall lateral load-deflection curve.

doi:10.6342/NTU202502280

CHAPTER 2 LITERATURE REVIEW

This chapter will elaborate the literatures conducted in the past, that are used as the basis to proposed lateral load-deflection curve in this research. The first part is the review of the existing models, consisting of stiffness, strength and the lateral-load deflection curves for brick infills and column. The second part is the experiments conducted in the past, used as the basis and validation for the proposed lateral load-displacement curve.

2.1 Existing Models

2.1.1 Brick Infill Stiffness

(1) ASCE/SEI 41-06 (2007)

ASCE/SEI 41-06 (2007), adopting the brick infill stiffness formulation in FEMA 356 (2000), represent the stiffness of a brick infill panel by an equivalent diagonal strut as shown in Figure 2-1. The strut width a is empirically formulated as follows,

$$a = 0.175(\lambda_1 h_c)^{-0.4} r_{inf} \tag{2-1}$$

Where h_c is the height of column and r_{inf} is the diagonal length of infill panel.

The coefficient λ_1 is formulated as follows,

$$\lambda_1 = \left[\frac{E_b t_b \sin 2\theta}{4 E_c I_c h_b}\right]^{\frac{1}{4}} \tag{2-2}$$

Where E_b is the modulus of elasticity of brick infill, E_c is the modulus of elasticity of concrete, I_c is the moment of inertia of column, h_b is the brick infill height, t_b is brick

doi:10.6342/NTU202502280

infill thickness, and θ is the angle of the equivalent diagonal strut to the horizontal axis.

The modulus elasticity of concrete E_c is formulated as follows,

$$E_c = 4700\sqrt{f_c'} \tag{2-3}$$

According to FEMA 356 (2000), the elastic modulus of brick infill E_b can be formulated as follows,

$$E_b = 550 f_m' \tag{2-4}$$

Where f_m' is the brick prism compressive strength determined by ASTM C1314 (2000). The brick prism specimen tested according to ASTM C1314 (2000) is illustrated in Figure 2-2.

And θ can be formulated as follows,

$$\theta = \tan^{-1}\left(\frac{h_b}{\ell_b}\right) \tag{2-5}$$

Where ℓ_b is the brick infill length.

Using the axial stiffness formulation for a member, we can derive the axial stiffness of the equivalent diagonal strut, K that is formulated as follows,

$$K = \frac{E_b A_{str}}{r_{inf}} \tag{2-6}$$

Where A_{str} is the strut area, formulated as follows,

$$A_{str} = a \times t_b = 0.175\left(\left[\frac{E_b t_b \sin 2\theta}{4E_c I_c h_b}\right]^{\frac{1}{4}} h_c\right)^{-0.4} r_{inf} \times t_b \tag{2-7}$$

Substituting Equation (2-7) into Equation (2-6), we then obtain

$$K = \frac{E_b \times 0.175\left(\left[\dfrac{E_b t_b \sin 2\theta}{4E_c I_c h_b}\right]^{\frac{1}{4}} h_c\right)^{-0.4} r_{inf} \times t_b}{r_{inf}} \tag{2-8}$$

Rearranging, we obtain

$$K = 0.2\left(\frac{E_c I_c}{h_c^4 \sin 2\theta} h_b (E_b t_b)^9\right)^{0.1} \tag{2-9}$$

However, the stiffness formulation shown in Equation (2-9) is the axial stiffness of the equivalent diagonal strut. In order to obtain the corresponding lateral stiffness of the brick infill wall, we need to do transformation from the axial stiffness of diagonal strut obtained in Equation (2-9) to the lateral stiffness as shown in Figure 2-3,

$$K = \frac{P_d}{\Delta_d} = \frac{V_b/\cos\theta}{\Delta_b \cos\theta} = 0.2\left(\frac{E_c I_c}{h_c^4 \sin 2\theta} h_b (E_b t_b)^9\right)^{0.1} \tag{2-10}$$

Where P_d is the equivalent diagonal strut force, Δ_d is the equivalent diagonal strut displacement, V_b is the lateral strength of brick infill, and Δ_b is the lateral displacement of brick infill.

Rearranging the Equation (2-10), we can obtain the lateral stiffness of brick infill K_b,

$$K_b = \frac{V_b}{\Delta_b} = 0.2\left(\frac{E_c I_c}{h_c^4 \sin 2\theta} h_b (E_b t_b)^9\right)^{0.1} \cos^2\theta \tag{2-11}$$

As θ is related to h_b/ℓ_b, as shown in Equation (2-5), the change in h_b/ℓ_b would lead to the change in K_b. Figure 2-4 shows the relationship between brick infill stiffness K_b and infill height-to-length ratio h_b/ℓ_b. As can be seen in Figure 2-4, greater h_b/ℓ_b leads to lesser K_b. For h_b/ℓ_b less than about 2, the brick infill stiffness K_b is rapidly decreasing. While for h_b/ℓ_b greater than about 2, the brick infill stiffness K_b is decreasing more gradually.

(2) ASCE/SEI 41-13 (2014)

ASCE/SEI 41-13 (2014), which method followed by ASCE/SEI 41-17 (2017), and ASCE/SEI 41-23 (2023), simulates the stiffness of an uncracked infilled frame by treating the structure as a composite cantilever column. In this method, the column acts as a flange and the brick infill as the web, as depicted in Figure 2-6. The stiffness of this cantilever column is formulated as follows,

$$K_{ini} = \frac{1}{\frac{1}{K_{fl}} + \frac{1}{K_{sh}}} \tag{2-12}$$

Where K_{fl} is the flexural stiffness of composite cantilever column, formulated as follows,

$$K_{fl} = \frac{3E_c I_{ce}}{h_{cb}^3} \tag{2-13}$$

Where I_{ce} is the moment of inertia of the equivalent transformed concrete, and h_{cb} is the height of the composite cantilever column.

On the other hand, K_{sh} is the shear stiffness of composite cantilever column, assuming that the shear stress only distributed to the brick infill wall section. Hence, the shear stiffness of composite cantilever column is formulated as follows,

$$K_{sh} = \frac{G_b A_w}{h_w} \tag{2-14}$$

Where A_w is the cross-sectional area of the brick infill wall, h_w is the height of the brick infill wall, and G_b is the shear modulus of the brick infill wall formulated according to TMS 402-11 (2011) as follows,

doi:10.6342/NTU202502280

$$G_b = 0.4E_b \tag{2-15}$$

Where the elastic modulus for clay masonry E_b is formulated as follows,

$$E_b = 700f'_m \tag{2-16}$$

f'_m is the brick prism compressive strength determined by ASTM C1314 (2000).

(3) Technology Handbook for Seismic Evaluation and Retrofit of School Buildings (Third Edition) (NCREE, 2013)

NCREE (2013) derived the stiffness of brick infill based on Hooke's Law, plane stress-strain and strain-displacement relationship as follows,

$$\frac{V_b}{\Delta_b} = \frac{E_u \times t_b}{\left[1.475\left(\frac{h_b}{\ell_b}\right)^{-1} + 2.2625\left(\frac{h_b}{\ell_b}\right) + 2.225\left(\frac{h_b}{\ell_b}\right)^{3}\right]} \tag{2-17}$$

Where E_u is the modulus of elasticity of brick infill, formulated as follows

$$E_u = \left(102.35 - 39.23\frac{h_b}{\ell_b}\right)\eta f_{bc}^{0.7} f_{mc}^{0.3} \tag{2-18}$$

Where $0.5 \leq {h_b}/{\ell_b} \leq 2$, η is the modification factor for the modulus of elasticity of brick infill, η is equal to 0.556 for four-sided confined brick infill and 0.367 for three-sided confined brick infill.

. Figure 2-5 shows the relationship between brick infill stiffness ${V_b}/{\Delta_b}$ and infill height-to-length ratio ${h_b}/{\ell_b}$ for the range limited between 0.5 and 2. As can be seen in Figure 2-5, greater ${h_b}/{\ell_b}$ leads to lesser K_b. Comparing the relationship between brick infill stiffness and ${h_b}/{\ell_b}$ of NCREE (2013) in Figure 2-5 and that of ASCE/SEI 41-06 (2007) in Figure 2-4, both agree that greater ${h_b}/{\ell_b}$ results in lesser brick infill stiffness.

However, the limited range of h_b/ℓ_b between 0.5 to 2 that is applicable to the brick infill stiffness formulation in NCREE (2013) makes it less robust for the case of brick infills with h_b/ℓ_b outside of that range.

2.1.2 Failure Path Strength - Chen (2003)

Chen (2003) suggests that the strength of brick infill wall can be estimated by considering its failure path.

(1) Failure mode strength

The failure path is consisted of three types of failure modes, the horizontal interface sliding failure, vertical interface splitting failure, and brick vertical splitting failure, as illustrated in Figure 2-7, Figure 2-8, and Figure 2-9, respectively. Each failure mode has its corresponding strength as will be described as follows,

a. Horizontal interface sliding shear strength (τ_f)

$$\tau_f = 0.0258(f_{mc})^{0.885} + (0.654 + 0.00514 f_{mc})\sigma_N \quad (2\text{-}19)$$

where f_{mc} is the 50-mm mortar cube compressive strength (MPa) determined by ASTM C109 (2008), and σ_N is the axial compressive stress (MPa).

b. Vertical interface splitting strength (f_{mt})

$$f_{mt} = 0.232(f_{mc})^{0.338} \quad (2\text{-}20)$$

c. Brick vertical splitting strength (f_{bt})

$$f_{bt} = 0.22 f_{bc} \quad (2\text{-}21)$$

Where f_{bc} is the solid clay brick compressive strength (MPa) determined by CNS 1127.

(2) Critical cracking angle

Chen (2003) also suggests different critical cracking angle for different types of bond as shown in Figure 2-10, as described as follows,

a. English bond

$$\tan\theta_c = \frac{2(h+g_h)}{2(w+g_v)} \tag{2-22}$$

b. Flemish bond

$$\tan\theta_c = \frac{2(h+g_h)}{w+\ell+2g_v} \tag{2-23}$$

c. Two stretching and one heading bond

$$\tan\theta_c = \frac{3(h+g_h)}{\ell+g_v} \tag{2-24}$$

d. Stretching bond

$$\tan\theta_c = \frac{2(h+g_h)}{\ell+g_v} \tag{2-25}$$

Where h is the brick unit height, ℓ is the brick unit length, g_h is the horizontal mortar gap width, and g_v is the vertical mortar gap width.

(3) Peak strength

By superimposing the failure mode strengths along the failure path multiplied by its corresponding cross-sectional area, we can obtain the peak strength of the entire brick infill wall. Depending on the confinement conditions of brick infill walls, Chen (2003) suggests different strength formulations for four-sided confined and three-sided confined brick infill walls, as described follows,

doi:10.6342/NTU202502280

a. Four-sided confined brick infill wall strength

Based on the infill height-to-length ratio and the critical cracking angle of bond used, the peak strength formulation for the four-sided confined brick infill wall is different.

- For $h_b/\ell_b \leq \tan\theta_c$,

When the infill height-to-length ratio h_b/ℓ_b is less than or equal to the tangent of bond critical cracking angle $\tan\theta_c$, the failure path of such brick infill wall is illustrated in Figure 2-11(a). The failure path of the brick infill wall is idealized to crack on left and right sections of the infill panel with bond critical cracking angle θ_c up to half of the brick infill wall height, and horizontal crack on the middle section of infill panel. Besides, the failure path occurs along the interface between brick units.

Based on the described failure path shown in Figure 2-11(a), the peak strength formulation for four-sided confined brick infill walls with h_b/ℓ_b less than or equal to $\tan\theta_c$ is formulated as follows,

$$V_b = \tau_f(\ell_b \times t_b) + 0.45 f_{mt}(h_b \times t_b) \tag{2-26}$$

Where the first part of the equation corresponds to the strength contribution from the horizontal interface sliding failure and the second part of the equation corresponds to the strength contribution from the vertical interface splitting failure.

Due to the experiment observation that vertical interface splitting strength f_{mt} is a

doi:10.6342/NTU202502280

brittle failure and the fact that strength of different vertical interface splitting failures at different locations in the panel cannot reach its strength at the same time, its strength contribution to the overall infill panel strength in Equation (2-26) is reduced to 45% of its original strength. This 45% reduction of strength is suggested based on the experiment observations. While for the horizontal interface sliding shear strength τ_f, due to the experimental observation that it is a ductile failure and its strength can be maintained through a long deformation, as shown in Figure 2-12, therefore no reduction of strengths is applied to it in Equation (2-26).

- For ${}^{h_b}/_{\ell_b} > \tan\theta_c$,

When the infill height-to-length ratio ${}^{h_b}/_{\ell_b}$ is greater than the tangent of bond critical angle $\tan\theta_c$, the failure path of such brick infill wall is illustrated in Figure 2-11(b). The failure path of the brick infill wall is idealized to crack on two sides of the panel with bond critical cracking angle θ_c up to half of the brick infill wall length, and vertical crack on the middle part of panel. The failure path on two sides of the panes occurs along the interface between brick units, while the failure path on middle part of panel splits both the interfaces between brick units and also the brick units.

This feature of the failure path crossing the brick units highlights the difference between failure paths of brick infills with ${}^{h_b}/_{\ell_b}$ less than or equal to $\tan\theta_c$ and brick infills with ${}^{h_b}/_{\ell_b}$ greater than $\tan\theta_c$. As the brick vertical splitting strength f_{bt} is

doi:10.6342/NTU202502280

usually greater than the horizontal interface sliding shear strength τ_f and the vertical interface splitting strength f_{mt}. Such brick infills with ${}^{h_b}/_{\ell_b}$ greater than $\tan\theta_c$ would be having greater strength advantage compared to the brick infills with ${}^{h_b}/_{\ell_b}$ less than or equal to $\tan\theta_c$.

Based on the described failure path shown in Figure 2-11(b), the peak strength formulation for four-sided confined brick infill walls with ${}^{h_b}/_{\ell_b}$ greater than $\tan\theta_c$ is formulated as follows,

$$\begin{aligned} V_b &= \tau_f(\ell_b \times t_b) + 0.45 f_{mt}(l_b \tan\theta_c \times t_b) \\ &\quad + 0.45\left(\frac{f_{mt}+f_{bt}}{2}\right)(h_b' - \ell_b \tan\theta_c) \times t_b \end{aligned} \tag{2-27}$$

Where h_b' is the effective height of failure path, formulated as follows,

$$h_b' = \min(h_b, \ell_b) \tag{2-28}$$

In Equation (2-27), the first part of the equation corresponds to the strength contribution from the horizontal interface sliding failures on the two sides of the panel, the second part of the equation corresponds to the strength contribution from the vertical interface splitting failures on two sides of the panel, and the third part of the equation corresponds to the average of the strength contributions from both the vertical interface splitting failures and brick vertical splitting failures on the middle part of the panel.

Similar to vertical interface splitting strength f_{mt} nature, experiment observation showed that brick vertical splitting strength f_{bt} is a brittle failure and the fact that strength of different brick vertical splitting failures at different locations in the panel

doi:10.6342/NTU202502280

cannot reach its strength at the same time, its strength contribution to the overall infill panel strength in Equation (2-27) is reduced to 45% of its original strength.

b. Three-sided confined brick infill wall strength

The idealized failure path of three-sided confined brick infill wall is shown in Figure 2-19. The failure path of the three-sided confined brick infill wall is idealized to crack on one side near the force end with critical cracking angle θ_c up to half of the brick infill wall length, and horizontal crack on the rest half section of the panel.

Based on the described failure path shown in Figure 2-13, the peak strength formulation for three-sided confined brick infill is formulated as follows,

$$V_b = \tau_f(\ell_b \times t_b) + 0.45 f_{mt}(h_2 \times t_b) \qquad (2\text{-}29)$$

Where

$$h_2 = 0.5\ell_b \tan\theta_c \leq h_b \qquad (2\text{-}30)$$

In Equation (2-29), the first part of the equation corresponds to strength contribution from the horizontal interface sliding failures, and the second part of the equation corresponds to the strength contribution from the vertical interface splitting failure. Due to its brittle nature, the vertical interface splitting strength f_{mt} in Equation (2-29) is reduced to 45% of its original strength.

(4) Residual strength

After reaching the peak lateral strength, the vertical splitting strengths f_{mt} and f_{bt} reduces gradually due to its brittle failure nature. While, the horizontal interface sliding

doi:10.6342/NTU202502280

shear strength τ_f with its ductile nature can still maintain its original strength. From the experimental observations, when the displacement reaches two times the peak lateral displacement ($2\Delta_b$), the vertical splitting strengths f_{mt} and f_{bt} are completely gone, leaving only the horizontal interface sliding shear strength τ_f contributing to the infill strength. In addition, based on the experimental observations this residual strength is limited to 0.6 times peak lateral strength ($0.6V_b$).

The formulation of residual strength for four-sided confined brick infill is formulated as follows,

$$V_r = \tau_f(\ell_b \times t_b) \leq 0.6V_b \tag{2-31}$$

The reduction from the peak lateral strength to residual strength is suggested to be linearly reducing.

(5) Ultimate point

Based on the experiment results, the residual strength is plateaued until it is completely gone at ultimate displacement (Δ_u). The ultimate displacement (Δ_u) is suggested to be 2% of infill wall height considering the experiment results and conservatism, formulated as follows,

$$\Delta_u = 0.02h_b \tag{2-32}$$

2.1.3 Lateral Load - Displacement Curve

Below are the existing models for the lateral load-displacement curve for brick infill wall in RC frame that are used as the basis and reference for the proposed model. Since the brick infill wall in RC frame consists of brick wall and columns to resist the lateral load, most of the existing models described herein used separated model for brick infill and column, and then used the method of curves superposition for combining the brick infill and column lateral load-deflection curves. The detail of the method of curves superposition will be explained in more detail in Chapter 3.

(1) NCREE/TEASPA (2020)

a. Four-sided confined brick infill

NCREE/TEASPA (2020) simulates the lateral load-deflection curve for four-sided confined brick infill, as shown in Figure 2-14.

- Stiffness

The formulated stiffness equation and the corresponding modulus of elasticity of brick infill are shown in Equation (2-17) and (2-18), respectively.

- Peak strength

For the peak lateral strength V_b, it is the same as formulated by Chen (2003), i.e., Equation (2-26) and Equation (2-27). Dividing the peak lateral strength by the stiffness formulated in Equation (2-17), we can obtain the peak lateral displacement Δ_b.

- Residual strength

The residual strength V_r follows the same formulation suggested by Chen (2003) in

Equation (2-31).

- Ultimate point

As suggested by Chen (2003), the ultimate displacement is suggested to be 2% of the infill wall height, as formulated in Equation (2-32).

b. Three-sided confined brick infill

From the results observations in (Chiou & Hwang, 2015), it is shown that the stiffness from the ASCE/SEI 41-06 (2007) compared to the stiffness from NCREE (2013) matches better with the stiffness of the test specimens. The reason for the better prediction of stiffness by ASCE/SEI 41-06 (2007) was assumed to be the incorporation of the column stiffness to the brick infill wall stiffness. This led to an attempt to improve the stiffness formulation of NCREE (2013) by Chiou (2015).

However, due to new update of the ASCE standard to ASCE/SEI 41-13 (2014), superseding the ASCE/SEI 41-06 (2007), the stiffness formulation of ASCE/SEI 41-13 (2014) was being adopted in NCREE/TEASPA (2020).

The overall lateral load-displacement curve of three-sided confined brick infill wall is depicted in Figure 2-16.

- Stiffness

The stiffness equation of brick infills in NCREE/TEASPA (2020) refers to the stiffness equation of an uncracked infilled frame K_{ini} specified in ASCE/SEI 41-13

doi:10.6342/NTU202502280

(2014), as shown in Equation (2-12). In order to obtain the stiffness of the brick infill itself the stiffness of the column K_c is deducted from the infilled frame stiffness K_{ini}. Then, based on the experiment results, it is multiplied by 0.35 to obtain the cracked stiffness of brick infill. The formulation of the obtained brick infill stiffness K_b is formulated below,

$$K_b = (K_{ini} - K_c) \times 0.35 \tag{2-33}$$

Where the column stiffness is formulated as follows,

$$K_c = \frac{3E_c I_c}{h_c^3} \tag{2-34}$$

Note that the elastic modulus of brick infill E_m follows the recommendation from FEMA 356 (2000), i.e., Equation (2-4).

- Peak strength

The formulation of peak strength V_b for three-sided confined brick infill is formulated as follows,

$$\begin{aligned} V_b = \tau_f \left(\frac{2}{3}\ell_b \times t_b\right) + 0.225 f_{mt} \left(\frac{2}{3}\ell_b \tan\theta_c \times t_b\right) \\ + 0.225\left(\frac{f_{mt} + f_{bt}}{2}\right)\left(h_b' - \frac{2}{3}\ell_b \tan\theta_c\right) \times t_b \end{aligned} \tag{2-35}$$

Where h_b' is the effective height of failure path.

For single-sided wing wall in Figure 2-15(a), the formulation of h_b' is as follows,

$$h_b' = \min\left(\frac{h_b}{\frac{2}{3}\ell_b + \ell_c - \frac{a_c}{3}} \times \frac{2}{3}\ell_b, \ell_b\right) \tag{2-36}$$

For double-sided wing wall in Figure 2-15(b), the formulation of h_b' is as follows,

$$h_b' = \min\left(\frac{h_b}{\frac{2}{3}\ell_b \times 2 + \ell_c} \times \frac{2}{3}\ell_b, \ell_b\right) \tag{2-37}$$

Where ℓ_c is the depth of column along the loading direction.

The elastic compression depth of column a_c can be formulated according to Paulay and Priestley (1992) as follows,

$$a_c = \left(0.25 + 0.85\frac{N}{A_g f_c'}\right)\ell_c \tag{2-38}$$

Where N is the axial compression load, and A_g is the gross cross-sectional area of column.

The lateral strength formulation for the three-sided confined brick infill wall in Equation (2-35) is similar to strength formulation of four-sided confined brick infill in Equation (2-27). It consisted of three parts of strength contribution, that are horizontal interface sliding strength in the first part, vertical interface splitting strength in the second part, and the average of the vertical interface splitting strength and the brick vertical splitting strength in the third part.

However, there are three differences between the Equation (2-35) and the Equation (2-27). First, the lengths of the crack in the first, second, and third part herein is $\frac{2}{3}\ell_b$, $\frac{2}{3}\ell_b \tan\theta_c$, and $h_b' - \frac{2}{3}\ell_b \tan\theta_c$. Second, due to the lesser restraints in the three-sided confined brick infill, the strength contribution from vertical interface splitting strength and brick vertical splitting strength is reduced to 22.5% of its original strength. Third, the formulation of the h_b' is also different for the three-sided confined brick infill wall,

doi:10.6342/NTU202502280

as formulated in Equation (2-36) and Equation (2-37).

- Residual strength

The residual strength V_r when the lateral displacement of brick infill reaches twice the peak displacement, i.e., $2\Delta_b$ is the same as that formulated by Chen (2003) in Equation (2-31).

- Ultimate point

Due to the fact that the three-sided confined brick infill wall has one less restraint side compared to that of four-sided confined brick infill wall, the residual strength V_r is assumed linearly decreasing until the ultimate displacement Δ_u is reached, which formulated in Equation (2-32).

(2) Cheng (2021)

The overall lateral load-displacement curves for four-sided confined brick infill and three-sided confined brick infill follow NCREE/TEASPA (2020), as depicted in Figure 2-14 and Figure 2-16, respectively.

a. Modified material strength

There is a difference in test methods for brick compressive strength f_{bc} in CNS 1127 (old code) and CNS 382 (new code) as depicted in Figure 2-17. In CNS 1127, the brick unit is firstly cut into half perpendicular to its length direction, then the two cut pieces are stacked together with cement bedding between the brick pieces The top and bottom

doi:10.6342/NTU202502280

of the specimen is also capped with cement. On the other hand, in CNS 382, the half-cut brick unit is used with pieces of paper capping the specimen.

Based on the research and experiments conducted by Lin (2013), the relationship between brick compressive strength f_{bc} determined by CNS 1127 (old code) and CNS 382 (new code) was established as shown in Figure 2-18.

The comparison of the mean of f_{bc} between the two test methods can be formulated as follows,

$$f_{bc,CNS1127} = \frac{f_{bc,CNS382}}{1.67} \tag{2-39}$$

It can be seen from Figure 2-18 that brick compressive strength f_{bc} tested in CNS 1127 produces lower strength than f_{bc} tested in CNS 382. Cheng (2021) argues that the CNS 1127 cannot well predict the uniaxial compressive strength of brick unit. One of the reasons is that the two half-cut pieces of brick unit might have different in strength, which exacerbated with not perfectly cut half pieces, leading to a different in size between the two pieces. Additionally, a typically lower cement strength compared to brick strength may affect the tested brick strength to be lower than it is supposed to be. As a result, CNS 382 is generally better at capturing the brick compressive strength f_{bc}.

Substituting $f_{bc,CNS1127}$ in Equation (2-21) with Equation (2-39), we obtain

$$f_{bt} = \frac{0.22}{1.67} f_{bc,CNS382} = 0.136 f_{bc,CNS382} \tag{2-40}$$

Therefore, if the brick compressive strength f_{bc} is determined by CNS 382 or ASTM C67 (2008) method, the brick vertical splitting strength f_{bt} should be calculated

doi:10.6342/NTU202502280

using Equation (2-40) as opposed to the original equation in Equation (2-21).

b. Four-sided and three-sided confined brick infill

- Stiffness

Chiou and Hwang (2015) compares the lateral load-displacement curves for four-sided confined brick infill wall from ASCE/SEI 41-06 (2007) and NCREE (2013). From the test observations, the stiffness equation of ASCE/SEI 41-06 (2007) matches the stiffness of the test specimens better than stiffness equation of NCREE (2013). This leads Cheng (2021) to propose the stiffness equation for four-sided confined brick infill using the ASCE/SEI 41-06 (2007) as the basis. Moreover, Cheng (2021) proposed to use the same stiffness equation basis for both four-sided and three-sided confined brick infill, making the stiffness equation more direct and simple.

Cheng (2021) uses stiffness formulation of the ASCE/SEI 41-06 (2007) shown in Equation (2-9) as the basis. In addition, Cheng (2021) introduced α, β, and γ parameters to the stiffness equation, as shown below,

$$K = 0.2\left(\frac{E_c I_c}{h_c^4 \sin 2\theta} h_b (E_b t_b)^9\right)^{0.1} \times \alpha\beta\gamma \tag{2-41}$$

Where α, β, and γ are the stiffness modification factors.

α is the infill length-to-height ratio $\left(\frac{1}{4} \leq \frac{\ell_b}{h_b} \leq \frac{3}{2}\right)$.

β is the integrity factor considering the column-brick wall separation during the loading. For four-sided confined brick infill wall, β is equal to 1. For three-sided

doi:10.6342/NTU202502280

confined brick infill wall, β is equal to 1 when the lateral loading strikes the column first or for double-sided brick wing wall, while β is equal to $\frac{1}{3}$ when the lateral loading strikes the brick wall first. This is due to the fact that when the load strikes the brick wall first, the column-wall separation is likely to happen, reducing the stiffness of the brick infill wall.

γ is the confinement factor considering the effect of the confinement conditions to the brick infill stiffness γ is equal to 1.2 for four-sided confined brick infill, and is equal to 1 for three-sided confined brick infill.

The introduction of β and γ parameters seems appropriate as the brick infill stiffness equation in Equation (2-9) may only applicable to four-sided confined brick infill and does not consider the column-wall separation effect caused by different loading direction in three-sided confined brick infill. However, the introduction of α parameter is not appropriate as the infill length-to-height ratio has been included implicitly in calculation of θ parameter, formulated in Equation (2-5).

In addition, the brick infill stiffness used by Cheng (2021) is an axial stiffness of diagonal strut as derived in Equation (2-9). To obtain the corresponding lateral stiffness, Equation (2-11) should be used instead.

- Peak strength

The peak lateral strength V_b and peak lateral displacement Δ_b for four-sided confined and three-sided confined brick infill follow the same formulations as in NCREE/TEASPA (2020).

- Residual strength

The residual strength V_r when the lateral displacement of brick infill reaches twice the peak displacement, i.e., $2\Delta_b$ follows the same formulation in NCREE/TEASPA (2020).

- Ultimate point

The formulation of ultimate deflection Δ_u follows the same formulation in NCREE/TEASPA (2020).

c. Brick infill walls with openings

In addition to four-sided and three-sided confined brick infill wall, Cheng (2021) also proposes the lateral load-displacement curve for the brick wall with opening and retrofit. The most important step in analyzing brick wall with opening is the shear element determination.

- Shear element

Figure 2-19 shows the shear element determination for a specimen with door and window openings. The middle infill panel between the openings is not included as shear element due to the fact that it is only two-sided confined and diagonal strut is not likely to occur on that panel.

doi:10.6342/NTU202502280

- Stiffness and strength

For the analysis of the brick infill wall with opening, it follows the same formulation of three-sided confined explained previously by considering each shear element as standalone element and use the method of curves superposition to obtain the overall lateral load-displacement curve.

d. Brick infill walls with openings and retrofit

- Shear element

Figure 2-20 shows the placement of CFRP retrofit on the original specimen with door and window openings. As a result of the retrofit, the strength of the retrofitted element is calculated using four-sided confined strength formulation in Equation (2-26) and Equation (2-27). In addition to that, the middle infill panel who was not included previously is now being considered as shear element, as shown in Figure 2-21.

- Stiffness and strength

As that there is no confining column on the middle panel in Figure 2-21, the stiffness formulation in Equation (2-41) is unable to be calculated. Cheng (2021) proposed the stiffness equation for shear element without confining column is to be formulated as follows,

$$K = 0.2\left(\frac{1}{\sin 2\theta}(E_b t_b)^{10}\right)^{0.1} \times \alpha\beta\gamma \tag{2-42}$$

Equation (2-42) is produced by setting the columns parameters in Equation (2-41)

doi:10.6342/NTU202502280

to 1, then h_b parameter is removed and the power of $E_b t_b$ is increased to make sure that the calculated result in Equation (2-42) is in stiffness unit.

As for the strength formulation, due to the additional retrofit, the four-sides of each brick infill panel in a brick wall with opening are now confined. Therefore, the strength formulation of four-sided confined brick infill is used to calculate the strength of each brick infill panel. The overall lateral load-displacement curve is then obtained through the method of curves superposition.

(3) Column lateral load-displacement curve - Shen et al. (2021), ASCE/SEI 41-13 (2014)

Depending on the failure modes of the column, ASCE/SEI 41-13 (2014) stipulates the lateral load-deflection curve of column. There are three types of column failure modes, that are flexural failure, flexural-shear failure, and shear failure.

Flexural failure occurs when the flexure strength of column V_{mn} is less than or equal to 0.6 times the column shear strength V_n, flexural-shear failure occurs when the flexure strength of column V_{mn} is between 0.6 to 1.0 times the column shear strength V_n, and shear failure occurs when flexure strength of column V_{mn} is greater than 1.0 times the column shear strength V_n.

As most of the column specimens in this research are classified as flexural-shear failure, the lateral load-deflection curve for column with flexural-shear failure will be

doi:10.6342/NTU202502280

elaborated as the following and the overall lateral load-displacement curve for column under flexural-shear failure is depicted on Figure 2-25.

a. Cracking point (V_{cr}, Δ_{cr})

For simplicity, the maximum strength of shear cracking point recommended in ASCE/SEI 41-13 (2014) is being used, that is 60% of the column shear strength.

$$V_{cr} = 0.6V_n \tag{2-43}$$

The shear strength of column V_n is calculated as follows,

$$V_n = \min\left(V_{n,c}, V_{n,t}\right) \tag{2-44}$$

Where $V_{n,c}$ is the shear compression strength, and $V_{n,t}$ is the shear tension strength.

The shear compression strength $V_{n,c}$ is calculated based on Softened Strut-and-Tie model (2017), as shown follows,

$$V_{n,c} = K\zeta f_c' A_{str} \cos\theta \tag{2-45}$$

Where θ is inclination angle between the primary diagonal strut and horizontal axis. θ is equal to $65°$ when shear tension strength $V_{n,t}$ is less than the shear compression strength $V_{n,c}$.

K is strut-and-tie index as formulated below,

$$K = \tan^A\theta + \cot^A\theta - 1 + 0.14B \leq 1.64 \tag{2-46}$$

ζ is softening coefficient of cracked reinforced concrete as formulated below,

$$\zeta = \frac{3.35}{\sqrt{f_c'}} \leq 0.52 \tag{2-47}$$

A_{str} is effective area at the end of diagonal strut as formulated below,

doi:10.6342/NTU202502280

$$A_{str} = b \times a_c \tag{2-48}$$

Where b is the width of the column cross section.

The shear tension strength $V_{n,t}$ is calculated using ASCE/SEI 41-13 (2014) formulation, as shown as follows,

$$V_{n,t} = \frac{A_v f_y d}{s} + \left(\frac{0.5\sqrt{f_c'}}{M/_{Vd}} \sqrt{1 + \frac{N}{0.5\sqrt{f_c'}A_g}} \right) 0.8A_g \tag{2-49}$$

Where A_v is the area of transverse reinforcements, f_y is the yield strength of transverse reinforcement, d is the effective depth of column, s is the spacing of transverse reinforcement, $M/_{Vd}$ is the ratio of the largest moment to shear times effective depth but shall not be taken greater than 4 or less than 2.

According to Shen et al. (2021), the displacement of the cracking point Δ_{cr} is calculated as follows,

$$\Delta_{cr} = \Delta_{f,cr} + \Delta_{s,cr} = \frac{V_{cr}H^3}{12\left(E_c I_{eff}\right)} + \frac{V_{cr}H}{0.4E_c bd} \tag{2-50}$$

Where H is clear height of the column, d is effective depth of column cross section $E_c I_{eff}$ is the effective flexural stiffness based on ASCE/SEI 41-13 (2014), as shown in Figure 2-22. It shows that columns with compression load greater than $0.5A_g f_c'$ are having $0.7E_c I_g$, while columns with compression load less than $0.1A_g f_c'$ are having $0.3E_c I_g$. For compression loads in between, linear interpolation is being used.

b. Strength point (V_{mn}, Δ_{mn})

For a column subjected to a double curvature bending, the shear corresponding to

doi:10.6342/NTU202502280

development of nominal moment strength is calculated as follows,

$$V_{mn} = \frac{2M_n}{H} \tag{2-51}$$

Where M_n is nominal moment strength (N-mm), in this case was calculated by sectional analysis and Whitney stress block.

According to Shen et al. (2021), Δ_{mn} can be calculated as follows,

$$\begin{aligned}\Delta_{mn} &= \Delta_{f,n} + \Delta_{s,n} \\ &= \frac{V_{mn}H^3}{12\left(E_c I_{eff}\right)} + \frac{V_{mn}L_B}{0.4E_c bd} + 2 \times 0.006 \sin 2\theta \times L_D \times \frac{V_{mn}}{V_n}\end{aligned} \tag{2-52}$$

Where L_D is length of column D-region, formulated as follows,

$$L_D = d \times \tan\theta \tag{2-53}$$

L_B is length of column B-region, formulated as follows,

$$L_B = H - 2 \times L_D \tag{2-54}$$

The D-region and B-region of column are depicted in Figure 2-23.

c. Post-strength point (V_{mn}, Δ_s)

The strength V_{mn} formulated in Equation (2-51) is plateaued until the lateral displacement reaches Δ_s. The modeling parameter a based on ASCE 41-13 (2014), as shown in Figure 2-24 is used to determine the displacement at post-strength point Δ_s, that is formulated as follows,

$$\Delta_s = \Delta_{mn} + a \times H \tag{2-55}$$

d. Collapse point ($0, \Delta_a$)

The modeling parameter b in ASCE 41-13 (2014), as shown in Figure 2-24 is used to determine the displacement at axial collapse point Δ_a, that is formulated as follows,

$$\Delta_a = \Delta_{mn} + b \times H \qquad (2\text{-}56)$$

2.2 Test Specimens

2.2.1 Four-sided Confined Brick Infill

(1) Specimens B39-L, B83-L, B39-T, and B83-T (Chiou and Hwang, 2015)

According to Chiou and Hwang (2015), there were 4 four-sided confined brick infill specimens being tested under cyclic lateral loading. The test setup of the specimens is shown in Figure 2-26. The detail configuration of the specimens is shown in Figure 2-27. The test parameters and material properties of the specimens are shown in Table 2-2. There was no axial load applied on the specimens, as listed in Table 2-1. These specimens are pre-laid brick infill specimens with English bond. The description of pre-laid brick infill and English bond will be explained in the next section (Specimen CS and IS).

Based on the aforementioned stiffness formulation in Equation (2-17) and strength formulation in Equation (2-26) or Equation (2-27), it is known that the main parameters that affecting stiffness and strength of brick infill wall are height-to-length ratio of brick infill h_b/ℓ_b, and mortar compressive strength f_{mc}. These two parameters were then used as the key parameters to observe the resulted behavior of the brick infill wall specimens under lateral loading. The height-to-length ratio of brick infill used were 0.39 and 0.83,

doi:10.6342/NTU202502280

and the mortar compressive strength used were below 10 MPa (low-strength brick infill) and above 10 MPa (typical-strength brick infill). The geometry of solid clay brick unit is 200x95x53mm and the brick is pre-laid using English bond. To obtain the height-to-length ratio of brick infill equal to 0.83, an intermediate column is placed in the middle of the specimen B83 series. The test curves of specimens B39-L, B83-L, B39-T, and B83-T are shown in Figure 2-28. The maximum lateral strength and displacement at maximum lateral strength of the specimens are shown in Table 2-3. The failure condition of specimens at maximum strength is shown in Figure 2-29.

Based on Figure 2-28 and Table 2-3, it can be seen that the peak strength of Specimen B39 series is lower than that of the Specimen B83 series. Comparing the Specimen L (low-strength mortar) series and Specimen T (typical-strength mortar) series, the peak strength of Specimen L series is lower than that of the corresponding Specimen T series. These test results show that height-to-length ratio and mortar compressive strength are indeed important parameters to be considered in the strength prediction of brick infill.

(2) Specimens CS and IS (Lin, 2016)

There were two four-sided confined brick infill specimens that are Specimen CS and IS being tested by Lin (2016) under cyclic lateral loading. The test setup of the specimens is shown in Figure 2-30. The configuration and details of the two specimens

doi:10.6342/NTU202502280

is shown in Figure 2-31. The material properties of the confining frame and brick infill of the specimens are shown in Table 2-4 and Table 2-5, respectively. The axial loads applied to the specimens are shown in Table 2-1.

C in Specimen CS stands for confined masonry and I in Specimen IS stands for infills masonry. Confined masonry is a type of structure where the masonry constructed first before being confined by the columns. The confined masonry acts as main bearing load resisting element. The confining columns act as a tie member, enhancing the strength of the confined masonry. This column tie member is typically 200mm x 150mm in size, similar to the thickness of the masonry. On the other hand, infills masonry is typically a non-structural element where the infill is constructed after the RC frame is built. In infills masonry, the main structural elements resisting vertical and lateral loads is RC frame, which translated by its larger dimensions and well-reinforced columns and beams.

While the brick wall in Specimen CS was constructed before the RC frame, the RC frame with columns size of 300mm x 500mm still act as primary load resisting elements. Hence, a term of “pre-laid brick infill” is more appropriate in describing the Specimen CS. Conversely, for Specimen IS with brick wall constructed after the RC frame is built, a term of “post-laid brick infill” can be used. As Taiwan is an earthquake-prone country, having a typically large size of columns, the terms “pre-laid brick infill” and “post-laid

doi:10.6342/NTU202502280

brick infill” are more proper for brick wall in RC frame.

Figure 2-32 shows the difference on the interface between brick infill and confining frame for pre-laid and post-laid brick infill. The pre-laid method would introduce parts of brick infill to protrude into the concrete frame. On the other hand, the post-laid method would introduce a gap between the brick infill and the concrete frame, which later would be filled by mortar. This difference in laying process of brick infill would be the key parameter in this experiment to observe the resulted behavior of the four-sided confined brick infill under lateral loading. The specimens are laid with English bond and with 1B thickness, as shown in Figure 2-33.

The lateral load-displacement curves of Specimen CS and IS are shown in Figure 2-34(a) and (b), respectively. The maximum lateral strength and displacement at maximum lateral strength of the specimens are shown in Table 2-6. The failure condition of specimens CS and IS at maximum strength is shown in Figure 2-35 and Figure 2-36, respectively. From the test curves, it is shown that the Specimen CS has higher peak strength than Specimen IS. In terms of stiffness, Specimen CS also exhibits higher stiffness compared to Specimen IS. The main reason behind the superiority of pre-laid brick infill specimen is better linkage between the brick infill and the confining frame. This better linkage would hinder the separation between brick wall and confining frame, causing the load from both lateral and axial loads to be better transferred and

doi:10.6342/NTU202502280

distributed throughout the brick infill specimen.

(3) Specimens P1 and P2 (Wu, 2017)

There were two four-sided confined brick infill specimens that are Specimen P and A being tested by Lin (2016) under cyclic lateral loading. In order to avoid having the same specimens name with the other specimens, Specimens P and A are renamed into Specimens P1 and P2 in this study. The test setup of the specimens is shown in Figure 2-37. The configuration and details of the two specimens is shown in Figure 2-38. The material properties of the confining frame and brick infill of the specimens are shown in Table 2-7 and Table 2-8, respectively. The main difference between Specimens P1 and P2 is that Specimen P1 is pre-laid brick infill, while Specimen P2 is post-laid brick infill. There was no axial load applied to the specimens, as listed in Table 2-1.

The lateral load-displacement curves of the specimens are shown in Figure 2-39. The maximum lateral strength and displacement at maximum lateral strength of the specimens are shown in Table 2-9. The failure condition of the specimens at maximum strength is shown in Figure 2-40.

2.2.2 Three-sided Confined Brick Infill

(1) Specimens A and B (Lo, 2010)

There were two specimens of three-sided confined tested in Lo (2010), that are Specimen A and B. The test setup of the experiments is shown in Figure 2-41. The

doi:10.6342/NTU202502280

configuration and details of Specimens A and B are shown in Figure 2-42 and Figure 2-43, respectively. The material properties of the confining frame and brick infill of the specimens are shown in Table 2-10 and Table 2-11, respectively. The axial loads applied on the specimens are shown in Table 2-1.

The difference between the two specimens is that Specimen A is a single-sided brick infill wing wall with brick infill only on one side of column, while Specimen B is a double-sided wing wall with brick infill on two sides of column. The lateral load-displacement curves of the specimens are shown in Figure 2-44. The maximum lateral strength and displacement at maximum lateral strength of the specimens are shown in Table 2-12. The failure condition of the specimens at maximum strength is shown in Figure 2-45.

Comparing the test curves of the specimens, Specimen B with two brick infill panels on two sides of column is shown having almost twice the strength of Specimen A with brick infill only on one side of column.

(2) Specimens C, AC, AL, BC, and BS (Lin, 2011)

Continuing the Lo (2010) experiments, Lin (2011) conducted experiments on five brick infill specimens. These 5 specimens are designed based on Specimen A and B and varied to observe the effect of the loading direction, loading type and brick infill length on the brick infill wing walls behavior.

doi:10.6342/NTU202502280

The test setup of the experiment is shown in Figure 2-46. The specimen configuration and details of Specimens C and AC are the same as Specimen A, shown in Figure 2-42. The difference between Specimens A and C is in the loading direction. Even though Specimens A and C have the same configuration and geometry, the lateral load in Specimen A strikes the column first, while in Specimen C it strikes the brick wall first. Specimen AC is subjected to cyclic loading, which is different from the monotonic loading applied to Specimen A and C. The specimen configuration of Specimen AL is shown in Figure 2-47. Specimen AL has the same loading direction and type as the Specimen A; however, the brick infill wall is longer.

The specimen configuration of Specimen BC is the same as Specimen B, as shown in Figure 2-43. However, the loading type between Specimens BC and B is different. Specimen BC is subjected to cyclic loading, while Specimen B is under monotonic loading. The specimen configuration of Specimen BS is shown in Figure 2-48. Specimen BS has the same loading direction and type as the Specimen B; however, the brick infill wall is shorter on both two sides.

The material properties of the confining frame and brick infill of the specimens are shown in Table 2-13 and Table 2-14, respectively. The axial loads applied on specimens are shown in Table 2-1. The lateral load-displacement curves of the specimens are shown in Figure 2-49. The maximum lateral strength and displacement at maximum

doi:10.6342/NTU202502280

lateral strength of the specimens are shown in Table 2-15. The failure condition of the specimens at maximum strength is shown in Figure 2-50.

Comparing test curves of Specimens A and C, the peak strength between the two specimens are similar; however, Specimen A exhibits higher stiffness than Specimen C. The reason for the higher stiffness in Specimen A is due to the loading in Specimen C strikes the brick wall first, causing the column and brick wall to separate more easily and the stiffness degradation would occur. Comparing test curves of Specimens A and C with AC, Specimen AC is shown to have lower strength than Specimens A and C due to more severe cracks caused by cyclic loading. Comparing test curves of Specimens A and AL, Specimen AL exhibits higher strength compared to Specimen A, due to the increase in brick wall length.

Similar to the comparison between Specimens AC and A, Specimen BC due to the cyclic loading, exhibits lower strength than Specimen B. With shorter brick wall length, Specimen BS exhibits lower strength and stiffness compared to Specimen B.

2.2.3 Brick Infill Walls with Openings

(1) Specimens CD and CW (Hsu, 2015)

There were two brick wall with opening specimens being tested by Hsu (2015), Specimens CD and CW. The test setup of the experiment is shown in Figure 2-51. The specimen configuration of Specimens CD and CW are shown in Figure 2-52 and Figure

doi:10.6342/NTU202502280

2-53, respectively. The material properties of the confining frame and brick infill of the specimens are shown in Table 2-16 and Table 2-17, respectively. The axial loads applied to specimens are shown in Table 2-1.

The difference between the two specimens is on the opening size, Specimen CD has larger opening, simulating a door opening, and Specimen CW has smaller opening to simulate a window opening. The lateral load-displacement curves of the specimens are shown in Figure 2-54. The maximum lateral strength and displacement at maximum lateral strength of the specimens are shown in Table 2-18. The failure condition of the specimens at maximum strength is shown in Figure 2-55.

Comparing the test curves of the two specimens, the stiffness of the specimens is similar; however, the Specimen CW exhibits higher strength than Specimen CD, due to its smaller opening.

(2) Specimen ID (Chao, 2015)

The test setup of the experiment is shown in Figure 2-56. The specimen configuration of Specimen ID is the same as Specimen CD shown in Figure 2-52; however, the brick infill in Specimen ID is post-laid instead of pre-laid in Specimen CD. The material properties of the confining frame and brick infill of the specimen are shown in Table 2-19 and Table 2-20, respectively. The axial load applied to the specimen is shown in Table 2-1.

doi:10.6342/NTU202502280

The test curve of Specimen ID is shown in Figure 2-57. The maximum lateral strength and displacement at maximum lateral strength of the specimen are shown in Table 2-21. The failure condition of the specimen at maximum strength is shown in Figure 2-58.

Comparing the test curves of Specimen CD and ID, Specimen ID with post-laid brick infill has lower peak strength and experienced more severe stiffness degradation before reaching its peak strength.

(3) Specimen IW (Tsai, 2016)

There was one brick infill wall with opening specimen tested by Tsai (2016), Specimen IW. The test setup of Specimen IW is shown in Figure 2-59. The configuration and details of Specimen IW is the same as Specimen CW shown in Figure 2-53; however, the brick infill is post-laid instead of pre-laid in Specimen CW. The material properties of the confining frame and brick infill of the specimens are shown in Table 2-16 and Table 2-22, respectively. The axial load applied on the specimens is shown in Table 2-1.

The test curve of Specimen IW is shown in Figure 2-60. The maximum lateral strength and displacement at maximum lateral strength of the specimen are shown in Table 2-23. The failure condition of the specimen at maximum strength is shown in Figure 2-61.

doi:10.6342/NTU202502280

Agreeing with the previously mentioned comparisons between pre-laid and post-laid specimens, Specimen IW with post-laid brick infill also exhibits lower strength and more severe stiffness degradation compared to Specimen CW.

(4) Specimens CD-e and ID-e (Lin, 2016)

There were two brick wall with opening specimens that are Specimens CD-e and ID-e being tested by Lin (2016). The brick infill in Specimen CD-e is pre-laid, while in Specimen ID-e it is post-laid. The test setup of the specimens is shown in Figure 2-30. The configuration and details of Specimens CD-e and ID-e are shown in Figure 2-62. The material properties of the confining frame and brick infill of the specimens are shown in Table 2-4 and Table 2-5, respectively. The axial loads applied on the specimens are shown in Table 2-1.

The test curves of the specimens are shown in Figure 2-63. The maximum lateral strength and displacement at maximum lateral strength of the specimens are shown in Table 2-24. The failure conditions of the Specimens CD-e and ID-e at maximum strength are shown in Figure 2-64 and Figure 2-65, respectively.

Matching with the comparison between pre-laid and post-laid four-sided confined brick infill specimens, Specimen ID-e with post-laid brick infill exhibits lower strength compared to Specimen CD-e.

doi:10.6342/NTU202502280

(5) Specimens CD-e-1.8 and CW-e-1.8 (Yang, 2017)

There were two brick infill wall with opening specimens being tested by Yang (2017), Specimens CD-e-1.8 and CW-e-.1.8. The test setup of the experiments is shown in Figure 2-66. The specimen configurations of Specimens CD-e-1.8 and CW-e-1.8 are shown in Figure 2-67 and Figure 2-68, respectively. The specimen configuration of Specimens CD-e-1.8 and CW-e-1.8 are similar to Specimens CD-e and CW-e, but with larger opening size. The material properties of the confining frame and brick infill of the specimens are shown in Table 2-25 and Table 2-26, respectively. The axial loads applied on the specimens are shown in Table 2-1.

The test curves of the specimens are shown in Figure 2-69. The maximum lateral strength and displacement at maximum lateral strength of the specimen are shown in Table 2-27. The failure conditions of Specimens CD-e-1.8 and CW-e-1.8 at maximum strength are shown in Figure 2-70 and Figure 2-71, respectively.

Comparing test curves of Specimen CD-e-1.8 and Specimen CD-e in Figure 2-63(a), Specimen CD-e exhibits higher strength. This shows that larger opening size has a negative effect on the strength of the brick infill wall with opening. Comparing test curves of Specimen CD-e-1.8 and Specimen CW-e-1.8, Specimen CW-e-1.8 exhibits higher strength than Specimen CD-e-1.8 due to its smaller opening size.

doi:10.6342/NTU202502280

(6) Specimens ID-e-1.8 and IW-e-1.8 (Tung, 2017)

There were two brick infill wall with opening specimens being tested by Tung (2017), Specimens ID-e-1.8 and IW-e-1.8. The test setup of the experiments is shown in Figure 2-72. The specimen configurations of Specimens ID-e-1.8 and IW-e-1.8 are the same as Specimen CD-e-1.8 and CW-e-1.8, as shown in Figure 2-67 and Figure 2-68, respectively. However, Specimens ID-e-1.8 and IW-e-1.8 are post-laid brick infill, while Specimen CD-e-1.8 and CW-e-1.8 are pre-laid brick infill. The material properties of the confining frame and brick infill of the specimens are shown in Table 2-28 and Table 2-29, respectively. The axial loads applied on the specimens are shown in Table 2-1.

The test curves of Specimens ID-e-1.8 and IW-e-1.8 are shown in Figure 2-73. The maximum lateral strength and displacement at maximum lateral strength of the specimens are shown in Table 2-30. The failure conditions of Specimens ID-e-1.8 and IW-e-1.8 at maximum strength are shown in Figure 2-74 and Figure 2-75, respectively.

Comparing test curves of Specimens CD-e-1.8 in Figure 2-69(a) and ID-e-1.8, both specimens have similar strength. This indicates that the strength difference between the pre-laid and post-laid specimens is not significant in larger door opening sizes.

Similar to the comparison between Specimens CD-e-1.8 and CW-e-1.8, Specimen ID-e-1.8 with door opening exhibits lower strength than in Specimen IW-e-1.8, due to its larger opening size.

doi:10.6342/NTU202502280

(7) Specimen IDW (Jhang, 2019)

There was one specimen of brick infill with opening being tested by Jhang (2019), Specimen IDW. The test setup of the experiments is shown in Figure 2-76. Specimen IDW is perforated with door and window openings, as shown in specimen configuration in Figure 2-77. The material properties of the confining frame and brick infill of Specimen IDW are shown in Table 2-31 and Table 2-32, respectively. The axial load applied on the specimen is shown in Table 2-1.

The test curve of Specimen IDW is shown in Figure 2-78. The maximum lateral strength and displacement at maximum lateral strength of the specimen are shown in Table 2-33. The failure condition of Specimen IDW at maximum strength are shown in Figure 2-79.

Comparing the test curve of Specimen IDW with that Specimen ID-e in Figure 2-63(b) and Specimen IW in Figure 2-60, Specimen IDW exhibits lower strength due to the presence of both door and window openings, increasing the overall opening size.

(8) Specimen ID-e-0.5B (Lin, 2023)

There was one post-laid perforated brick infill with door opening specimen tested by Lin (2023), Specimen ID-e-0.5B. The test setup and detail configuration of the specimen are shown in Figure 2-80 and Figure 2-81, respectively. The material properties of the confining frame and brick infill of Specimen ID-e-0.5B are shown in

doi:10.6342/NTU202502280

Table 2-34 and Table 2-35, respectively. In contrast to the English bond used by the previously described specimens, Specimen ID-e-0.5B is laid by stretching bond with 0.5B thickness. The schematic diagram for stretching bond 0.5B is shown in Figure 2-82. There was no axial load applied on the specimen, as shown in Table 2-1

The test curve of Specimen ID-e-0.5B is shown in Figure 2-83. The maximum lateral strength and displacement at maximum lateral strength of the specimen are shown in Table 2-36. The failure condition of Specimen ID-e-0.5B at maximum strength is shown in Figure 2-84.

2.2.4 Retrofitted Brick Infill Walls with Openings

(1) Specimen ID-e-1.8R (Tung, 2017)

In addition to testing two specimens of brick infill wall with opening Specimen ID-e-1.8 and IW-e-1.8, Tung (2017) also tested one retrofitted brick infill wall with opening, Specimen ID-e-1.8R. The test setup of the experiment is shown in Figure 2-72. Specimen ID-e-1.8R has the same configuration as Specimen ID-e-1.8 but retrofitted with C-shaped steel and steel rod, as shown in Figure 2-85. The material properties of the confining frame and brick infill of Specimen ID-e-1.8R are shown in Table 2-28 and Table 2-29, respectively. The axial load applied to the specimen is shown in Table 2-1.

The lateral load-displacement curves of Specimen ID-e-1.8R is shown in Figure 2-86. The maximum lateral strength and displacement at maximum lateral strength of

doi:10.6342/NTU202502280

the specimen are shown in Table 2-37. The failure condition of Specimen ID-e-1.8R at maximum strength is shown in Figure 2-87.

Compared to the test curve of Specimen ID-e-1.8 in Figure 2-73(a), Specimen ID-e-1.8R exhibits greater strength than Specimen ID-e-1.8.

(2) Specimens IDW_CFRP, IDW_STEEL, IW_CFRP, and IW_STEEL (Jhang, 2019)

In addition to testing one specimen of brick infill wall with opening, Specimen IDW, Jhang (2017) also tested four retrofitted brick infill wall with openings, Specimen IDW_CFRP, IDW_STEEL, IW_CFRP, and IW_STEEL The prototype Specimens IDW and IW are used as a reference design and retrofitted by CFRP or steel angle to observe any improvement in the structural behavior. The specimen configurations of Specimen IDW_CFRP, IDW_STEEL, IW_CFRP, and IW_STEEL are shown in Figure 2-88, Figure 2-89, Figure 2-90, and Figure 2-91, respectively. The material properties of the confining frame and brick infill of the specimens are shown in Table 2-31 and Table 2-32, respectively. The axial loads applied to the specimens are shown in Table 2-1.

The lateral load-displacement curves of the retrofitted specimens are shown in Figure 2-92. The maximum lateral strength and displacement at maximum lateral strength of the specimens are shown in Table 2-38. The failure conditions of Specimens IDW_CFRP, IDW_STEEL, IW_CFRP, and IW_STEEL at maximum strength are

doi:10.6342/NTU202502280

shown in Figure 2-93, Figure 2-94, Figure 2-95, and Figure 2-96, respectively.

Comparing the test curves of Specimen IDW in Figure 2-78 and IW in Figure 2-60 with the test curves of retrofitted specimens in Figure 2-92, it is shown that the retrofit elements of CFRP and steel angle can effectively increase both the strength and stiffness of the brick infill with opening specimens. Additionally, comparing the effectiveness between the retrofitted elements, it is observed that the increase in strength is more significant when the specimen is retrofitted by CFRP.

2.2.5 Column

(1) Specimen AC_C (Lin, 2011)

Specimen AC_C the same column specimen used in Specimen AC as tested by Lin (2011). Specimen AC_C was tested after the Specimen AC experiment. The test setup of the experiment is shown in Figure 2-46. The specimen configuration of Specimen AC_C is shown in Figure 2-97. The material properties of the frame is shown in Table 2-13. The axial load applied on the specimen is shown in Table 2-1.

The test curve of Specimen AC_C is shown in Figure 2-98. The maximum lateral strength and displacement at maximum lateral strength of the specimen are shown in Table 2-39. The failure condition of Specimen AC_C at maximum strength is depicted in Figure 2-99. From the test curve, it can be shown that column AC_C still remains elastic after being used in Specimen AC experiment. Another observation is that the

doi:10.6342/NTU202502280

failure mode of the column AC_C is flexural or flexural-shear failure.

(2) Specimen ID_BF (Chao, 2015)

Similar to AC_C, Specimen ID_BF is a frame specimen used in Specimen ID experiment tested by Chao (2015). The Specimen ID_BF is tested after Specimen ID experiment. The test setup of the experiment is shown in Figure 2-56. The specimen configuration of Specimen ID_BF is shown in Figure 2-100. The material properties of the frame is shown in Table 2-19. The axial load applied on the specimen is shown in Table 2-1.

The test curve of Specimen ID_BF is shown in Figure 2-101. The maximum lateral strength and displacement at maximum lateral strength of the specimen are shown in Table 2-40. The failure condition of Specimen ID_BF at maximum strength is shown in Figure 2-102.

The test curve of Specimen ID_BF shows that the frame used in Specimen ID still maintained elastic behavior after the end of the test of Specimen ID. From the test curve, it can also be seen that the columns in Specimen ID_BF exhibits flexural-shear failure. It is also observed that the strength of columns in Specimen ID_BF contributes more than half of the Specimen ID strength.

doi:10.6342/NTU202502280

CHAPTER 3 PROPOSED ANALYTICAL MODEL

The principle to determine the lateral load-displacement curve for brick infill wall with opening and brick infill wall with opening and retrofit is based on the lateral load-displacement curves of four-sided and three-sided confined brick infill wall. Combined with the column lateral load-displacement curve, the method of curves superposition is implemented to obtain the lateral load displacement curves for brick infill wall with opening and brick infill wall with opening and retrofit.

Based on the past observations stated in the literature review chapter, the lateral load-deflection curves for four-sided and three-sided confined brick infill and also column will be defined in this chapter.

3.1 Four-sided and Three-sided Confined Brick Infill

3.1.1 Axial Load

The axial loads applied to the brick wall and column are calculated through the distribution of the axial stiffness between the brick infill and column, as shown in two equations below,

$$N_b = \frac{E_b A_b}{E_b A_b + E_c A_c} \times N_{total} \tag{3-1}$$

and

$$N_c = \frac{E_c A_c}{E_b A_b + E_c A_c} \times N_{total} \tag{3-2}$$

3.1.2 Failure Mode Strength

The horizontal interface sliding strength τ_f is formulated in Equation (2-19), re-stated as

doi:10.6342/NTU202502280

follows,

$$\tau_f = 0.0258(f_{mc})^{0.885} + (0.654 + 0.00514f_{mc})\sigma_N \tag{2-19}$$

where f_{mc} is the 50-mm mortar cube compressive strength (MPa) determined by ASTM C109 (2008), and σ_N is the axial compressive stress (MPa) determined using the axial load distributed to brick wall N_b in Equation (3-1).

The vertical interface splitting strength f_{mt} is calculated using Equation (2-20), re-stated as follows,

$$f_{mt} = 0.232(f_{mc})^{0.338} \tag{2-20}$$

While for the brick vertical splitting strength f_{bt} is calculated using Equation (2-40) proposed by Cheng (2021), re-stated as follows,

$$f_{bt} = 0.136f_{bc} \tag{2-40}$$

Where brick compressive strength f_{bc} is determined using CNS 382 or ASTM C67 (2008).

3.1.3 Stiffness

The lateral stiffness equation of ASCE/SEI 41-06 (2007) in Equation (2-11) is used as the basis for the proposed brick infill stiffness equation. Then, it is modified accordingly to better match the lateral load-displacement curve of test specimens. The original stiffness equation in Equation (2-11) is modified as follows,

$$K_b = 0.2\left(\frac{E_cI_c}{h_c^4 \sin 2\theta} h_b(E_bt_b)^9\right)^{0.1} \cos^2\theta \times \beta \tag{3-3}$$

The modification factor β introduced by Cheng (2021) is used in Equation (3-3), but

doi:10.6342/NTU202502280

defined with different values.

β is the integrity factor, that is equal to 1 for four-sided confined brick infill, for three-sided confined brick infill in case when the load strikes the column first and for the double-sided brick infill wing wall. β is otherwise equal to 0.25 for three-sided confined brick infill when the load strikes the brick wall first. The integrity factor β is defined to take into account the column-wall separation that may occur when the load strikes the brick wall first in three-sided confined brick infill, which would reduce the overall stiffness.

3.1.4 Peak Strength

(1) Four-sided confined brick infill

The strength equation for four-sided confined brick infill wall is formulated based on Chen (2003), re-stated as follows,

For ${}^{h_b}/_{\ell_b} \leq \tan\theta_c$,

$$V_b = \tau_f(\ell_b \times t_b) + 0.45 f_{mt}(h_b \times t_b) \tag{2-26}$$

For ${}^{h_b}/_{\ell_b} > \tan\theta_c$,

$$\begin{aligned} V_b = {} & \tau_f(\ell_b \times t_b) + 0.45 f_{mt}(l_b \tan\theta_c \times t_b) \\ & + 0.45\left(\frac{f_{mt} + f_{bt}}{2}\right)(h'_b - \ell_b \tan\theta_c) \times t_b \end{aligned} \tag{2-27}$$

Where h'_b is the effective height of failure path, formulated as follows,

$$h'_b = \min(h_b, \ell_b) \tag{2-28}$$

(2) Three-sided confined brick infill

The strength equation for three-sided confined brick infill wall is formulated in Equation (2-35) based on NCREE/TEASPA (2020), re-stated as follows,

$$\begin{aligned} V_b = \tau_f\left(\frac{2}{3}\ell_b \times t_b\right) + 0.225 f_{mt}\left(\frac{2}{3}\ell_b \tan\theta_c \times t_b\right) \\ + 0.225\left(\frac{f_{mt}+f_{bt}}{2}\right)\left(h_b' - \frac{2}{3}\ell_b \tan\theta_c\right) \times t_b \end{aligned} \tag{2-35}$$

Where h_b' is the effective height of failure path

For single-sided wing wall, h_b' is formulated as follows,

$$h_b' = \min\left(\frac{h_b}{\frac{2}{3}\ell_b + \ell_c - \frac{a_c}{3}} \times \frac{2}{3}\ell_b, \ell_b\right) \tag{2-36}$$

For double-sided wing wall, h_b' is formulated as follows,

$$h_b' = \min\left(\frac{h_b}{\frac{2}{3}\ell_b \times 2 + \ell_c} \times \frac{2}{3}\ell_b, \ell_b\right) \tag{2-37}$$

3.1.5 Peak Displacement

The displacement at peak strength Δ_b is obtained by dividing the strength V_b with the stiffness K_b, formulated as follows,

$$\Delta_b = \frac{V_b}{K_b} \tag{3-4}$$

3.1.6 Residual Strength

When the displacement reaches $2\Delta_b$, the strength reduced to the residual strength V_r. The formulation of residual strength V_r proposed by Chen (2003) is used, re-stated as follows,

$$V_r = \tau_f(\ell_b \times t_b) \leq 0.6V_b \tag{2-31}$$

3.1.7 Ultimate Point

The ultimate displacement Δ_u is formulated based on suggestion by Chen (2003), re-stated as follows,

$$\Delta_u = 0.02h_b \tag{2-32}$$

Using the suggestion from NCREE/TEASPA (2020), for four-sided confined brick infill, the residual strength is plateaued until it reaches the ultimate displacement Δ_u. For three-sided confined brick infill, the residual strength is linearly decreasing until it reaches zero at the ultimate displacement, The overall lateral load-displacement curves for four-sided and three-sided confined brick infill are depicted in Figure 3-1 and Figure 3-2, respectively.

3.2 Column

The lateral load-displacement curve for column follows the lateral load-displacement curve proposed by Shen et al. (2021) and ASCE/SEI 41-13 (2014) as described in Chapter 2. The overall lateral load-deflection curve for column with flexural-shear failure is depicted in Figure 2-25.

3.3 Method of Curves Superposition

After the lateral load-deflection curves from brick infill wall and column are obtained. The lateral load-deflection curve from brick infill wall and column is combined to obtain the overall lateral load-displacement curve. The schematic diagram for the overall lateral load-deflection curve is shown in Figure 3-3. The proposed lateral load-deflection curve in Figure 3-3 is obtained by adding up the lateral forces from brick walls and columns at specified displacement.

doi:10.6342/NTU202502280

3.4 Brick Infill Walls with Openings

For determining the lateral load-displacement curve for brick infill wall with opening, the main step is to determine the shear element present when certain type of load is acting on the brick infill.

3.4.1 Shear Element

The shear element is considered to exist if the brick infill panel is four-sided or three-sided confined. If that is the case, then the shear element can contribute to resisting the lateral load. As for two-sided confined brick infill (confined on top and bottom), the shear element is not present as the failure mode of such brick infill would be a horizontal sliding failure. Example for determination of shear element for Specimen IW under positive and negative loading are depicted in Figure 3-4 and Figure 3-5, respectively. While for determination of shear element for Specimen IDW under positive and negative loading are depicted in Figure 3-6 and Figure 3-7, respectively.

3.4.2 Lateral Load - Displacement Curve

As the shear elements depicted in Figure 3-4, Figure 3-5, Figure 3-6, and Figure 3-7 are three-sided confined, the formulation of three-sided confined brick infill wall is used to model the lateral load-deflection curve of each shear element. Then, the method of curves superposition is applied to obtain the overall lateral load-deflection curve for brick infill wall with opening.

doi:10.6342/NTU202502280

3.5 Retrofitted Brick Infill Walls with Openings

The purpose of retrofit is to increase the confinement for the brick infill panel. As the confinement for the brick infill increases, it would induce and activate more parts of the infill panel to resist the lateral load, increasing the overall strength and stiffness.

3.5.1 Shear Element

As for Specimen IW_CFRP, the shear element determinations for positive and negative loadings are shown in Figure 3-8 and Figure 3-9, respectively. Notice that there is no difference in shear element between Specimen IW without retrofit depicted in Figure 3-4 and Figure 3-5 and Specimen IW_CFRP depicted in Figure 3-8 and Figure 3-9. As for Specimen IDW_CFRP, the shear element determinations for positive and negative loadings are depicted in Figure 3-10 and Figure 3-11, respectively. Notice that the two-sided confined brick infill panel in the middle of the specimen between the openings is now regarded as shear element due to the confinement from CFRP.

3.5.2 Stiffness

(1) Retrofitted three-sided confined brick infill

As for the retrofitted three-sided confined brick infill panels, the stiffness formulation follows the stiffness formulation for three-sided confined brick infill in Equation (3-3). Where β is equal to 1 when the load strikes the column first. However, when the load strikes the brick wall first, the column-wall separation would be less

doi:10.6342/NTU202502280

pronounced due to the additional confinement from the retrofit elements. As such, β is set to 0.5 for the retrofitted three-sided confined brick infill panel in case when the load strikes the brick wall first.

(2) Retrofitted two-sided confined brick infill

As for the retrofitted two-sided confined brick infill, the stiffness formulation for four-sided and three-sided confined brick infill, which requires column parameters in Equation (3-3) cannot be calculated. Therefore, the modified stiffness equation proposed by Cheng (2021) in Equation (2-42) is used as the basis. Combining with the stiffness formulation for four-sided and three-sided confined brick infill proposed by this research in Equation (3-3), the proposed stiffness formulation for retrofitted two-sided confined brick infill without confining column is formulated as follows,

$$K = 0.2\left(\frac{1}{\sin 2\theta}(E_b t_b)^{10}\right)^{0.1}\cos^2\theta \times \beta \tag{3-5}$$

Where β is equal to 0.5, following the β value for retrofitted three-sided confined brick infill when the load strikes the brick wall first..

Substituting β value into Equation (3-5), we can obtain the following formulation for retrofitted two-sided confined brick infill,

$$K = 0.1\left(\frac{1}{\sin 2\theta}(E_b t_b)^{10}\right)^{0.1}\cos^2\theta \tag{3-6}$$

3.5.3 Strength

Due to the additional confinement from retrofit elements, the shear elements

doi:10.6342/NTU202502280

depicted in Figure 3-8, Figure 3-9, Figure 3-10, and Figure 3-11 would have a strength increase. Therefore, as opposed to using three-sided confined strength formulation, the four-sided confined strength formulations in Equation (2-26) and Equation (2-27) are used to model the lateral strength of these retrofitted infill panels.

Nonetheless, due to the confinement created by retrofit elements is not as good as confinement from RC column, the lateral load-displacement curve is linearly decreasing from the residual strength point to the ultimate point as suggested by Cheng (2021), depicted in Figure 3-2.

doi:10.6342/NTU202502280

CHAPTER 4 RESULTS AND DISCUSSION

This chapter compares the proposed lateral load-deflection curves defined in Chapter 3 with the test curves of specimens in Chapter 2.

4.1 Four-sided Confined Brick Infill

4.1.1 Lateral Load - Deflection Curves Comparison

(1) Specimens B39-L, B83-L, B39-T, and B83-T (Chiou and Hwang, 2015)

The proposed lateral load-deflection curve and the comparison with the test curve for Specimens B39-L, B83-L, B39-T, and B83-T are shown in Figure 4-1, Figure 4-2, Figure 4-3, and Figure 4-4, respectively.

(2) Specimens CS, IS (Lin, 2016)

The proposed lateral load-deflection curve and the comparison with the test curve for Specimens CS and IS are shown in Figure 4-5 and Figure 4-6, respectively.

(3) Specimens P1 and P2 (Wu, 2016)

The proposed lateral load-deflection curve and the comparison with the test curve for Specimens P1 and P2 are shown in Figure 4-7 and Figure 4-8, respectively.

4.1.2 Discussion

The comparisons of maximum lateral strength and lateral displacement at maximum lateral strength for four-sided confined brick infill specimens between test and analytical results are shown in Table 4-1 and Figure 4-9. It shows that the specimens

doi:10.6342/NTU202502280

strengths are slightly underestimated with an average between the maximum lateral strengths of 1.26 and coefficient of variation (COV) of 0.22. Simultaneously, the analytical displacements at maximum strength are on average 3.03 times lower than the test displacement at maximum strength with COV of 0.98.

The model shows having overestimation of strengths in post-laid brick infill specimens under negative loading, Specimens IS- and P2-. This shows that current strength formulation for four-sided confined brick infill wall does not accurately predict the failure path of the post-laid brick infill specimens under negative loading. Compared with the observation of failure condition of Specimen IS in Figure 2-36, the current strength formulation may overestimate the presence of vertical splitting cracks in post-laid brick infill specimens as the actual failure path may be more dominated by horizontal sliding cracks.

4.2 Three-sided Confined Brick Infill

4.2.1 Lateral Load – Deflection Curves Comparison

(1) Specimen A and B (Lo, 2010)

The proposed lateral load-deflection curve and the comparison with the test curve for Specimens A and B are shown in Figure 4-10 and Figure 4-11, respectively.

(2) Specimen C, AC, AL, BC, and BS (Lin, 2011)

The proposed lateral load-deflection curve and the comparison with the test curve for

doi:10.6342/NTU202502280

Specimens C, AC+, AC-, AL, BC, and BS are shown in Figure 4-12, Figure 4-13, Figure 4-14, Figure 4-15, Figure 4-16, and Figure 4-17, respectively.

4.2.2 Discussion

The comparisons of maximum lateral strength and lateral displacement at maximum lateral strength for three-sided confined brick infill specimens between test and analytical results are shown in Table 4-2 and Figure 4-18. It shows that the specimens strengths are slightly underestimated with an average between the maximum lateral strengths of 1.22 and coefficient of variation (COV) of 0.17. Simultaneously, the analytical displacements at maximum strength are on average 2.08 times lower than the test displacement at maximum strength with COV of 0.55.

Based on the average and COV of the maximum strength and lateral displacement at maximum strength, the analytical model in three-sided confined brick infill shows a better performance compared with the analytical model in four-sided confined brick infill. This may be due to no post-laid three-sided confined brick infill specimens used in this study.

4.3 Brick Infill Walls with Openings

4.3.1 Lateral Load – Deflection Curves Comparison

(1) Specimen CD and CW (Hsu, 2015)

The proposed lateral load-deflection curve and the comparison with the test curve for

doi:10.6342/NTU202502280

Specimens CD and CW are shown in Figure 4-19 and Figure 4-20, respectively.

(2) Specimen ID (Chao, 2015)

The proposed lateral load-deflection curve and the comparison with the test curve for Specimen ID is shown in Figure 4-21.

(3) Specimen IW (Tsai, 2016)

The proposed lateral load-deflection curve and the comparison with the test curve for Specimen IW is shown in Figure 4-22.

(4) Specimen CD-e and ID-e (Lin, 2016)

The proposed lateral load-deflection curve and the comparison with the test curve for Specimens CD-e and ID-e under positive and negative loading are shown in Figure 4-23, Figure 4-24, Figure 4-25, and Figure 4-26, respectively.

(5) Specimens CD-e-1.8 and CW-e-1.8 (Yang, 2017)

The proposed lateral load-deflection curve and the comparison with the test curve for Specimens CD-e-1.8 and CW-e-1.8 under positive and negative loading are shown in Figure 4-27, Figure 4-28, Figure 4-29, and Figure 4-30, respectively.

(6) Specimens ID-e-1.8 and IW-e-1.8 (Tung, 2017)

The proposed lateral load-deflection curve and the comparison with the test curve for Specimens ID-e-1.8 and IW-e-1.8 under positive and negative loading are shown in Figure 4-31, Figure 4-32, Figure 4-33, and Figure 4-34, respectively.

doi:10.6342/NTU202502280

(7) Specimen IDW (Jhang, 2019)

The proposed lateral load-deflection curve and the comparison with the test curve for Specimen IDW under positive and negative loading are shown in Figure 4-35 and Figure 4-36, respectively.

(8) Specimen ID-e-0.5B (Lin, 2023)

The proposed lateral load-deflection curve and the comparison with the test curve for Specimen ID-e-0.5B under positive and negative loading is shown in Figure 4-37.

4.3.2 Discussion

The comparisons of maximum lateral strength and lateral displacement at maximum lateral strength for brick infill walls with openings specimens between test and analytical results are shown in Table 4-3 and Figure 4-39. The average of the maximum lateral strengths is shown to be 1.01 with coefficient of variation (COV) of 0.37. On the lateral displacement side, the analytical displacements at maximum strength are on average 2.05 times lower than the test displacement at maximum strength with COV of 1.55.

The model shows having a severe overestimation of strength in Specimens ID,-e-, CD-e-1.8-, CW-e-1.8-, ID-e-1.8-, and IW-e-1.8-. The overestimation of strength in Specimen ID-e- but not in the Specimen CD-e- confirms the previous discussion in four-sided confined brick infill that the current strength formulation does not well

doi:10.6342/NTU202502280

predict the failure path of post-laid brick infill specimens, especially under negative loading. The overestimation of strength in both pre-laid and post-laid brick infills of Specimens CD-e-1.8-, CW-e-1.8-, ID-e-1.8-, and IW-e-1.8-, may also raise the importance of considering the effect of opening sizes into the failure path determination.

4.4 Retrofitted Brick Infill Walls with Openings

4.4.1 Lateral Load – Deflection Curves Comparison

(1) Specimen ID-e-1.8R (Tung, 2017)

The proposed lateral load-deflection curve and the comparison with the test curve for Specimen ID-e-1.8R is shown in Figure 4-40.

(2) Specimens IDW_CFRP, IDW_STEEL, IW_CFRP, and IW_STEEL (Jhang, 2019)

The proposed lateral load-deflection curve and the comparison with the test curve for Specimens IDW_CFRP and IDW_STEEL under positive and negative loading are shown in Figure 4-41, Figure 4-42, Figure 4-43, Figure 4-44, respectively. And the proposed lateral load-deflection curve and the comparison with the test curve for Specimens IW_CFRP and IW_STEEL are shown in Figure 4-45 and Figure 4-46, respectively.

4.4.2 Discussion

The comparisons of maximum lateral strength and lateral displacement at maximum

doi:10.6342/NTU202502280

lateral strength for brick infill walls with openings and retrofit specimens between test and analytical results are shown in Table 4-4 and Figure 4-47. The maximum lateral strengths is shown to be slightly overestimated with an average of 0.97 and coefficient of variation (COV) of 0.16. On the lateral displacement side, the analytical displacements at maximum strength are predicted quite well with an average of 1.17 and COV of 0.37.

The model shows having a more significant overestimation of strength in Specimen ID-e-1.8R. In addition, the model can conservatively predict the strength of the specimens retrofitted with CFRP but underestimates the strength of the specimens retrofitted with steel angles. The strength of the retrofitted brick infill seems to be mainly affected by the design and configuration of retrofit elements. Comparing the maximum strengths of Specimens IDW_CFRP and IW_CFRP retrofitted by CFRP with those of Specimens IDW_STEEL and IW_STEEL retrofitted by steel angles, the specimens retrofitted by CFRP seems to be more superior in strength. This raises the importance of a standard in retrofit design, to effectively and accurately predict the strength of the retrofitted brick infill.

doi:10.6342/NTU202502280

4.5 Column

4.5.1 Lateral Load – Deflection Curves Comparison

(1) Specimen AC_C (Lin, 2011)

The proposed lateral load-deflection curve and the comparison with the test curve for Specimen AC_C is shown in Figure 4-48.

(2) Specimen ID_BF (Chao, 2015)

The proposed lateral load-deflection curve and the comparison with the test curve for Specimen ID_BF is shown in Figure 4-49.

4.5.2 Discussion

From the comparison of column lateral load-deflection curves of Specimen AC_C and ID_BF. The column model used in this study quiet accurately predict the flexural strengths of the columns. However, the column model estimated higher stiffness and smaller ultimate displacement compared to the bare frame specimens. This study argues that these higher estimated stiffness and smaller ultimate displacement may be beneficial during the analysis of brick infill wall in RC frames. This is because the interaction between brick infill and column may increase the original stiffness of column and restrict the lateral displacement of column, leading to earlier failure of the column.

doi:10.6342/NTU202502280

CHAPTER 5 CONCLUSIONS

5.1 Conclusions

This study proposes the modified stiffness equation in the determination of lateral load-deflection curves for four-sided confined brick infill, three-sided confined brick infill, brick infill walls with openings and brick infill walls with openings and retrofits. The proposed lateral load deflection curves are also compared and validated by the experiments conducted in the past. From the comparison with the test curves, the proposed model seems to perform quite well for pre-laid confined brick infill specimens. The current strength formulations for brick infill seems to not suitable for post-laid brick infill, especially under negative loading. For the purpose of simplicity, the proposed stiffness equation does not consider the difference in stiffness between pre-laid and post-laid brick infills. This study argues to using the same lateral load-deflection curves formulations for both pre-laid and post-laid brick infill, as it is difficult to differentiate existing pre-laid and post-laid brick infill walls in the real world.

5.2 Suggestions

In order to more accurately and conservatively predict the lateral load-deflection curves of post-laid brick infill walls, the strength formulations should consider the difference of failure path in pre-laid and post-laid brick infills. From the observation of the failure condition of test specimens in this study, the main type of failure for post-laid brick infill under negative loading or

doi:10.6342/NTU202502280

when the load strikes the brick wall first is horizontal sliding shear failure. Reducing or eliminating the vertical splitting failure strength contribution to the brick infill strength formulation can be one of the methods to more conservatively predict the actual strength.

The proposed stiffness equations are also suggested to be validated with other brick infill specimens, having configurations different from those studied in this research. The proposed stiffness equation for the retrofitted brick infill walls with openings can also be extended for stiffness prediction of retrofitted four-sided confined brick infill, once validated by experiments.

doi:10.6342/NTU202502280

REFERENCES

ASCE/SEI 41-06. (2007). *Seismic rehabilitation of existing buildings* (ASCE/SEI 41-06). Reston, VA: American Society of Civil Engineers. https://doi.org/10.1061/9780784408841

ASCE/SEI 41-13. (2014). *Seismic evaluation and retrofit of existing buildings* (ASCE/SEI 41-13). Reston, VA: American Society of Civil Engineers. https://doi.org/10.1061/9780784412855

ASCE/SEI 41-17. (2017). *Seismic evaluation and retrofit of existing buildings* (ASCE/SEI 41-13). Reston, VA: American Society of Civil Engineers. https://doi.org/10.1061/9780784414859

ASCE/SEI 41-23. (2023). *Seismic evaluation and retrofit of existing buildings* (ASCE/SEI 41-13). Reston, VA: American Society of Civil Engineers. https://doi.org/10.1061/9780784416112

ASTM C1314. (2000). *Standard test method for compressive strength of masonry prisms* (ASTM C1314-00a). ASTM International.

ASTM C109/C109M. (2008). *Standard test method for compressive strength of hydraulic cement mortars (using 2-in. or [50-mm] cube specimens)* (ASTM C109/C109M-08). ASTM International.

ASTM C67. (2008). *Standard test methods for sampling and testing brick and* *structural clay tile* (ASTM C67-08). ASTM International.

Chao, Y. F. (2015). *Experiment of in-filled masonry panels with openings in RC frames under in-plane loading* (Master’s thesis, National Cheng Kung University). (In Chinese).

Chen, Y. H. (2003). *Seismic evaluation of RC buildings infilled with brick walls* (Doctoral dissertation, National Cheng Kung University). (In Chinese).

Cheng, C. C. (2021). *A study on in-plane lateral load displacement curve of brick infill in RC frames with openings* (Master’s thesis, National Taiwan University). (In Chinese).

Chiou, T. C. (2015). *Development and verification on the rapid seismic evaluation of low rise RC residential buildings* (Doctoral dissertation, National Taiwan University). (In Chinese).

Chiou, T. C., & Hwang, S. J. (2015), Tests on cyclic behavior of reinforced concrete frames with brick infill. *Earthquake Engineering & Structural Dynamics*, 44, 1939–1958. https://doi.org/10.1002/eqe.2564

FEMA 356. (2000). *Prestandard and commentary for the seismic rehabilitation of buildings* (FEMA 356). Washington, DC: Federal Emergency Management Agency.

Hsu, Y. H. (2015). *Lateral loading experiments for confined masonry panels with* *different opening types* (Master's thesis, National Cheng Kung University). (In Chinese).

Hwang, S. J., Tsai, R. J., Lam, W. K., & Moehle, J. P. (2017). Simplification of softened strut-and-tie model for strength prediction of discontinuity regions. *ACI Structural Journal*, 114, 1239-1248. https://doi.org/10.14359/51689787

Jhang, J. S. (2019). *A study on seismic retrofitting for brick infill in RC frames with openings* (Master's thesis, National Taiwan University). (In Chinese).

Lin, H. Y. (2023). *In-plane load test and pushover analysis model for infilled masonry panel with opening in RC frame* (Master's thesis, National Cheng Kung University). (In Chinese).

Lin, P. C. (2011). *Experiment and analysis of confined masonry wing-walls under in-plane loading* (Master's thesis, National Cheng Kung University). (In Chinese).

Lin, Y. C. (2013). *Assessment of masonry wall under out-of-plane force for historic building*. (Doctoral dissertation, National Cheng Kung University). (In Chinese).

Lin, Y. S. (2016). *In-plane load tests for confined and infilled masonry panels in RC frames with eccentric openings* (Master's thesis, National Cheng Kung University). (In Chinese).

Lo, T. Y. (2010). *Experiment and analysis of slender confined masonry infill panels under in-plane loading* (Master's thesis, National Cheng Kung University). (In

doi:10.6342/NTU202502280

Chinese).

NCREE. (2013). *Technology handbook for seismic evaluation and retrofit of school buildings (Third Edition)* (Technical Report NCREE-13-023). National Center for Research on Earthquake Engineering. (In Chinese).

NCREE/TEASPA. (2020). *Technical handbook for Taiwan earthquake assessment and strengthening of structures by pushover analysis (TEASPA V4.0)* (Technical Report NCREE-20-005). National Center for Research on Earthquake Engineering. (In Chinese).

Paulay, T., & Priestley, M. J. N. (1992). *Seismic design of reinforced concrete and masonry buildings*. John Wiley & Sons.

Shen, W. C., Hwang, S. J., Li, Y. A, & Moehle, J. P. (2021). Force-displacement model for shear-critical reinforced concrete columns. *ACI Structural Journal*. https://doi.org/10.14359/51728092

TMS 402-11 (2011). *Building Code Requirements for Masonry Structures (TMS 402-11/ACI 530-11/ASCE 5-11)*. Masonry Standards Joint Committee.

TMS 602-11 (2011). *Specification for masonry structures (TMS 602-11/ACI 530.1-11/ASCE 6-11).* Masonry Standards Joint Committee.

Tsai, M. H. (2016). *Material and in-plane load tests for infilled masonry panels with window-type opening* (Master’s thesis, National Cheng Kung University). (In

Chinese).

Tung, I. T. (2017). *In-plane load tests and retrofit for in-filled masonry panels in RC frames with eccentric openings* (Master's thesis, National Cheng Kung University). (In Chinese).

Wu, G. W. (2017). *Seismic retrofitting of reinforced concrete frames with brick infills* (Master's thesis, National Cheng Kung University). (In Chinese).

Yang, T. W. (2017). *In-plane load tests for confined masonry panels in RC frames with eccentric door and window openings* (Master's thesis, National Cheng Kung University). (In Chinese).

doi:10.6342/NTU202502280

TABLES

Table 2-1 Axial load of the specimens

Specimen Type	Specimen	Axial Load (kN)
Four-sided confined brick infill	B39-L	-
	B83-L	-
	B39-T	-
	B83-T	-
	CS	390.3
	IS	390.3
	P1	-
	P2	-
Three-sided confined brick infill	A	326.5
	B	330.4
	C	329.2
	AC	301.4
	AL	325.1
	BC	317.2
	BS	327.9
Brick infill wall with opening	CD	470.64
	CW	470.72
	ID	470.92
	IW	474.19
	CD-e	390.3
	ID-e	390.3
	CD-e-1.8	391.50
	CW-e-1.8	391.38
	ID-e-1.8	391.57
	IW-e-1.8	391.58
	IDW	208.125*
	ID-e-0.5B	-
Brick infill wall with opening and retrofit	ID-e-1.8R	390.76
	IDW_CFRP	208.125*
	IDW_STEEL	208.125*
	IW_CFRP	474.19*
	IW_STEEL	474.19*
Column	AC_C	125.6
	ID_BF	470.76

* Assumed due to limited information

doi:10.6342/NTU202502280

Table 2-2 Test parameters and material properties of Specimens B39-L, B83-L, B39-T, and B83-T (Chiou & Hwang, 2015)

Specimen	Brick infill			RC column		
	h_b/ℓ_b	f_{mc} (MPa)	f_{bc} (MPa)	f_c' (MPa)	f_y (MPa)	
					D19	D10
B39-L	0.39	7	38	25	412	349
B83-L	0.83	7	38	30	412	349
B39-T	0.39	13	38	27	412	349
B83-T	0.83	10	38	28	412	349

Table 2-3 Maximum lateral strength and displacement at maximum lateral strength of Specimens B39-L, B83-L, B39-T, and B83-T (Chiou & Hwang, 2015)

Specimen	V_{max} (kN)	$\Delta_{V_{max}}$ (mm) (Drift %)
B39-L	668	21.75 (0.75)
B83-L	1177	-14.5 (-0.50)
B39-T	847	3.625 (0.125)
B83-T	1327	14.5 (0.50)

Table 2-4 Material properties of confining frames of Specimens CS, IS, CD-e, and ID-e (Lin, 2016)

		Column	Beam
Schematic Diagram		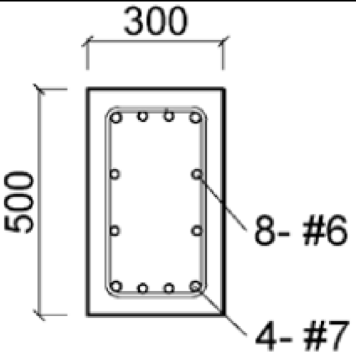	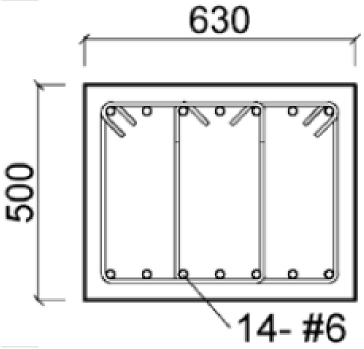
Cross-sectional size		300 mmx500 mm	630 mmx500 mm
Concrete strength f_c'		33.85 MPa	42.27 MPa
Longitudinal rebar	Number	4-#7, 8-#6	14-#6
	Yield strength f_y	#6: 463.5 MPa #7: 483.9 MPa	#6: 463.5 MPa
Transverse rebar	Number	#3@250 mm Joint area: #3@250 mm 90° hook tie	Beam end: #3@120 mm Beam midspan: #3@200 mm 2 sets of U-stirrup and cap tie
	Yield strength f_y	#3: 377.4 MPa	#3: 377.4 MPa
Concrete cover		40 mm	40 mm

Table 2-5 Material properties of brick infill of Specimens CS, IS, CD-e, and ID-e (Lin, 2016)

		Brick Infill
Bond type		English bond
Thickness		200 mm
Solid clay brick	Unit size	200 mmx95 mmx53 mm
	Strength f_{bc}	23.88 MPa
Mortar strength f_{mc}		CS and CD-e: 24.79 MPa IS and ID-e: 14.10 MPa
Brick prism strength f_m'		CS and CD-e: 15.50 MPa IS and ID-e: 21.32 MPa

Table 2-6 Maximum lateral strength and displacement at maximum lateral strength of Specimens CS and IS (Lin, 2016)

Specimen	V^{+}_{max} (kN)	$\Delta_{V^{+}_{max}}$ (mm) (Drift %)	V^{-}_{max} (kN)	$\Delta_{V^{-}_{max}}$ (mm) (Drift %)
CS	1001.00	2.18 (0.067)	-934.80	-1.83 (-0.057)
IS	853.40	15.85 (0.491)	-549.80	-48.41 (-1.499)

Table 2-7 Material properties of confining frames of Specimens P1 and P2 (Wu, 2017)

		Column	Beam
Schematic Diagram		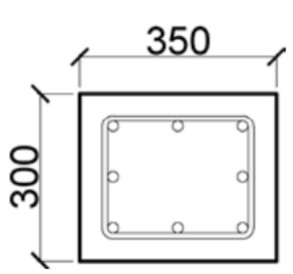	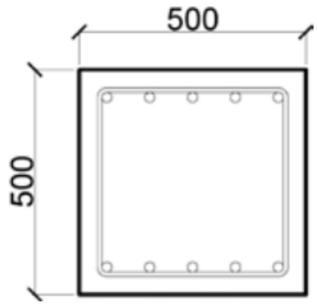
Cross-sectional size		300 mmx300 mm	500 mmx500 mm
Concrete strength f_c'		33. MPa	33.7 MPa
Longitudinal rebar	Number	8-#6	10-#7
	Yield strength f_y	#6: 456.6 MPa	#: 440.7 MPa
Transverse rebar	Number	#3@250 mm 90° hook tie	#3@150 mm 90° hook tie
	Yield strength f_y	#3: 331.5 MPa	#3: 331.5 MPa
Concrete cover		40 mm	40 mm

Table 2-8 Material properties of brick infill of Specimens P1 and P2 (Wu, 2017)

		Brick Infill
Bond type		English bond
Thickness		200 mm
Solid clay brick	Unit size	200 mmx95 mmx53 mm
	Strength f_{bc}	P1: 21.2 MPa P2: 31.3 MPa
Mortar strength f_{mc}		P1: 21.0 MPa P2: 24.7 MPa
Brick prism strength f_m'		P1: 11.2 MPa P2: 13.6 MPa

Table 2-9 Maximum lateral strength and displacement at maximum lateral strength of Specimens P1 and P2 (Wu, 2017)

Specimen	V_{max}^{+} (kN)	$\Delta_{V_{max}^{+}}$ (mm) (Drift %)	V_{max}^{-} (kN)	$\Delta_{V_{max}^{-}}$ (mm) (Drift %)
P1	801.218	12.63 (0.632)	-618.051	-10.02 (-0.501)
P2	669.546	4.58 (0.229)	-490.789	-7.54 (-0.377)

Table 2-10 Material properties of confining frames of Specimens A and B (Lo, 2010)

		Column	Beam
Schematic Diagram		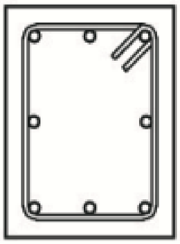	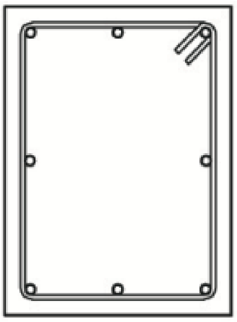
Cross-sectional size		300 mmx400 mm	450 mmx600 mm
Concrete strength f_c'		A: 29.9 MPa B: 30.9 MPa	A: 29.9 MPa B: 30.9 MPa
Longitudinal rebar	Number	8-#6	8-#6
	Yield strength f_y	#6: 439.2 MPa	#6: 439.2 MPa
Transverse rebar	Number	#3@250 mm	#3@100 mm
	Yield strength f_y	#3: 318.9 MPa	#3: 318.9 MPa
Concrete cover		40 mm	40 mm

Table 2-11 Material properties of brick infill of Specimens A and B (Lo, 2010)

		Brick Infill
Bond type		English bond
Thickness		200 mm
Solid clay brick	Unit size	200 mmx95 mmx53 mm
	Strength f_{bc}	62.9 MPa
Mortar strength f_{mc}		15.5 MPa
Brick prism strength f_m'*		17.4 MPa

* brick prism size: 201mmx204mmx486mm

doi:10.6342/NTU202502280

Table 2-12 Maximum lateral strength and displacement at maximum lateral strength of Specimens A and B (Lo, 2010)

Specimen	V_{max} (kN)	$\Delta_{V_{max}}$ (mm) (Drift %)
A	283	7 (0.26)
B	500	15 (0.56)

Table 2-13 Material properties of confining frames of Specimens C, AC, AL, BC, BS, and AC_C (Lin, 2011)

		Column	Beam
Schematic Diagram		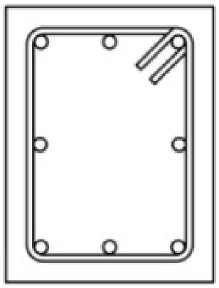	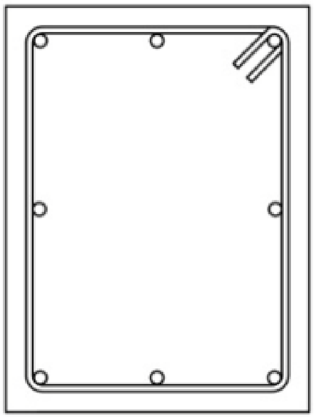
Cross-sectional size		300 mmx400 mm	450 mmx600 mm
Concrete strength f_c'		C: 30.7 MPa AC: 32.2 MPa AL: 36.2 MPa BC: 30.7 MPa BS: 33.4 MPa	C: 30.7 MPa AC: 32.2 MPa AL: 36.2 MPa BC: 30.7 MPa BS: 33.4 MPa
Longitudinal rebar	Number	8-#6	8-#6
	Yield strength f_y	#6: 490.5 MPa	#6: 490.5 MPa
Transverse rebar	Number	#3@250 mm	#3@100 mm
	Yield strength f_y	#3: 400.3 MPa	#3: 400.3 MPa
Concrete cover		40 mm	40 mm

Table 2-14 Material properties of brick infill of Specimens C, AC, AL, BC, and BS (Lin, 2011)

		Brick Infill
Bond type		English bond
Thickness		200 mm
Solid clay brick	Unit size	200 mmx95 mmx53 mm
	Strength f_{bc}	14.42 MPa
Mortar strength f_{mc}		13.9 MPa
Brick prism strength f'_m*		19.4 MPa

* brick prism size: 203 mmx205 mmx464 mm

Table 2-15 Maximum lateral strength and displacement at maximum lateral strength of Specimens C, AC, AL, BC, and BS (Lin, 2011)

Specimen	V^+_{max} (kN)	$\Delta_{V^+_{max}}$ (mm) (Drift %)	V^-_{max} (kN)	$\Delta_{V^-_{max}}$ (mm) (Drift %)
C	266.74	61.42 (2.27)	-	-
AC	220.03	32.22 (1.19)	-213.23	-32.64 (-1.21)
AL	346.87	23 (0.85)	-	-
BC	485.31	15.84 (0.59)	-442.2	-14.46 (-0.54)
BS	304.14	14 (0.52)	-	-

doi:10.6342/NTU202502280

Table 2-16 Material properties of confining frames of Specimens CD, CW, and IW (Hsu, 2015)

		Column	Beam
Schematic Diagram		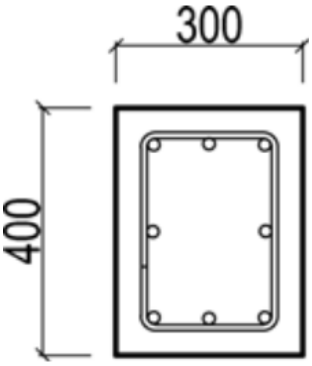	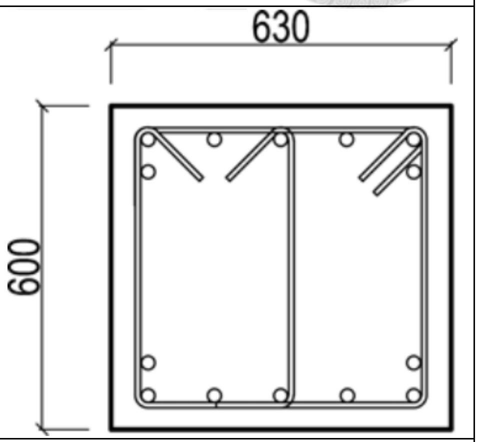
Cross-sectional size		300 mmx400 mm	630 mmx600 mm
Concrete strength f_c'		CD and IW: 28.8 MPa CW: 28.25 MPa	CD and IW: 28.8 MPa CW: 28.25 MPa
Longitudinal rebar	Number	8-#6	14-#8
	Yield strength f_y	#6: 442.5 MPa	#8: 446.3 MPa
Transverse rebar	Number	#3@250 mm 90° hook	#3@150 mm 135° hook
	Yield strength f_y	#3: 360.1 MPa	#3: 360.1 MPa
Concrete cover		40 mm	40 mm

Table 2-17 Material properties of brick infill of Specimens CD and CW (Hsu, 2015)

		Brick Infill
Bond type		English bond
Thickness		198 mm
Solid clay brick	Unit size	198 mmx92 mmx50 mm
	Strength f_{bc}	31.09 MPa
Mortar strength f_{mc}		17.56 MPa
Brick prism strength f_m'		11.58 MPa

Table 2-18 Maximum lateral strength and displacement at maximum lateral strength of Specimens CD and CW (Hsu, 2015)

Specimen	V^{+}_{max} (kN)	$\Delta_{V^{+}_{max}}$ (mm) (Drift %)	V^{-}_{max} (kN)	$\Delta_{V^{-}_{max}}$ (mm) (Drift %)
CD	487.24	7.82 (0.253)	-403.56	-6.99 (-0.226)
CW	609.62	12.89 (0.417)	-596.38	-11.56 (-0.374)

Table 2-19 Material properties of confining frames of Specimens ID and ID_BF (Chao, 2015)

		Column	Beam
Schematic Diagram		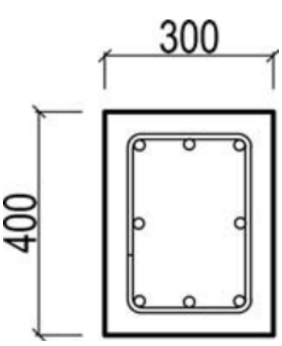	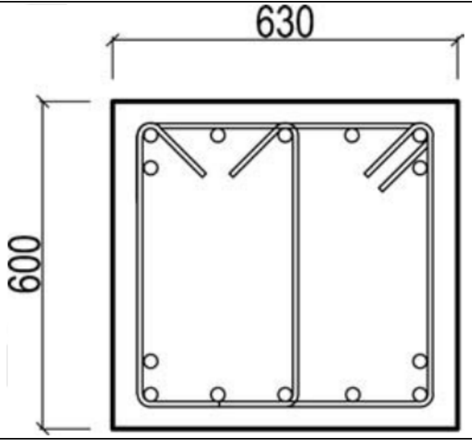
Cross-sectional size		300 mmx400 mm	630 mmx600 mm
Concrete strength f_c'		27.70 MPa	27.70 MPa
Longitudinal rebar	Number	8-#6	14-#8
	Yield strength f_y	#6: 442.5 MPa	#8: 446.3 MPa
Transverse rebar	Number	#3@250 mm 90° hook	#3@150 mm U-stirrup and cap tie with cross-tie on midspan section
	Yield strength f_y	#3: 360.1 MPa	#3: 360.1 MPa
Concrete cover		40 mm	40 mm

Table 2-20 Material properties of brick infill of Specimen ID (Chao, 2015)

		Brick Infill
Bond type		English bond
Thickness		198 mm
Solid clay brick	Unit size	198 mmx92 mmx50 mm
	Strength f_{bc}	31.09 MPa
Mortar strength f_{mc}		12.77 MPa
Brick prism strength f'_m		17.97 MPa

Table 2-21 Maximum lateral strength and displacement at maximum lateral strength of Specimen ID (Chao, 2015)

Specimen	V_{max}^{+} (kN)	$\Delta_{V_{max}^{+}}$ (mm) (Drift %)	V_{max}^{-} (kN)	$\Delta_{V_{max}^{-}}$ (mm) (Drift %)
ID	347.28	23.35 (0.76)	-409.64	-17.13 (-0.55)

Table 2-22 Material properties of brick infill of Specimen IW (Tsai, 2016)

		Brick Infill
Bond type		English bond
Thickness		200 mm
Solid clay brick	Unit size	200 mmx95 mmx53 mm
	Strength f_{bc}	25.34 MPa
Mortar strength f_{mc}		14.73 MPa
Brick prism strength f'_m		21.32 MPa

Table 2-23 Maximum lateral strength and displacement at maximum lateral strength of Specimen IW (Tsai, 2016)

Specimen	V_{max}^{+} (kN)	$\Delta_{V_{max}^{+}}$ (mm) (Drift %)	V_{max}^{-} (kN)	$\Delta_{V_{max}^{-}}$ (mm) (Drift %)
IW	395.96	24.6 (0.796)	-352.42	-29.78 (-0.964)

Table 2-24 Maximum lateral strength and displacement at maximum lateral strength of Specimens CD-e and ID-e (Lin, 2016)

Specimen	V_{max}^{+} (kN)	$\Delta_{V_{max}^{+}}$ (mm) (Drift %)	V_{max}^{-} (kN)	$\Delta_{V_{max}^{-}}$ (mm) (Drift %)
CD-e	666.80	2.70 (0.084)	-627.24	-32.14 (-0.995)
ID-e	359.86	48.41 (1.499)	-275.76	-84.57 (-1.504)

Table 2-25 Material properties of confining frames of Specimens CD-e-1.8 and CW-e-1.8 (Yang, 2017)

		Column	Beam
Schematic Diagram		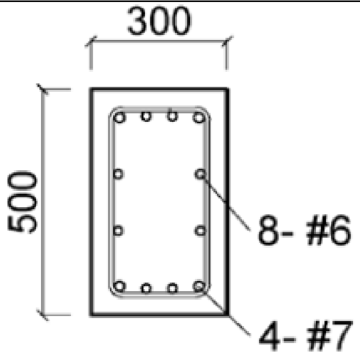	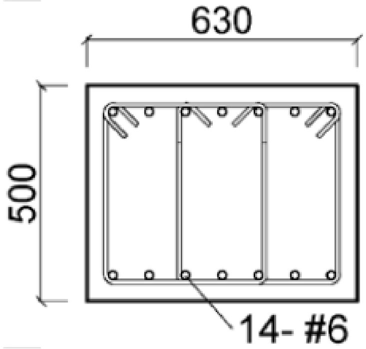
Cross-sectional size		300 mmx500 mm	630 mmx500 mm
Concrete strength f_c'		19.80 MPa	19.80 MPa
Longitudinal rebar	Number	4-#7, 8-#6	14-#6
	Yield strength f_y	#7: 454.6 MPa #6: 456.2 MPa	#6: 456.2 MPa
Transverse rebar	Number	#3@250 mm Joint area: #3@120 mm 90° hook tie	Beam end: #3@120 mm Beam midspan: #3@200 mm 2 sets of U-stirrup and cap tie
	Yield strength f_y	#3: 380.9 MPa	#3: 380.9 MPa
Concrete cover		40 mm	40 mm

Table 2-26 Material properties of brick infill of Specimens CD-e-1.8 and CW-e-1.8 (Yang, 2017)

		Brick Infill
Bond type		English bond
Thickness		200 mm
Solid clay brick	Unit size	200 mmx95 mmx53 mm
	Strength f_{bc}	40.34 MPa
Mortar strength f_{mc}		21.07 MPa
Brick prism strength f'_m		11.42 MPa

Table 2-27 Maximum lateral strength and displacement at maximum lateral strength of Specimens CD-e-1.8 and CW-e-1.8 (Yang, 2017)

Specimen	V^{+}_{max} (kN)	$\Delta_{V^{+}_{max}}$ (mm) (Drift %)	V^{-}_{max} (kN)	$\Delta_{V^{-}_{max}}$ (mm) (Drift %)
CD-e-1.8	451.66	7.95 (0.246)	-283.86	-5.66 (-0.175)
CW-e-1.8	466.12	8.08 (0.250)	-400.9	-24.10 (-0.746)

Table 2-28 Material properties of confining frames of Specimens ID-e-1.8, IW-e-1.8, and ID-e-1.8R (Tung, 2017)

		Column	Beam
Schematic Diagram		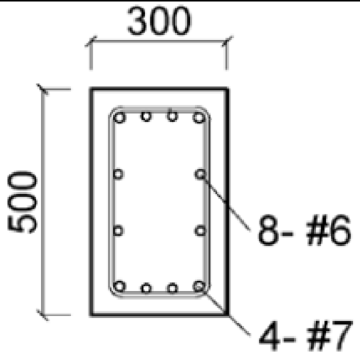	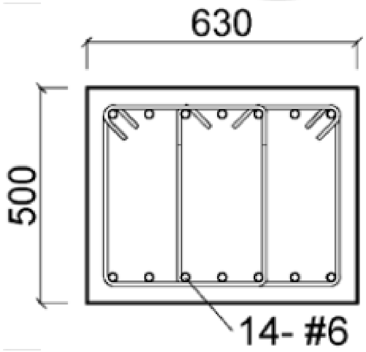
Cross-sectional size		300 mmx500 mm	630 mmx500 mm
Concrete strength f_c'		18.97 MPa	18.97 MPa
Longitudinal rebar	Number	4-#7, 8-#6	14-#6
	Yield strength f_y	#7: 454.6 MPa #6: 456.2 MPa	#6: 456.2 MPa
Transverse rebar	Number	#3@250 mm Joint area: #3@120 mm 90° hook tie	Beam end: #3@120 mm Beam midspan: #3@200 mm 2 sets of U-stirrup and cap tie
	Yield strength f_y	#3: 380.9 MPa	#3: 380.9 MPa
Concrete cover		40 mm	40 mm

Table 2-29 Material properties of brick infill of Specimens ID-e-1.8, IW-e-1.8, and ID-e-1.8R (Tung, 2017)

		Brick Infill
Bond type		English bond
Thickness		200 mm
Solid clay brick	Unit size	200 mmx95 mmx53 mm
	Strength f_{bc}	55.50 MPa
Mortar strength f_{mc}		20.19 MPa
Brick prism strength f_m'		17.87 MPa

Table 2-30 Maximum lateral strength and displacement at maximum lateral strength of Specimens ID-e-1.8 and IW-e-1.8 (Tung, 2017)

Specimen	V_{max}^{+} (kN)	$\Delta_{V_{max}^{+}}$ (mm) (Drift %)	V_{max}^{-} (kN)	$\Delta_{V_{max}^{-}}$ (mm) (Drift %)
ID-e-1.8	460.86	7.19 (0.223)	-244.60	-64.65 (-2.002)
IW-e-1.8	604.5	11.13 (0.345)	-253.76	-48.71 (-1.508)

Table 2-31 Material properties of confining frames of Specimens IDW, IDW_CFRP, IDW_STEEL, IW_CFRP, and IW_STEEL (Jhang, 2019)

		Column	Beam
Schematic Diagram		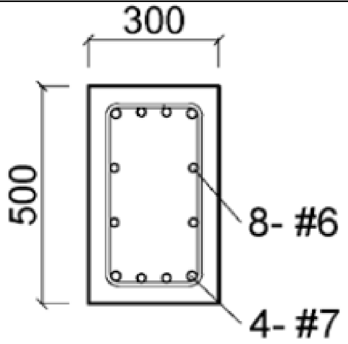	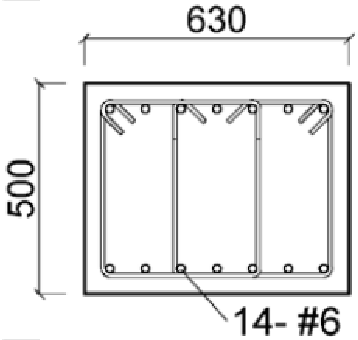
Cross-sectional size		300 mmx500 mm	630 mmx500 mm
Concrete strength f_c'		IDW: 27.75 MPa IDW_CFRP: 28.51 MPa IDW_STEEL: 30.26 MPa IW_CFRP: 31.13 MPa IW_STEEL: 30.19 MPa	IDW: 27.75 MPa IDW_CFRP: 28.51 MPa IDW_STEEL: 30.26 MPa IW_CFRP: 31.13 MPa IW_STEEL: 30.19 MPa
Longitudinal rebar	Number	4-#7, 8-#6	14-#6
	Yield strength f_y	#7: 482.9 MPa #6: 464.4 MPa	#6: 464.4 MPa
Transverse rebar	Number	#3@250 mm Joint area: #3@120 mm 90° hook tie	Opening section: #3@120 mm Other section: #3@200 mm 2 sets of U-stirrup and cap tie
	Yield strength f_y	#3: 357.9 MPa	#3: 357.9 MPa
Concrete cover		40 mm	40 mm

Table 2-32 Material properties of brick infill of Specimens IDW, IDW_CFRP, IDW_STEEL, IW_CFRP, and IW_STEEL (Jhang, 2019)

		Brick Infill
Bond type		English bond
Thickness		200 mm
Solid clay brick	Unit size	200 mmx95 mmx53 mm
	Strength f_{bc}	22.89 MPa
Mortar strength f_{mc}		25.78 MPa
Brick prism strength f'_m		15.09 MPa

Table 2-33 Maximum lateral strength and displacement at maximum lateral strength of Specimen IDW (Jhang, 2019)

Specimen	V^+_{max} (kN)	$\Delta_{V^+_{max}}$ (mm) (Drift %)	V^-_{max} (kN)	$\Delta_{V^-_{max}}$ (mm) (Drift %)
IDW	385.8	48.11 (1.5)	-275.3	-24.37 (-0.75)

Table 2-34 Material properties of confining frames of Specimen ID-e-0.5B (Lin, 2023)

		Near Wall Column	Independent Column	Beam
Schematic Diagram		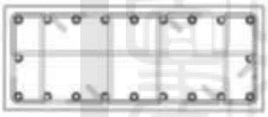	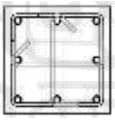	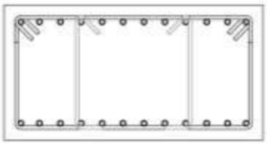
Cross-sectional size		750 mmx300 mm	300 mmx300 mm	960 mmx500 mm
Concrete strength f'_c		34.5 MPa	34.5 MPa	50.0 MPa
Longitudinal rebar	Number	20-#6	8-#6	20-#6
	Yield strength f_y	#6: 472.6 MPa	#6: 472.6 MPa	#6: 472.6 MPa
Transverse rebar	Number	Closed tie: #3@120 mm Cross-tie: #3@240 mm 90° hook tie	Closed tie: #3@120 mm Cross-tie: #3@240 mm 90° hook tie	#4@200 mm 135° hook tie
	Yield strength f_y	#3: 321.3 MPa	#3: 321.3 MPa	#3: 321.3 MPa
Concrete cover		20 mm	20 mm	40 mm

Table 2-35 Material properties of brick infill of Specimen ID-e-0.5B (Lin, 2016)

		Brick Infill
Bond type		Stretching bond
Thickness		95 mm
Solid clay brick	Unit size	200 mmx95 mmx53 mm
	Strength f_{bc}	40.98 MPa
Mortar strength f_{mc}		19.23 MPa
Brick prism strength f_m'		20.43 MPa

Table 2-36 Maximum lateral strength and displacement at maximum lateral strength of Specimen ID-e-0.5B (Lin, 2023)

Specimen	V_{max}^{+} (kN)	$\Delta_{V_{max}^{+}}$ (mm) (Drift %)	V_{max}^{-} (kN)	$\Delta_{V_{max}^{-}}$ (mm) (Drift %)
ID-e-0.5B	361.94	10.83 (0.38)	-361.27	-113.35 (-4)

Table 2-37 Maximum lateral strength and displacement at maximum lateral strength of Specimen ID-e-1.8R (Tung, 2017)

Specimen	V_{max}^{+} (kN)	$\Delta_{V_{max}^{+}}$ (mm) (Drift %)	V_{max}^{-} (kN)	$\Delta_{V_{max}^{-}}$ (mm) (Drift %)
ID-e-1.8R	772	48.53 (1.502)	-540.02	-32.39 (-1.003)

Table 2-38 Maximum lateral strength and displacement at maximum lateral strength of Specimens IDW_CFRP, IDW_STEEL, IW_CFRP, and IW_STEEL (Tung, 2017)

Specimen	V_{max}^{+} (kN)	$\Delta_{V_{max}^{+}}$ (mm) (Drift %)	V_{max}^{-} (kN)	$\Delta_{V_{max}^{-}}$ (mm) (Drift %)
IDW_CFRP	572.2	32 (1)	-540.8	-30.75 (-1)
IDW_STEEL	425.4	24.25 (0.75)	-505.1	-24.26 (-0.75)
IW_CFRP	638.7	24.13 (0.75)	-683.1	-24.21 (-0.75)
IW_STEEL	556.0	24.1 (0.75)	-539	-24.29 (-0.75)

Table 2-39 Maximum lateral strength and displacement at maximum lateral strength of Specimen AC_C (Lin, 2011)

Specimen	V_{max}^{+} (kN)	$\Delta_{V_{max}^{+}}$ (mm) (Drift %)	V_{max}^{-} (kN)	$\Delta_{V_{max}^{-}}$ (mm) (Drift %)
AC_C	102.9	100.12 (3.71)	-	-

Table 2-40 Maximum lateral strength and displacement at maximum lateral strength of Specimen ID_BF (Chao, 2015)

Specimen	V_{max}^{+} (kN)	$\Delta_{V_{max}^{+}}$ (mm) (Drift %)	V_{max}^{-} (kN)	$\Delta_{V_{max}^{-}}$ (mm) (Drift %)
ID_BF	220.62	78.37 (2.54)	-214.64	-77.71 (-2.51)

Table 4-1 Comparisons of maximum lateral strength and displacement at maximum lateral strength of four-sided confined brick infill specimens between test and analytical results

Specimen	$V_{max,test}$ (kN)	$\Delta_{V_{max,test}}$ (mm)	$V_{max,anal.}$ (kN)	$\Delta_{V_{max,anal.}}$ (mm)	$\frac{V_{max,test}}{V_{max,anal.}}$	$\frac{\Delta_{V_{max,test}}}{\Delta_{V_{max,anal.}}}$
B39-L	668	21.75	400.05	18	1.67	1.21
B83-L	1177	14.5	801.83	3.98	1.47	3.64
B39-T	847	3.625	523.72	3.03	1.62	1.20
B83-T	1327	14.5	888.2	3.88	1.49	3.74
CS+	1001	2.18	810.35	6.9	1.24	0.32
CS-	934.8	1.83	810.35	6.9	1.15	0.27
IS+	853.4	15.85	624.2	4.06	1.37	3.90
IS-	549.8	48.41	624.2	4.06	0.88	11.92
P1+	801.218	12.63	578.86	3.47	1.38	3.64
P1-	618.051	10.02	578.86	3.47	1.07	2.89
P2+	669.546	4.58	634.38	3.3	1.06	1.39
P2-	490.789	7.54	634.38	3.3	0.77	2.28
				Average	1.26	3.03
				COV	0.22	0.98

Table 4-2 Comparisons of maximum lateral strength and displacement at maximum lateral strength of three-sided confined brick infill specimens between test and analytical results

Specimen	$V_{mx,test}$ (kN)	$\Delta_{V_{max,test}}$ (mm)	$V_{max,anal.}$ (kN)	$\Delta_{V_{max,anal.}}$ (mm)	$\frac{V_{max,test}}{V_{max,anal.}}$	$\frac{\Delta_{V_{max,test}}}{\Delta_{V_{max,anal.}}}$
A	283	7	242.65	10.76	1.17	0.65
B	500	15	421.56	10.27	1.19	1.46
C	266.74	61.42	259.79	30.84	1.03	1.99
AC+	220.03	32.22	184.26	7.52	1.19	4.28
AC-	213.23	32.64	256.92	30.09	0.83	1.08
AL	346.87	23	228.98	6.13	1.51	3.75
BC+	485.31	15.84	327.49	7.37	1.48	2.15
BC-	442.2	14.46	327.49	7.37	1.35	1.96
BS	304.14	14	247.74	10.28	1.23	1.36
				Average	1.22	2.08
				COV	0.17	0.55

Table 4-3 Comparisons of maximum lateral strength and displacement at maximum lateral strength of brick infill walls with openings specimens between test and analytical results

Specimen	$V_{max,test}$ (kN)	$\Delta_{V_{max,test}}$ (mm)	$V_{max,anal.}$ (kN)	$\Delta_{V_{max,anal.}}$ (mm)	$\frac{V_{max,test}}{V_{max,anal.}}$	$\frac{\Delta_{V_{max,test}}}{\Delta_{V_{max,anal.}}}$
CD+	487.24	7.82	425.37	34.19	1.15	0.23
CD-	403.56	6.99	425.37	34.19	0.95	0.20
CW+	609.62	12.89	373.17	34.27	1.63	0.38
CW-	596.38	11.56	373.17	34.27	1.60	0.34
ID+	347.28	23.35	423.11	22.56	0.82	1.04
ID-	409.64	17.13	423.11	22.56	0.97	0.76
IW+	395.96	24.6	388.86	19.11	1.02	1.29
IW-	352.42	29.78	388.86	19.11	0.91	1.56
CD-e+	666.8	2.7	468.31	4.9	1.42	0.55
CD-e-	627.24	32.14	587.85	19.61	1.07	1.64
ID-e+	359.86	48.41	387.32	3.11	0.93	15.57
ID-e-	275.76	84.57	463.14	12.44	0.60	6.80
CD-e-1.8+	451.66	7.95	468.18	8.74	0.96	0.91
CD-e-1.8-	283.86	5.66	575.12	34.95	0.49	0.16
CW-e-1.8+	466.12	8.08	357.11	4.31	1.31	1.87
CW-e-1.8-	400.9	24.1	577.45	34.79	0.69	0.69
ID-e-1.8+	460.86	7.19	539.55	7.01	0.85	1.03
ID-e-1.8-	244.6	64.65	653.95	28.03	0.37	2.31
IW-e-1.8+	604.5	11.13	405.99	3.37	1.49	3.30
IW-e-1.8-	253.76	48.71	653.96	28.03	0.39	1.74
IDW+	385.8	48.11	217.57	27.76	1.77	1.73
IDW-	275.3	24.37	323.25	33.98	0.85	0.72
ID-e-0.5B+	361.94	10.83	356.35	28.37	1.02	0.38
ID-e-0.5B-	361.27	113.35	380.54	28.37	0.95	4.00
				Average	1.01	2.05
				COV	0.37	1.55

doi:10.6342/NTU202502280

Table 4-4 Comparisons of maximum lateral strength and displacement at maximum lateral strength of brick infill walls with openings and retrofit specimens between test and analytical results

Specimen	$V_{max,test}$ (kN)	$\Delta_{V_{max,test}}$ (mm)	$V_{max,anal.}$ (kN)	$\Delta_{V_{max,anal.}}$ (mm)	$\frac{V_{max,test}}{V_{max,anal.}}$	$\frac{\Delta_{V_{max,test}}}{\Delta_{V_{max,anal.}}}$
ID-e-1.8R+	772	48.53	872.51	20.92	0.88	2.32
ID-e-1.8R-	540.02	32.39	872.51	20.92	0.62	1.55
IDW_CFRP+	572.2	32	474.11	26.64	1.21	1.20
IDW_CFRP-	540.8	30.75	527.84	26.64	1.02	1.15
IDW_STEEL+	425.4	24.25	477.95	26.5	0.89	0.92
IDW_STEEL-	505.1	24.26	531.04	26.5	0.95	0.92
IW_CFRP+	638.7	24.13	592.15	26.26	1.08	0.92
IW_CFRP-	683.1	24.21	592.15	26.26	1.15	0.92
IW_STEEL+	556	24.1	590.62	26.35	0.94	0.91
IW_STEEL-	539	24.29	590.62	26.35	0.91	0.92
Average					0.97	1.17
COV					0.16	0.37

FIGURES

Figure 1-1 Brick wall with openings

doi:10.6342/NTU202502280

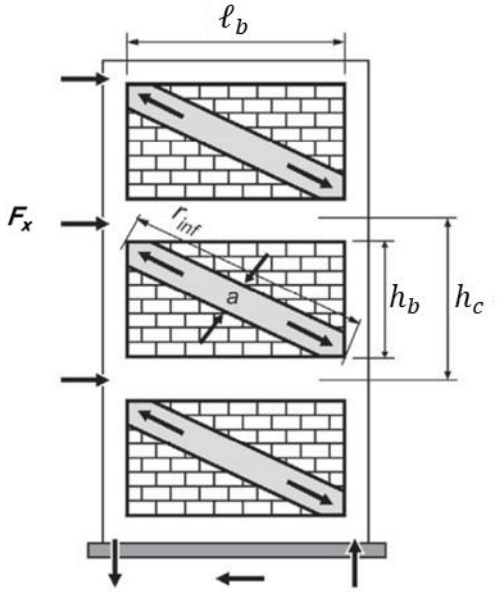

Figure 2-1 Equivalent diagonal strut of brick wall (Modified from ASCE/SEI 41-06, 2007)

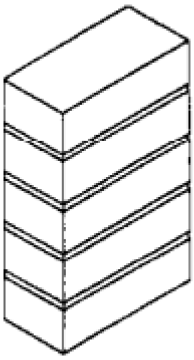

Figure 2-2 Solid unit prism (ASTM C1314, 2000)

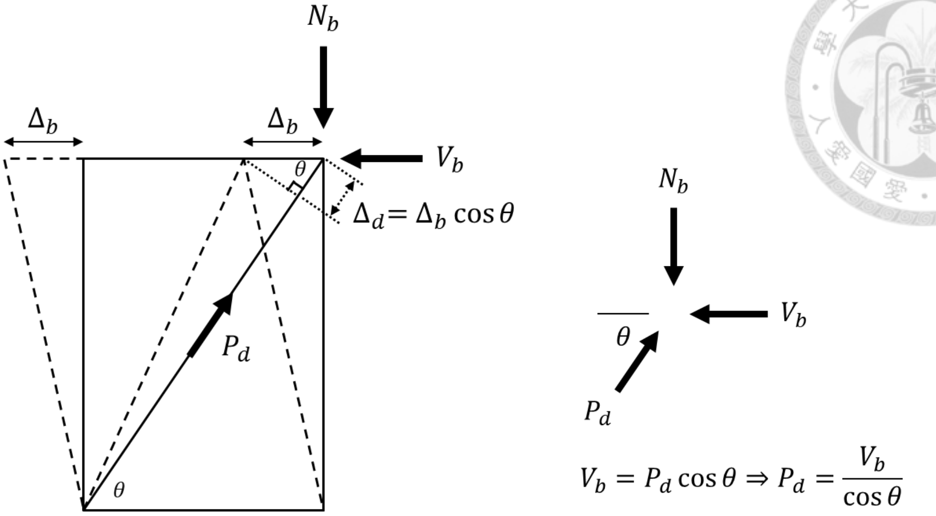

Figure 2-3 Transformation from axial stiffness of diagonal strut to lateral stiffness

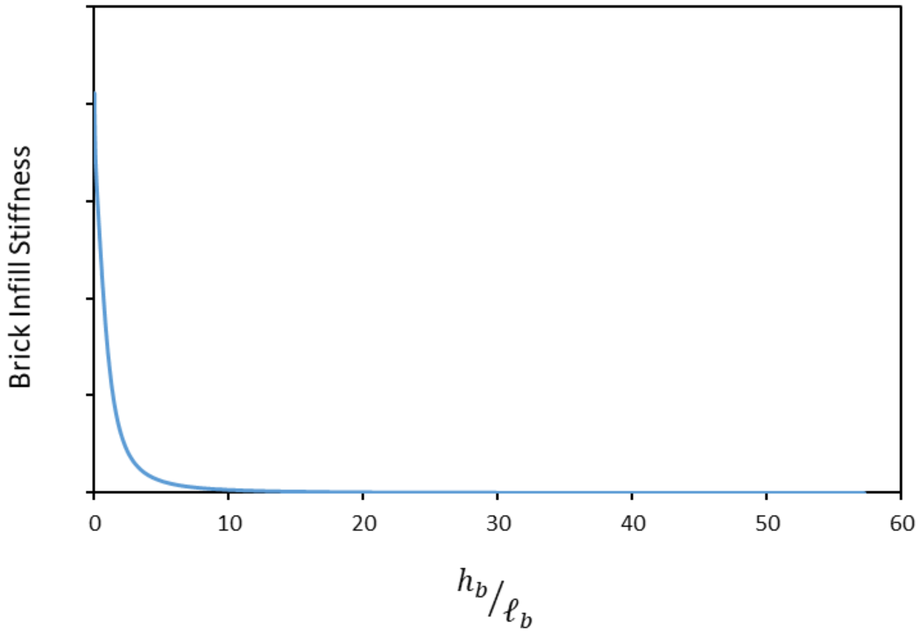

Figure 2-4 Relationship between brick infill stiffness and infill height-to-length ratio in ASCE/SEI 41-06.

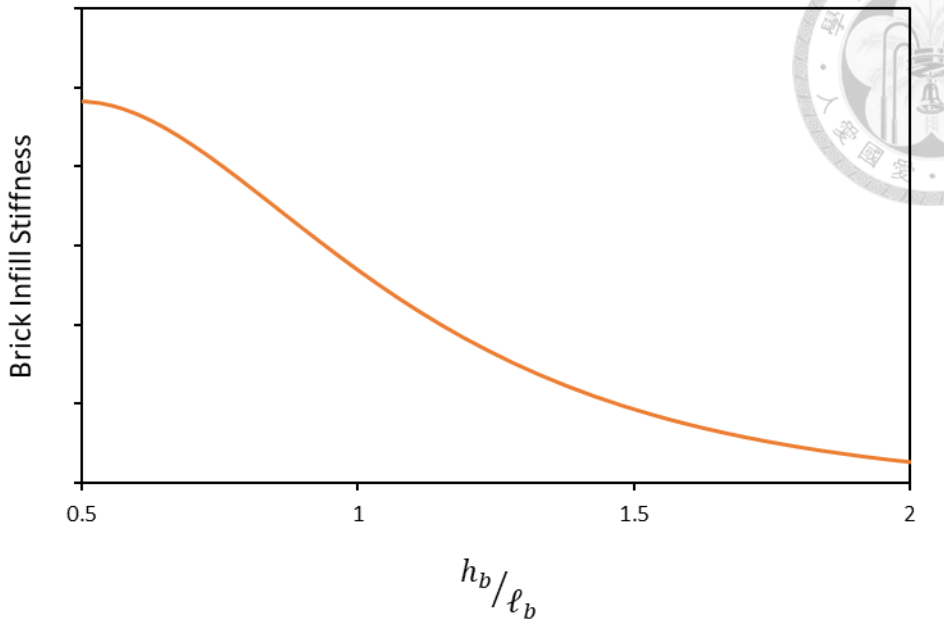

Figure 2-5 Relationship between brick infill stiffness and infill height-to-length ratio in Technical Report NCREE-13-023.

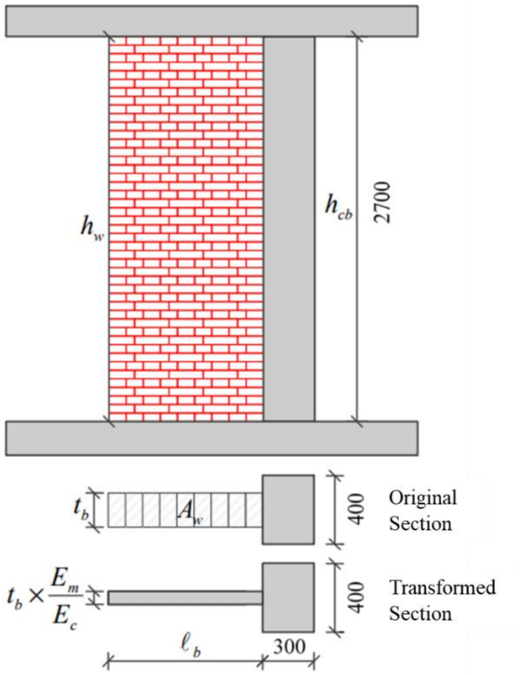

Figure 2-6 Transformed composite column section (Modified from Chiou, 2015)

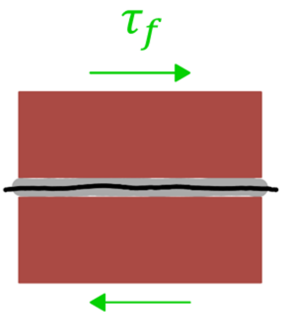

Figure 2-7 Horizontal interface sliding failure

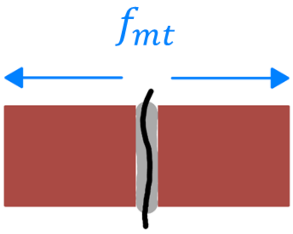

Figure 2-8 Vertical interface splitting failure

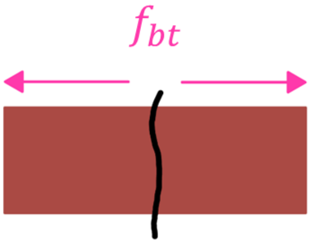

Figure 2-9 Brick vertical splitting failure

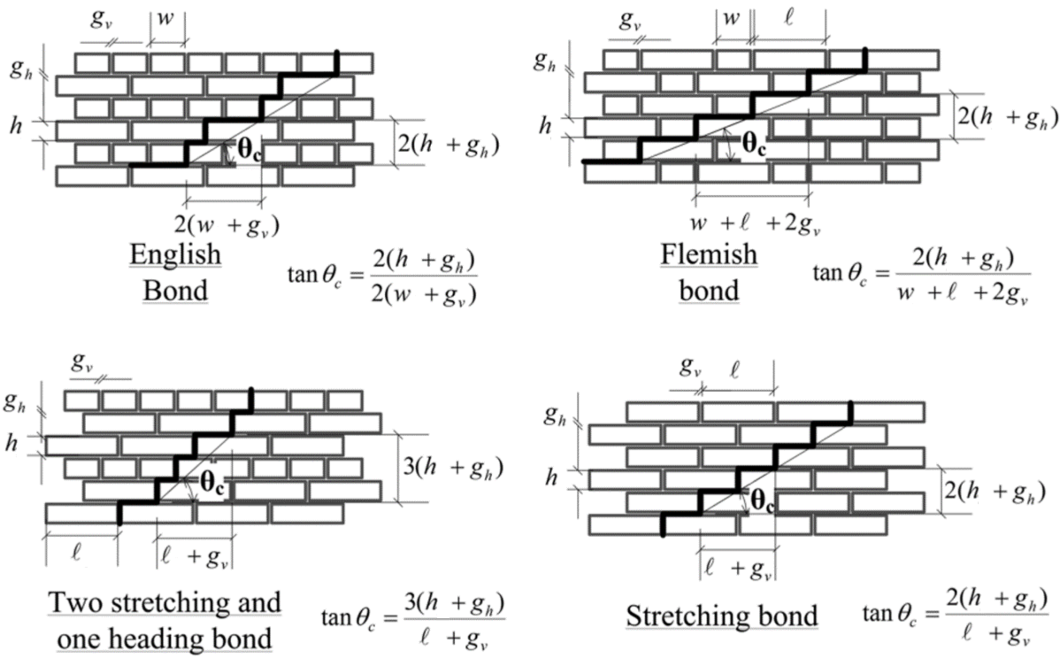

Figure 2-10 Critical cracking angles for different types of bond (Modified from Chiou & Hwang, 2015)

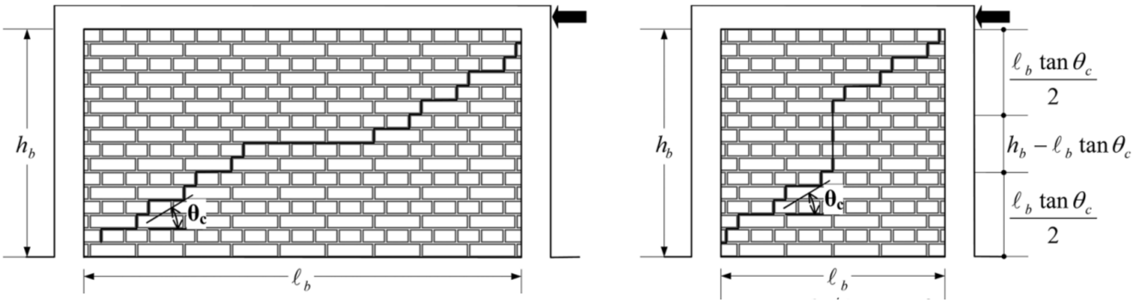

(a) $h_b/\ell_b \le \tan\theta_c$ (b) $h_b/\ell_b > \tan\theta_c$

Figure 2-11 Idealized failure path of four-sided confined brick infill wall for different infill height-to-length ratio (Chiou & Hwang, 2015)

doi:10.6342/NTU202502280

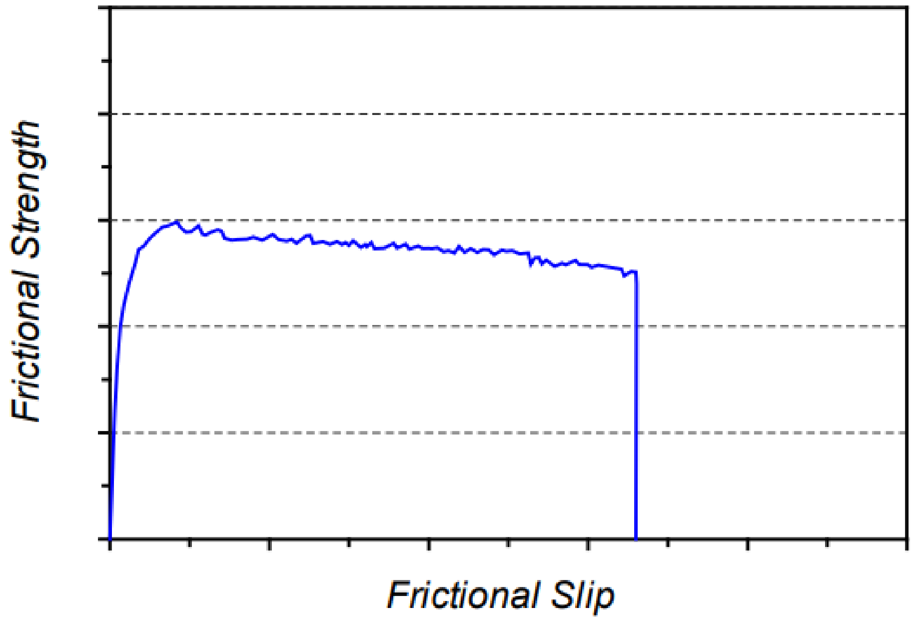

Figure 2-12 Horizontal interface sliding shear strength experiment curve (Chen, 2003)

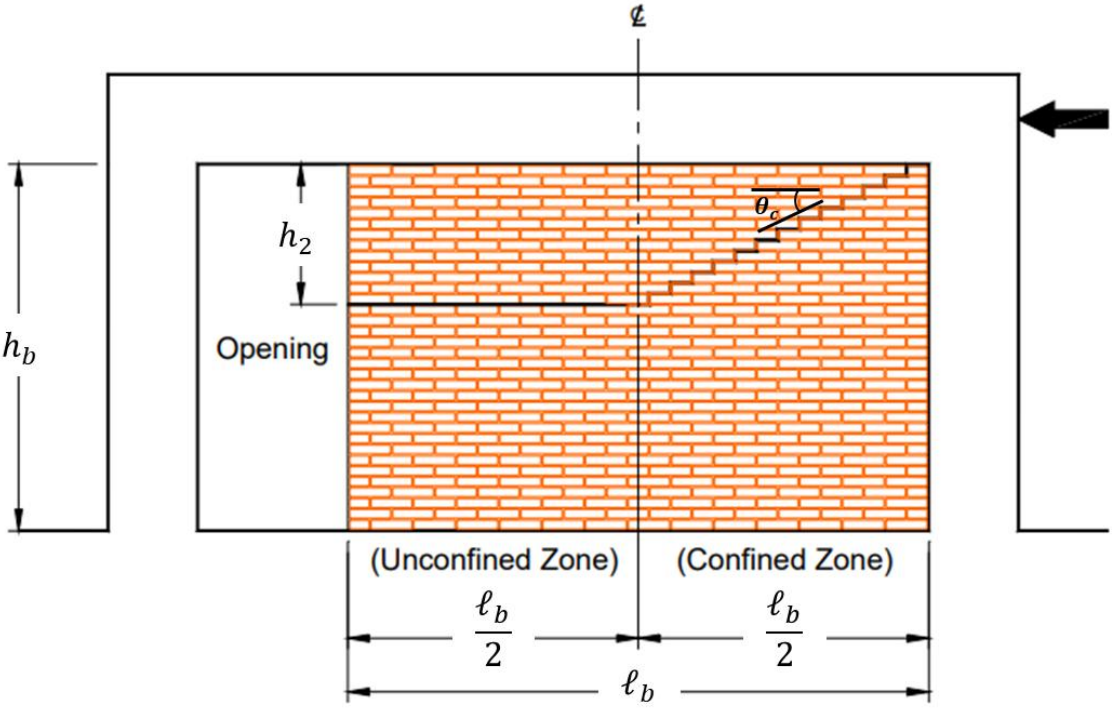

Figure 2-13 Idealized failure path of three-sided confined brick infill wall (Modified from Chen, 2003)

doi:10.6342/NTU202502280

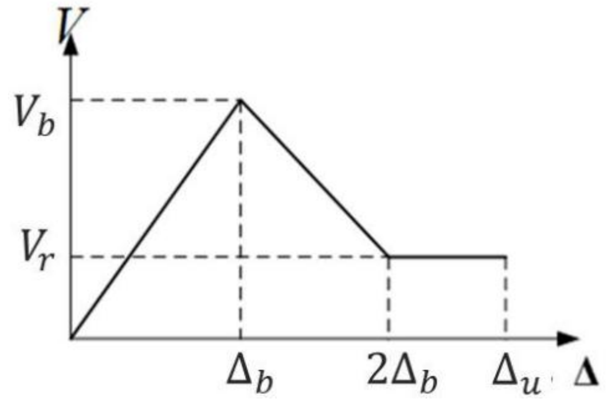

Figure 2-14 Lateral load-displacement curve of four-sided confined brick infill wall

(NCREE/TEASPA, 2020)

doi:10.6342/NTU202502280

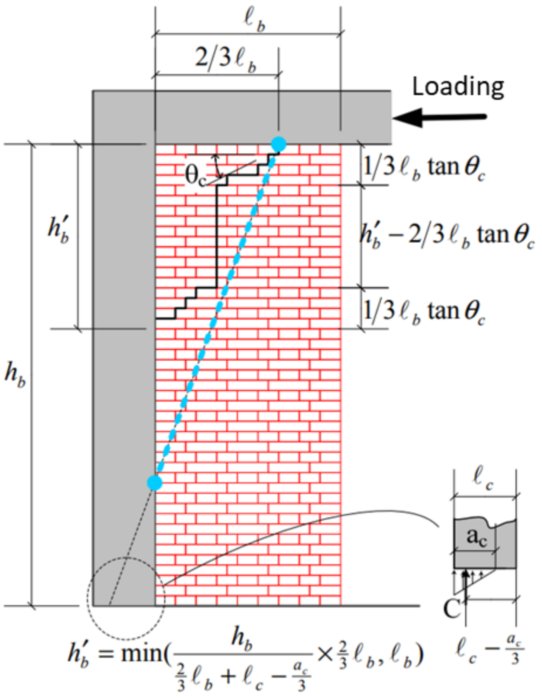

(a) Single-sided brick infill wing wall

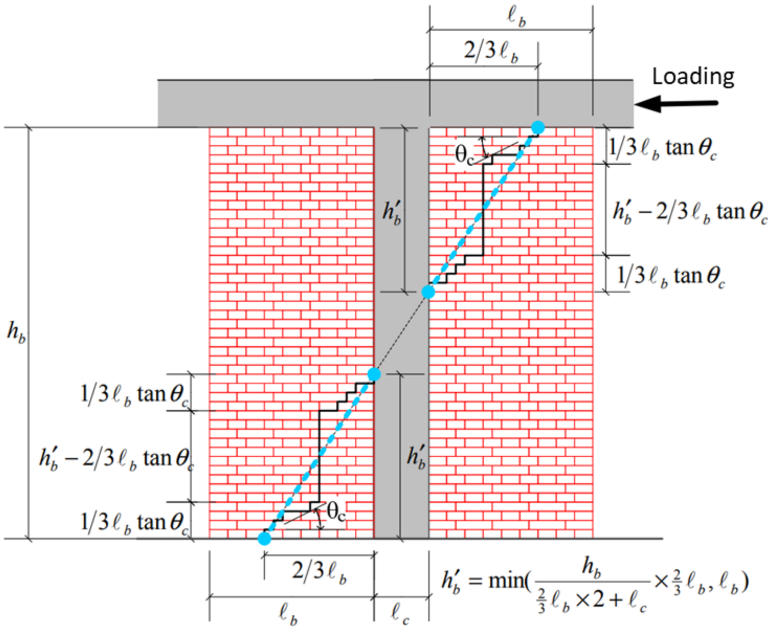

(b) Double-sided brick infill wing wall

Figure 2-15 Failure path of three-sided confined brick infill wall (Adapted from Chiou, 2015)

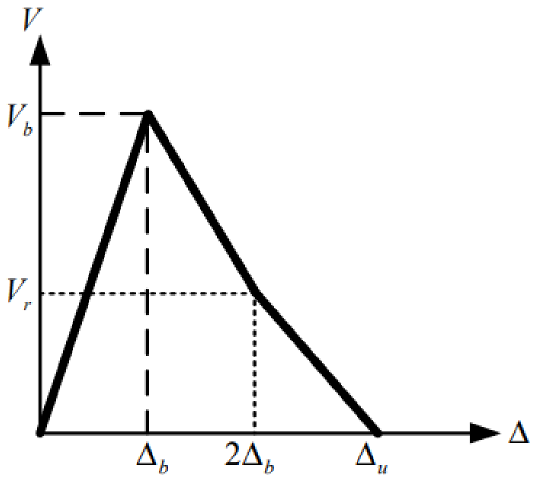

Figure 2-16 Lateral load-displacement curve of three-sided confined brick infill wall (Chiou, 2015)

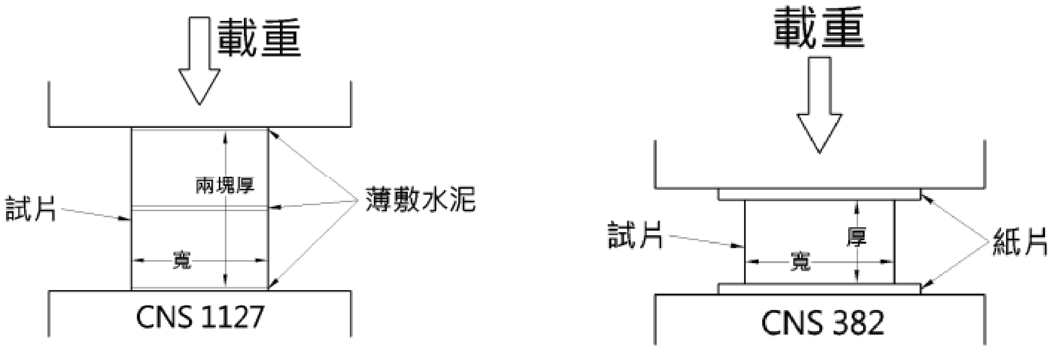

(a) CNS 1127 (b) CNS 382

Figure 2-17 Comparison between brick compressive strength f_{bc} test methods in CNS 1127 and CNS 382 (Lin, 2013)

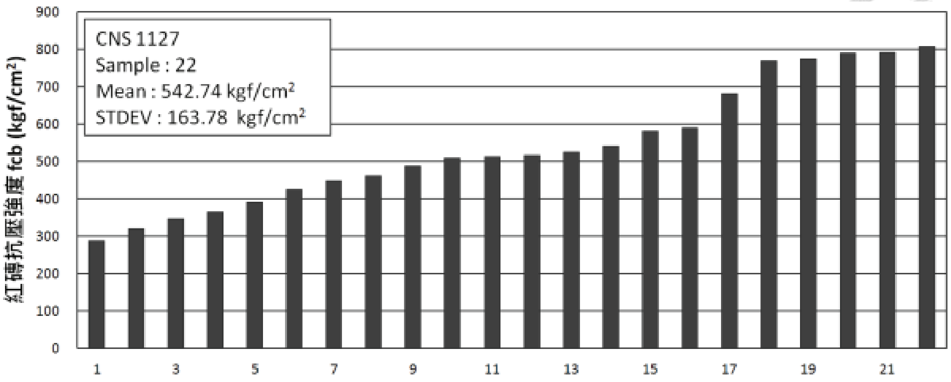

(a) Distribution of brick compressive strengths f_{bc} tested as in CNS 1127

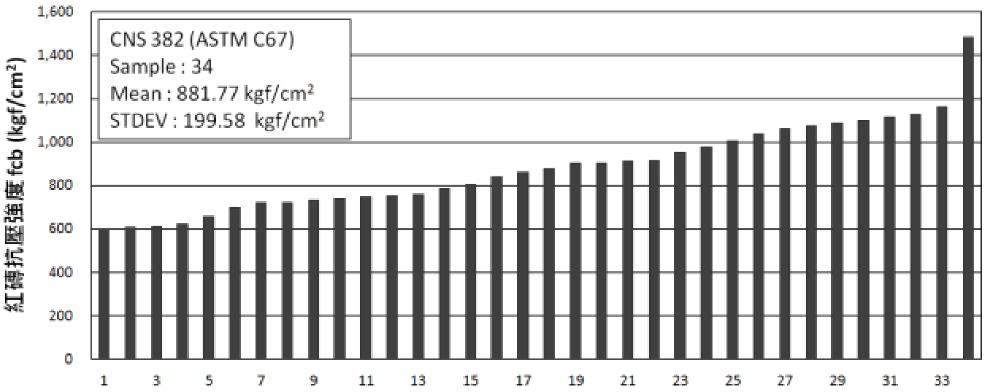

(b) Distribution of brick compressive strengths f_{bc} tested as in CNS 382

Figure 2-18 Brick compressive strengths f_{bc} distribution of specimens tested using CNS 1127 and CNS 382 methods (Lin, 2013)

doi:10.6342/NTU202502280

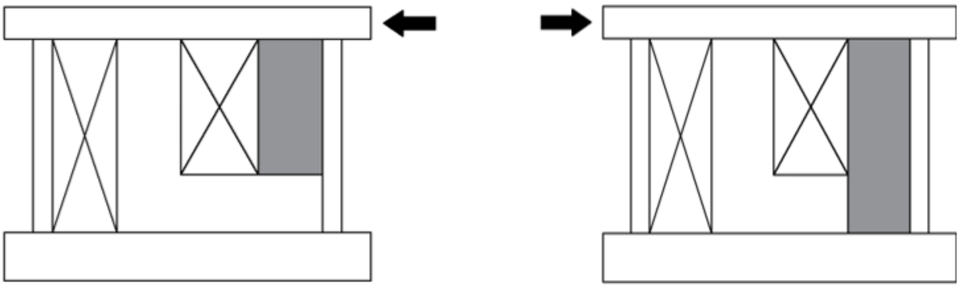

(a) Positive loading direction (b) Negative loading direction

Figure 2-19 Shear element determination for brick wall with opening (Cheng, 2021)

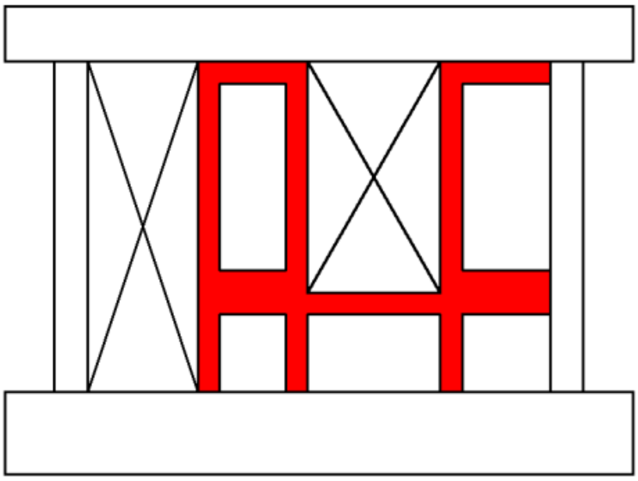

Figure 2-20 Brick wall with openings retrofitted with CFRP (Cheng, 2021)

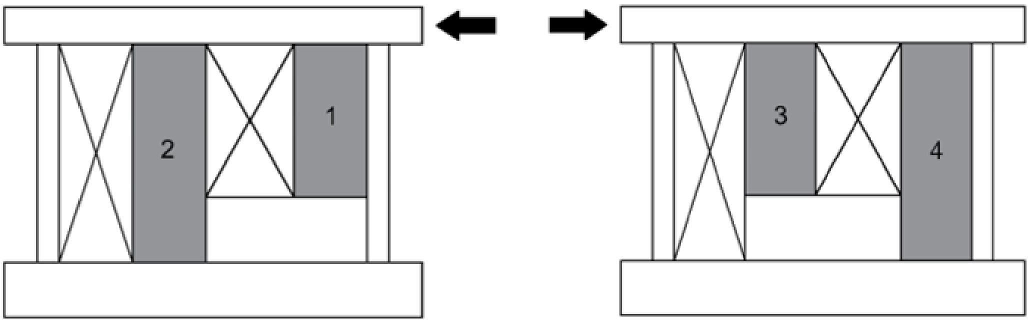

(a) Positive loading direction (b) Negative loading direction

Figure 2-21 Shear element determination for brick wall with openings retrofitted by steel angles or CFRP (Cheng, 2021)

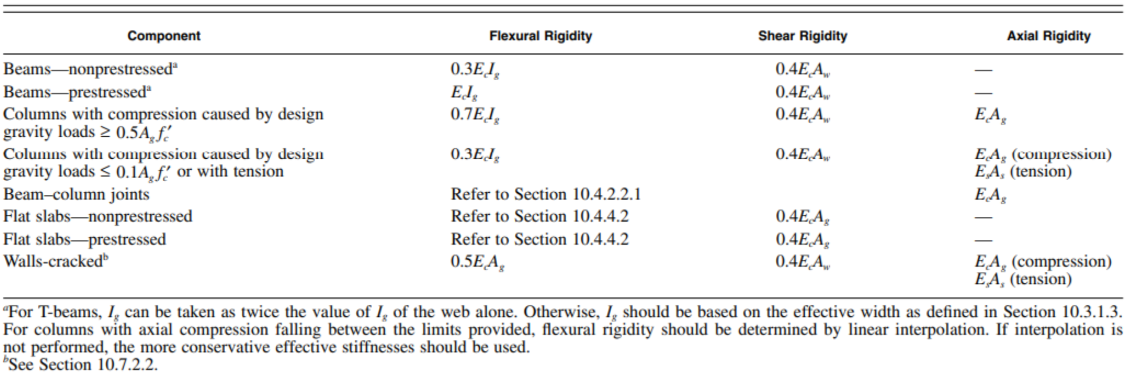

Component	Flexural Rigidity	Shear Rigidity	Axial Rigidity
Beams—nonprestressed[a]	$0.3E_cI_g$	$0.4E_cA_w$	—
Beams—prestressed[a]	E_cI_g	$0.4E_cA_w$	—
Columns with compression caused by design gravity loads $\geq 0.5A_gf_c'$	$0.7E_cI_g$	$0.4E_cA_w$	E_cA_g
Columns with compression caused by design gravity loads $\leq 0.1A_gf_c'$ or with tension	$0.3E_cI_g$	$0.4E_cA_w$	E_cA_g (compression) E_sA_s (tension)
Beam–column joints	Refer to Section 10.4.2.2.1		E_cA_g
Flat slabs—nonprestressed	Refer to Section 10.4.4.2	$0.4E_cA_g$	—
Flat slabs—prestressed	Refer to Section 10.4.4.2	$0.4E_cA_g$	—
Walls-cracked[b]	$0.5E_cA_g$	$0.4E_cA_w$	E_cA_g (compression) E_sA_s (tension)

[a] For T-beams, I_g can be taken as twice the value of I_g of the web alone. Otherwise, I_g should be based on the effective width as defined in Section 10.3.1.3. For columns with axial compression falling between the limits provided, flexural rigidity should be determined by linear interpolation. If interpolation is not performed, the more conservative effective stiffnesses should be used.
[b] See Section 10.7.2.2.

Figure 2-22 Effective stiffness values for different types of member (ASCE, 2014)

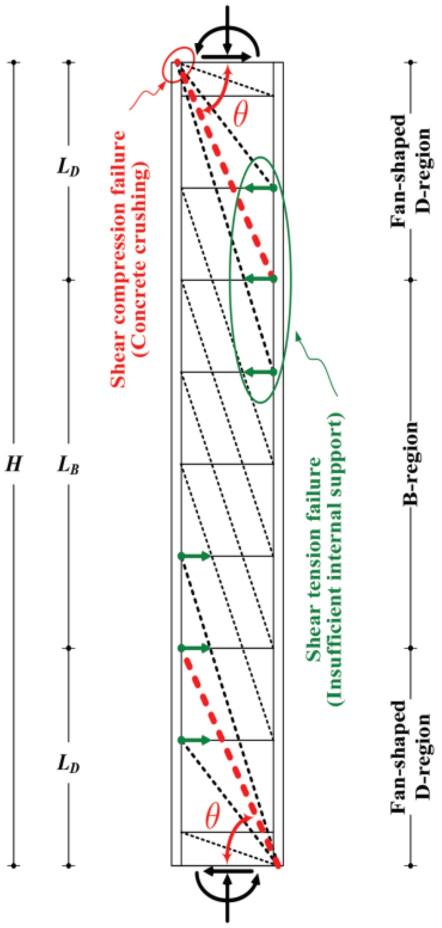

Figure 2-23 D-region and B-region of column (Shen, et. al., 2021)

doi:10.6342/NTU202502280

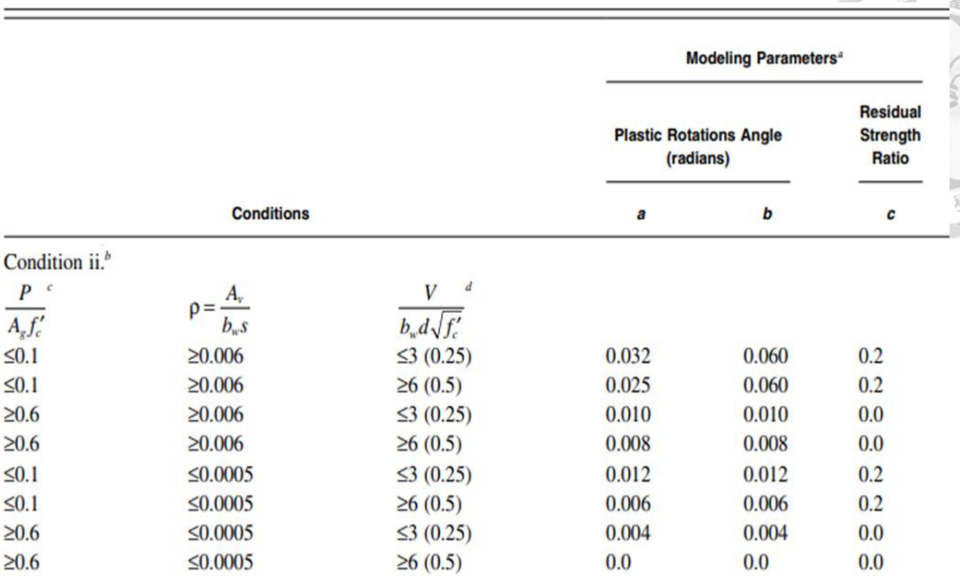

Conditions			Modeling Parameters[a]		
			Plastic Rotations Angle (radians)		Residual Strength Ratio
			a	b	c
Condition ii.[b]					
$\frac{P}{A_g f'_c}$ [c]	$\rho = \frac{A_v}{b_w s}$	$\frac{V}{b_w d \sqrt{f'_c}}$ [d]			
≤0.1	≥0.006	≤3 (0.25)	0.032	0.060	0.2
≤0.1	≥0.006	≥6 (0.5)	0.025	0.060	0.2
≥0.6	≥0.006	≤3 (0.25)	0.010	0.010	0.0
≥0.6	≥0.006	≥6 (0.5)	0.008	0.008	0.0
≤0.1	≤0.0005	≤3 (0.25)	0.012	0.012	0.2
≤0.1	≤0.0005	≥6 (0.5)	0.006	0.006	0.2
≥0.6	≤0.0005	≤3 (0.25)	0.004	0.004	0.0
≥0.6	≤0.0005	≥6 (0.5)	0.0	0.0	0.0

Figure 2-24 Modeling parameters a and b for column under flexural-shear failure

(Excerpted from ASCE, 2014)

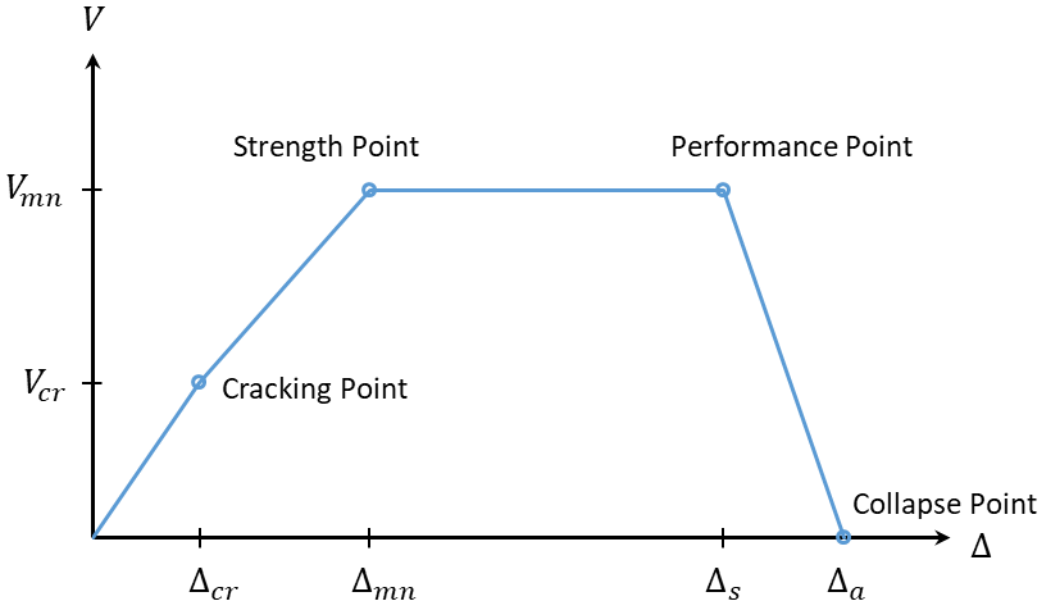

Figure 2-25 Lateral load-deflection curve of column under flexural-shear failure

Figure 2-26 Test setup (Chiou & Hwang, 2015)

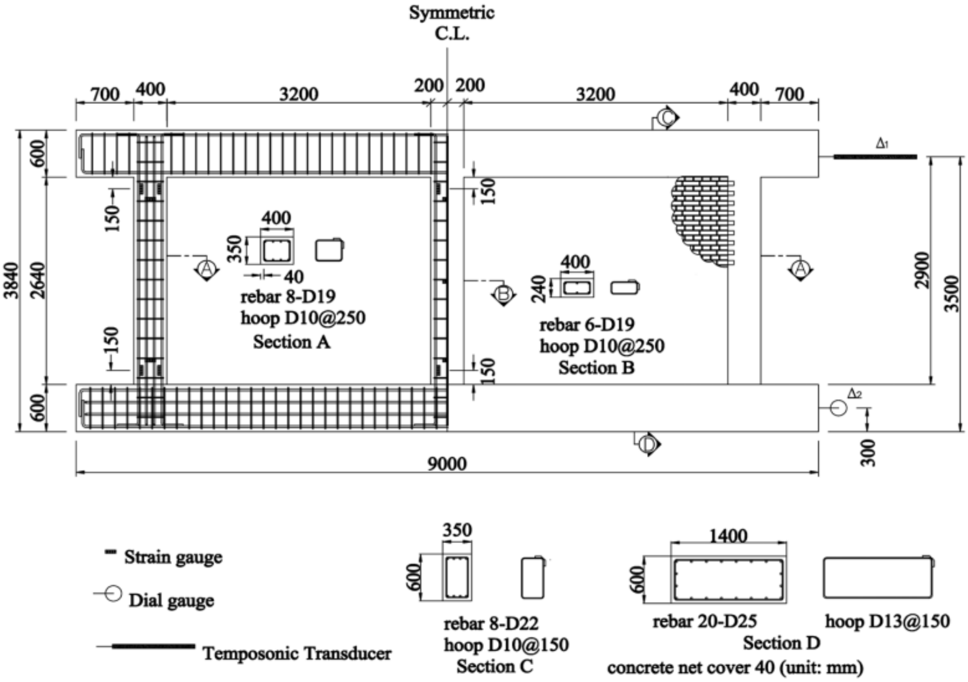

Figure 2-27 Specimen details (unit: mm) (Chiou & Hwang, 2015)

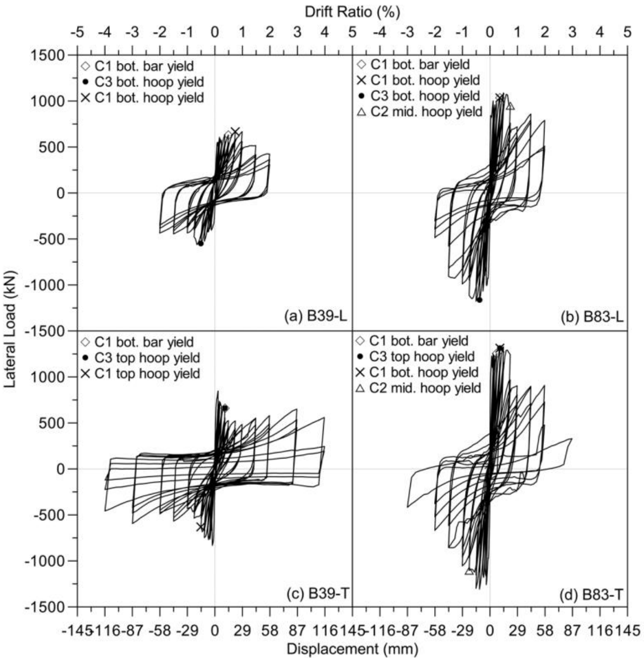

Figure 2-28 Hysteresis curves of Specimens B39-L, B83-L, B39-T, and B83-T (Chiou & Hwang, 2015)

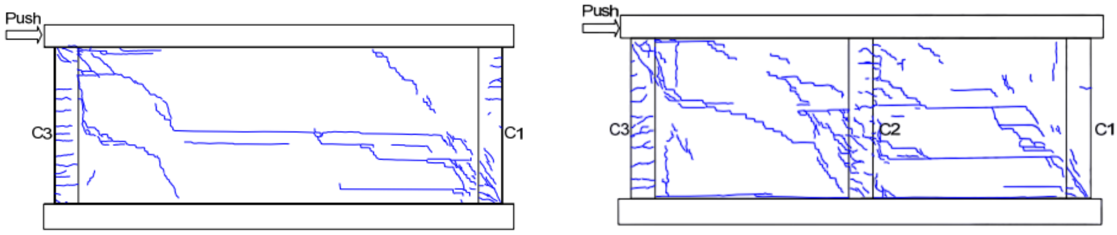

(a) B39-L (0.75%) (b) B83-L* (0.50%)

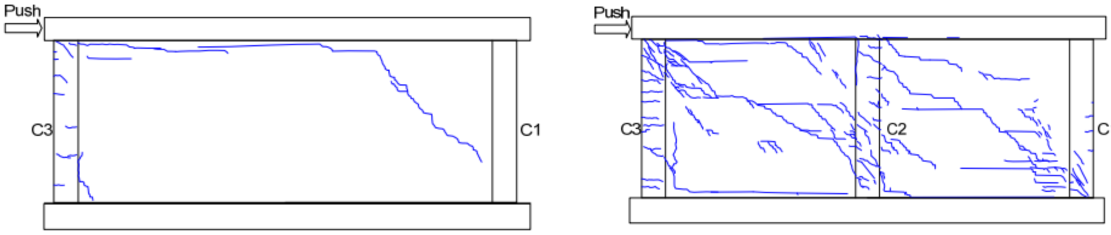

(c) B39-T (0.125%) (d) B89-T (0.50%)

* V_{max} occurs at -0.50% drift

Figure 2-29 Failure condition of Specimens B39-L, B83-L, B39-T, and B83-T at maximum strength (Chiou, 2015)

doi:10.6342/NTU202502280

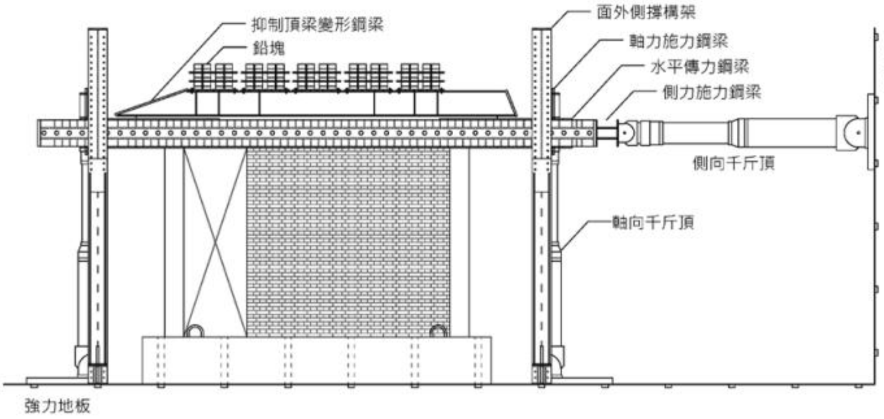

(a) Schematic view

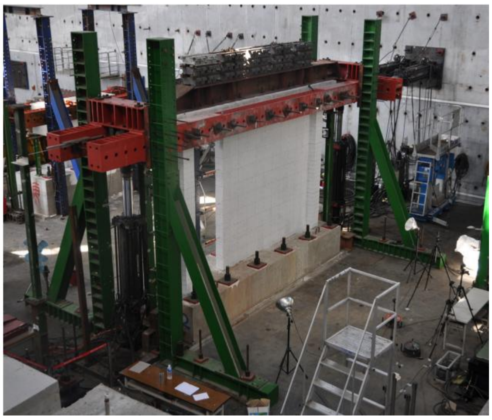

(b) Photo

Figure 2-30 Test setup of Specimens CS, IS, CD-e, and ID-e (Lin, 2016)

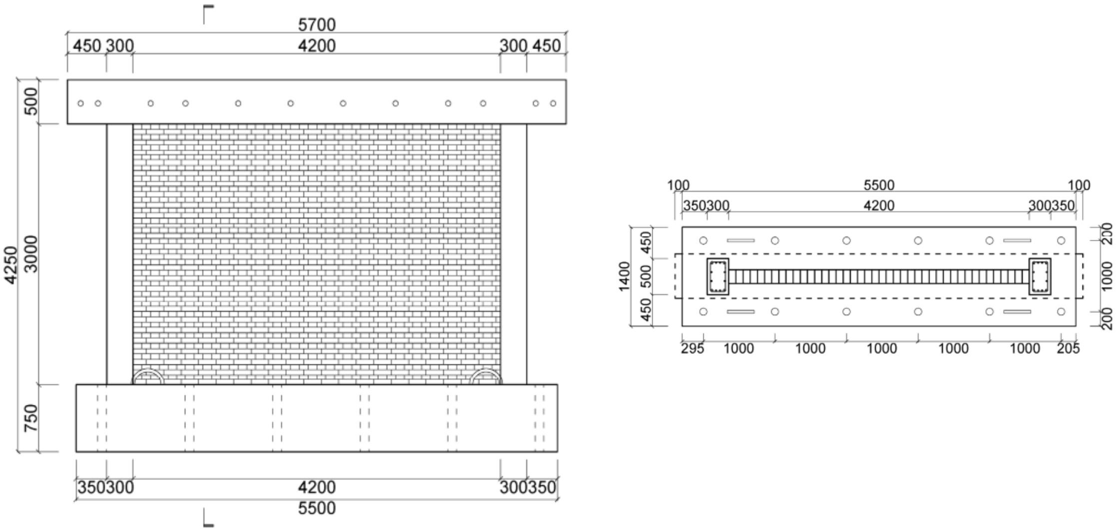

(a) Elevation view

(b) Plan view

Figure 2-31 Specimen CS, IS details (unit: mm) (Lin, 2016)

doi:10.6342/NTU202502280

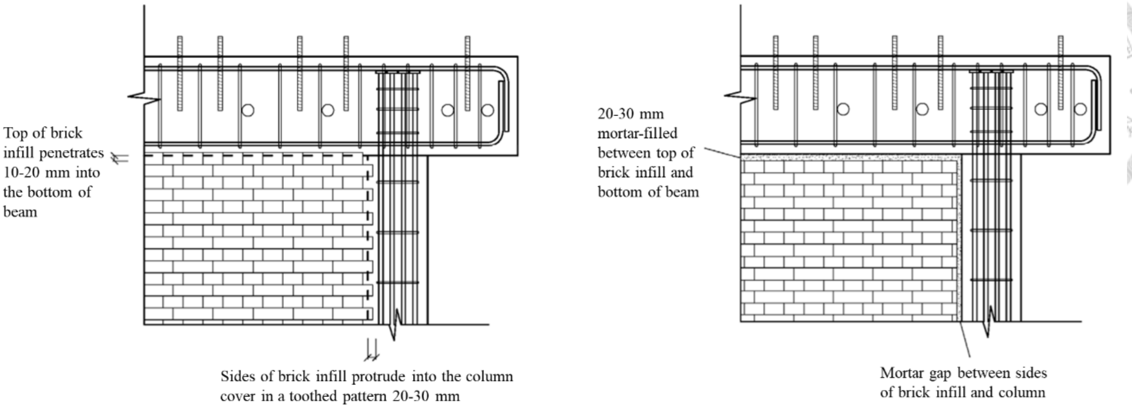

(a) Pre-laid (b) Post-laid

Figure 2-32 Interface between brick infill and confining frame for pre-laid and post-laid brick infill (Lin, 2016)

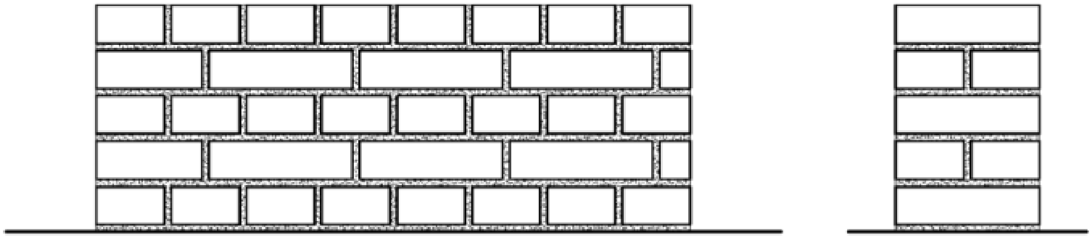

(a) Front elevation view (b) Side elevation view

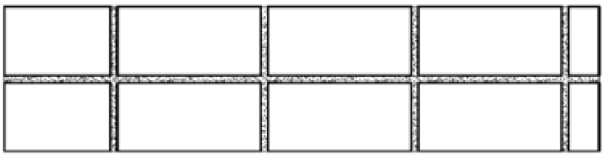

(c) Stretching brick plan view

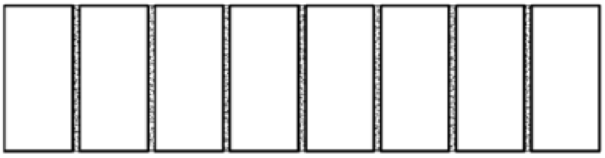

(d) Heading brick plan view

Figure 2-33 English bond 1B schematic diagram (Lin, 2016)

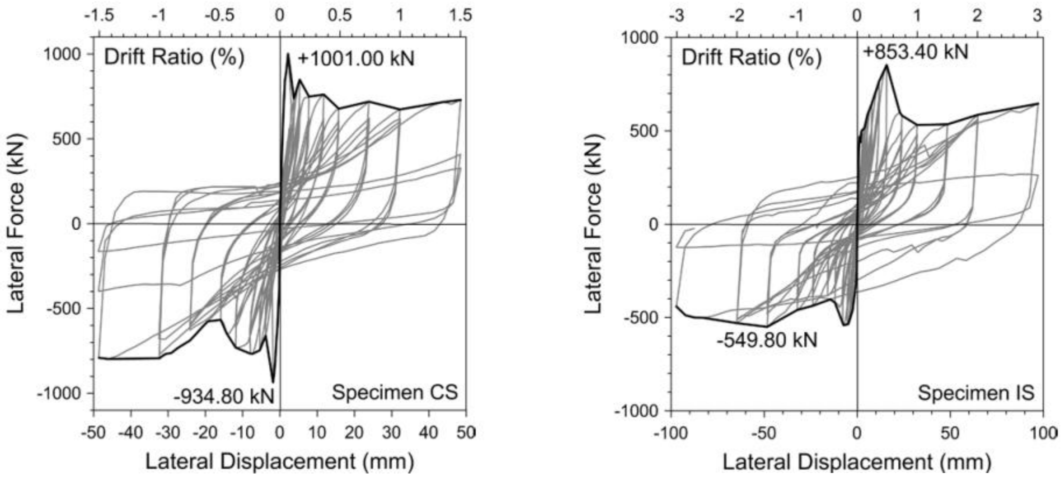

(a) Specimen CS (b) Specimen IS

Figure 2-34 Test curves of Specimens CS and IS (Lin, 2016)

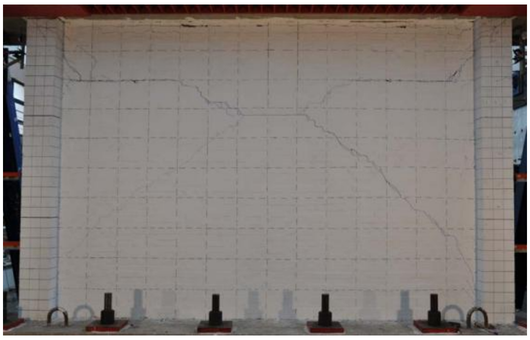

Figure 2-35 Failure condition of Specimen CS (-0.081%) at maximum strength (Lin, 2016)

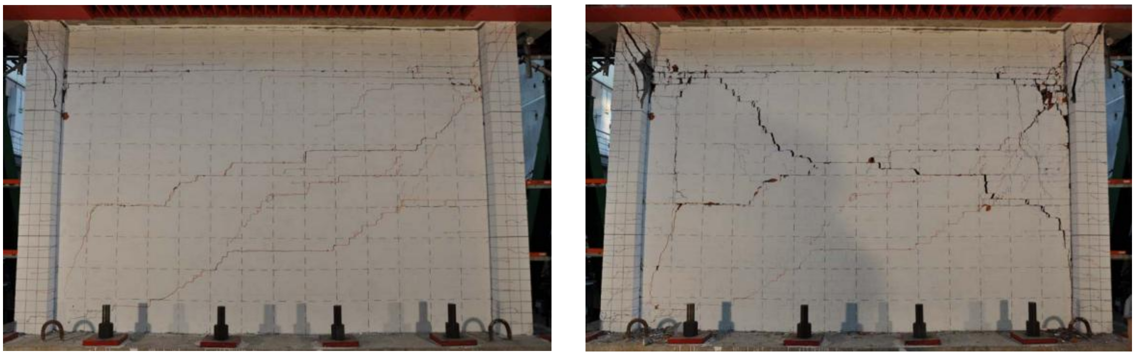

(a) Positive loading (0.491%) (b) Negative loading (-1.499%)

Figure 2-36 Failure condition of Specimen IS at maximum strength under positive and negative loading (Lin, 2016)

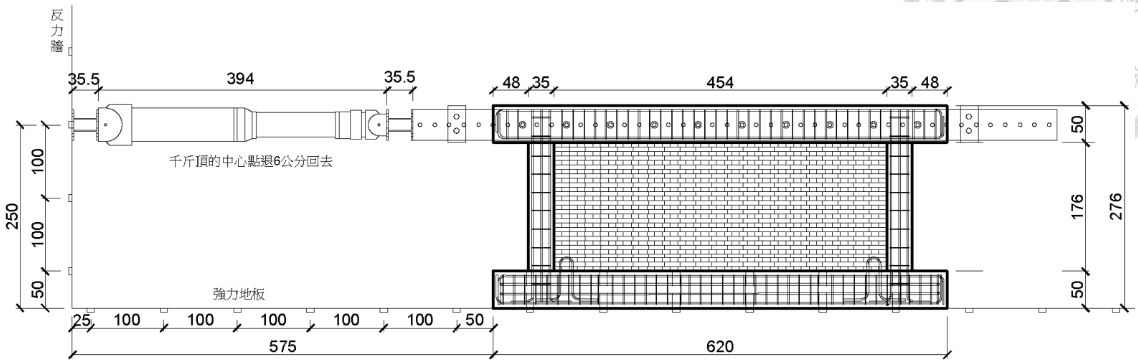

(a) Schematic view (in cm)

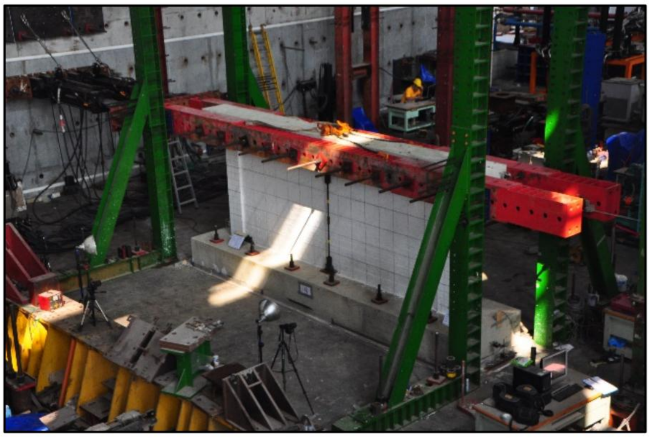

(b) Photo

Figure 2-37 Test setup of Specimens P1 and P2 (Wu, 2017)

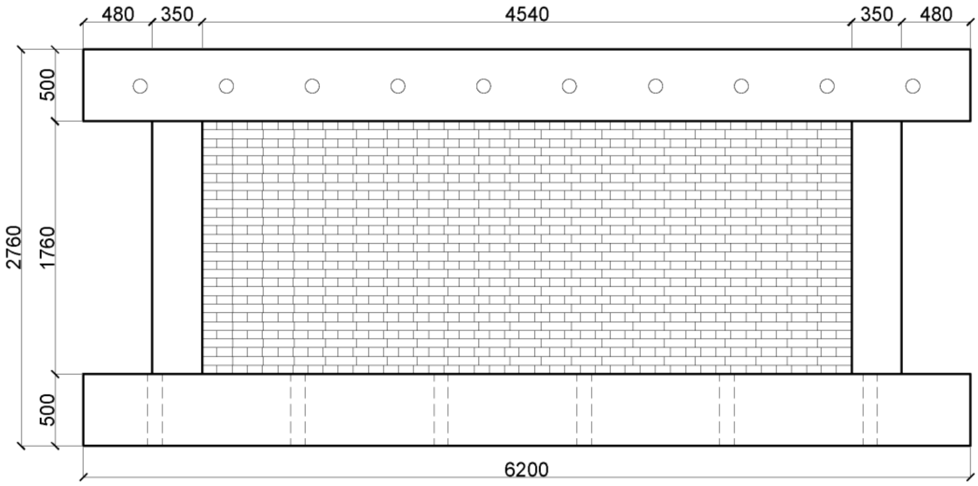

Figure 2-38 Specimens P1 and P2 details (unit: mm) (Wu, 2017)

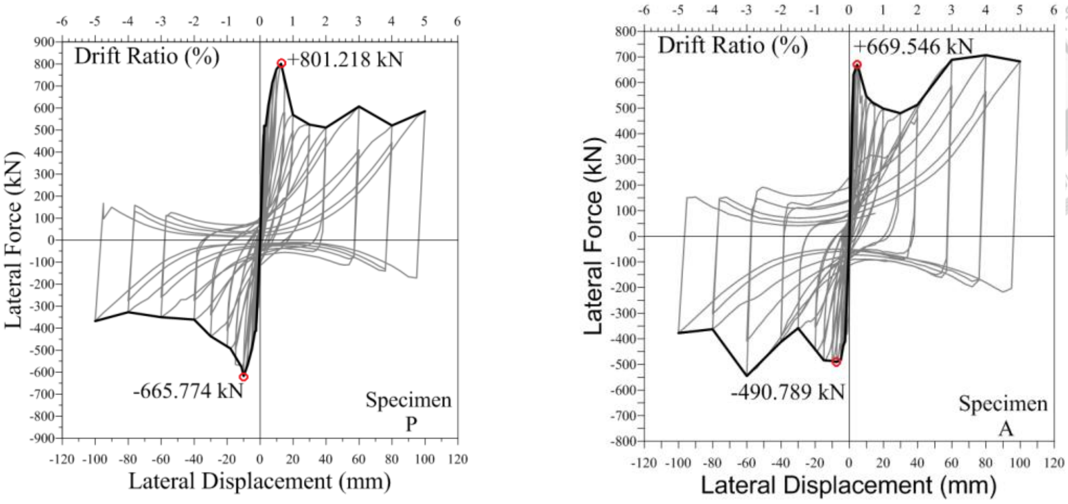

(a) Specimen P1

(b) Specimen P2

Figure 2-39 Test curves of Specimens P1 and P2 (Wu, 2017)

(a) Specimen P1 (0.75%)

(b) Specimen P2 (0.25%)

Figure 2-40 Failure condition of Specimens P1 and P2 at maximum strength (Wu, 2017)

doi:10.6342/NTU202502280

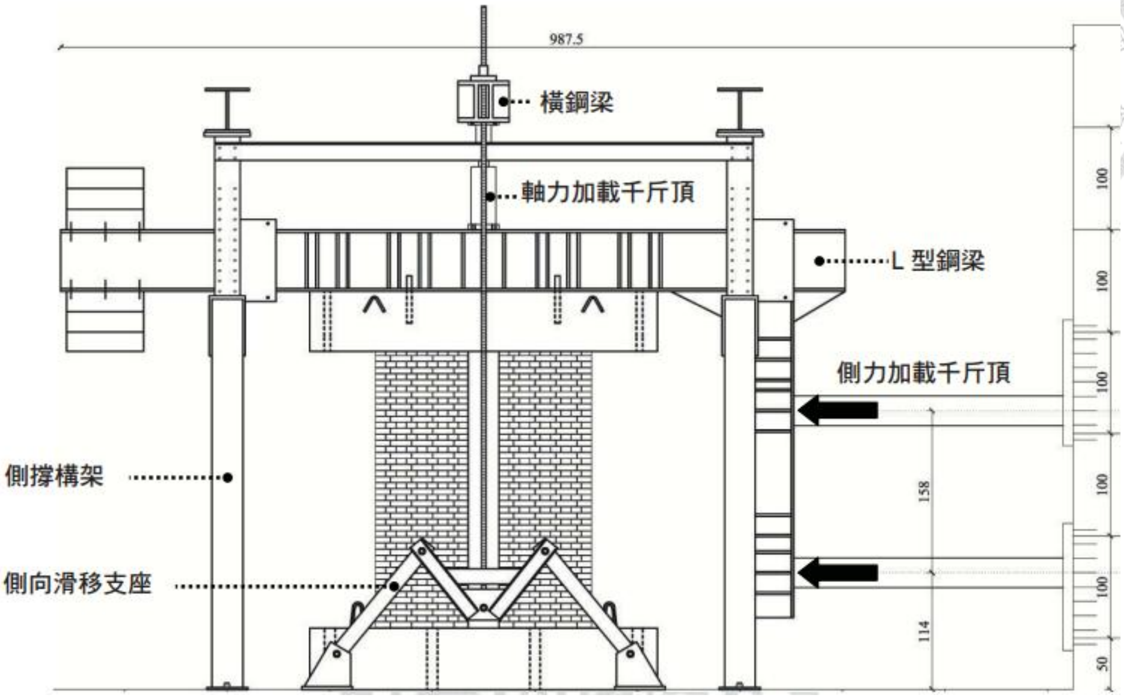

(a) Schematic view (in mm)

(b) Photo

Figure 2-41 Test setup of Specimens A and B (Lo, 2010)

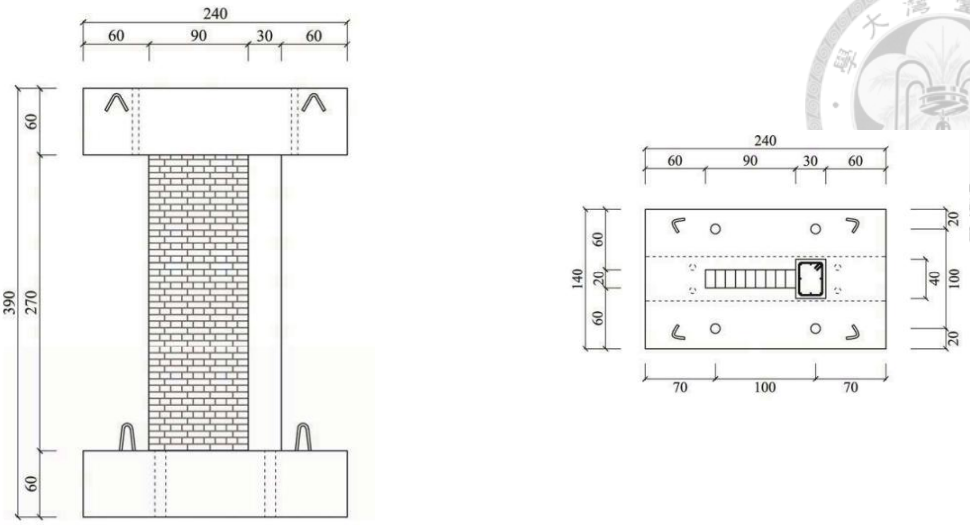

(a) Elevation view (b) Plan view

Figure 2-42 Specimens A, C, and AC details (unit: cm) (Lo, 2010)

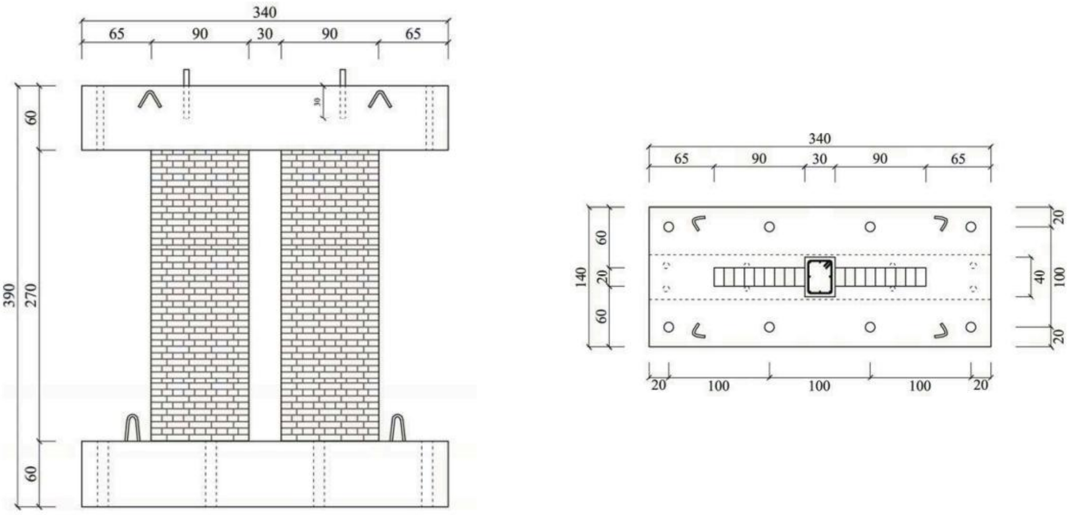

(a) Elevation view (b) Plan view

Figure 2-43 Specimens B and BC details (unit: cm) (Lo, 2010)

doi:10.6342/NTU202502280

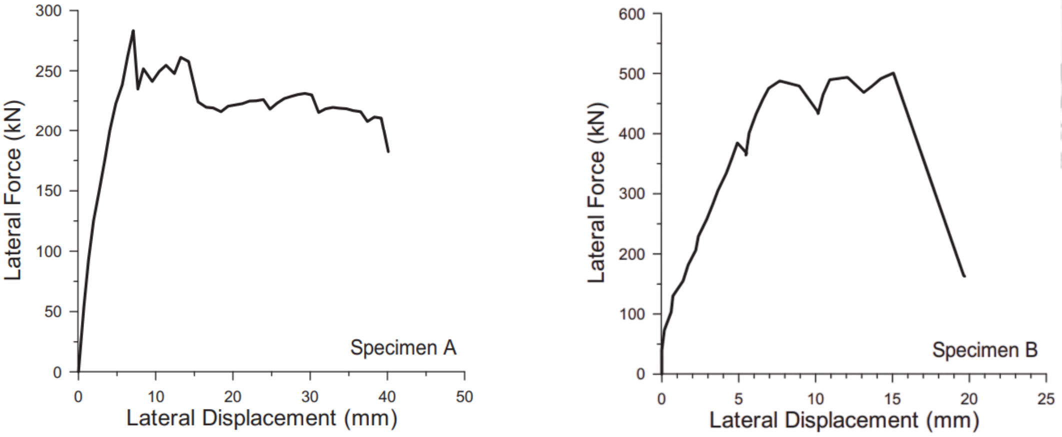

(a) Specimen A (b) Specimen B

Figure 2-44 Test curves of Specimens A and B (Lo, 2010)

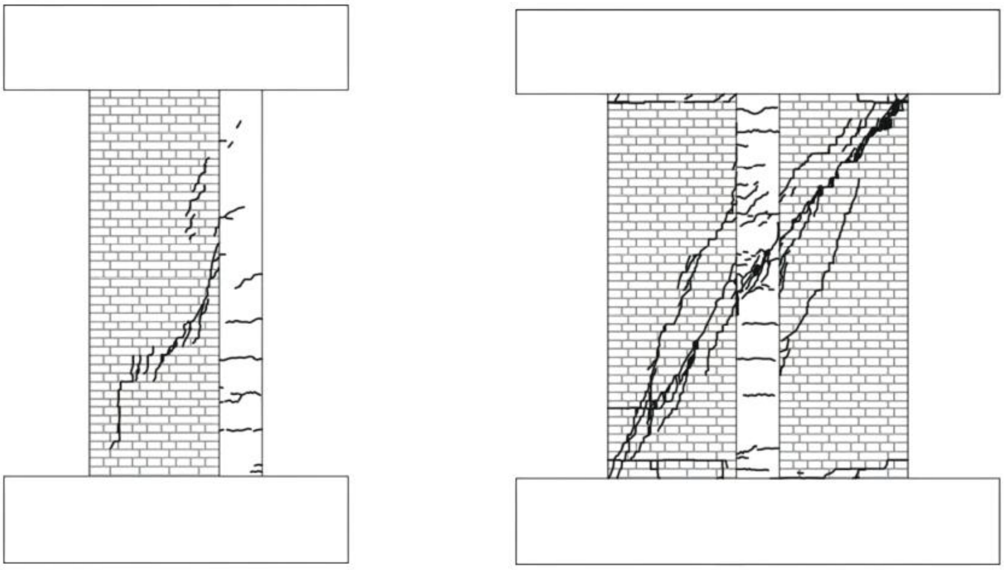

(a) Specimen A (0.26%) (b) Specimen B (0.56%)

Figure 2-45 Failure condition of Specimens A and B at maximum strength (Lo, 2010)

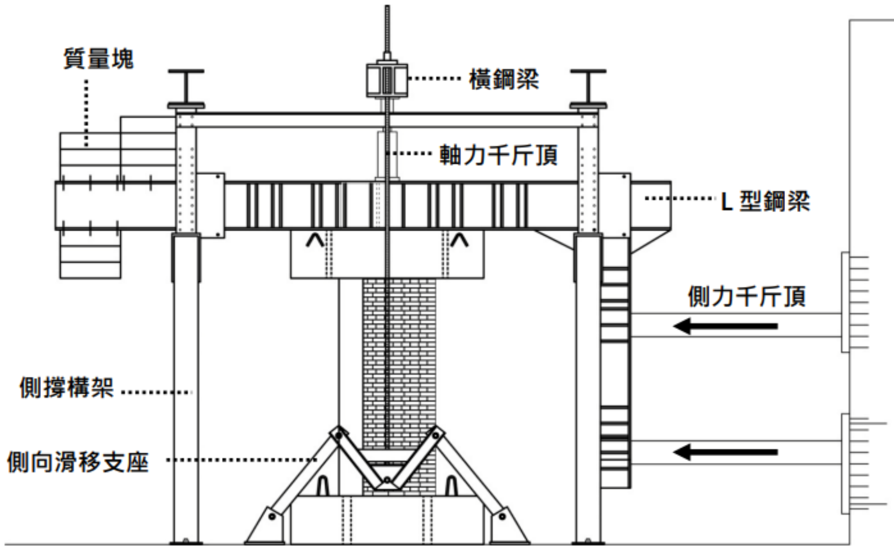

(a) Schematic view

(b) Photo

Figure 2-46 Test setup of Specimens C, AC, AL, BC, BS, and AC_C (Lin, 2011)

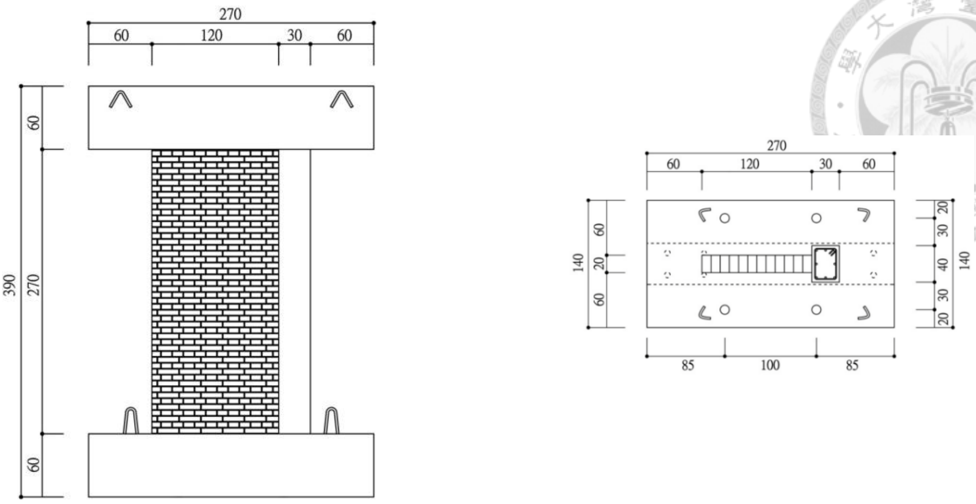

(a) Elevation view (b) Plan view

Figure 2-47 Specimen AL details (unit: cm) (Lin, 2011)

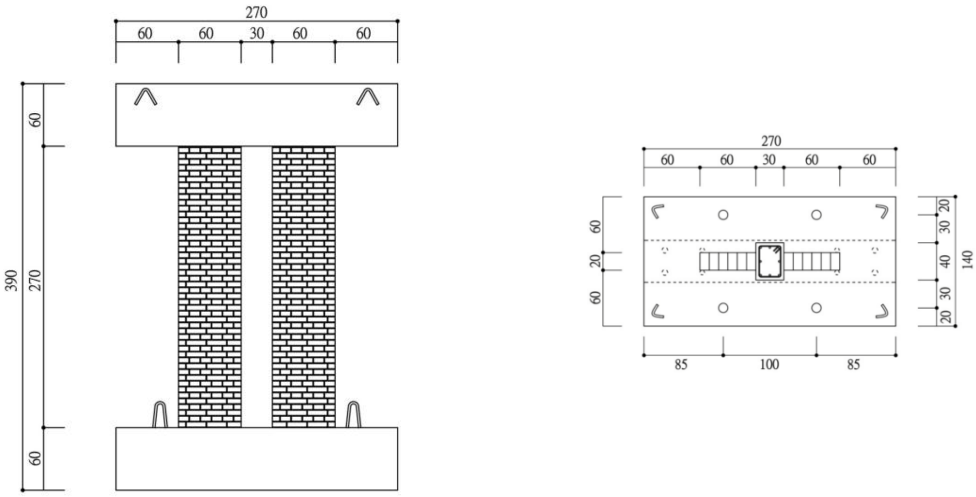

(a) Elevation view (b) Plan view

Figure 2-48 Specimen BS details (unit: cm) (Lin, 2011)

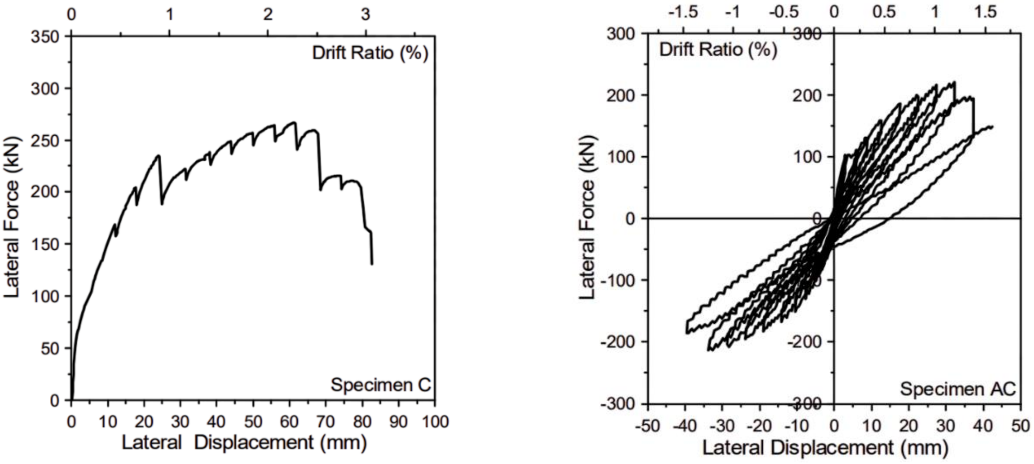

(a) Specimen C (b) Specimen AC

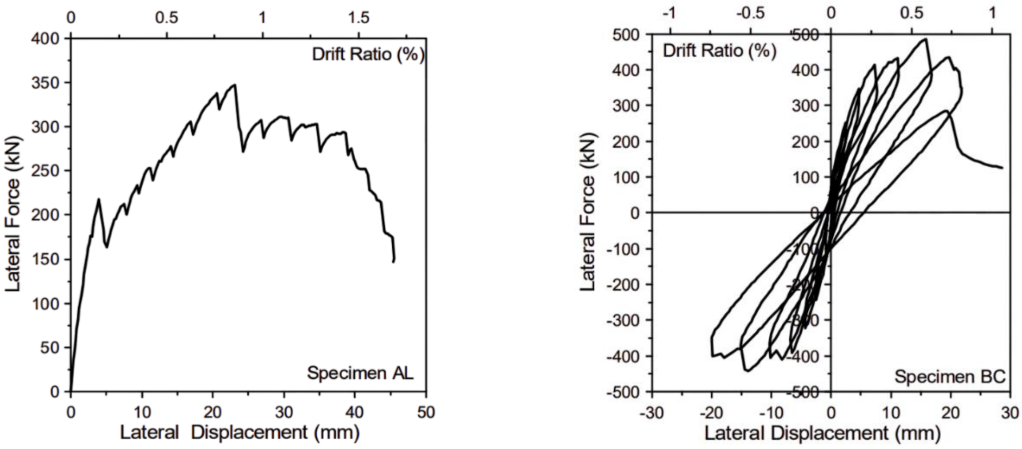

(c) Specimen AL (d) Specimen BC

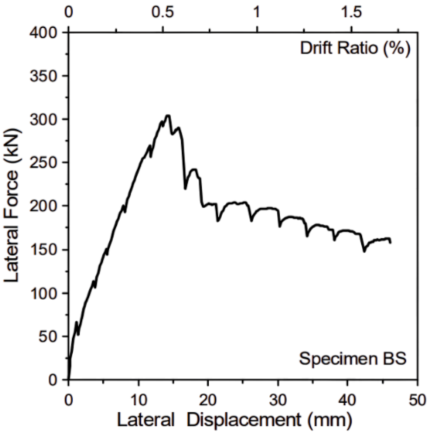

(e) Specimen BS

Figure 2-49 Test curves of Specimens C, AC, AL, BC, and BS (Lin, 2011)

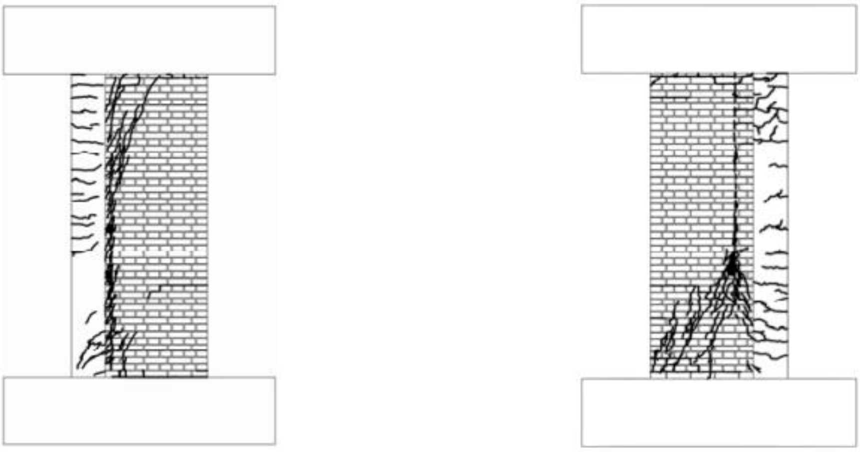

(a) Specimen C (b) Specimen AC

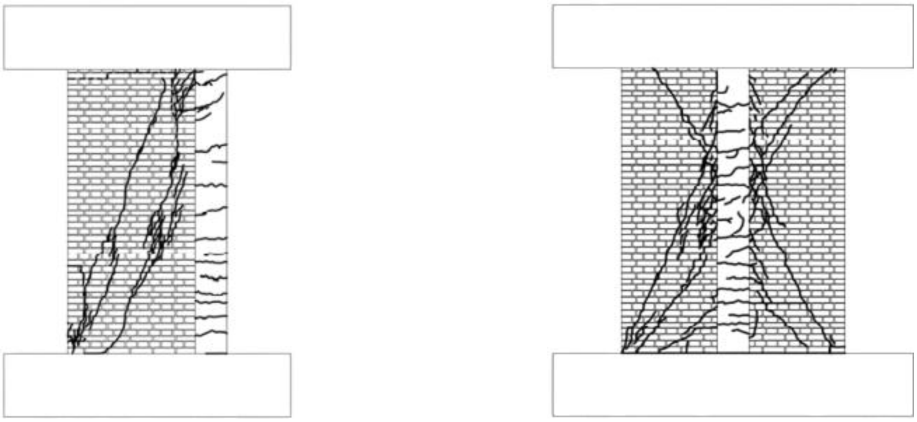

(c) Specimen AL (d) Specimen BC

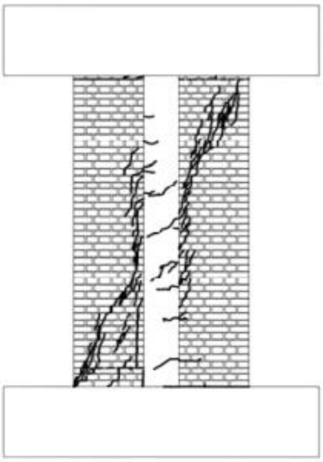

(e) Specimen BS

Figure 2-50 Schematic failure condition of Specimens C, AC, AL, BC, and BS at maximum strength (Lin, 2011)

doi:10.6342/NTU202502280

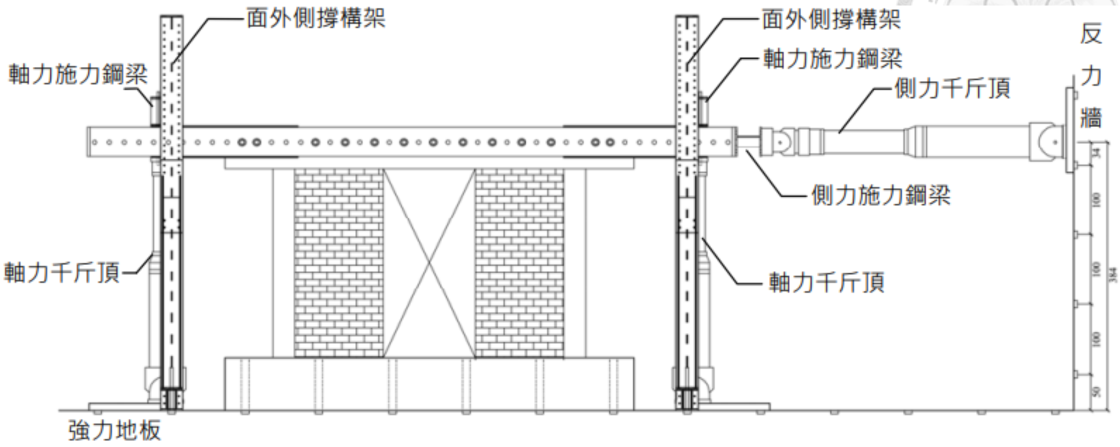

(a) Schematic view

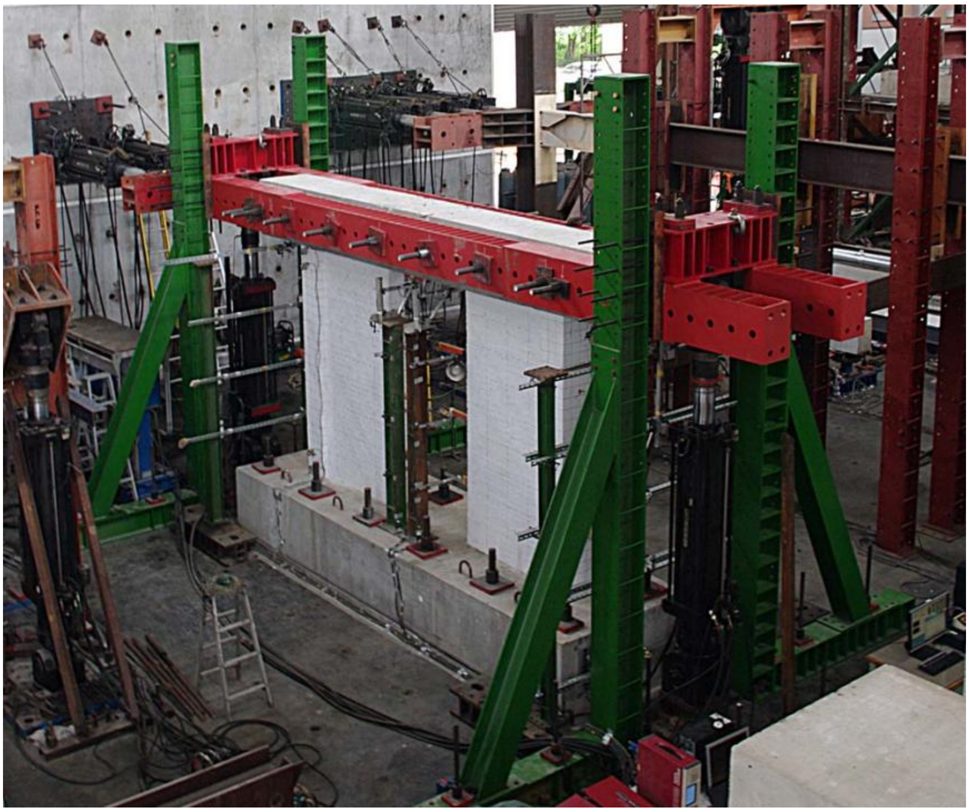

(b) Photo

Figure 2-51 Test setup of Specimens CD and CW (Hsu, 2015)

doi:10.6342/NTU202502280

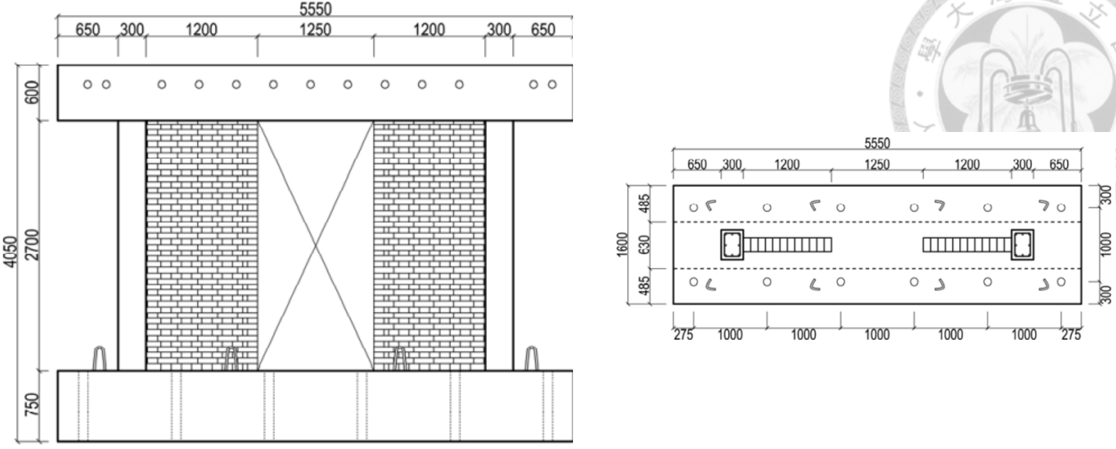

(a) Elevation view (b) Plan view

Figure 2-52 Specimens CD and ID details (unit: mm) (Hsu, 2015)

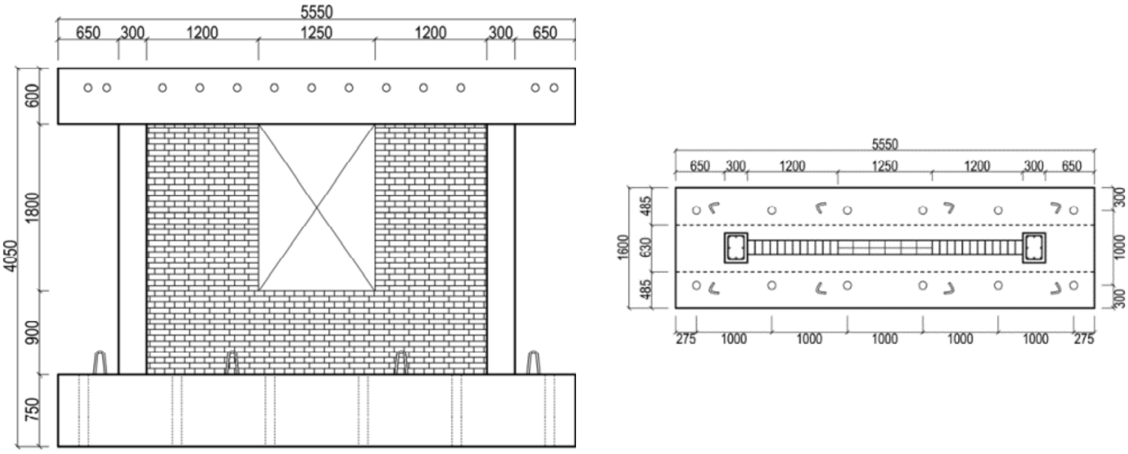

(a) Elevation view (b) Plan view

Figure 2-53 Specimens CW and IW details (unit: mm) (Hsu, 2015)

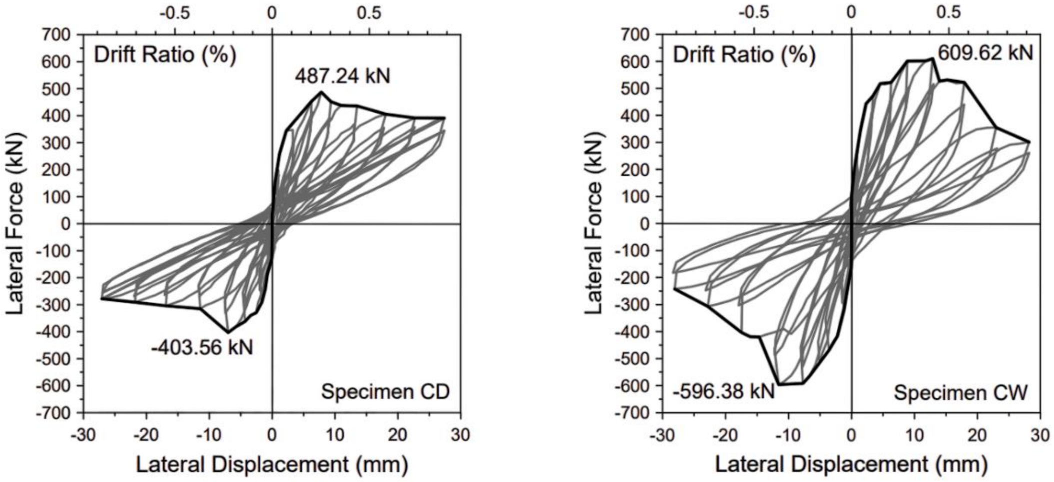

(a) Specimen CD (b) Specimen CW

Figure 2-54 Test curves of Specimens CD and CW (Hsu, 2015)

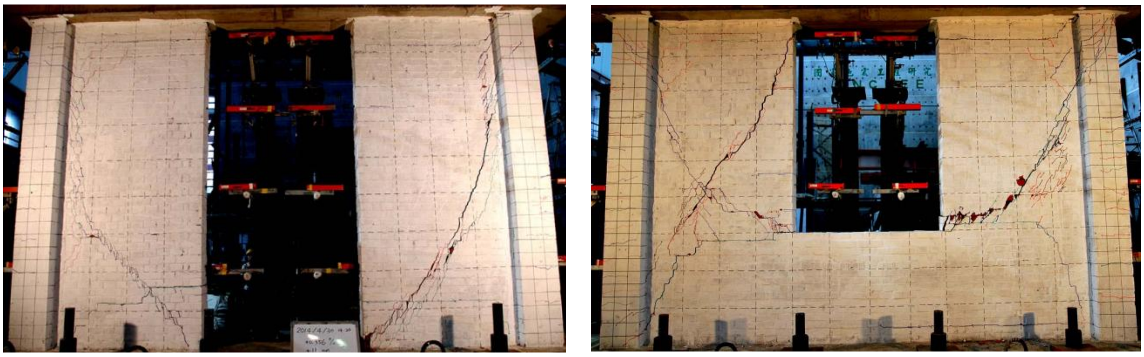

(a) Specimen CD (0.303%) (b) Specimen CW (0.417%)

Figure 2-55 Failure condition of Specimens CD and CW at maximum strength (Hsu, 2015)

doi:10.6342/NTU202502280

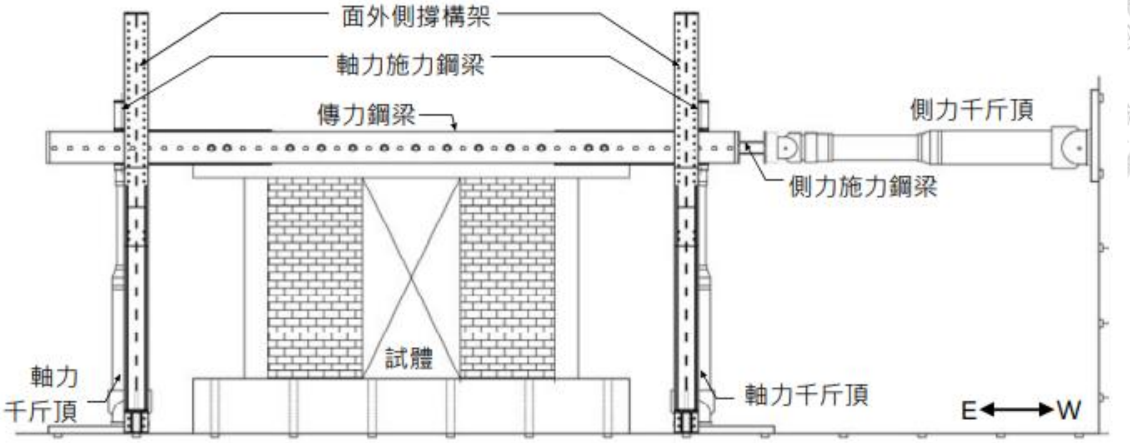

(a) Schematic view

(b) Photo

Figure 2-56 Test setup of Specimens ID and ID_BF (Chao, 2015)

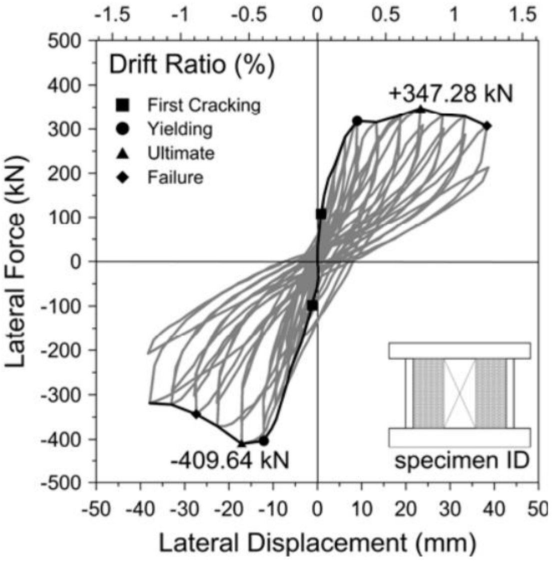

Figure 2-57 Test curve of Specimen ID (Chao, 2015)

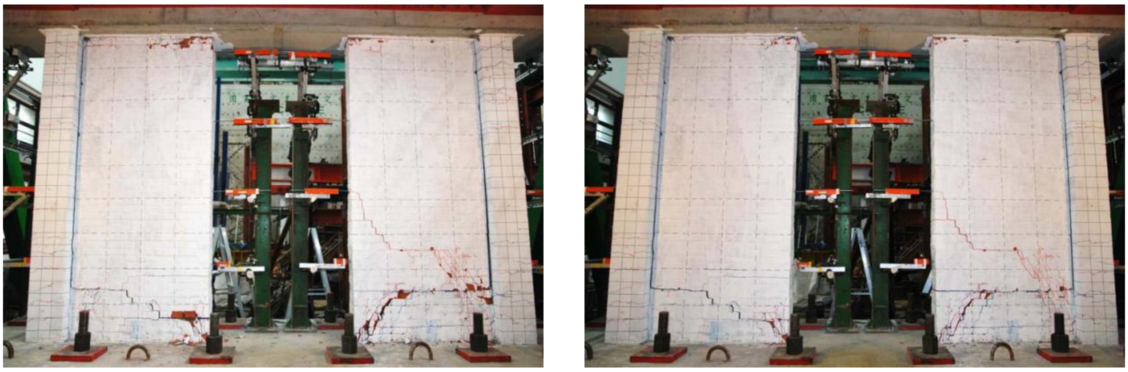

(a) Positive loading (0.76%)

(b) Negative loading (-0.55%)

Figure 2-58 Failure condition of Specimen ID at maximum strength under positive and negative loading (Chao, 2015)

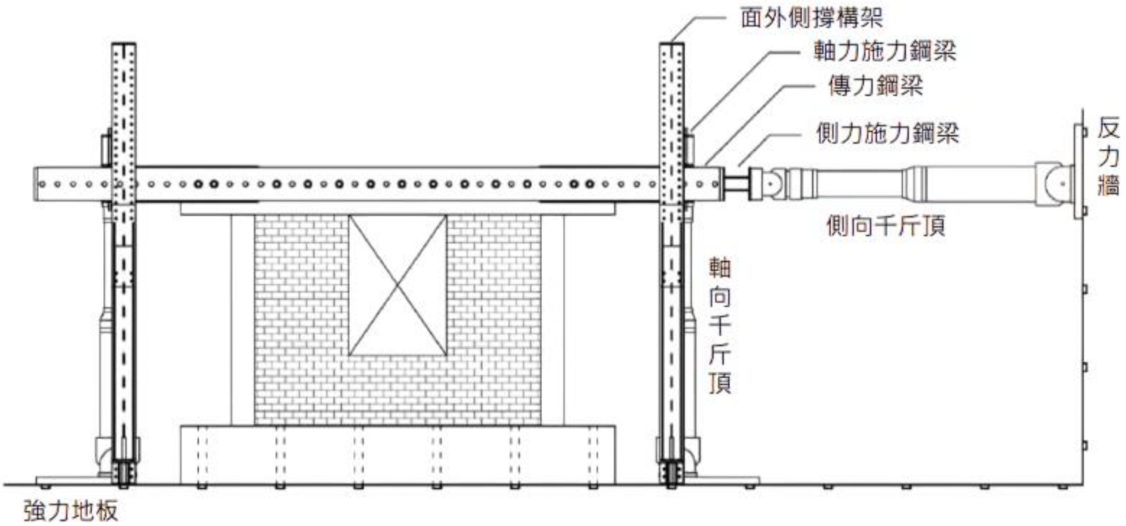

(a) Schematic view

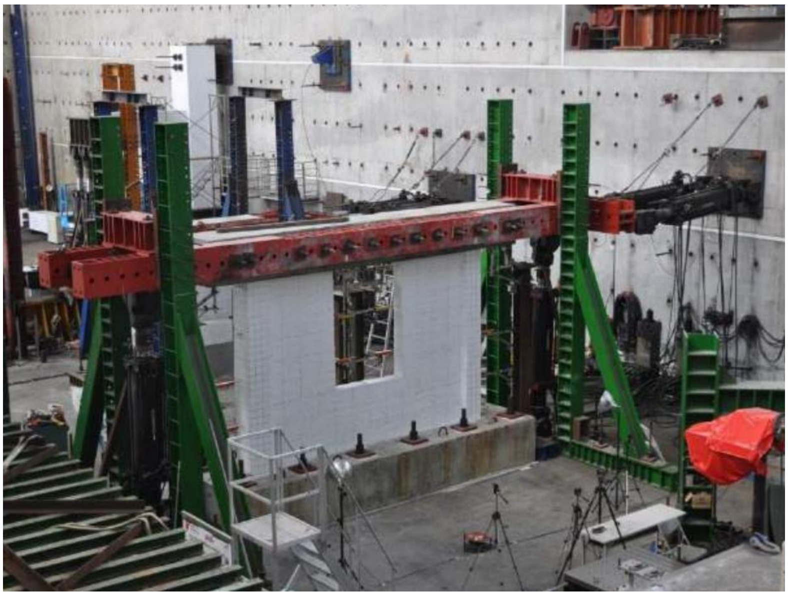

(b) Photo

Figure 2-59 Test setup of Specimen IW (Tsai, 2016)

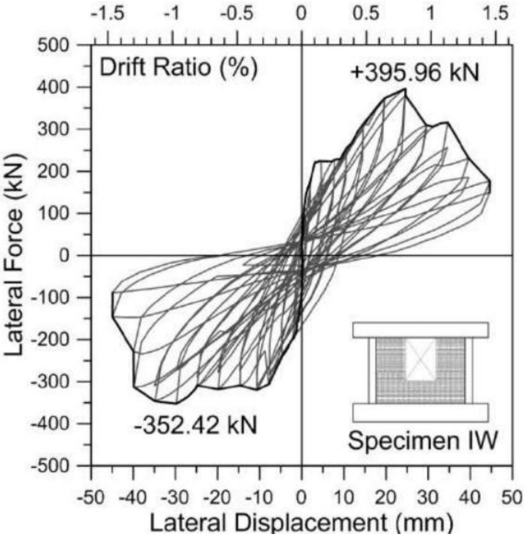

Figure 2-60 Test curve of Specimen IW (Tsai, 2016)

(c) Positive loading (0.796%)

(d) Negative loading (-0.964%)

Figure 2-61 Failure condition of Specimen IW at maximum strength under positive and negative loading (Tsai, 2016)

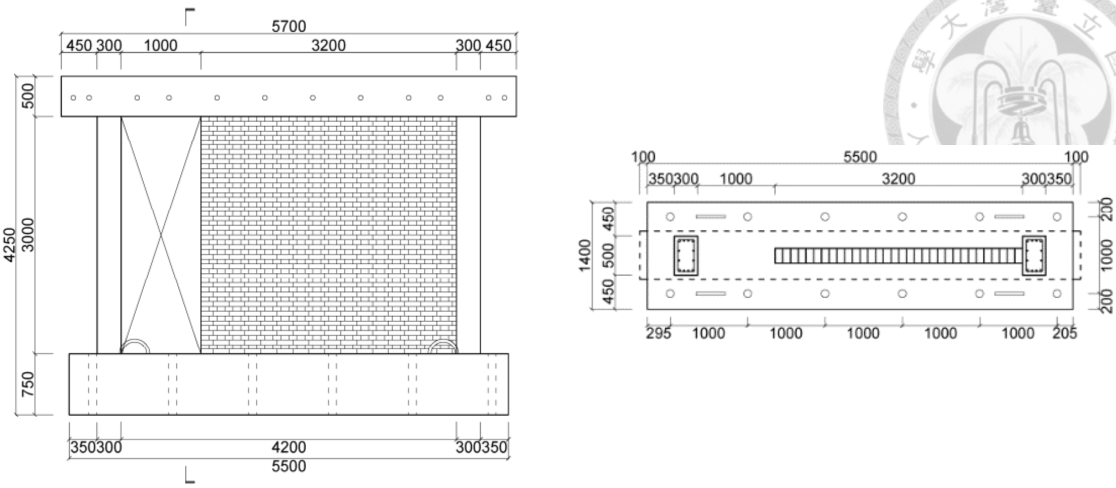

(a) Elevation view (b) Plan view

Figure 2-62 Specimens CD-e and ID-e details (unit: mm) (Lin, 2016)

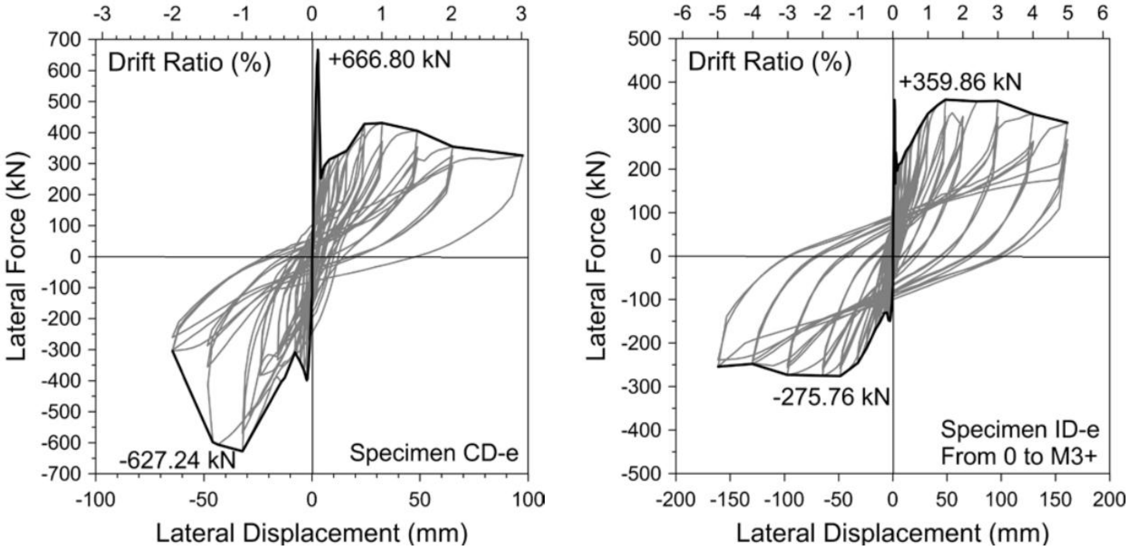

(a) Specimen CD-e (b) Specimen ID-e

Figure 2-63 Test curves of Specimens CD-e, ID-e (Lin, 2016)

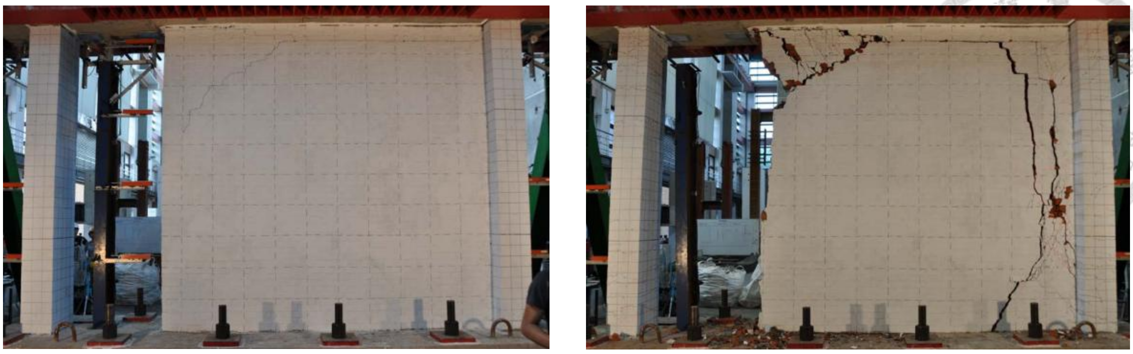

(a) Positive loading (0.084%)　(b) Negative loading (-0.995%)

Figure 2-64 Failure condition of Specimens CD-e at maximum strength under positive and negative loading (Lin, 2016)

(a) Positive loading (1.499%)　(b) Negative loading (-1.504%)

Figure 2-65 Failure condition of Specimen ID-e at maximum strength under positive and negative loading (Lin, 2016)

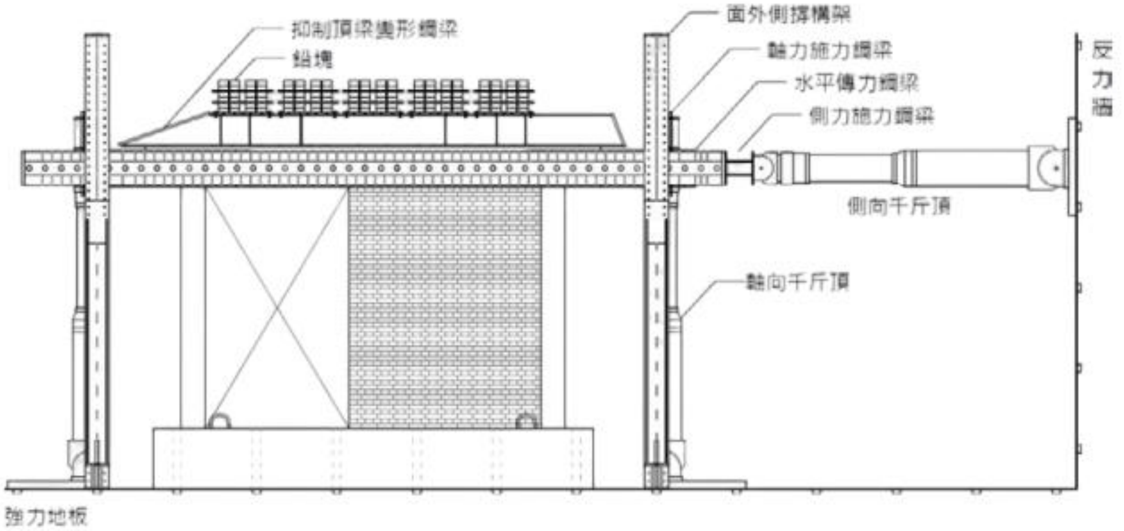

(a) Schematic view

(b) Photo

Figure 2-66 Test setup of Specimens CD-e-1.8 and CW-e-1.8 (Yang, 2017)

doi:10.6342/NTU202502280

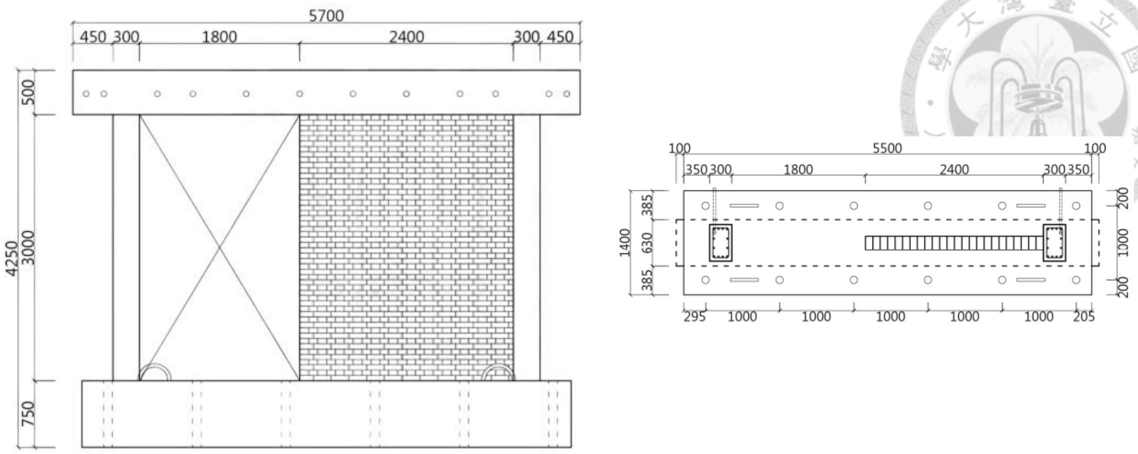

(a) Elevation view (b) Plan view

Figure 2-67 Specimens CD-e-1.8 and ID-e-1.8 details (unit: mm) (Tung, 2017)

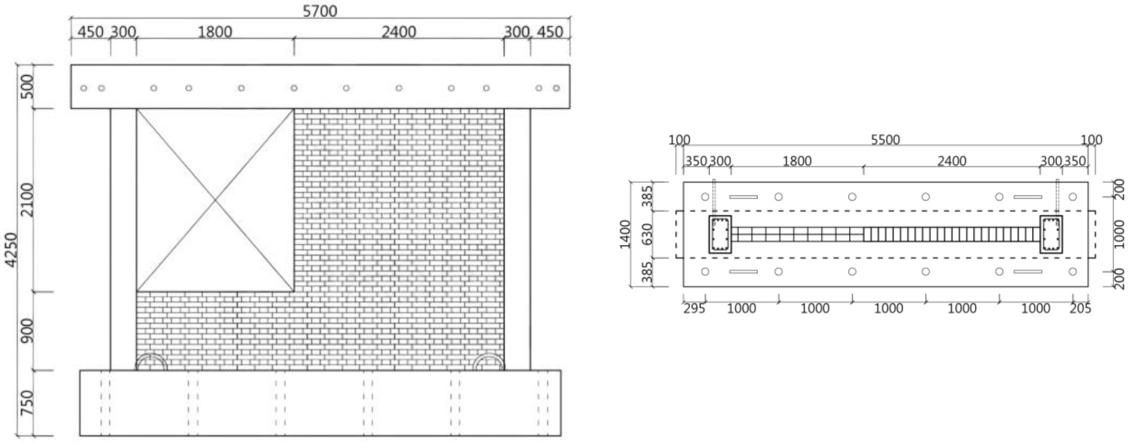

(a) Elevation view (b) Plan view

Figure 2-68 Specimen CW-e-1.8 and IW-e-1.8 details (unit: mm) (Tung, 2017)

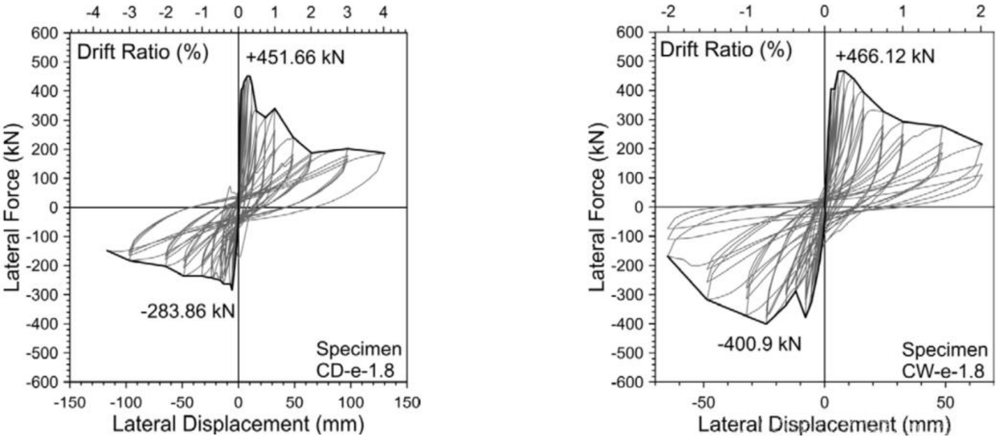

(a) Specimen CD-e-1.8 (b) Specimen CW-e-1.8

Figure 2-69 Test curves of Specimens CD-e-1.8 and CW-e-1.8 (Yang, 2017)

(a) Positive loading (0.246%) (b) Negative loading (-0.175%)

Figure 2-70 Failure condition of Specimen CD-e-1.8 at maximum strength under positive and negative loading (Yang, 2017)

(a) Positive loading (0.25%) (b) Negative loading (-0.746%)

Figure 2-71 Failure condition of Specimen CW-e-1.8 at maximum strength under positive and negative loading (Yang, 2017)

doi:10.6342/NTU202502280

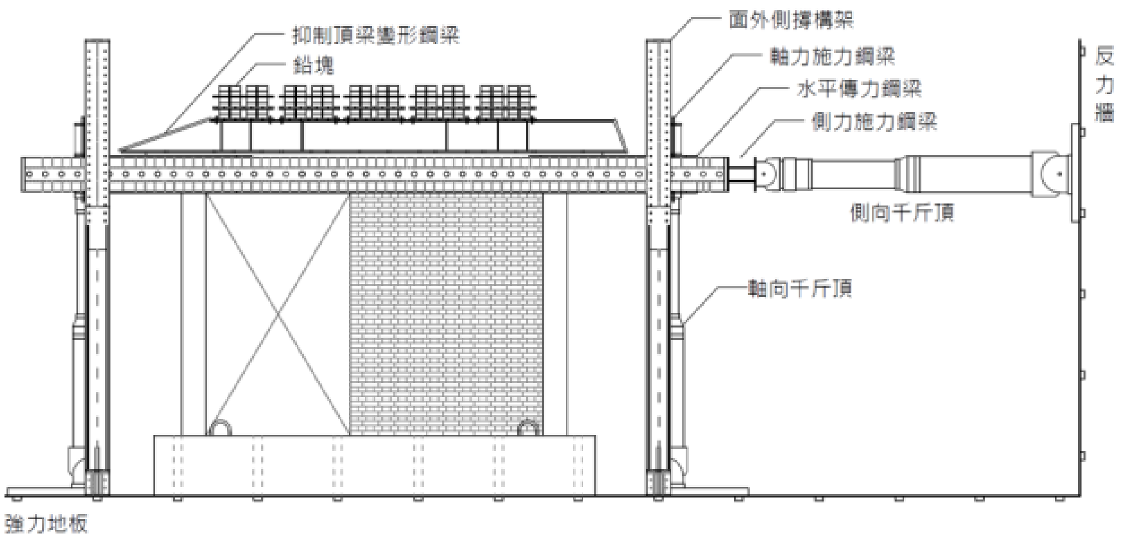

(a) Schematic view

(b) Photo

Figure 2-72 Test setup of Specimens ID-e-1.8, IW-e-1.8, and ID-e-1.8R (Tung, 2017)

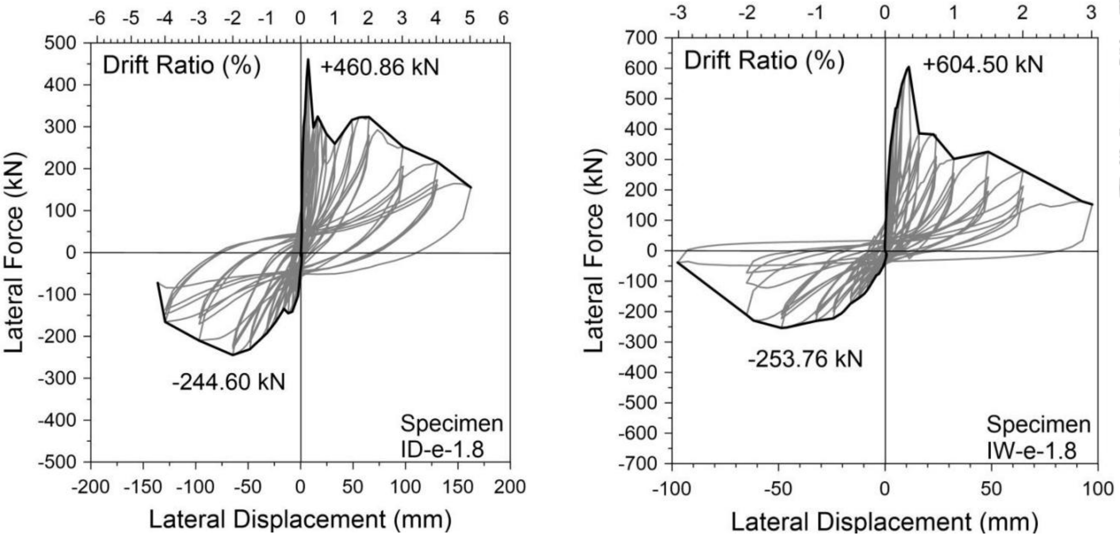

(a) Specimen ID-e-1.8 (b) Specimen IW-e-1.8

Figure 2-73 Test curves of Specimens ID-e-1.8 and IW-e-1.8 (Tung, 2017)

(a) Positive loading (0.223%) (b) Negative loading (-2.002%)

Figure 2-74 Failure condition of Specimen ID-e-1.8 at maximum strength under positive and negative loading (Tung, 2017)

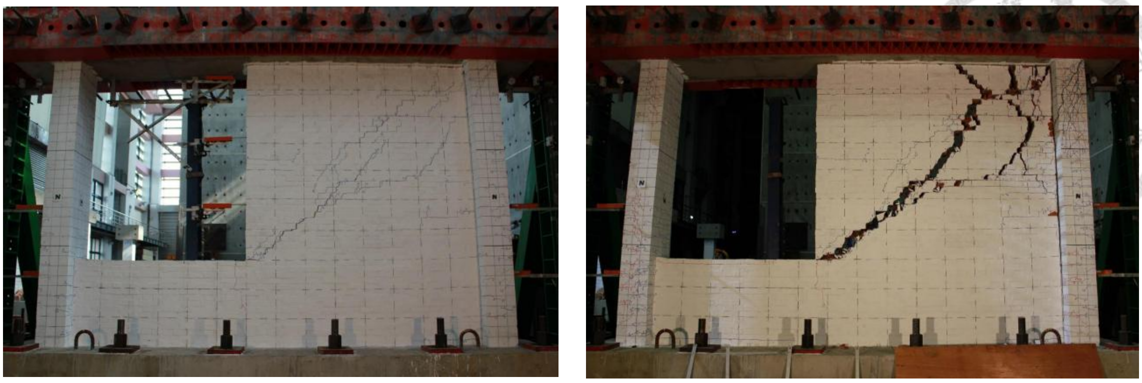
(a) Positive loading (0.345%) (b) Negative loading (-1.508%)

Figure 2-75 Failure condition of Specimen IW-e-1.8 at maximum strength under positive and negative loading (Tung, 2017)

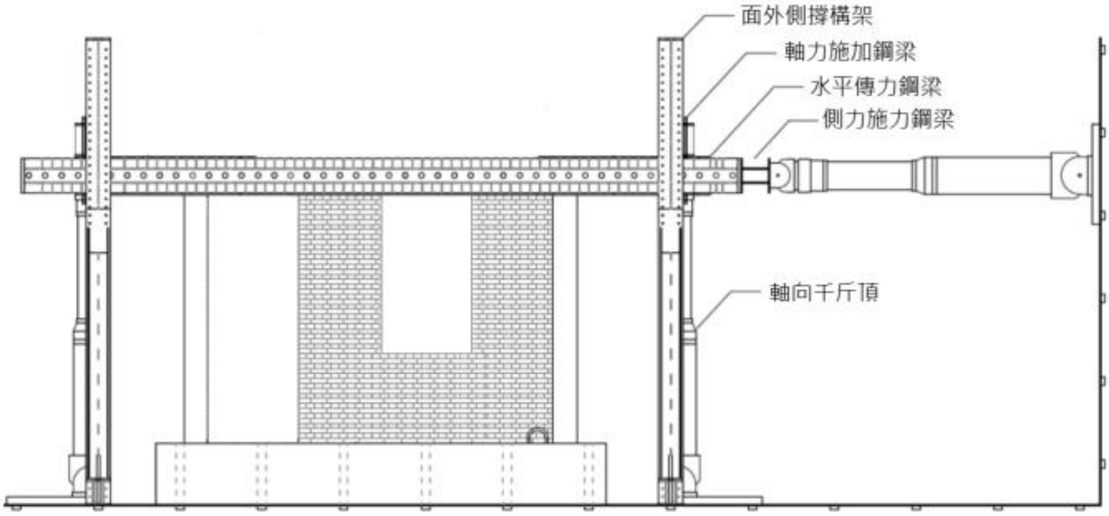

Figure 2-76 Test setup of Specimens IDW, IDW_CFRP, IDW_STEEL, IW_CFRP, and IW_STEEL (Jhang, 2019)

doi:10.6342/NTU202502280

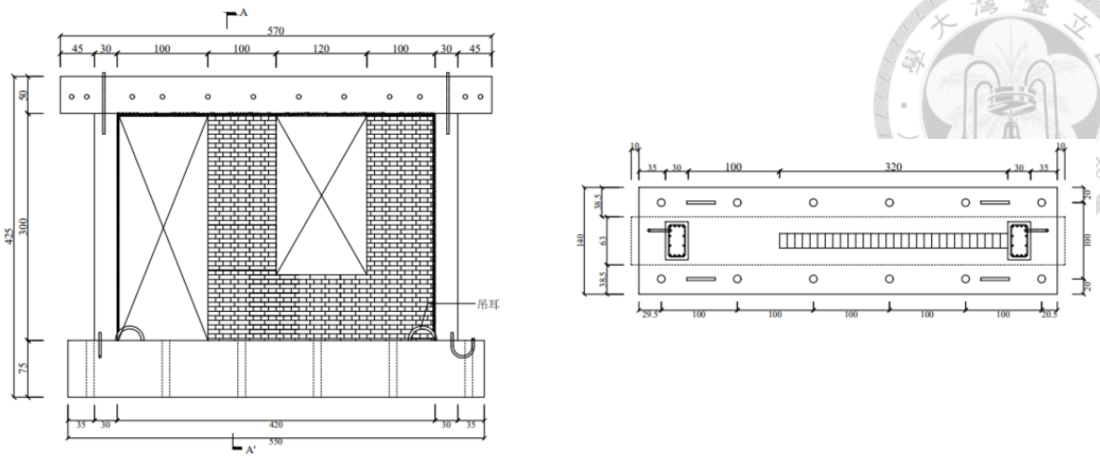

(a) Elevation view (b) Plan view

Figure 2-77 Specimen IDW details (unit: cm) (Jhang, 2019)

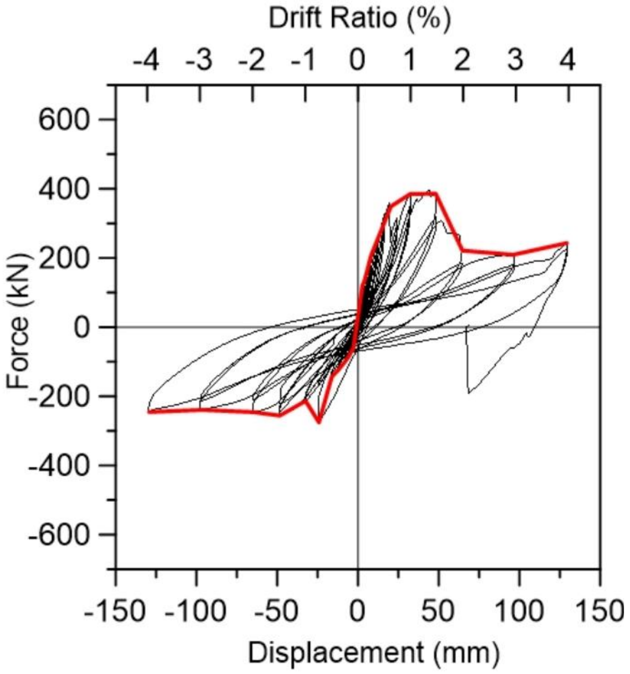

Figure 2-78 IDW test curve (Jhang, 2019)

doi:10.6342/NTU202502280

(a) Positive loading (1.5%) (b) Negative loading (-0.75%)

Figure 2-79 Failure condition of Specimen IDW at maximum strength under positive and negative loading (Jhang, 2019)

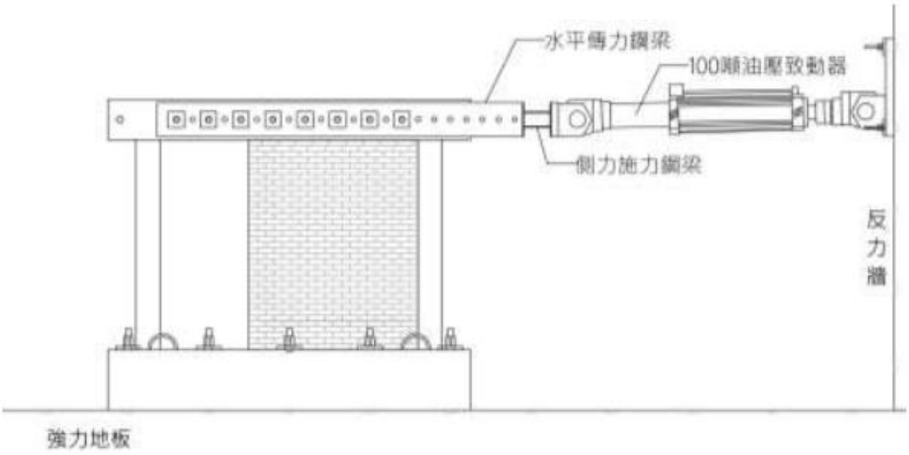

(a) Schematic view

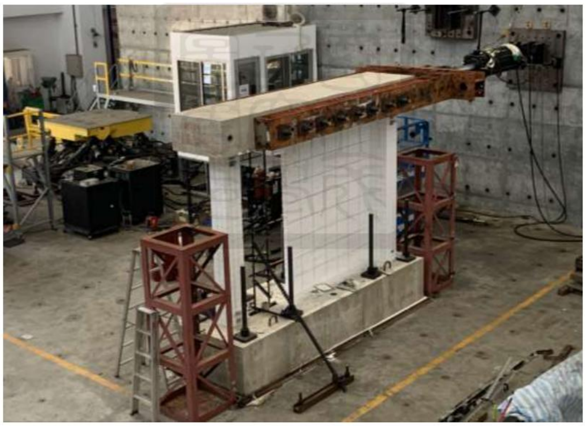

(b) Photo

Figure 2-80 Test setup of Specimen ID-e-0.5B (Lin, 2023)

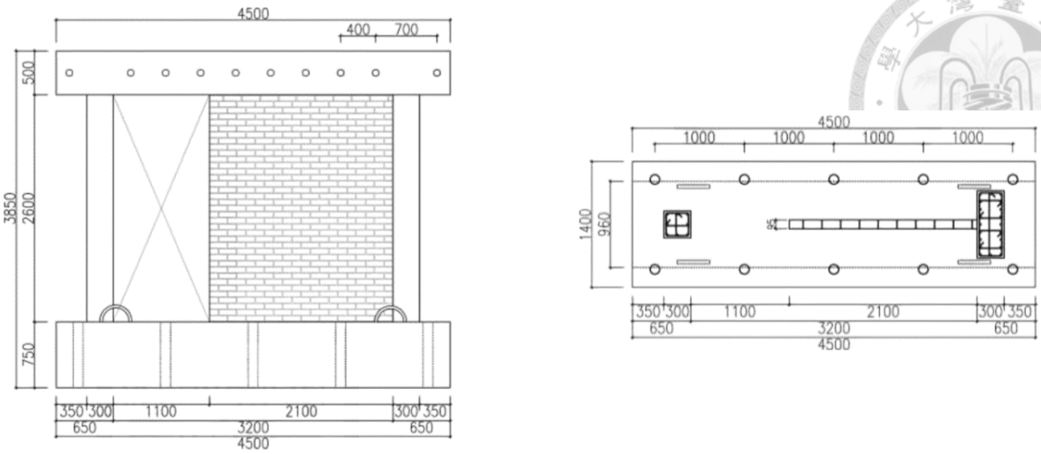

(a) Elevation view (b) Plan view

Figure 2-81 Specimen ID-e-0.5B details (unit: cm) (Lin, 2023)

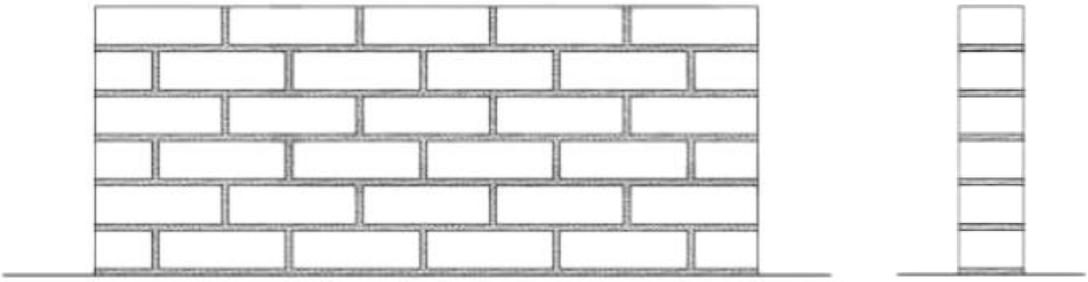

(a) Front elevation view (b) Side elevation view

(c) Plan view

Figure 2-82 Stretching bond 0.5B schematic diagram (Lin, 2023)

doi:10.6342/NTU202502280

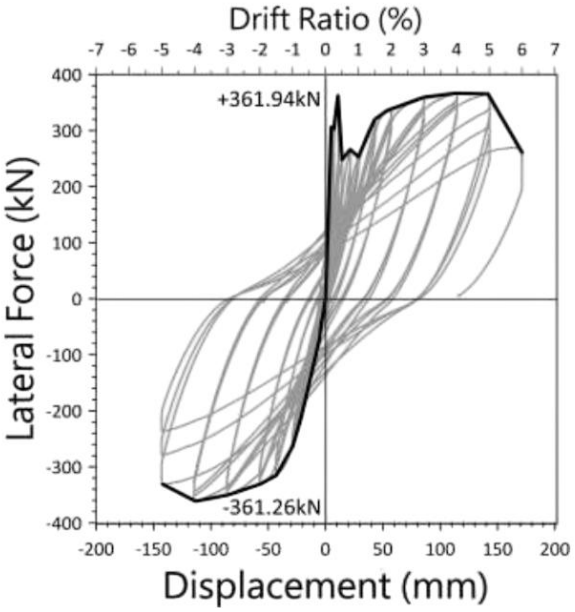

Figure 2-83 Test curve of Specimen ID-e-0.5B (Lin, 2023)

`

(a) Positive loading (0.38%)

(b) Negative loading (-4%)

Figure 2-84 Failure condition of Specimen ID-e-0.5B at maximum strength under positive and negative loading (Lin, 2023)

doi:10.6342/NTU202502280

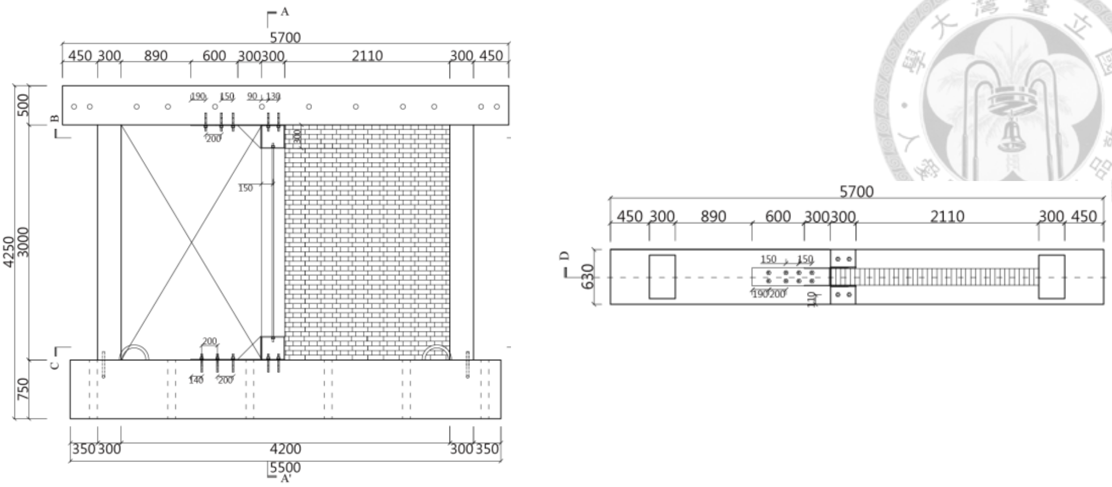

(a) Elevation view (b) Plan view

Figure 2-85 Specimen ID-e-1.8R details (unit: mm) (Tung, 2017)

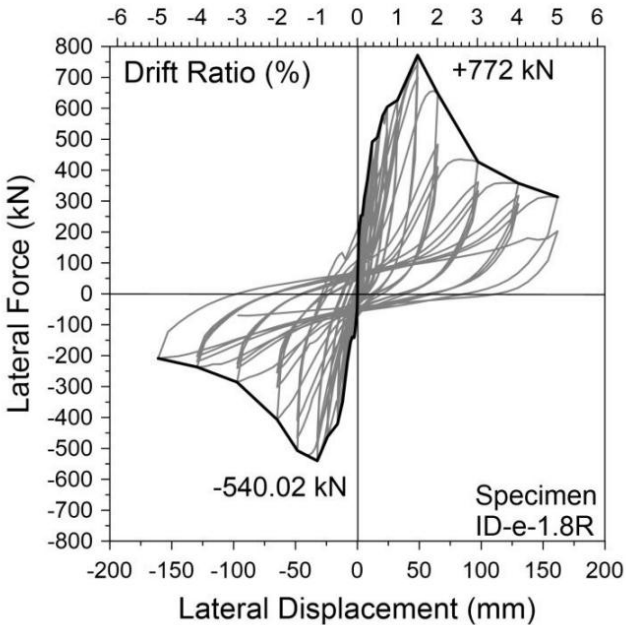

Figure 2-86 Test curve of Specimen ID-e-1.8R (Tung, 2017)

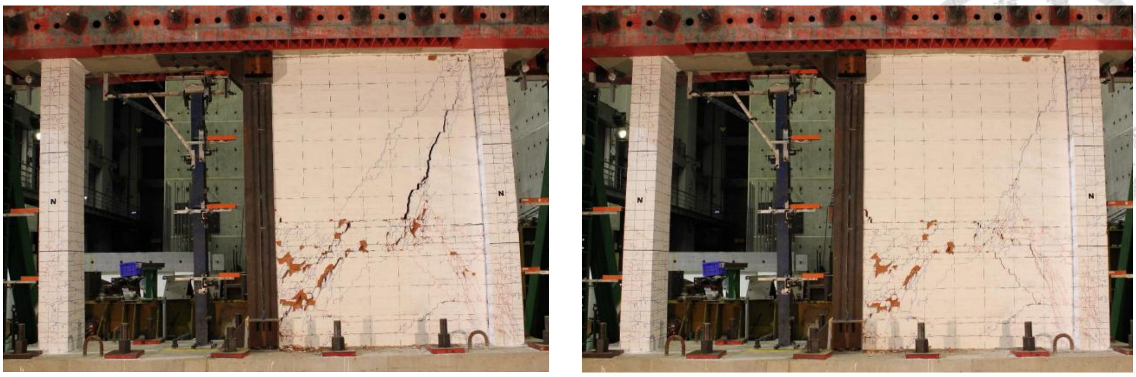

(a) Positive loading (1.502%) (b) Negative loading (-1.003%)

Figure 2-87 Failure condition of Specimen ID-e-1.8R at maximum strength under positive and negative loading (Tung, 2017)

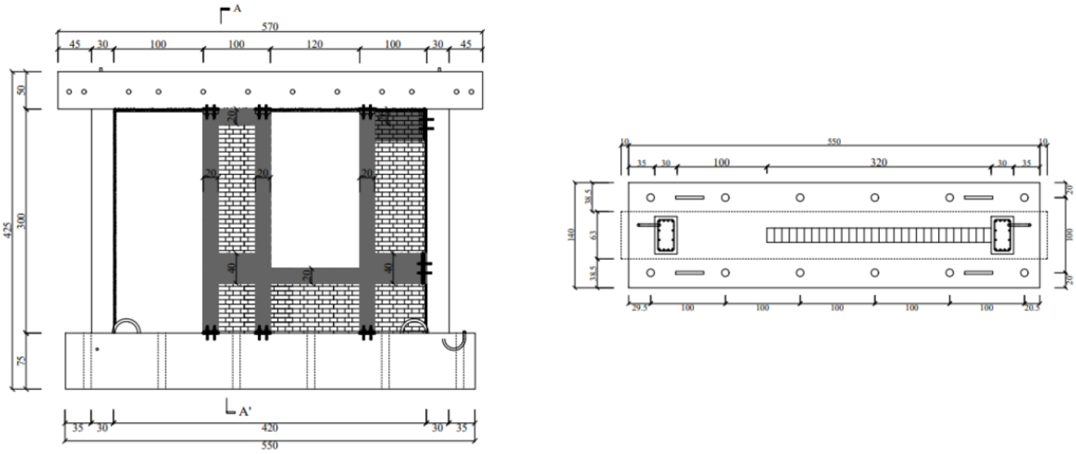

(a) Elevation view (b) Plan view

Figure 2-88 Specimen IDW_CFRP details (unit: cm) (Jhang, 2019)

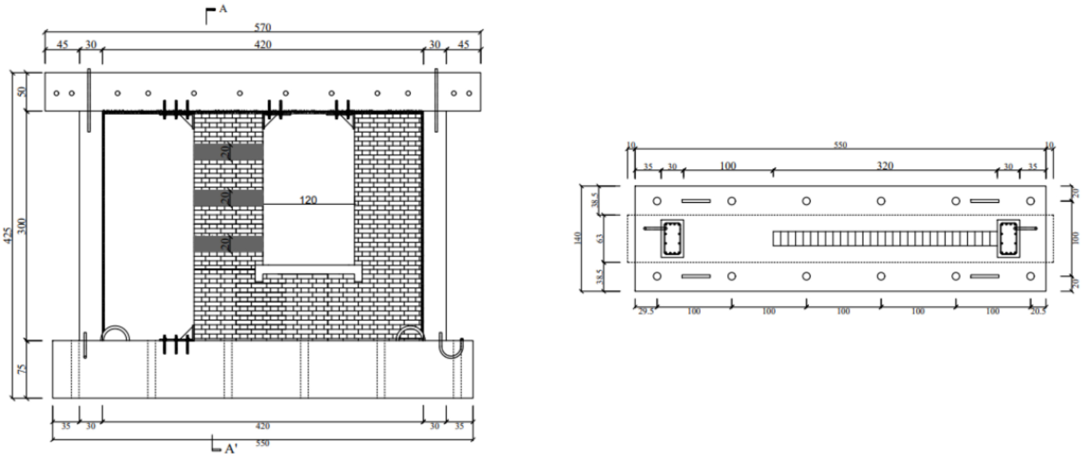

(a) Elevation view (b) Plan view

Figure 2-89 Specimen IDW_STEEL details (unit: cm) (Jhang, 2019)

doi:10.6342/NTU202502280

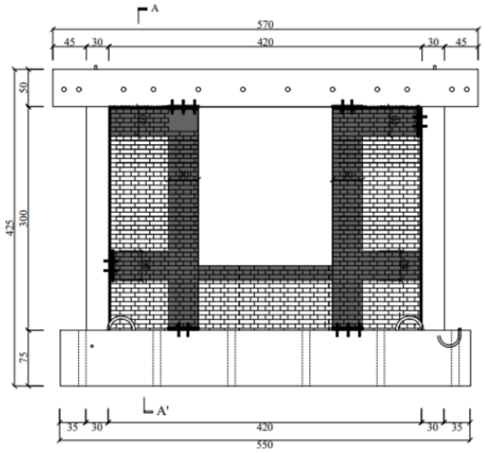

Figure 2-90 Specimen IW_CFRP details (unit: cm) (Jhang, 2019)

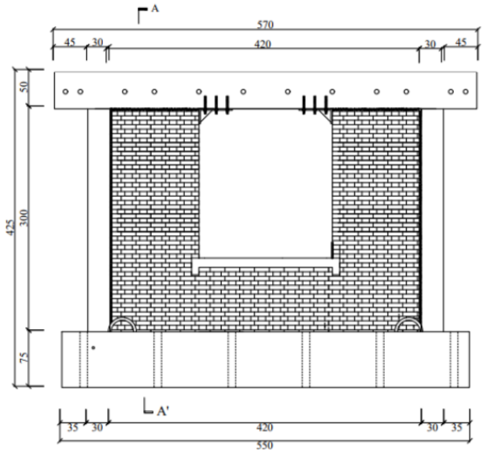

Figure 2-91 Specimen IW_STEEL details (unit: cm) (Jhang, 2019)

doi:10.6342/NTU202502280

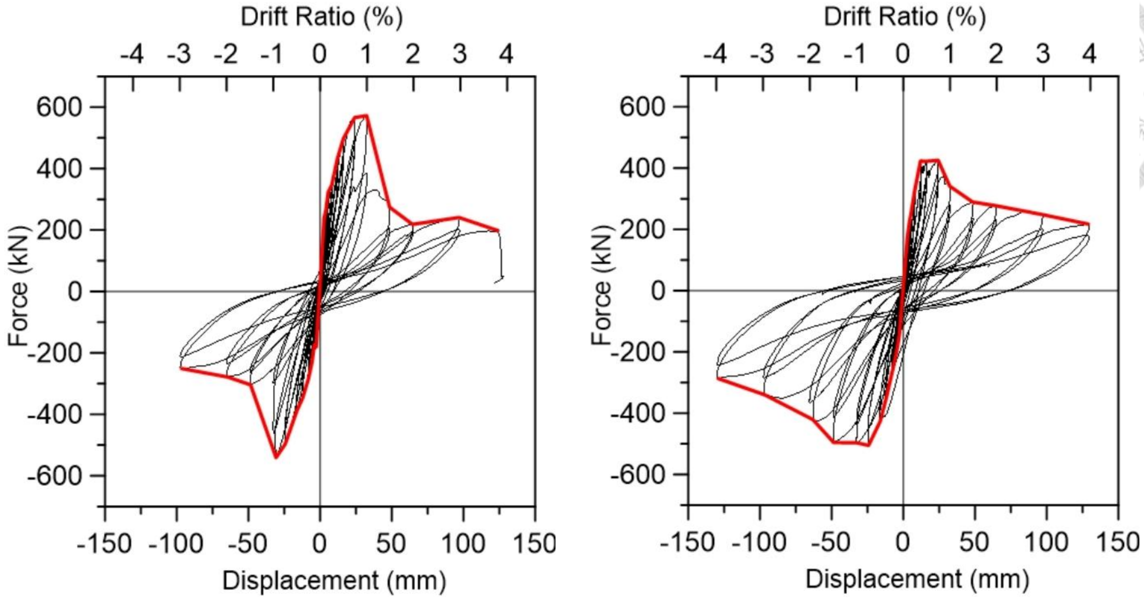

(a) Specimen IDW_CFRP (b) Specimen IDW_STEEL

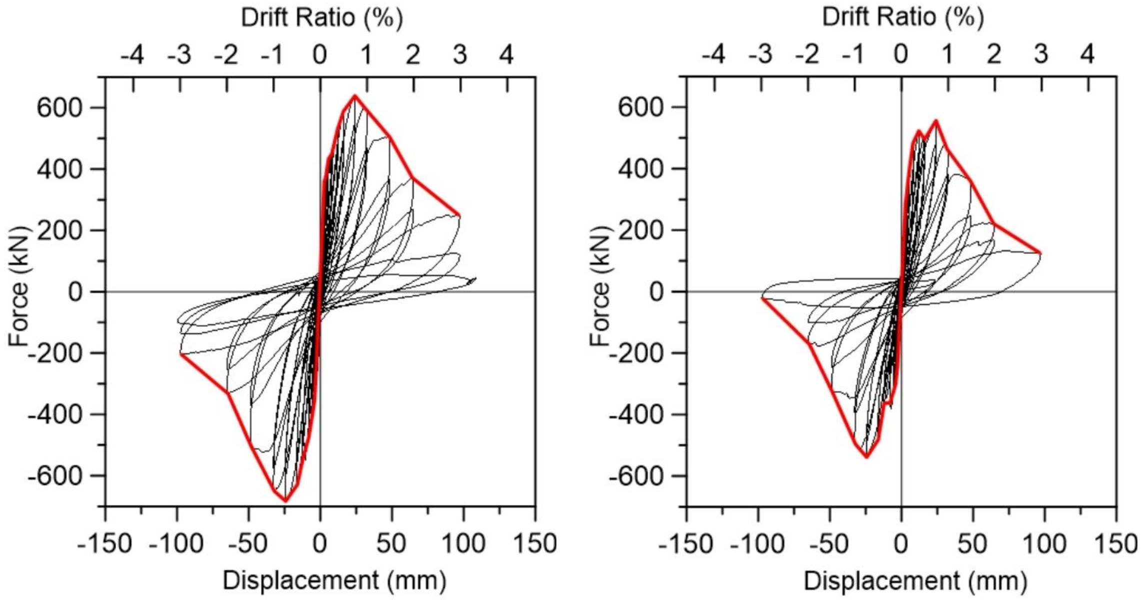

(c) Specimen IW_CFRP (d) Specimen IW_STEEL

Figure 2-92 Test curves of Specimens IDW_CFRP, IDW_STEEL, IW_CFRP, and IW_STEEL (Jhang, 2019)

doi:10.6342/NTU202502280

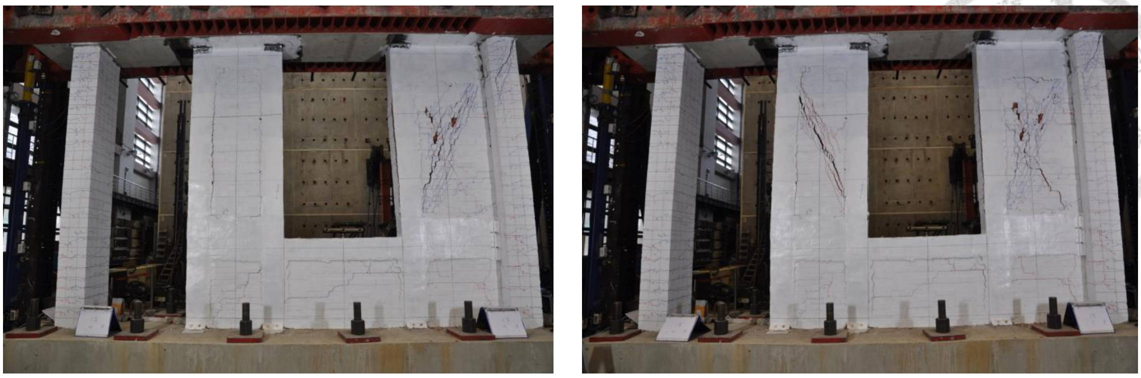

(a) Positive loading (1%) (b) Negative loading (-1%)

Figure 2-93 Failure condition of Specimen IDW_CFRP at maximum strength under positive and negative loading (Jhang, 2019)

(a) Positive loading (0.75%) (b) Negative loading (-0.75%)

Figure 2-94 Failure condition of Specimen IDW_STEEL at maximum strength under positive and negative loading (Jhang, 2019)

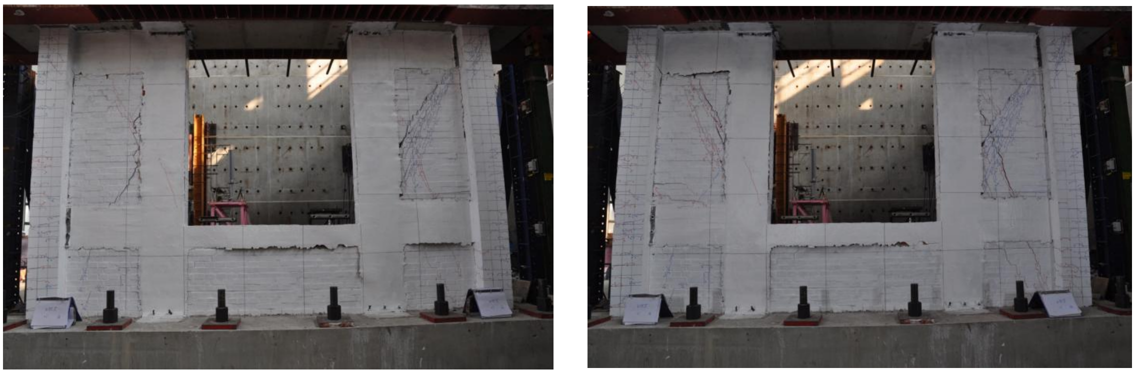

(a) Positive loading (0.75%) (b) Negative loading (-0.75%)

Figure 2-95 Failure condition of Specimen IW_CFRP at maximum strength under positive and negative loading (Jhang, 2019)

doi:10.6342/NTU202502280

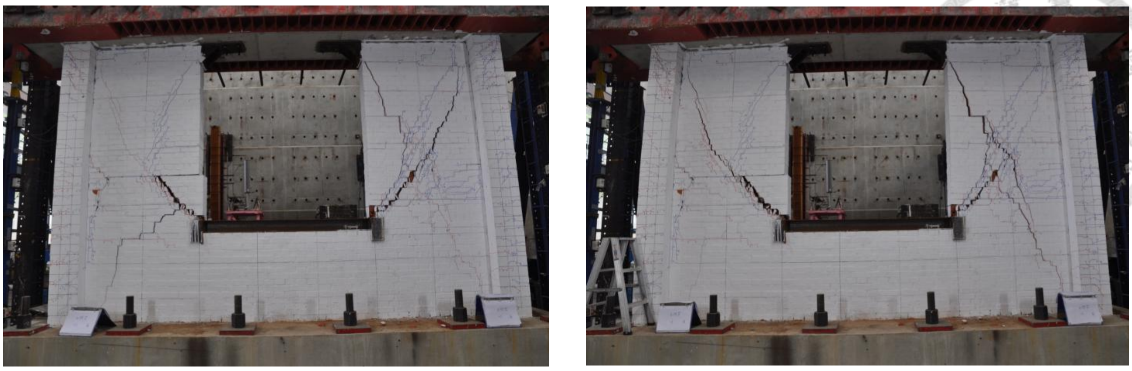

(a) Positive loading (0.75%)　　(b) Negative loading (-0.75%)

Figure 2-96 Failure condition of Specimen IW_STEEL at maximum strength under positive and negative loading (Jhang, 2019)

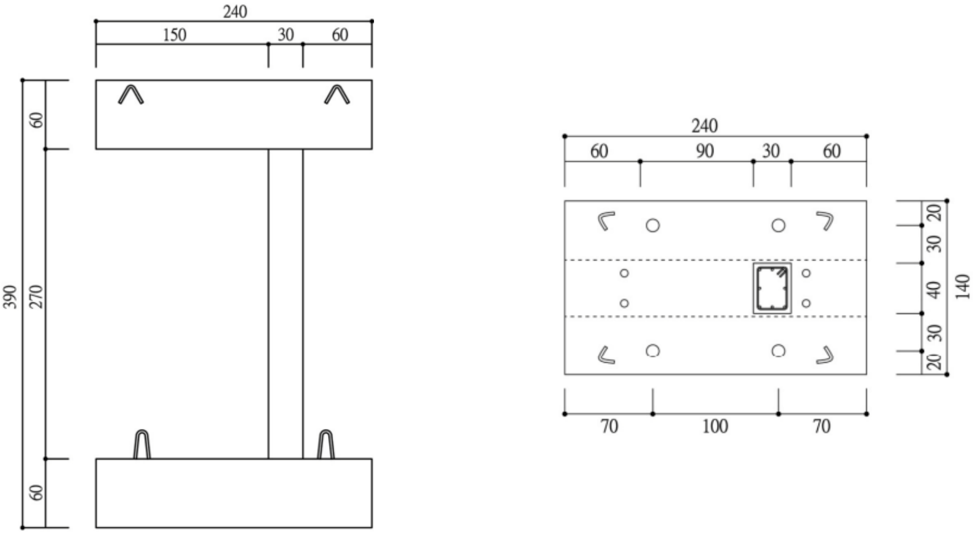

(a) Elevation view　　(b) Plan view

Figure 2-97 Specimen AC_C details (unit: cm) (Lin, 2011)

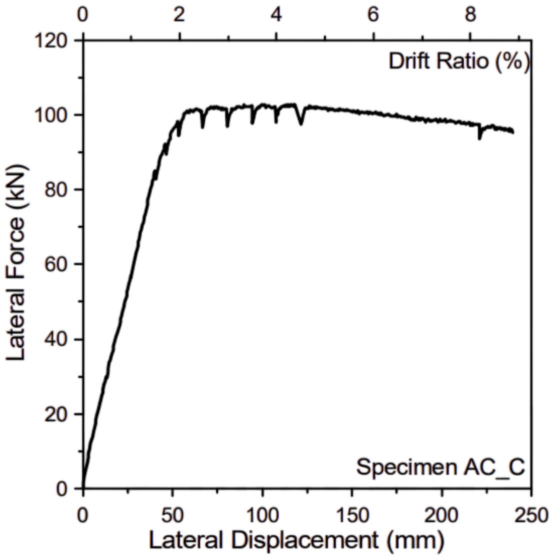

Figure 2-98 Test curve of Specimen AC_C (Lin, 2011)

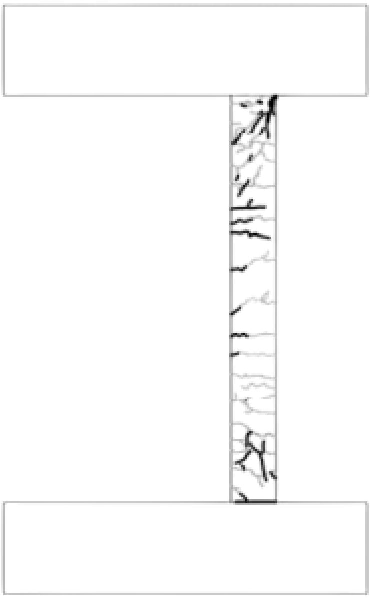

Figure 2-99 Schematic failure condition of Specimen AC_C (2.97%) at maximum strength (Lin, 2011)

doi:10.6342/NTU202502280

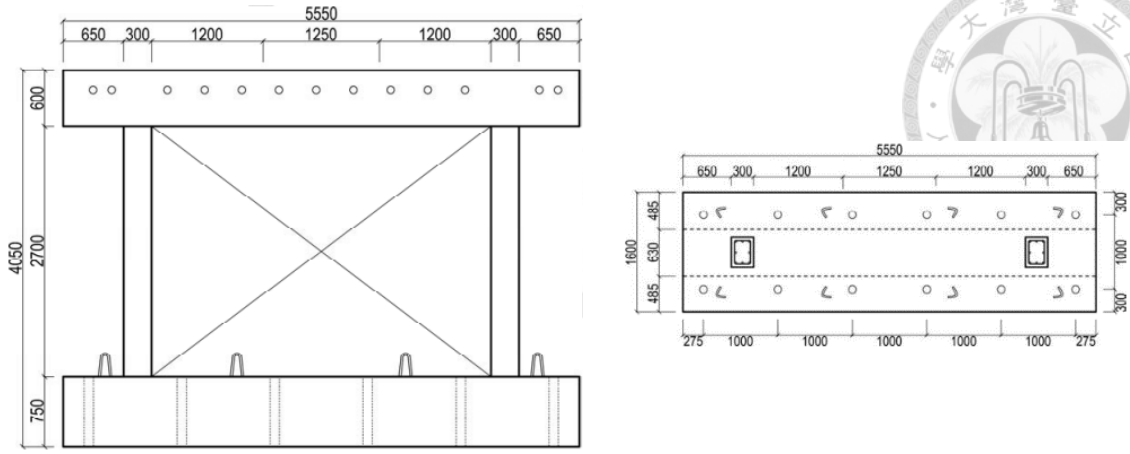

(a) Elevation view (b) Section view

Figure 2-100 Specimen ID_BF details (unit: mm) (Chao, 2015)

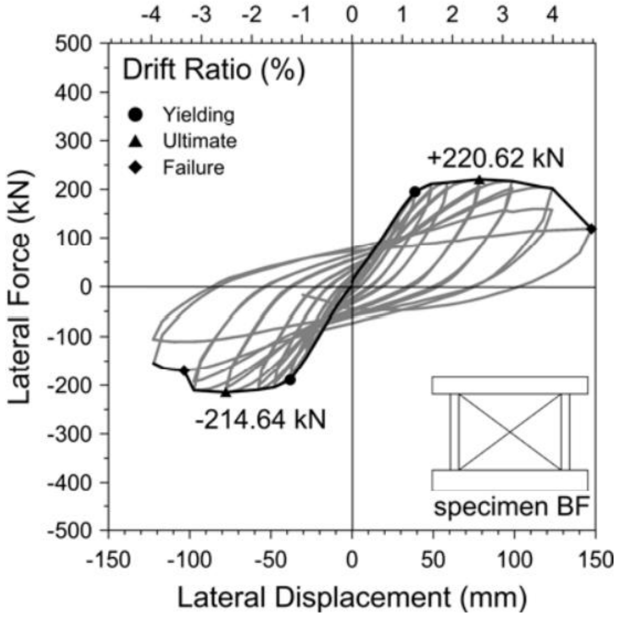

Figure 2-101 ID_BF test curve (Chao, 2015)


(a) Positive loading (2.54%) (b) Negative loading (-2.51%)

Figure 2-102 Failure condition of Specimen ID_BF at maximum strength under positive and negative loading (Chao, 2015)

doi:10.6342/NTU202502280

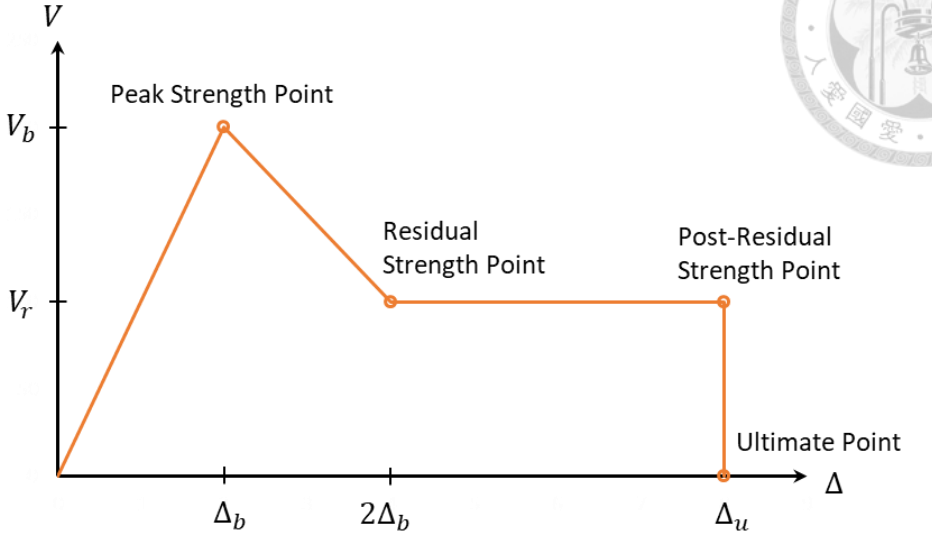

Figure 3-1 Lateral load-displacement curve for four-sided confined brick infill

(NCREE/TEASPA, 2020)

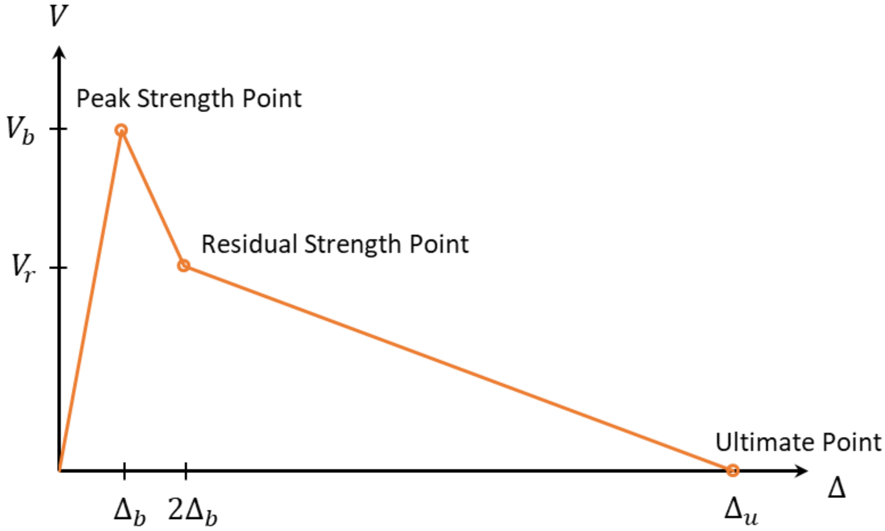

Figure 3-2 Lateral load-displacement curve for three-sided confined brick infill

(NCREE/TEASPA, 2020)

doi:10.6342/NTU202502280

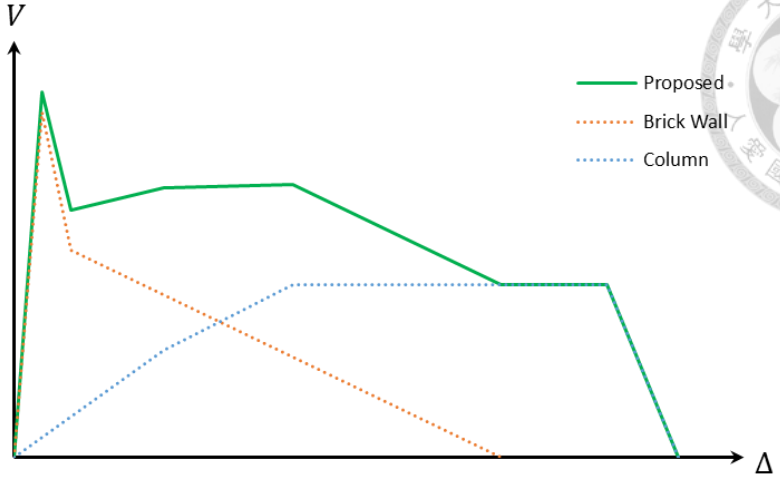

Figure 3-3 Method of curves superposition

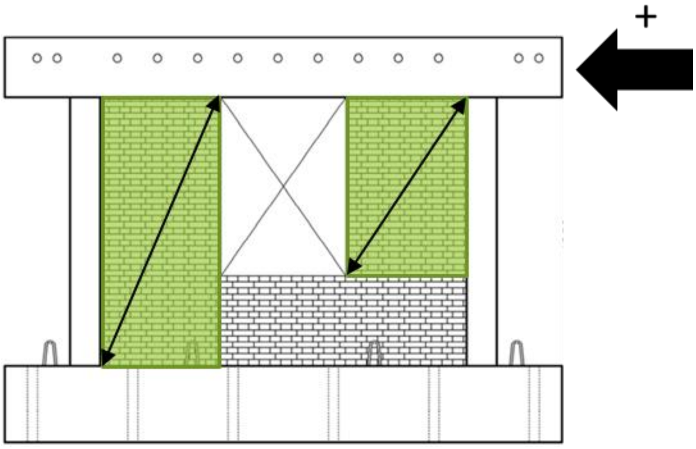

Figure 3-4 Shear element determination for Specimen IW under positive loading

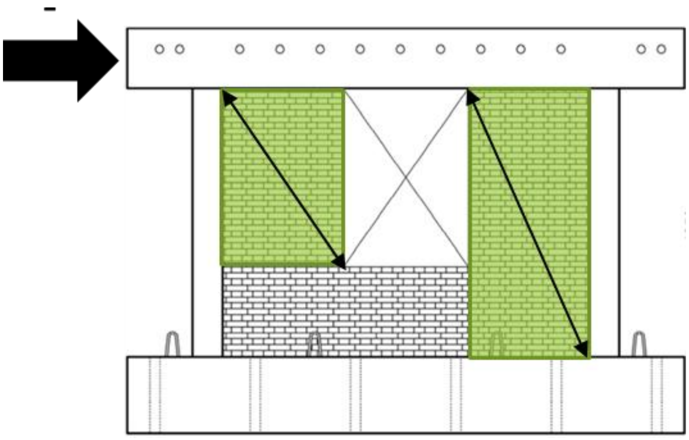

Figure 3-5 Shear element determination for Specimen IW under negative loading

doi:10.6342/NTU202502280

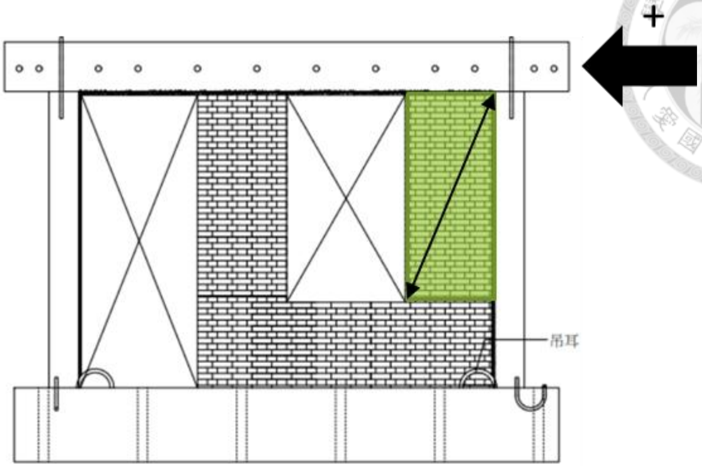

Figure 3-6 Shear element determination for Specimen IDW under positive loading

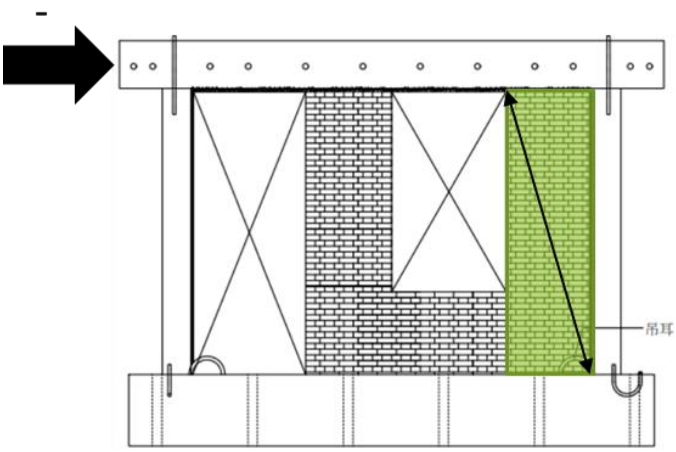

Figure 3-7 Shear element determination for Specimen IDW under negative loading

doi:10.6342/NTU202502280

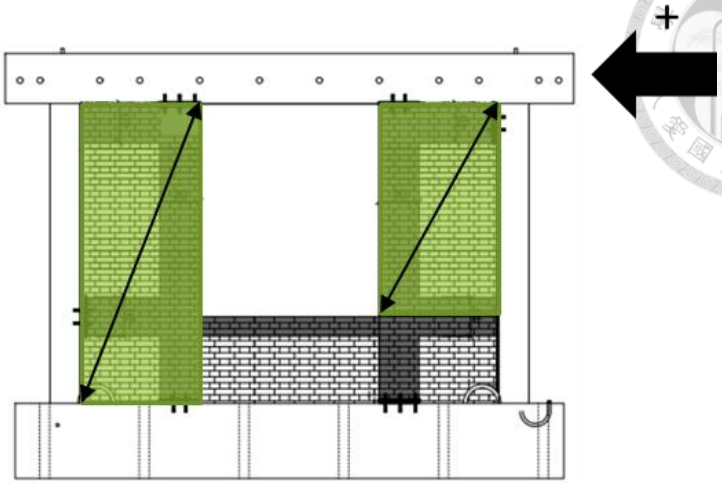

Figure 3-8 Shear element determination for Specimen IW_CFRP under positive loading

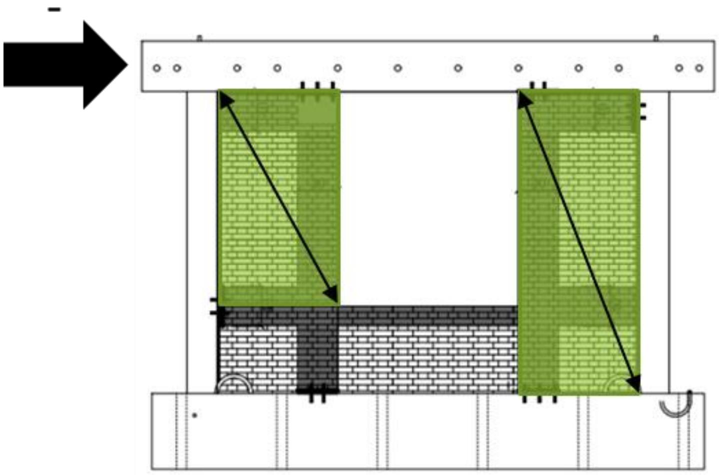

Figure 3-9 Shear element determination for Specimen IW_CFRP under negative loading

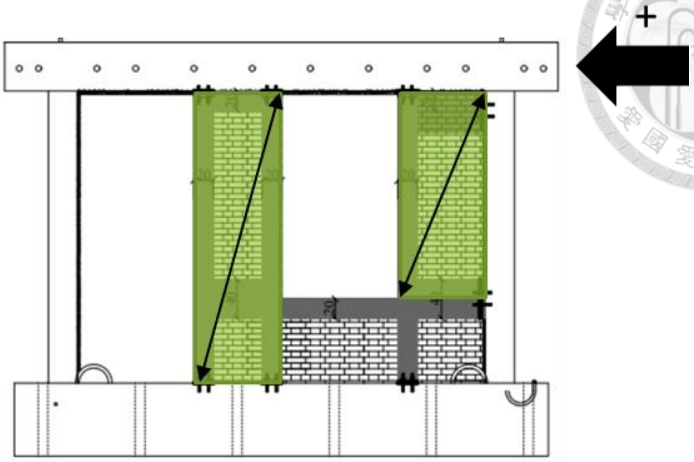

Figure 3-10 Shear element determination for Specimen IDW_CFRP under positive loading

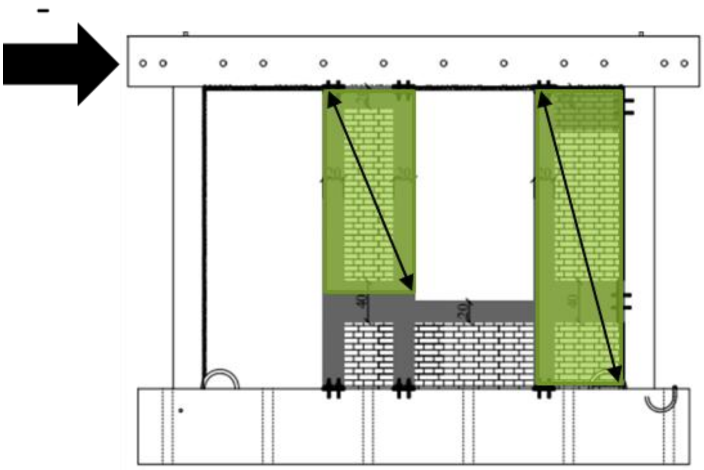

Figure 3-11 Shear element determination for Specimen IDW_CFRP under negative loading

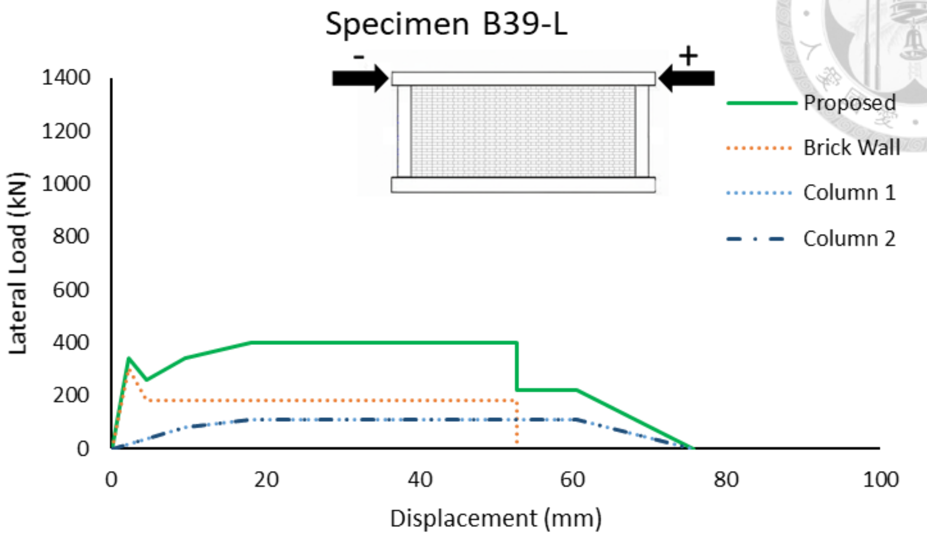

(a) Proposed lateral load-deflection curve

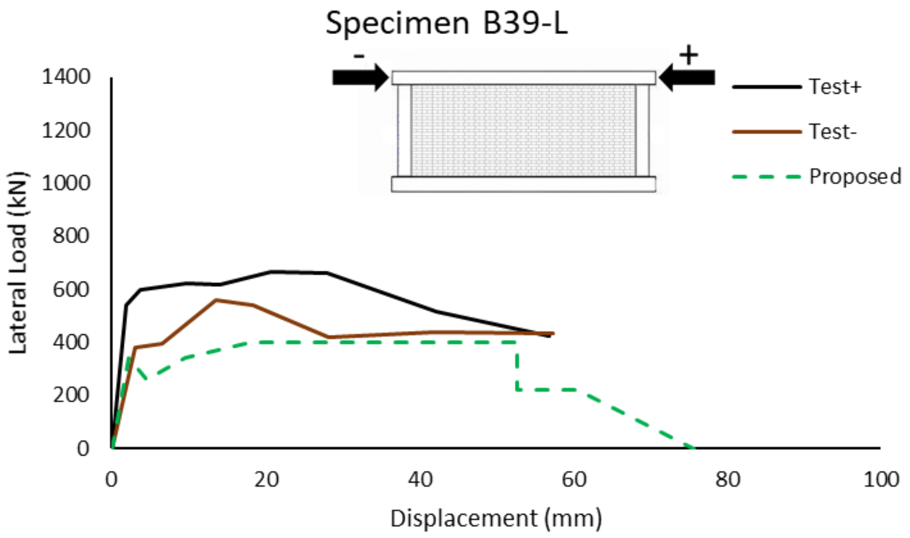

(b) Comparison with test curve

Figure 4-1 Lateral load-deflection curve comparison of Specimen B39-L under positive and negative loading

doi:10.6342/NTU202502280

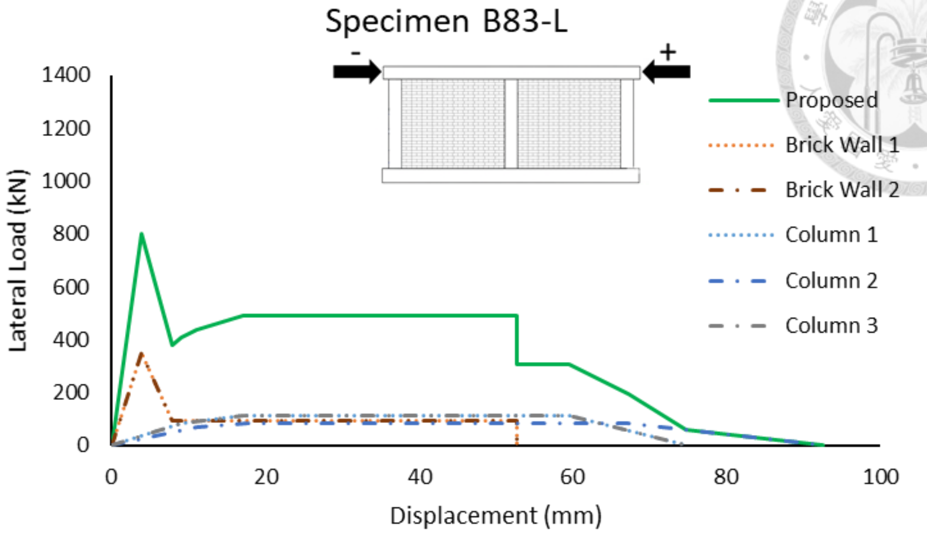

(a) Proposed lateral load-deflection curve

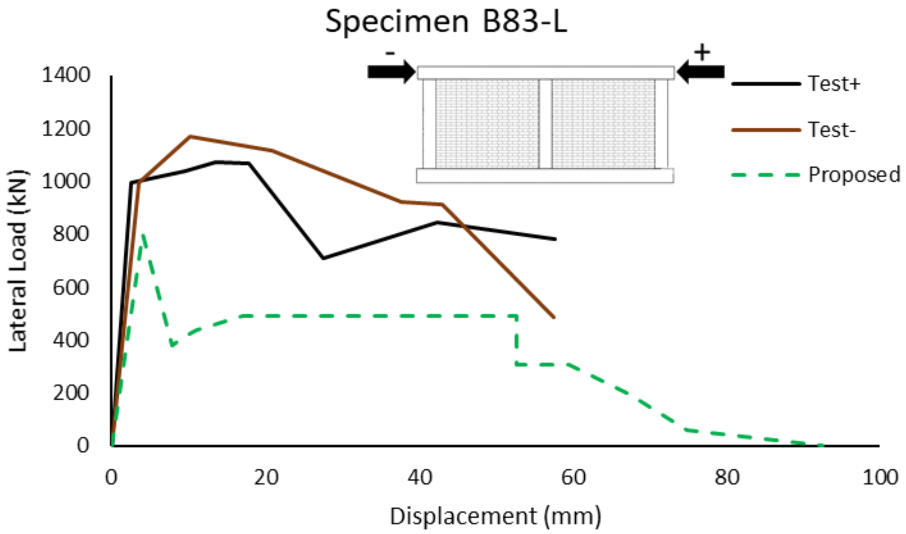

(b) Comparison with test curve

Figure 4-2 Lateral load-deflection curve comparison of Specimen B83-L under positive and negative loading

doi:10.6342/NTU202502280

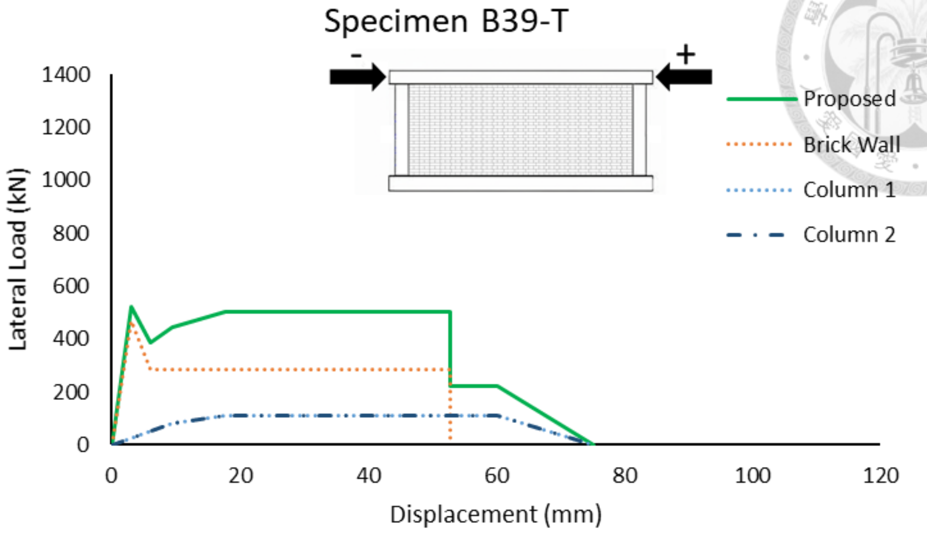

(a) Proposed lateral load-deflection curve

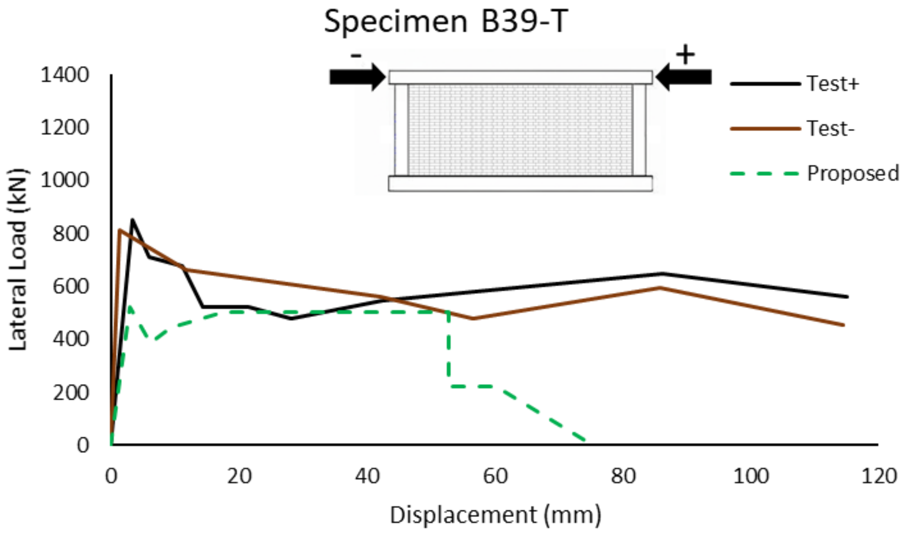

(b) Comparison with test curve

Figure 4-3 Lateral load-deflection curve comparison of Specimen B39-T under positive and negative loading

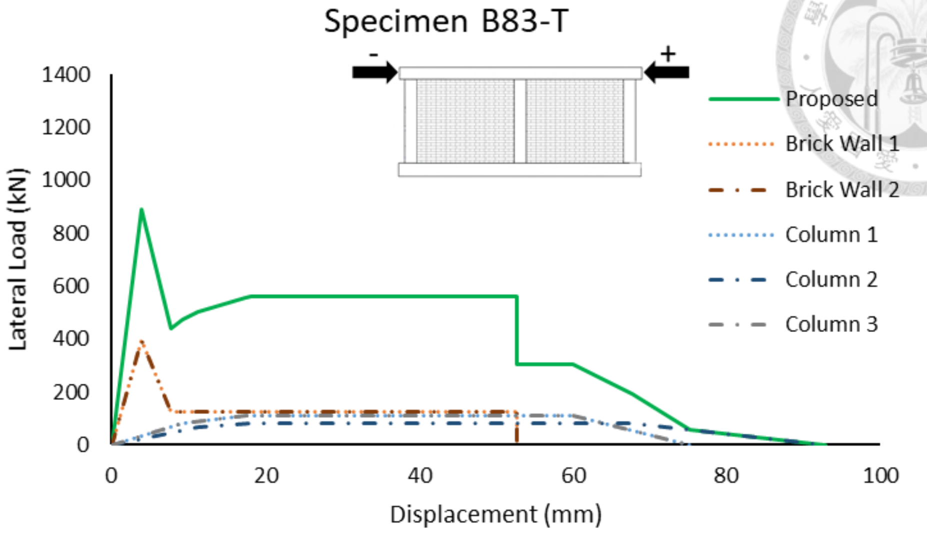

(a) Proposed lateral load-deflection curve

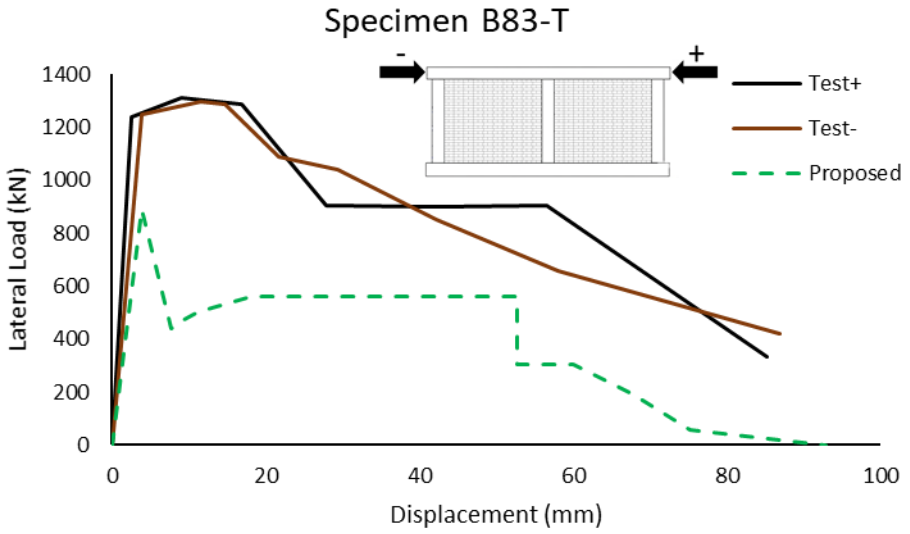

(b) Comparison with test curve

Figure 4-4 Lateral load-deflection curve comparison of Specimen B83-T under positive and negative loading

doi:10.6342/NTU202502280

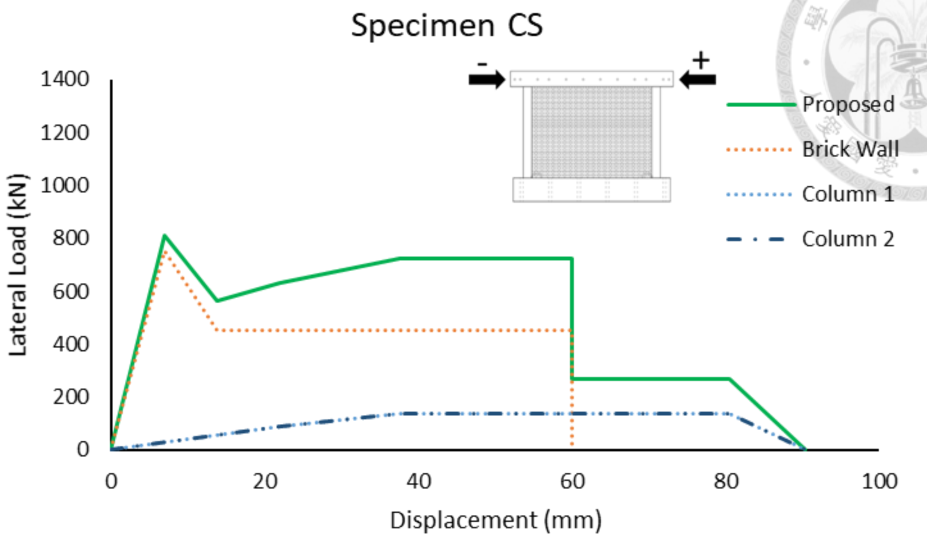

(a) Proposed lateral load-deflection curve

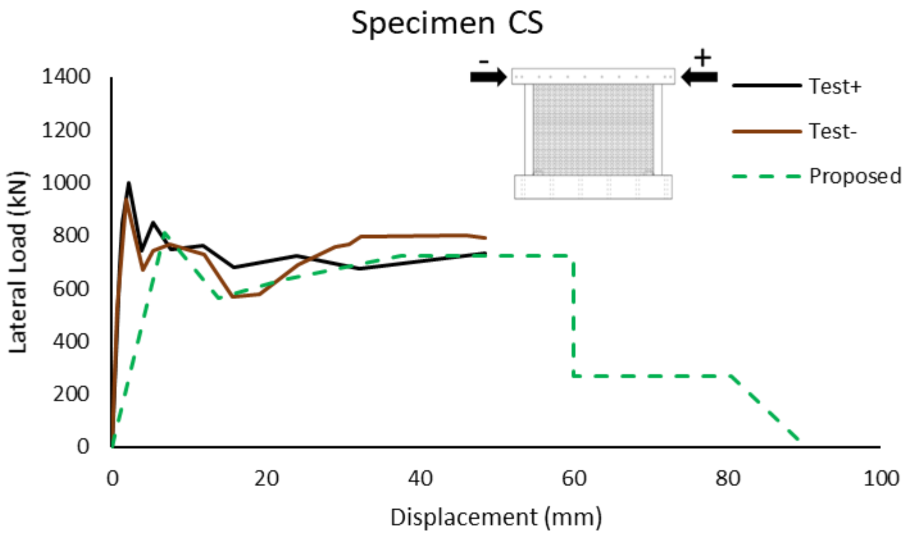

(b) Comparison with test curve

Figure 4-5 Lateral load-deflection curve comparison of Specimen CS under positive and negative loading

doi:10.6342/NTU202502280

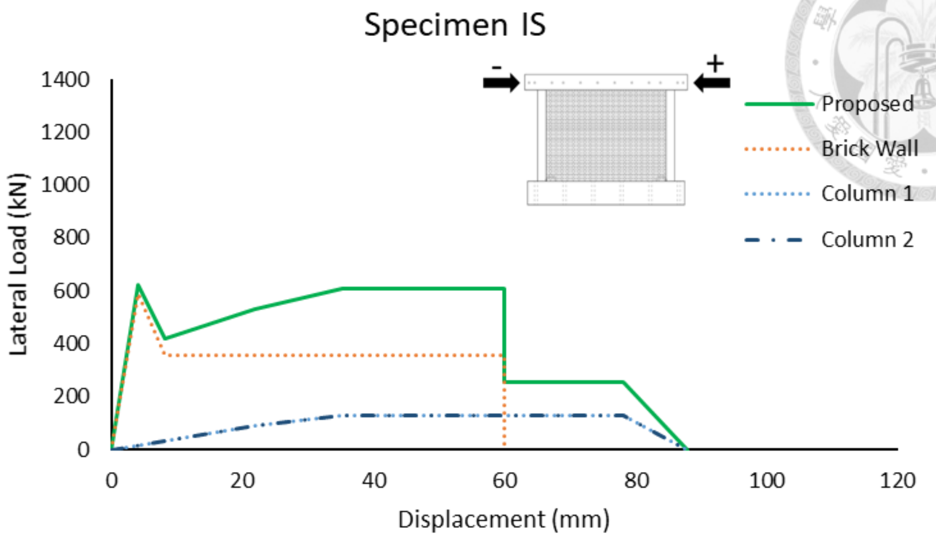

(a) Proposed lateral load-deflection curve

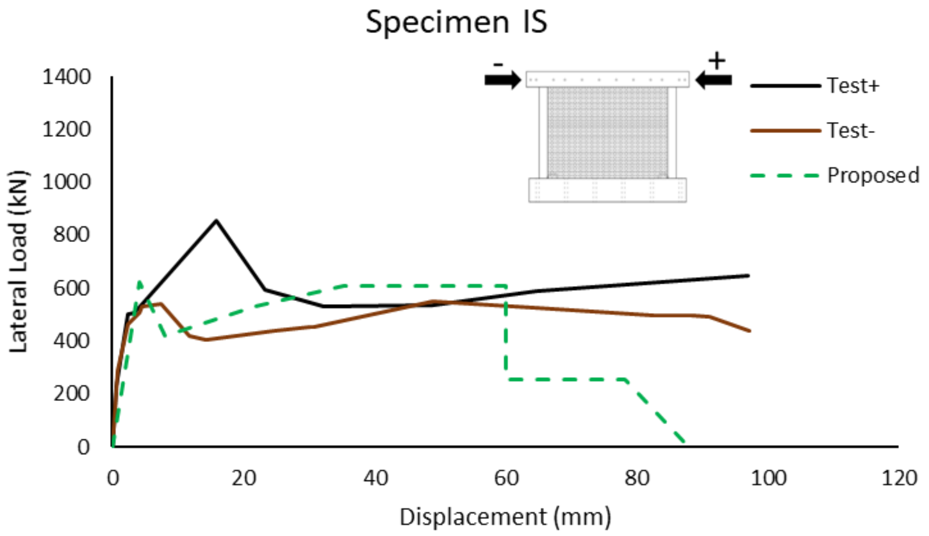

(b) Comparison with test curve

Figure 4-6 Lateral load-deflection curve comparison of Specimen IS under positive and negative loading

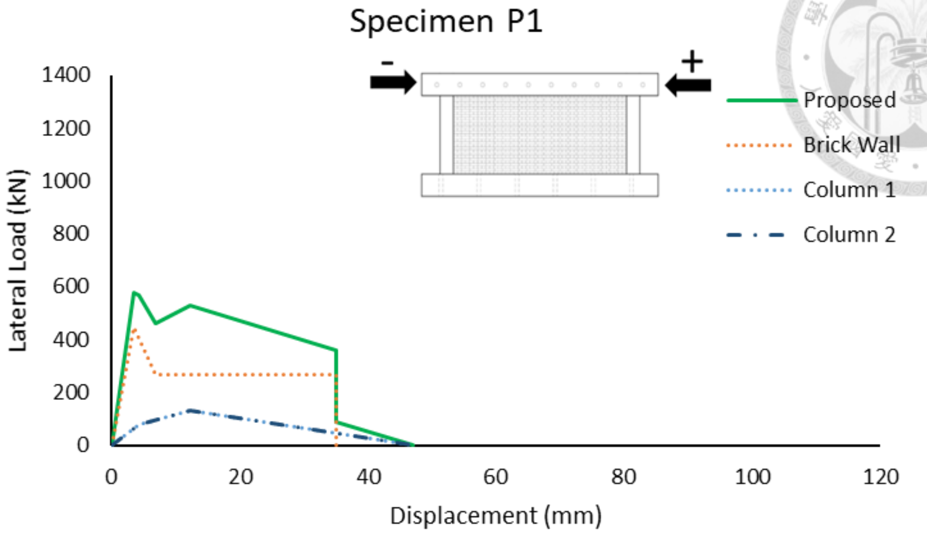

(a) Proposed lateral load-deflection curve

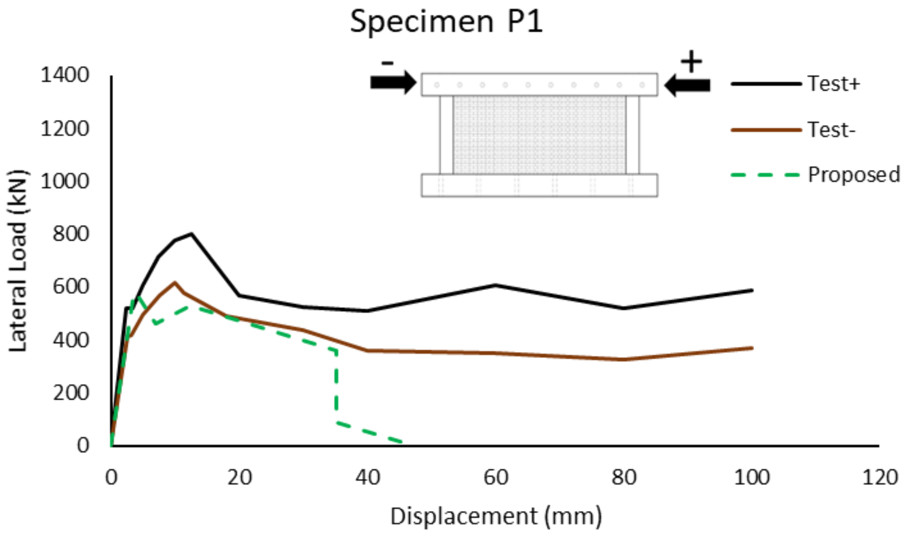

(b) Comparison with test curve

Figure 4-7 Lateral load-deflection curve comparison of Specimen P1 under positive and negative loading

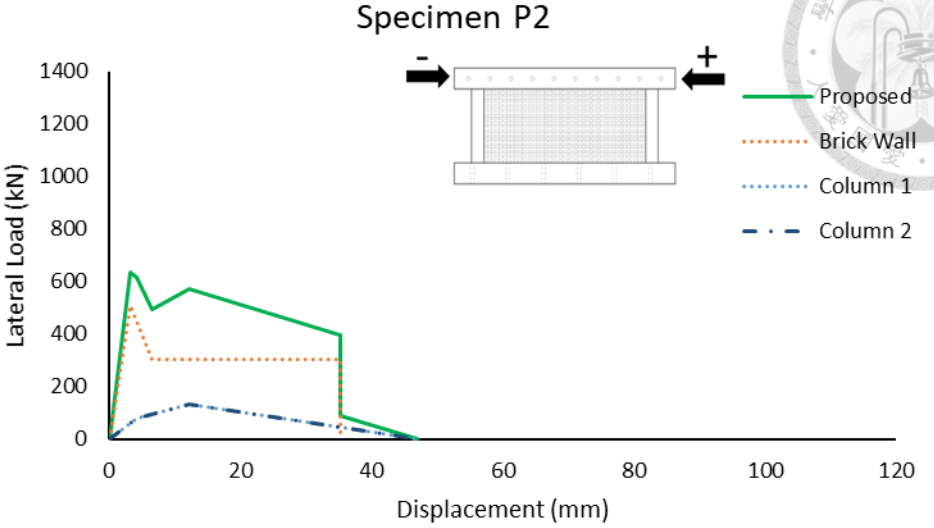

(a) Proposed lateral load-deflection curve

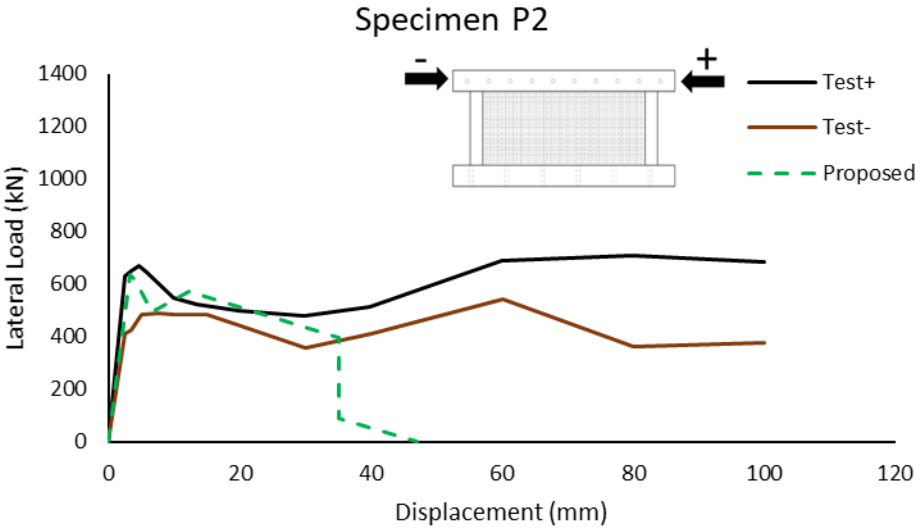

(b) Comparison with test curve

Figure 4-8 Lateral load-deflection curve comparison of Specimen P2 under positive and negative loading

doi:10.6342/NTU202502280

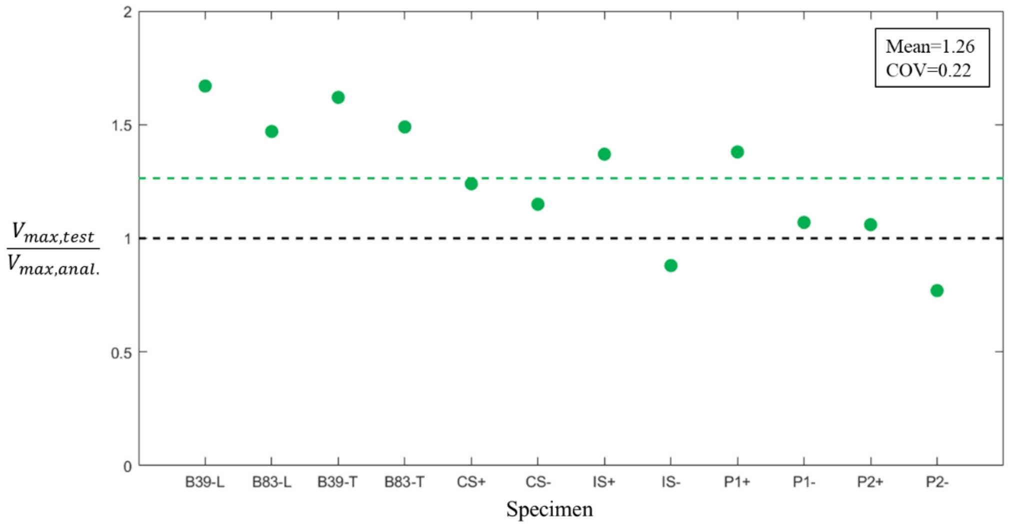

(a) Peak strength comparison

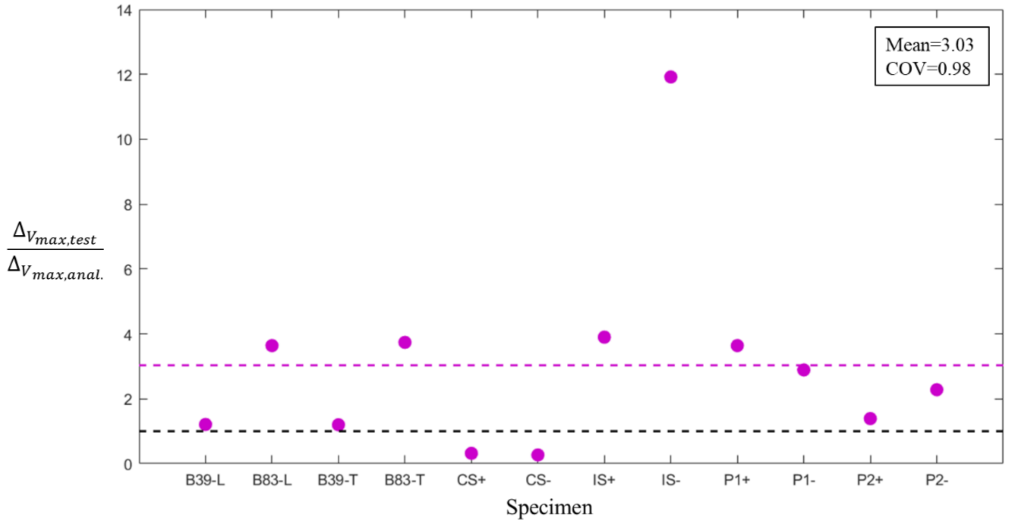

(b) Displacement at peak strength comparison

Figure 4-9 Statistical comparison between test and analytical values of four-sided confined brick infill specimens

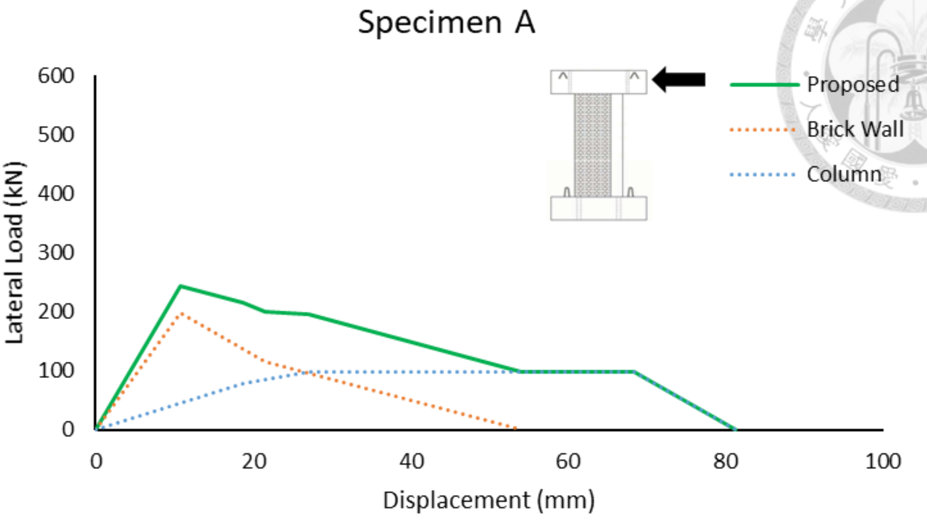

(a) Proposed lateral load-deflection curve

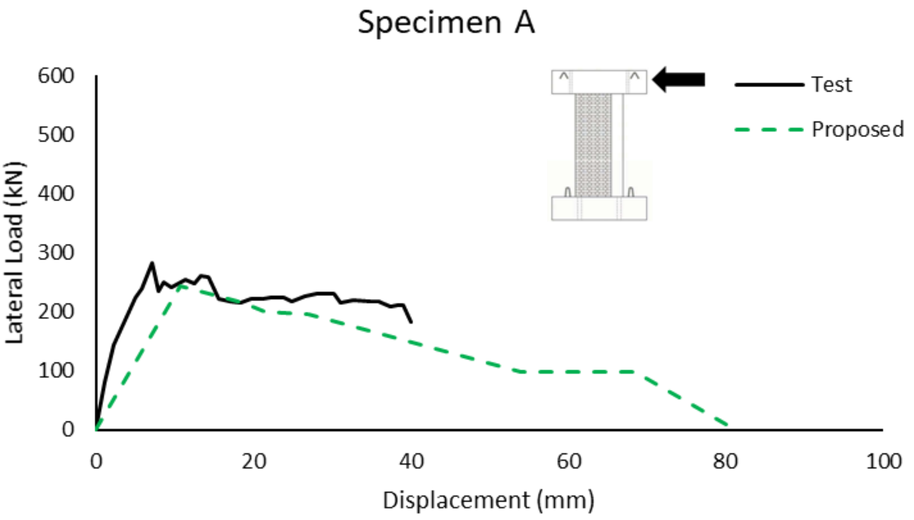

(b) Comparison with test curve

Figure 4-10 Lateral load-deflection curve comparison of Specimen A

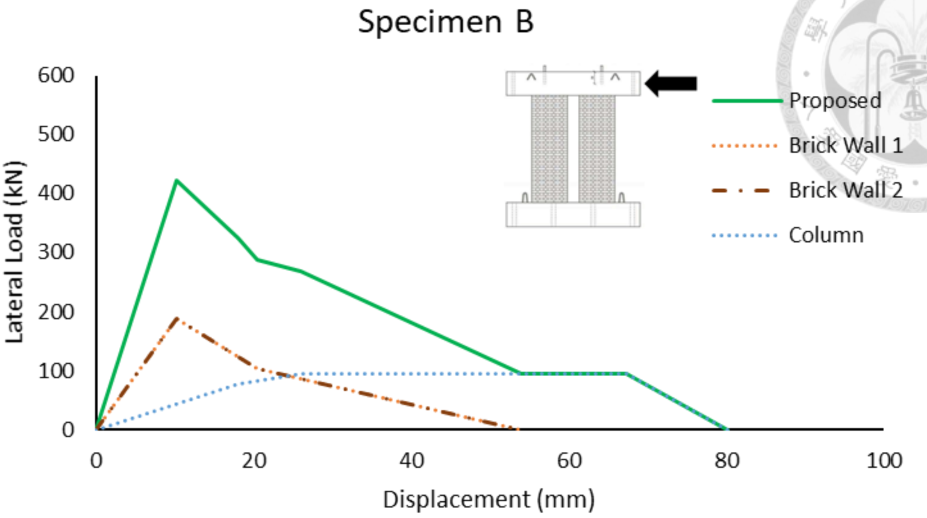

(a) Proposed lateral load-deflection curve

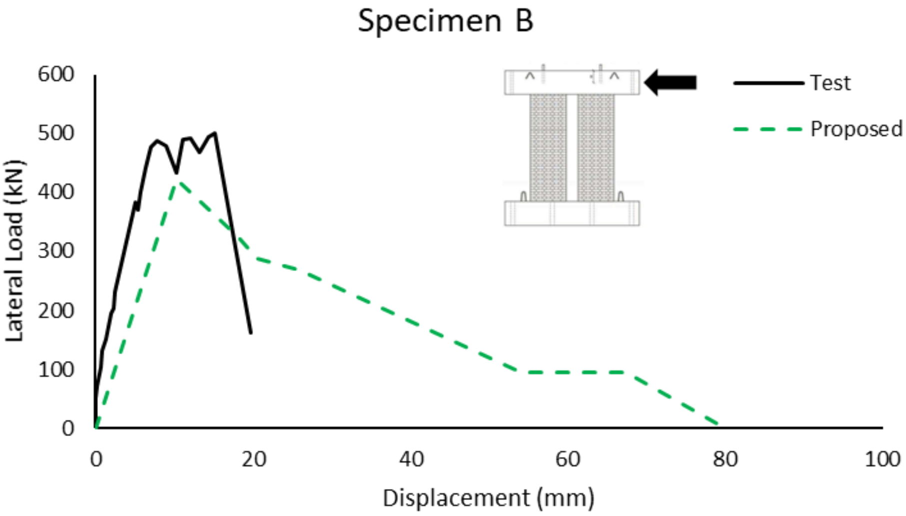

(b) Comparison with test curve

Figure 4-11 Lateral load-deflection curve comparison of Specimen B

doi:10.6342/NTU202502280

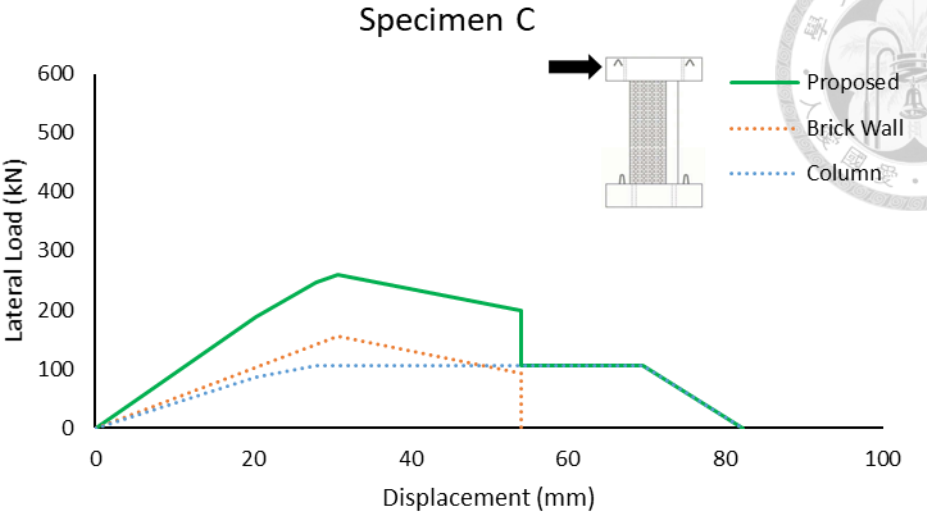

(a) Proposed lateral load-deflection curve

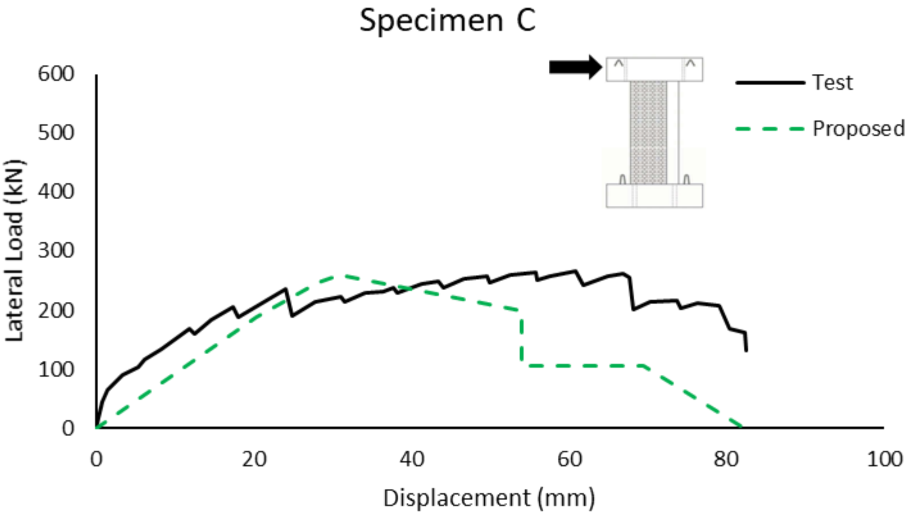

(b) Comparison with test curve

Figure 4-12 Lateral load-deflection curve comparison of Specimen C

doi:10.6342/NTU202502280

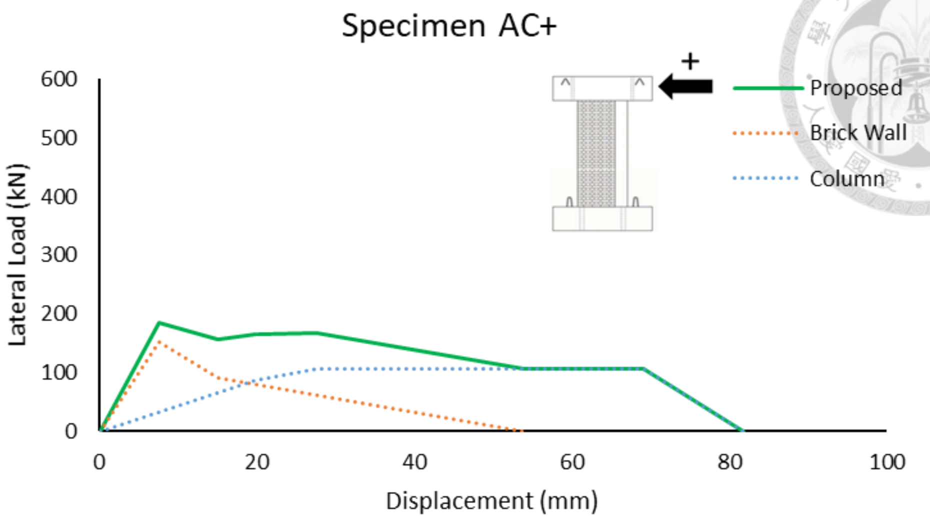

(a) Proposed lateral load-deflection curve

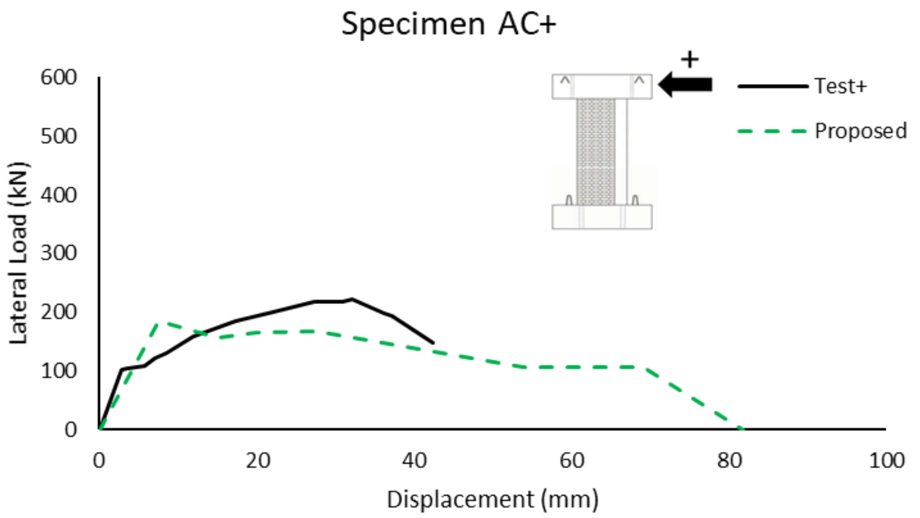

(b) Comparison with test curve

Figure 4-13 Lateral load-deflection curve comparison of Specimen AC under positive loading

doi:10.6342/NTU202502280

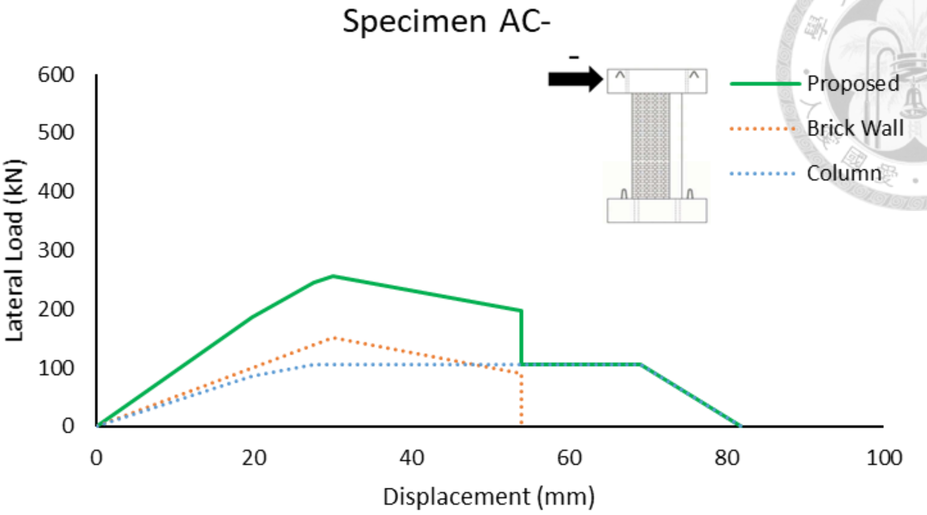

(a) Proposed lateral load-deflection curve

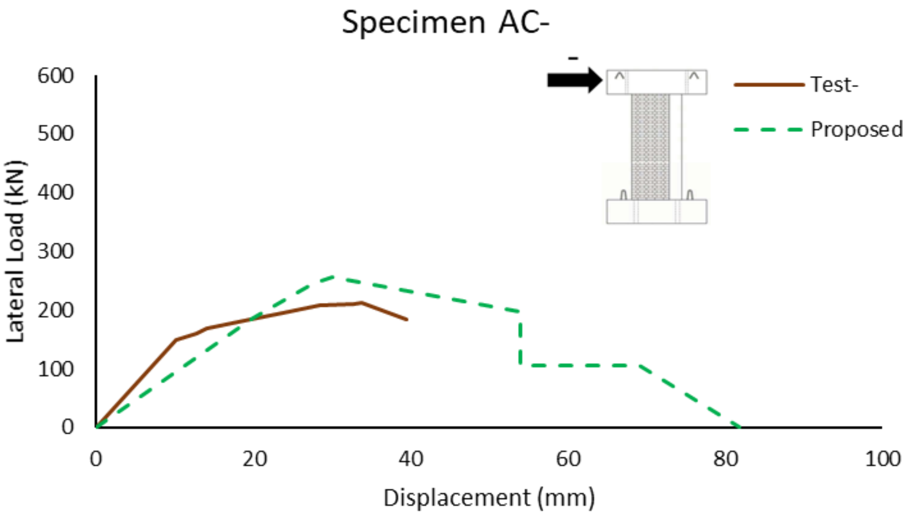

(b) Comparison with test curve

Figure 4-14 Lateral load-deflection curve comparison of Specimen AC under negative loading

doi:10.6342/NTU202502280

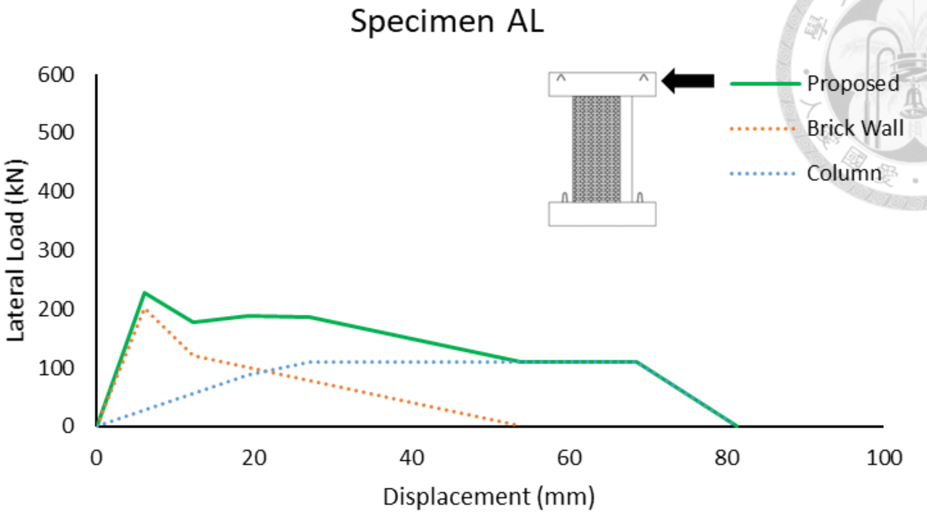

(a) Proposed lateral load-deflection curve

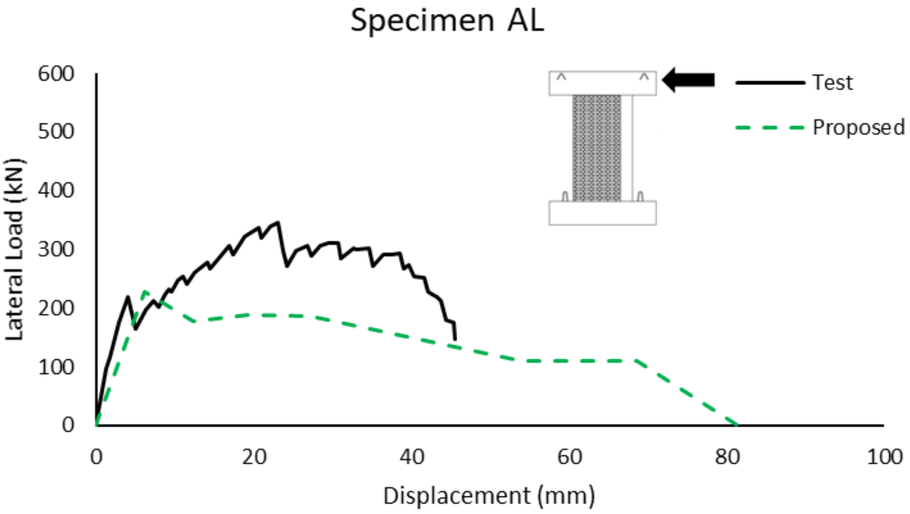

(b) Comparison with test curve

Figure 4-15 Lateral load-deflection curve comparison of Specimen AL

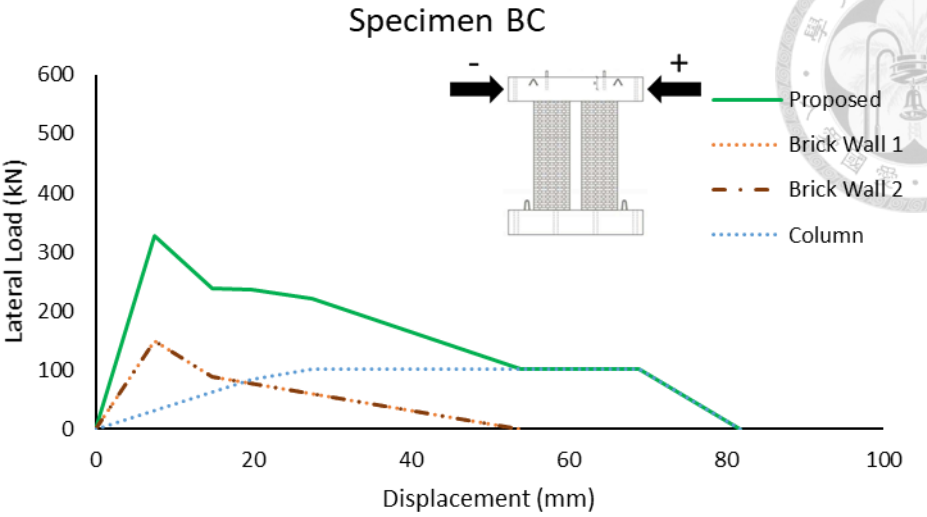

(a) Proposed lateral load-deflection curve

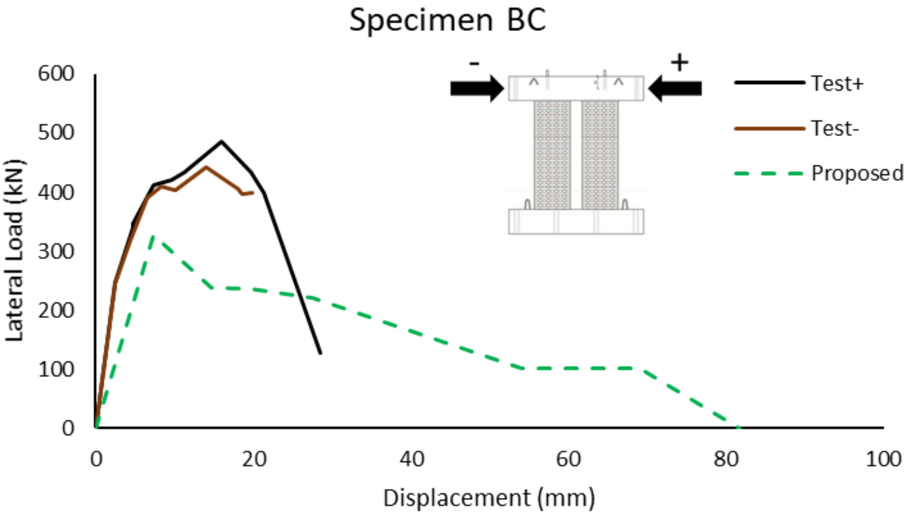

(b) Comparison with test curve

Figure 4-16 Lateral load-deflection curve comparison of Specimen BC under positive and negative loading

doi:10.6342/NTU202502280

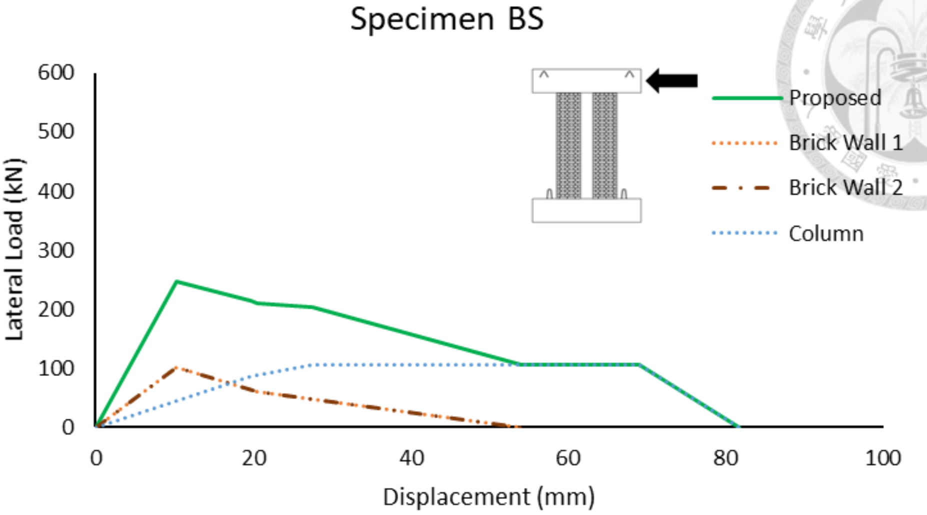

(a) Proposed lateral load-deflection curve

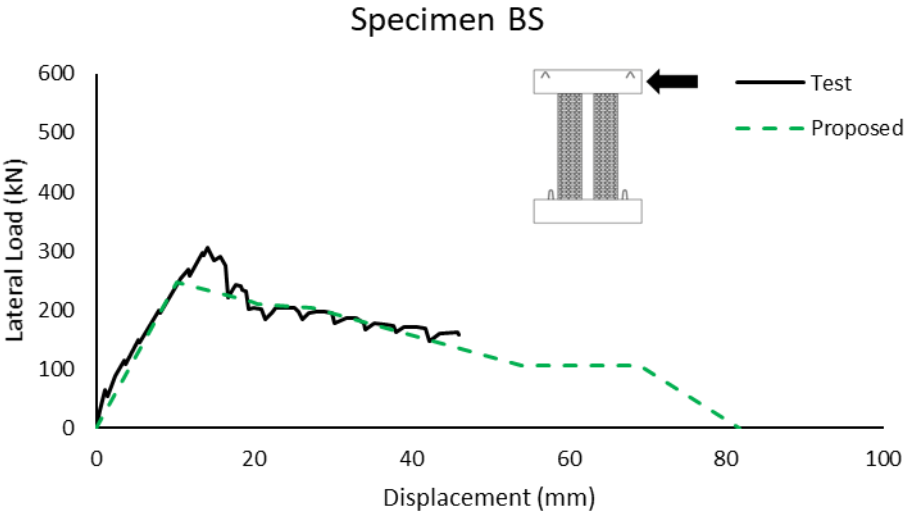

(b) Comparison with test curve

Figure 4-17 Lateral load-deflection curve comparison of Specimen BS

doi:10.6342/NTU202502280

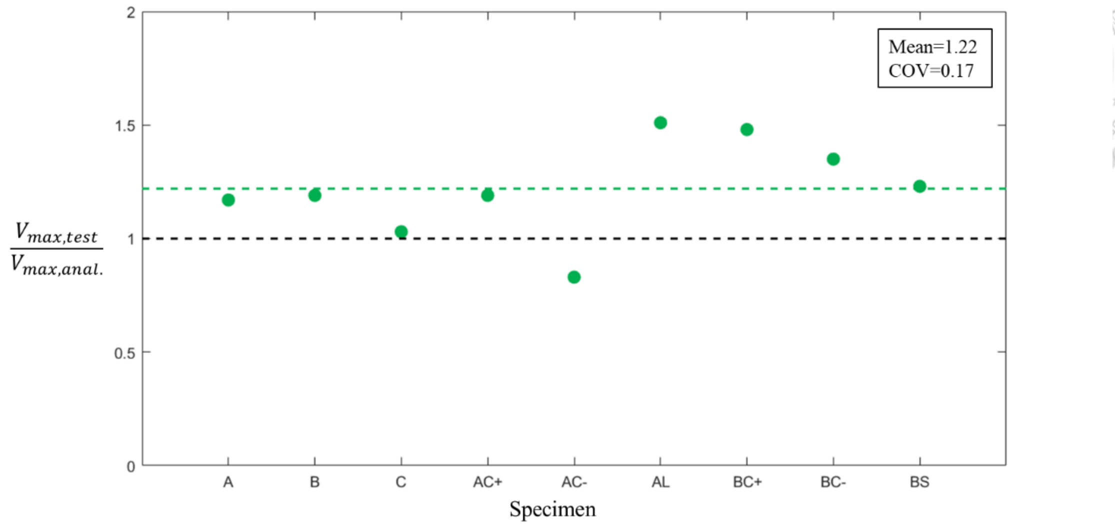

(a) Peak strength comparison

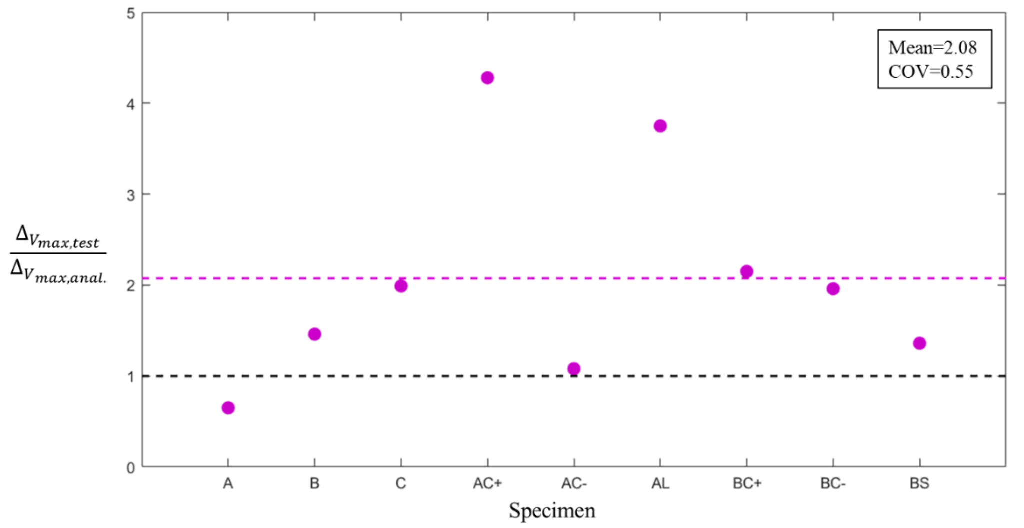

(b) Displacement at peak strength comparison

Figure 4-18 Statistical comparison between test and analytical values of three-sided confined brick infill specimens

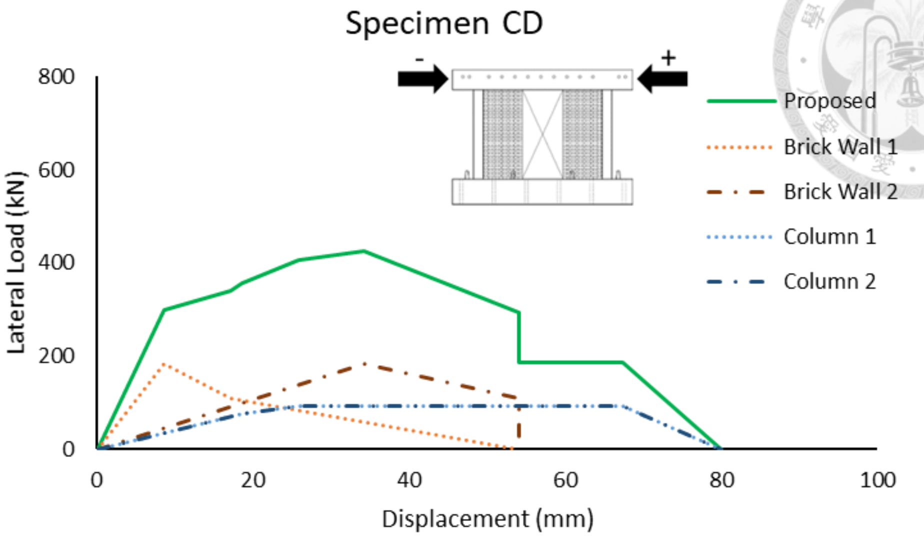

(a) Proposed lateral load-deflection curve

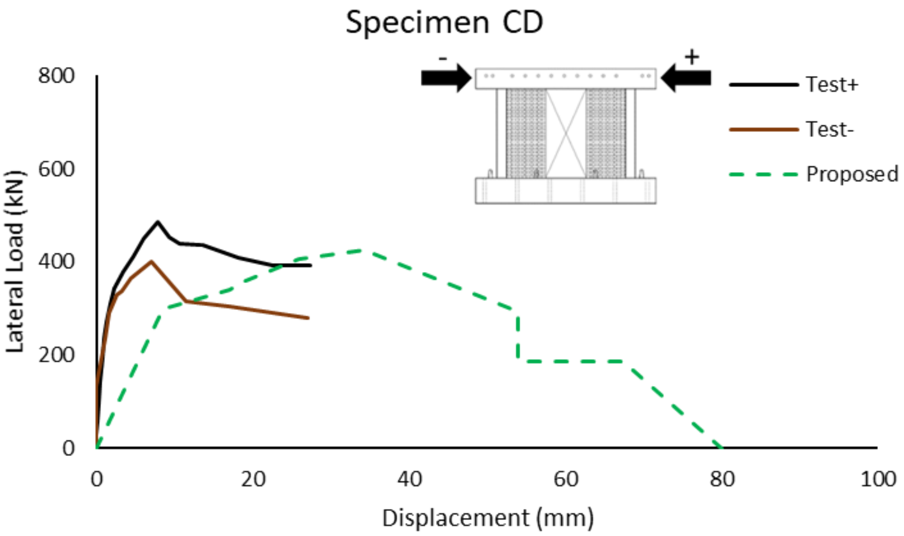

(b) Comparison with test curve

Figure 4-19 Lateral load-deflection curve comparison of Specimen CD under positive and negative loading

doi:10.6342/NTU202502280

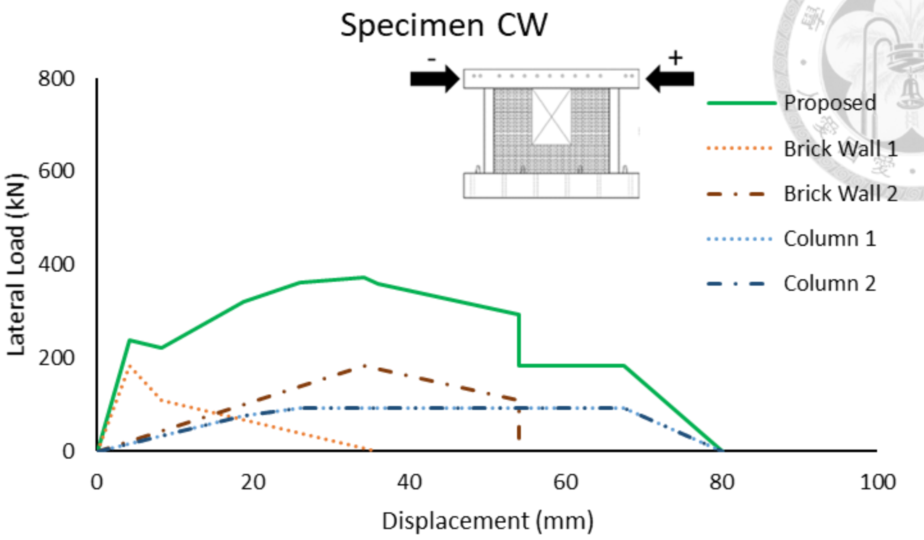

(a) Proposed lateral load-deflection curve

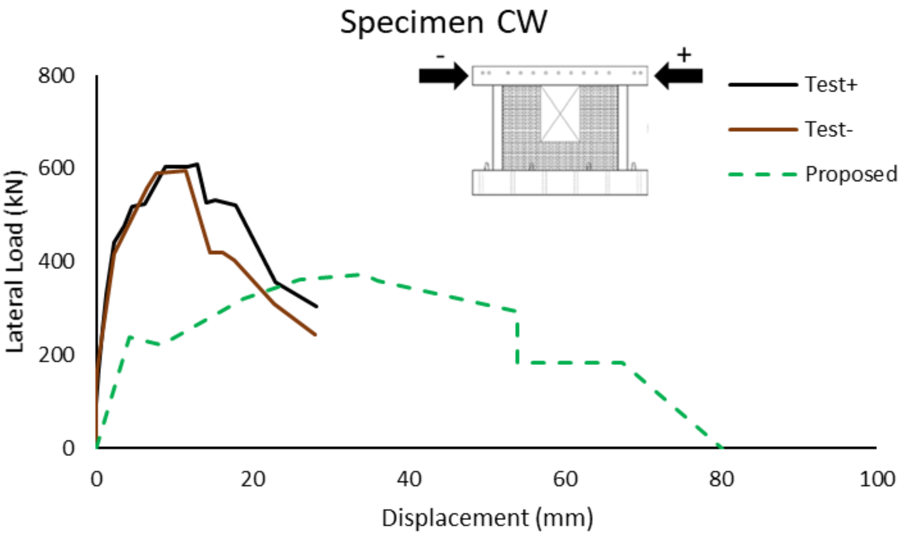

(b) Comparison with test curve

Figure 4-20 Lateral load-deflection curve comparison of Specimen CW under positive and negative loading

doi:10.6342/NTU202502280

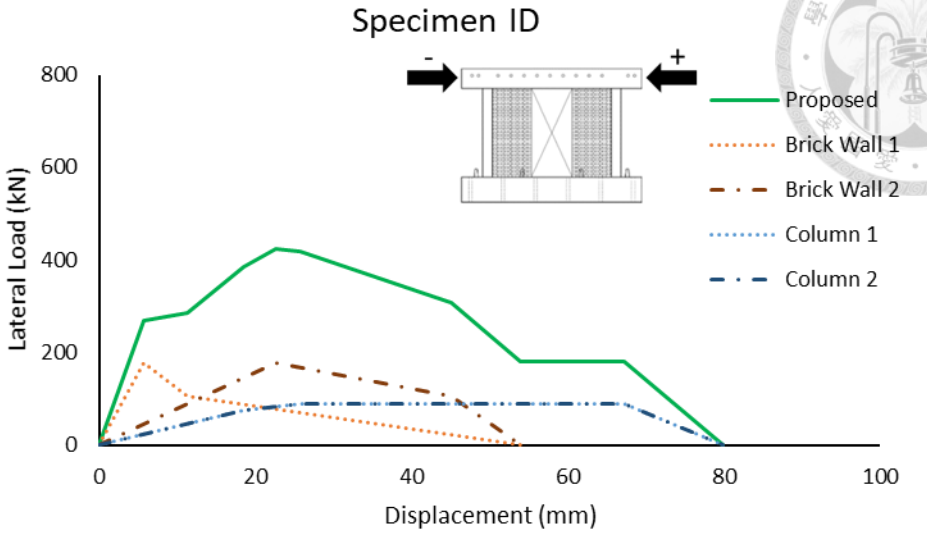

(a) Proposed lateral load-deflection curve

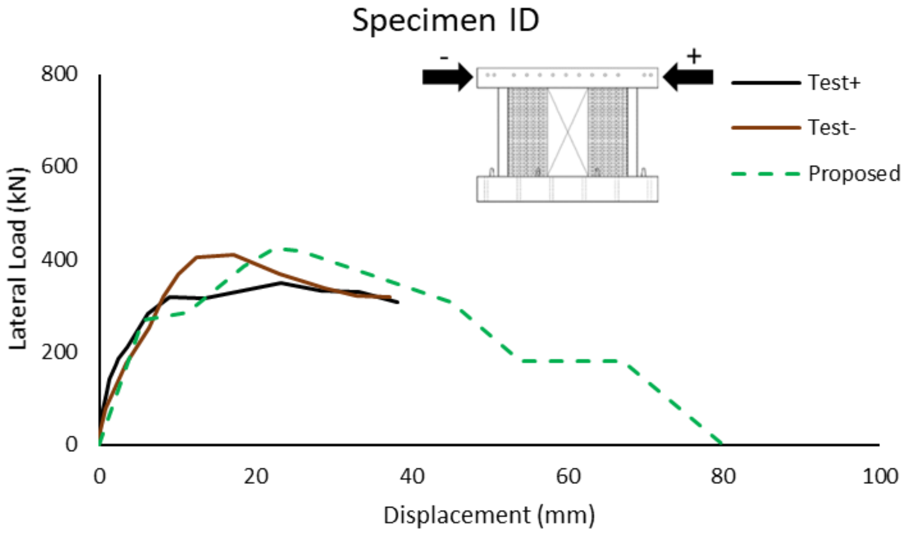

(b) Comparison with test curve

Figure 4-21 Lateral load-deflection curve comparison of Specimen ID under positive and negative loading

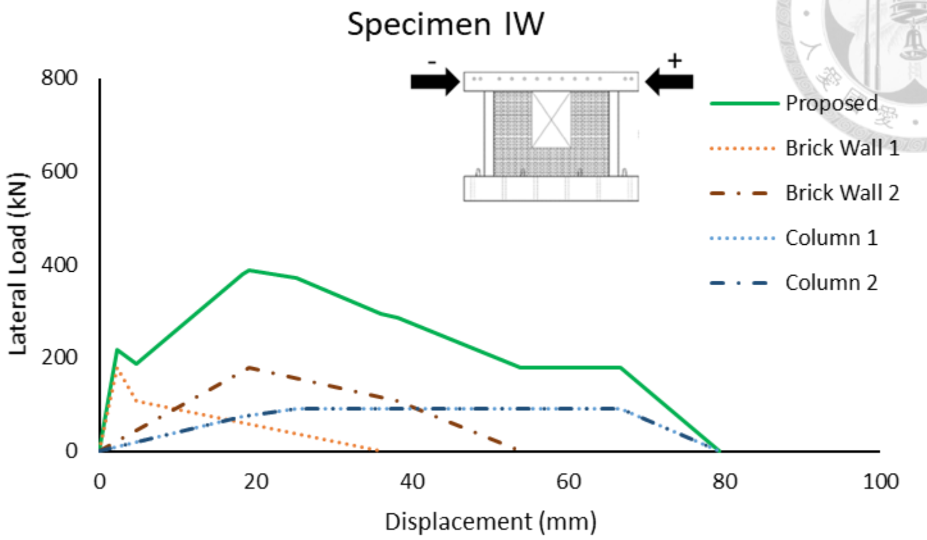

(a) Proposed lateral load-deflection curve

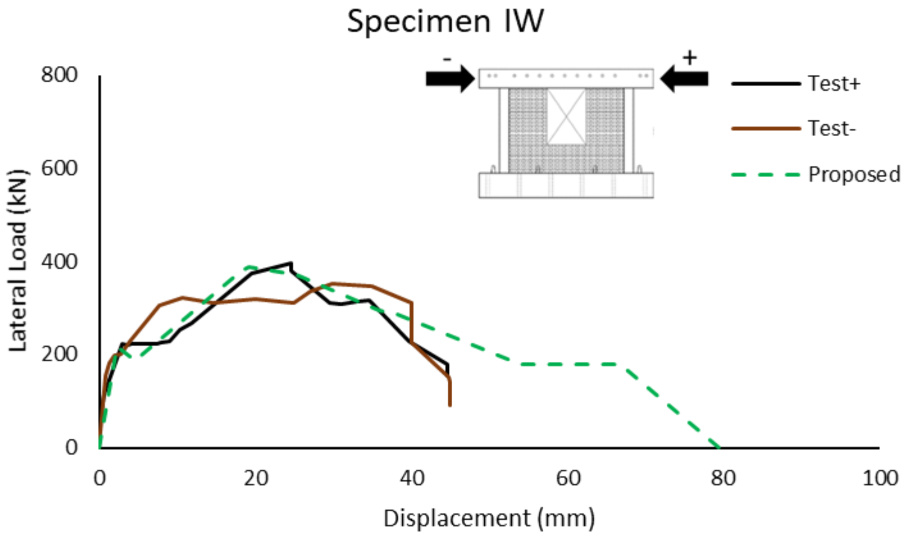

(b) Comparison with test curve

Figure 4-22 Lateral load-deflection curve comparison of Specimen IW under positive and negative loading

doi:10.6342/NTU202502280

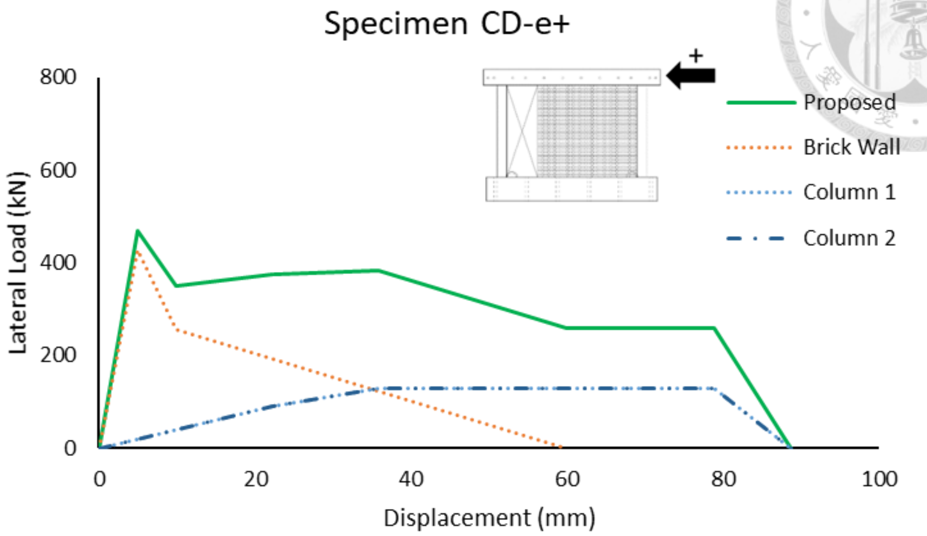

(a) Proposed lateral load-deflection curve

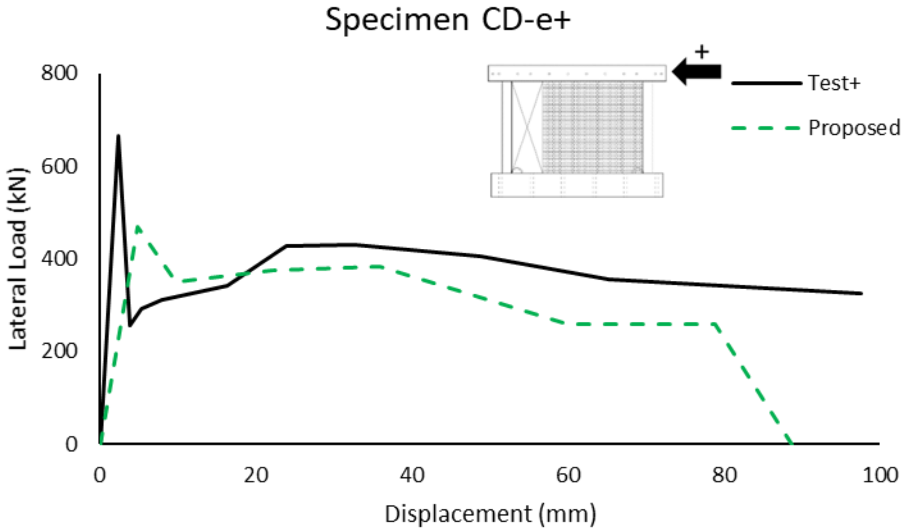

(b) Comparison with test curve

Figure 4-23 Lateral load-deflection curve comparison of Specimen CD-e under positive loading

doi:10.6342/NTU202502280

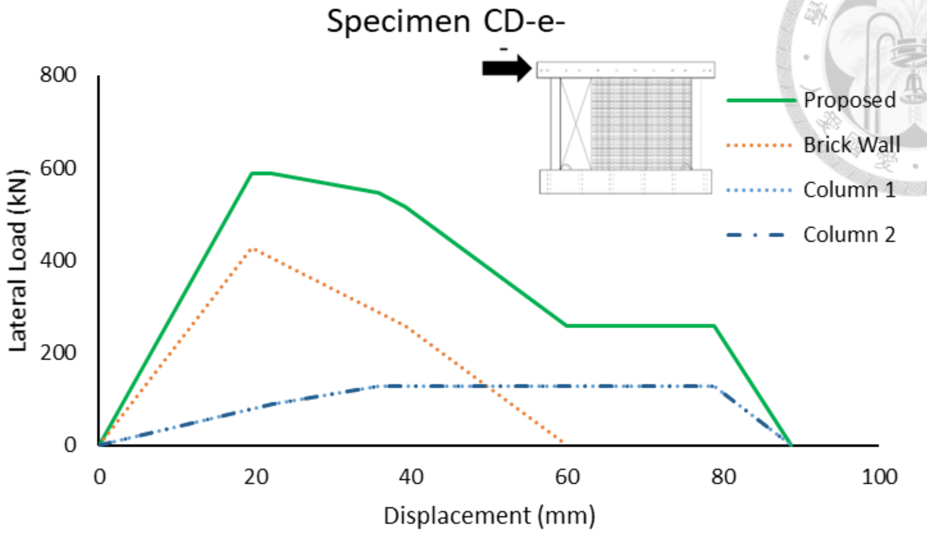

(a) Proposed lateral load-deflection curve

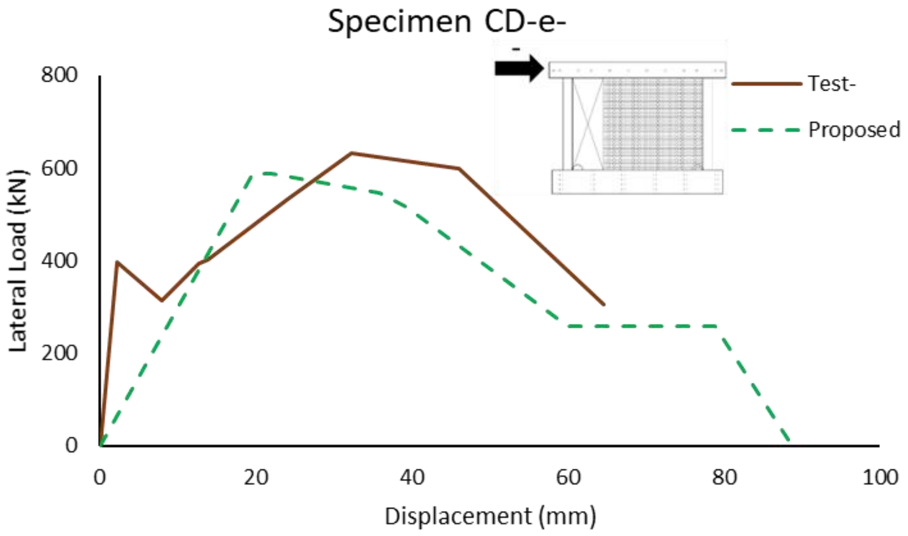

(b) Comparison with test curve

Figure 4-24 Lateral load-deflection curve comparison of Specimen CD-e under negative loading

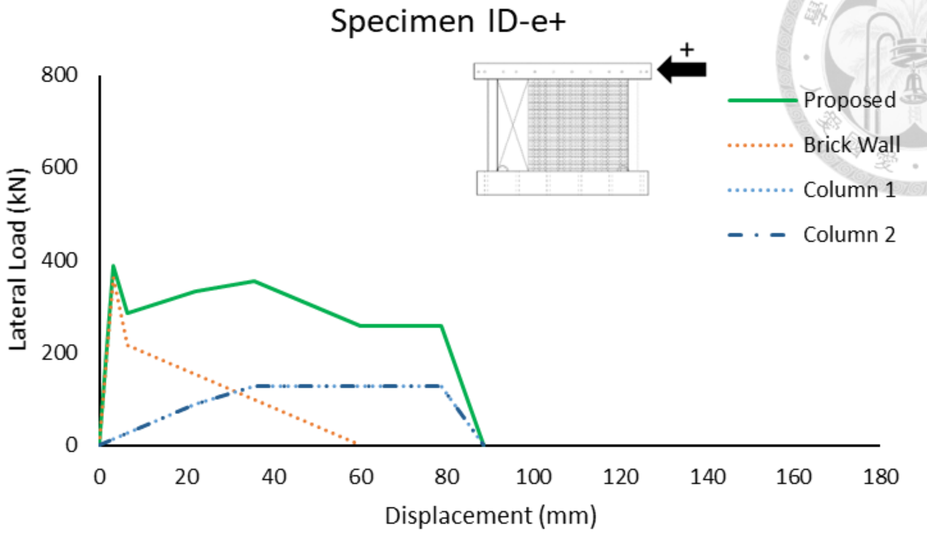

(a) Proposed lateral load-deflection curve

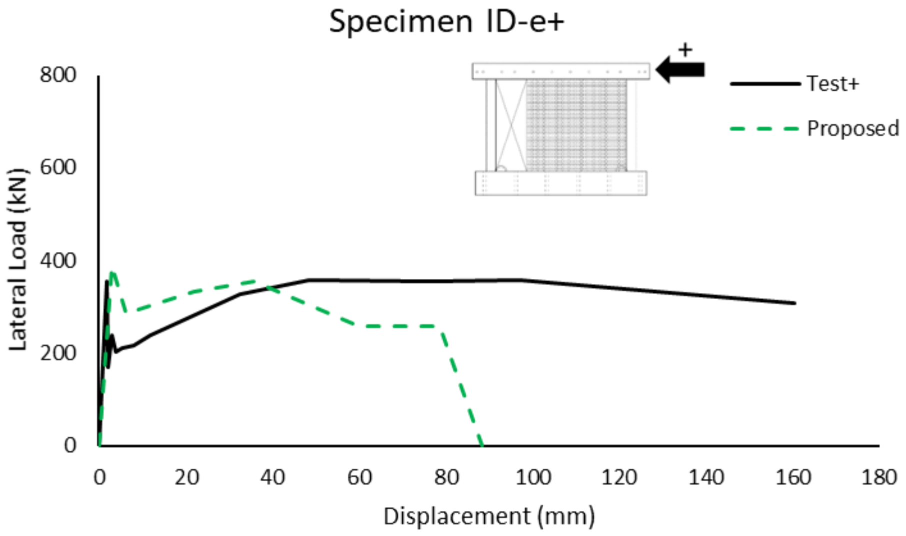

(b) Comparison with test curve

Figure 4-25 Lateral load-deflection curve comparison of Specimen ID-e under positive loading

doi:10.6342/NTU202502280

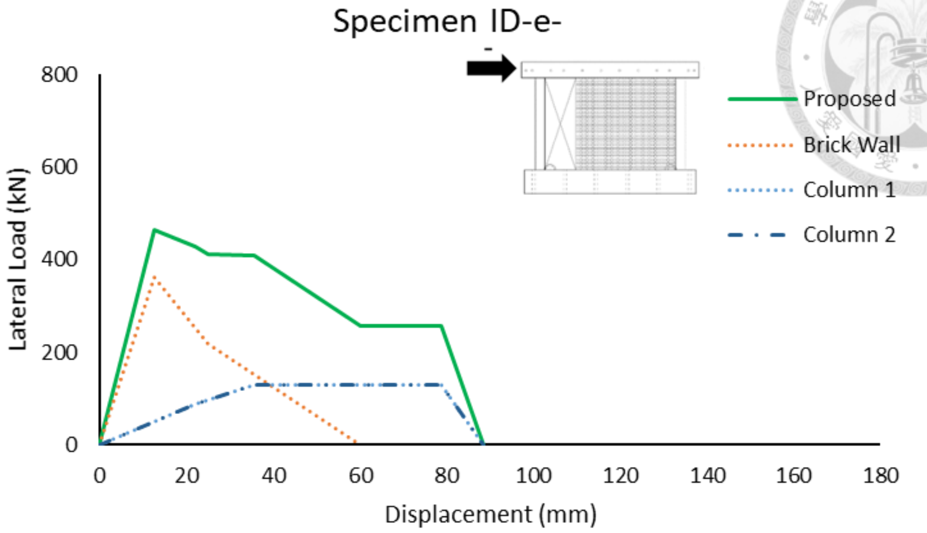

(a) Proposed lateral load-deflection curve

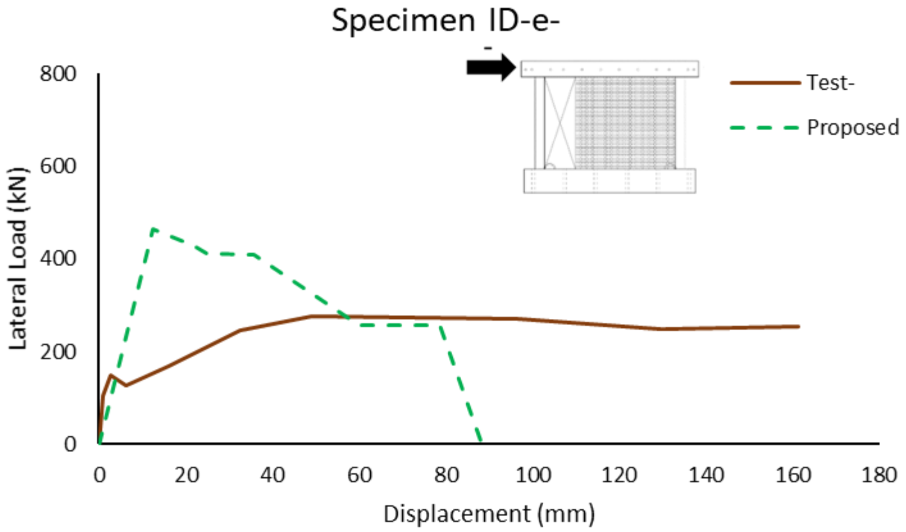

(b) Comparison with test curve

Figure 4-26 Lateral load-deflection curve comparison of Specimen ID-e under negative loading

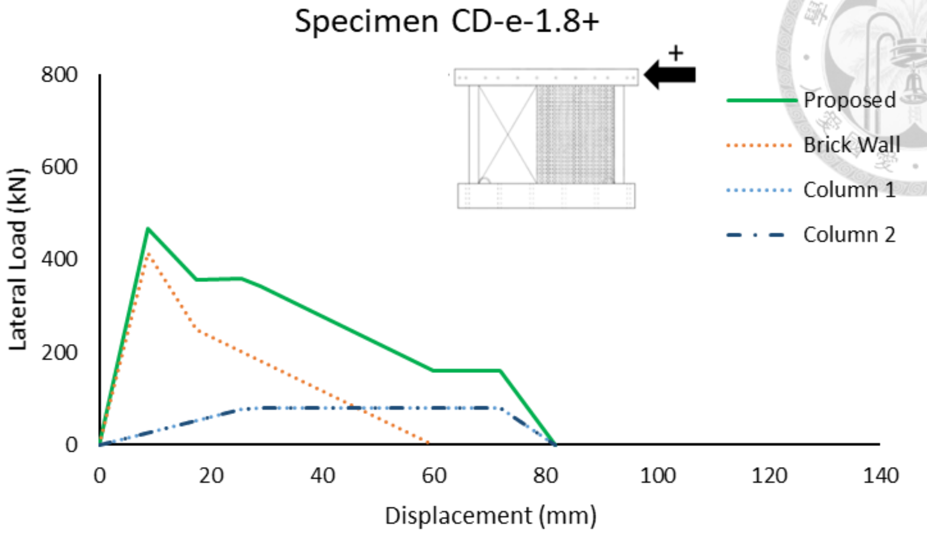

(a) Proposed lateral load-deflection curve

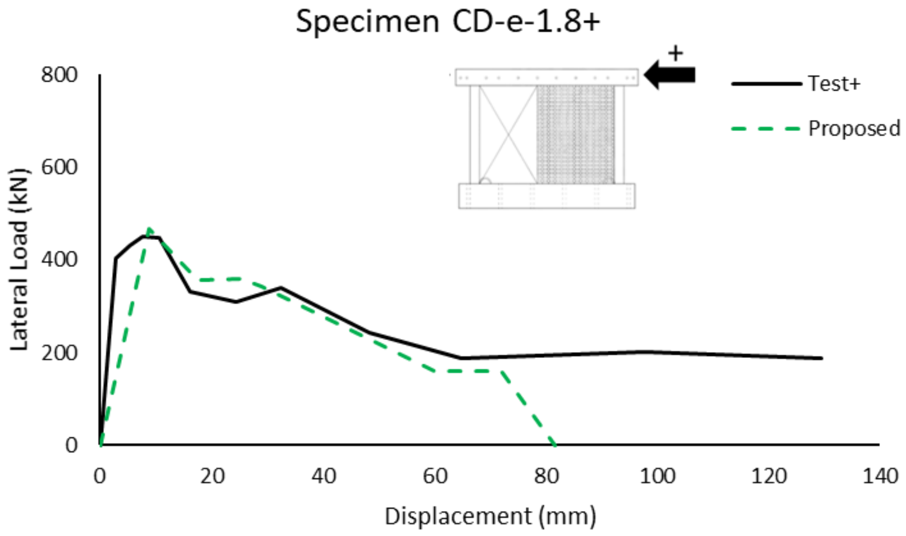

(b) Comparison with test curve

Figure 4-27 Lateral load-deflection curve comparison of Specimen CD-e-1.8 under positive loading

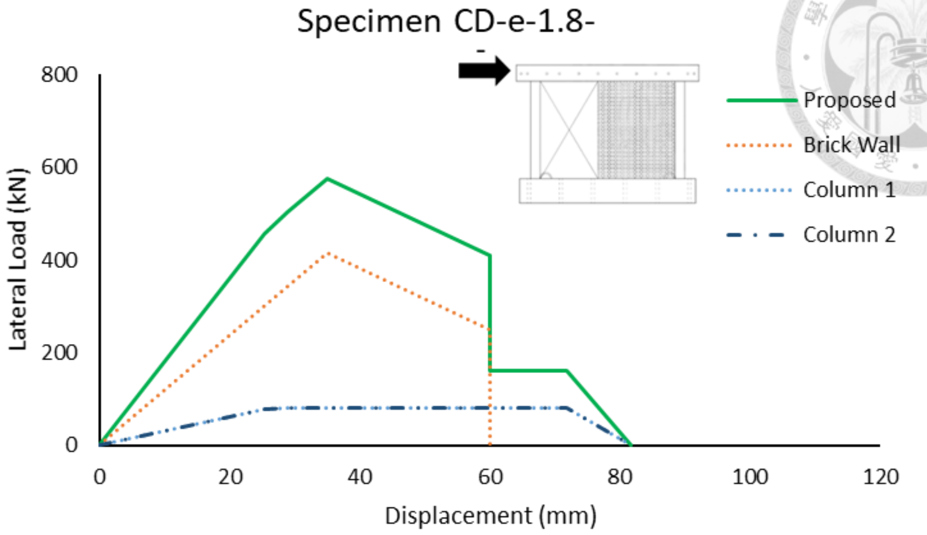

(a) Proposed lateral load-deflection curve

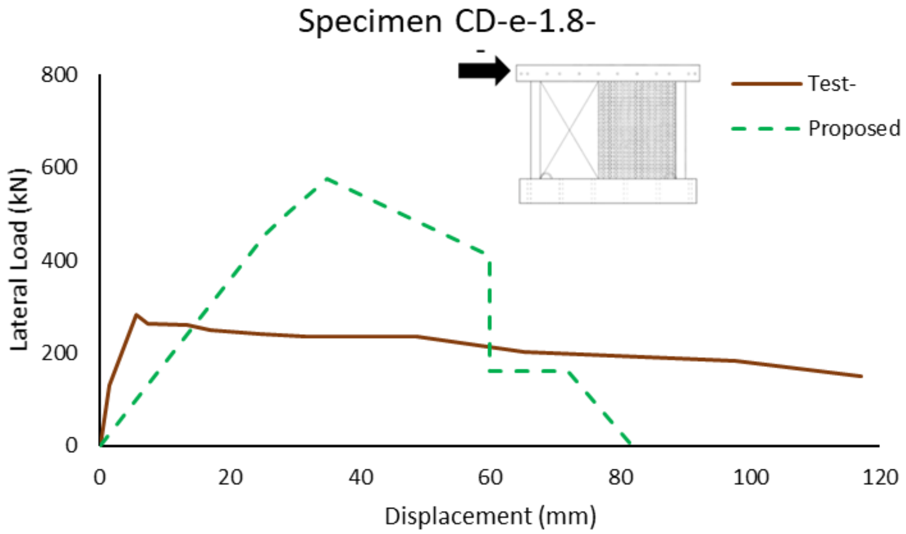

(b) Comparison with test curve

Figure 4-28 Lateral load-deflection curve comparison of Specimen CD-e-1.8 under negative loading

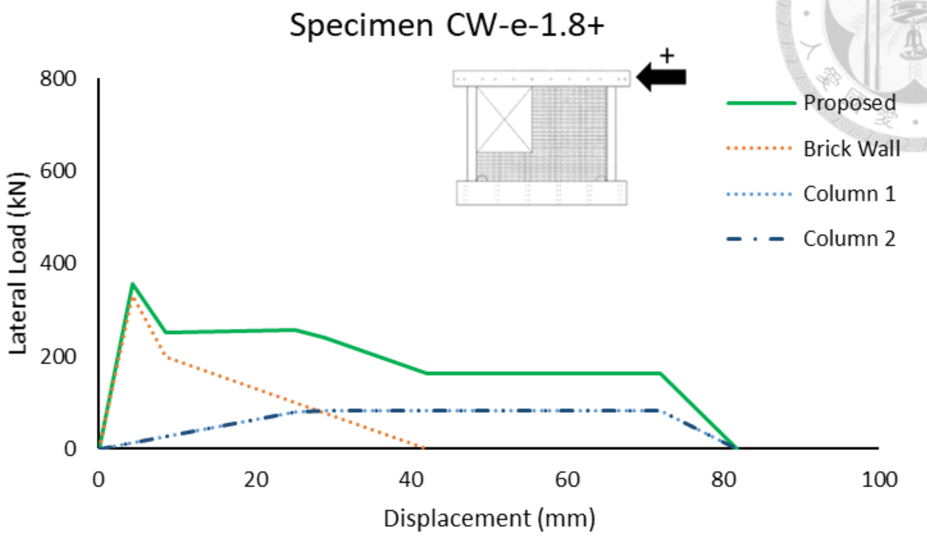

(a) Proposed lateral load-deflection curve

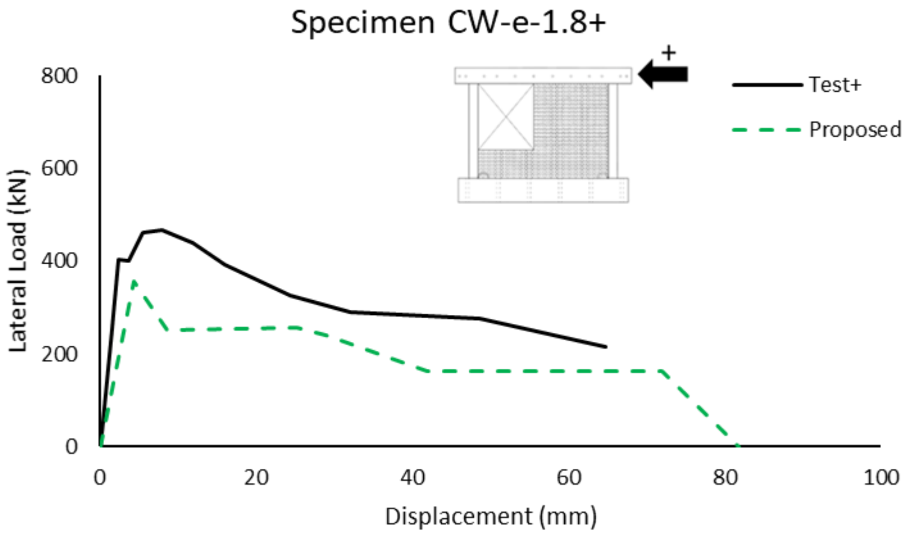

(b) Comparison with test curve

Figure 4-29 Lateral load-deflection curve comparison of Specimen CW-e-1.8 under positive loading

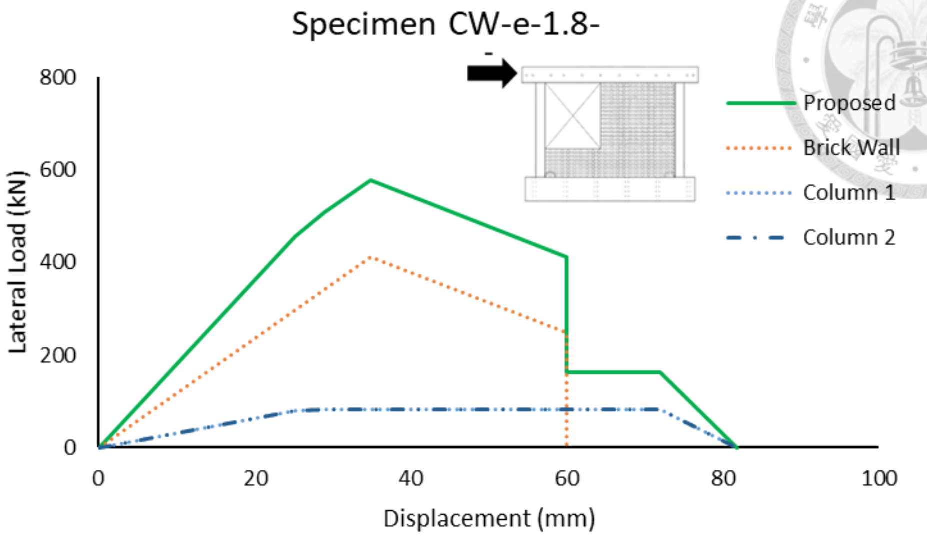

(a) Proposed lateral load-deflection curve

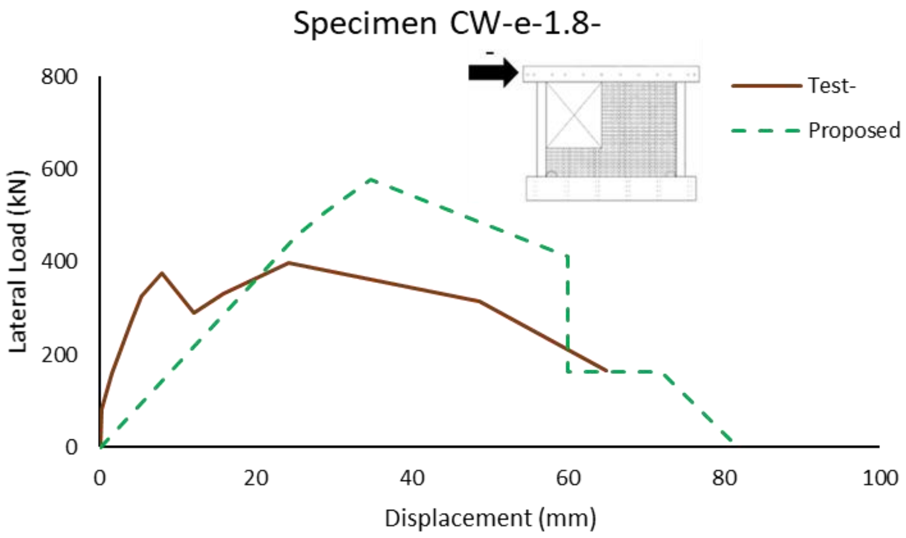

(b) Comparison with test curve

Figure 4-30 Lateral load-deflection curve comparison of Specimen CW-e-1.8 under negative loading

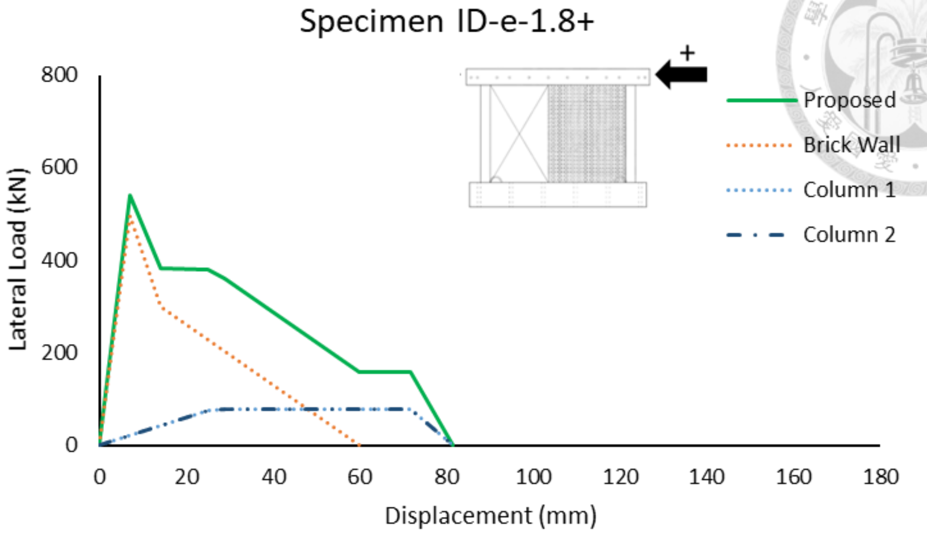

(a) Proposed lateral load-deflection curve

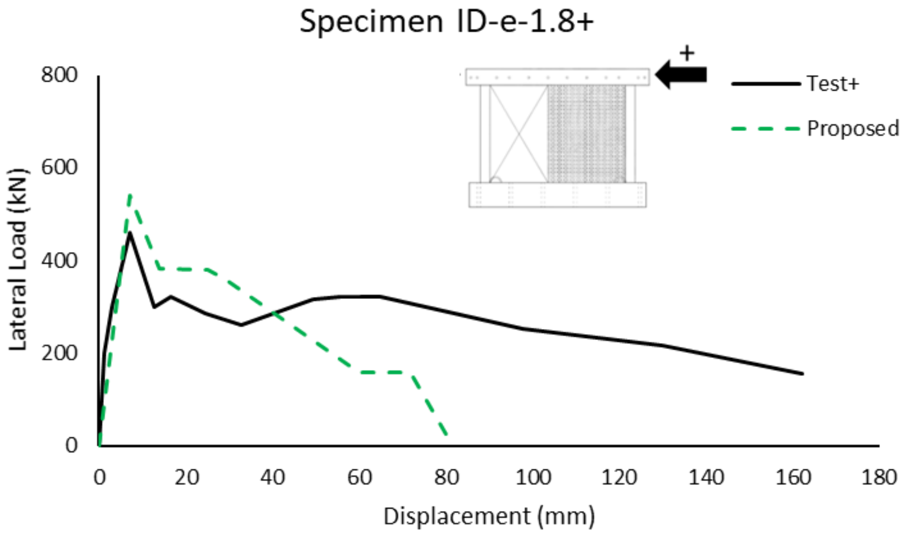

(b) Comparison with test curve

Figure 4-31 Lateral load-deflection curve comparison of Specimen ID-e-1.8 under positive loading

doi:10.6342/NTU202502280

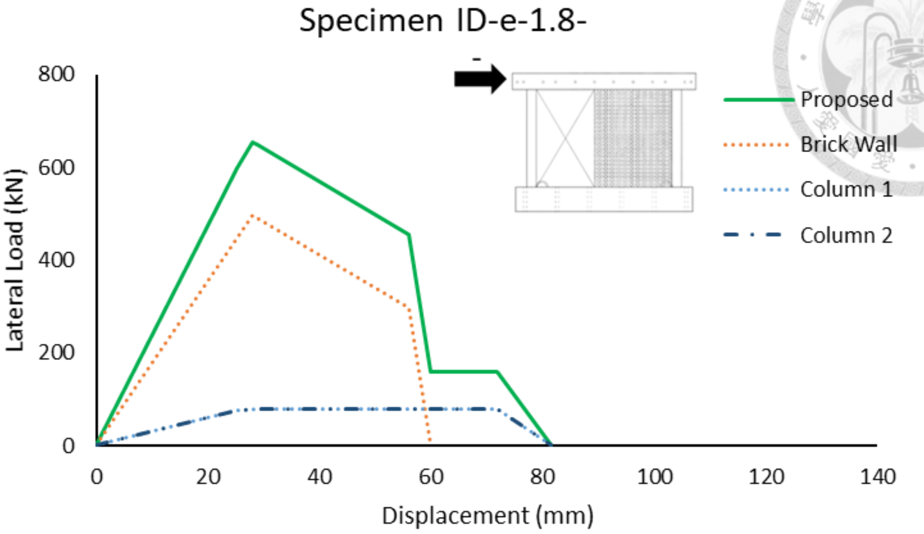

(a) Proposed lateral load-deflection curve

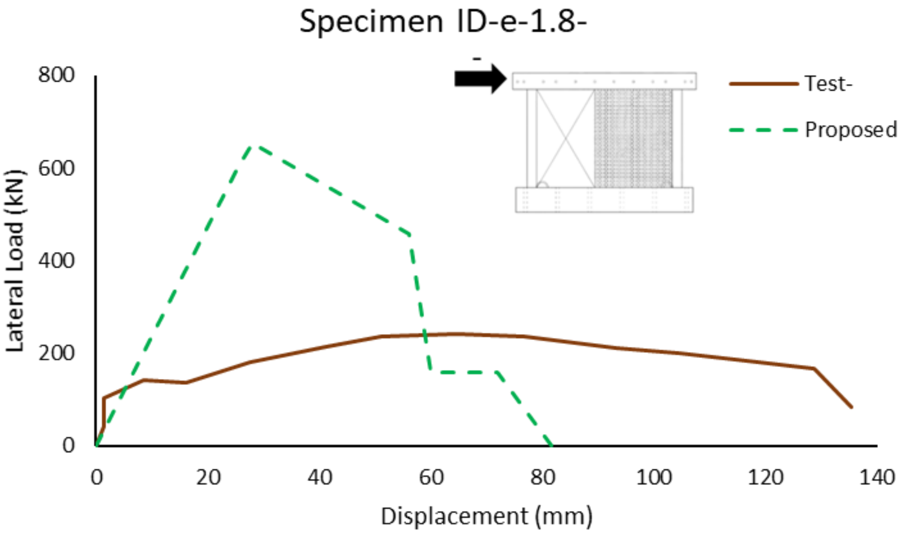

(b) Comparison with test curve

Figure 4-32 Lateral load-deflection curve comparison of Specimen ID-e-1.8 under negative loading

doi:10.6342/NTU202502280

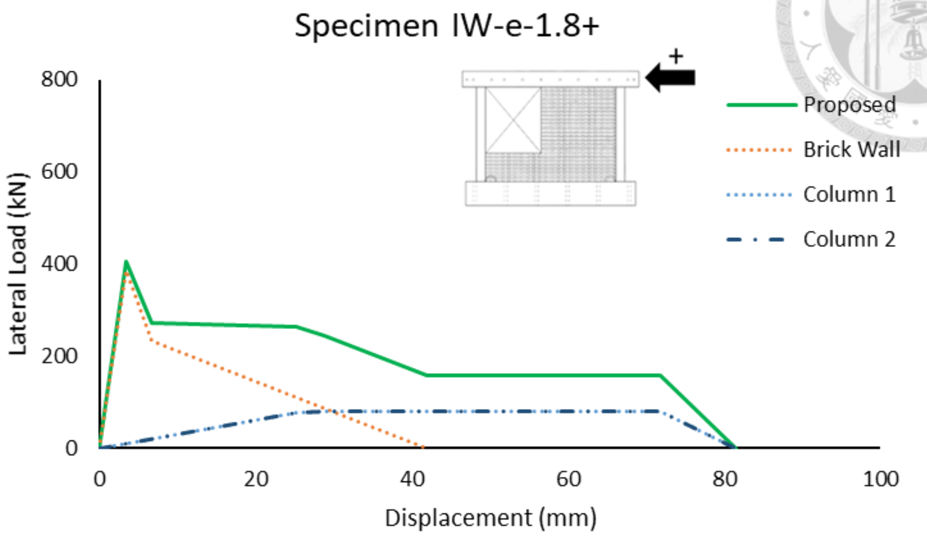

(a) Proposed lateral load-deflection curve

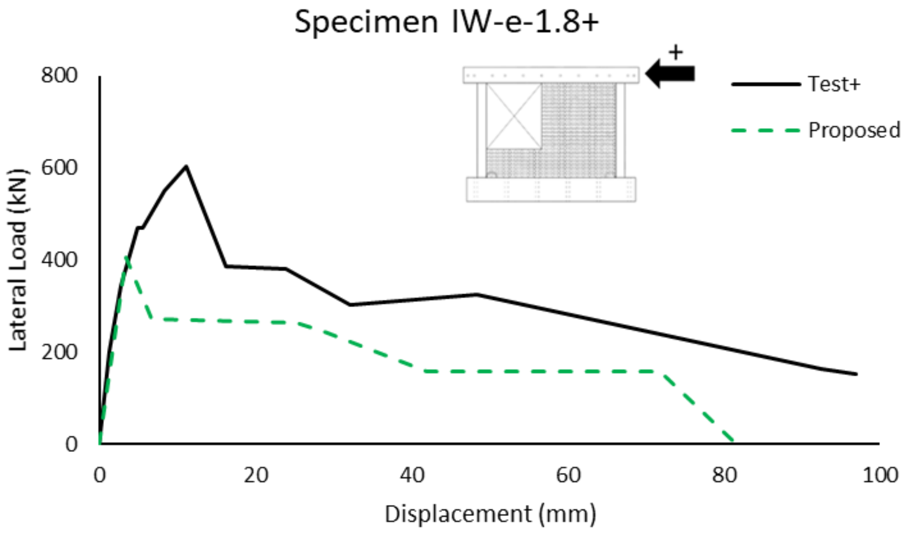

(b) Comparison with test curve

Figure 4-33 Lateral load-deflection curve comparison of Specimen IW-e-1.8 under positive loading

doi:10.6342/NTU202502280

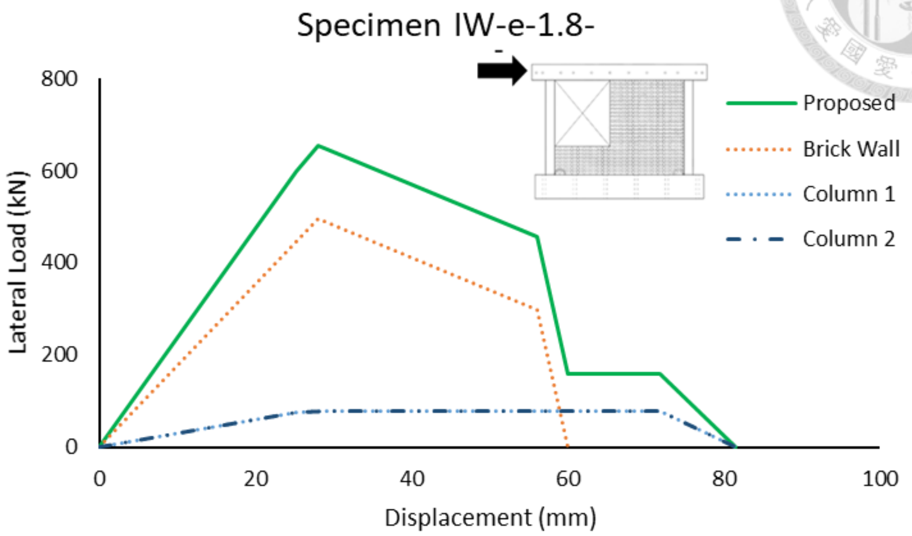

(a) Proposed lateral load-deflection curve

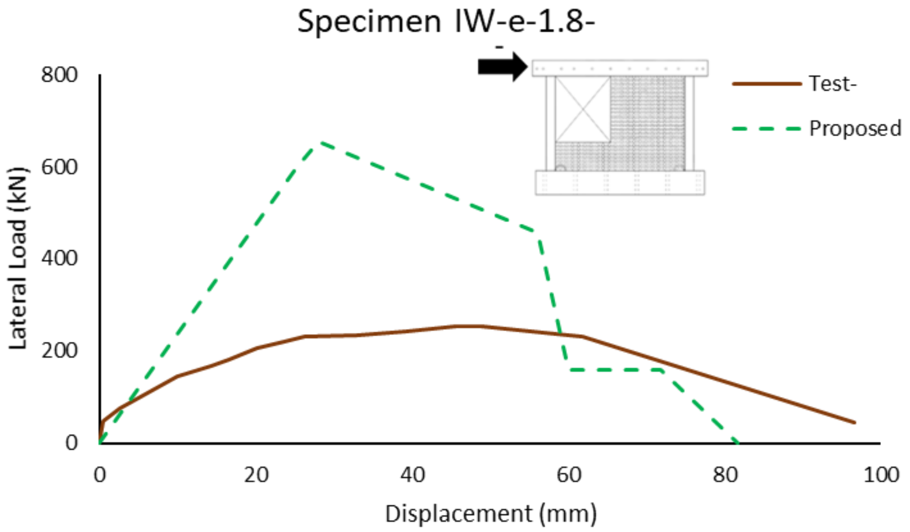

(b) Comparison with test curve

Figure 4-34 Lateral load-deflection curve comparison of Specimen IW-e-1.8 under negative loading

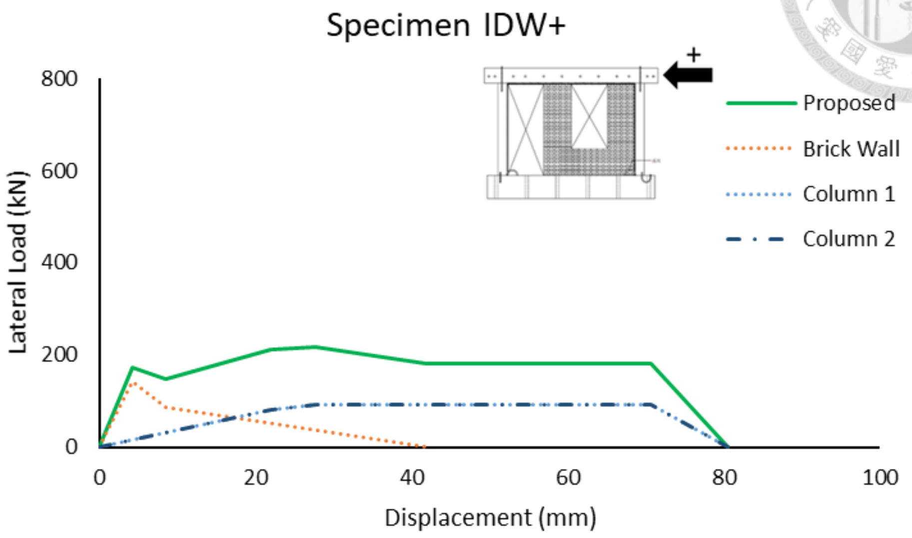

(a) Proposed lateral load-deflection curve

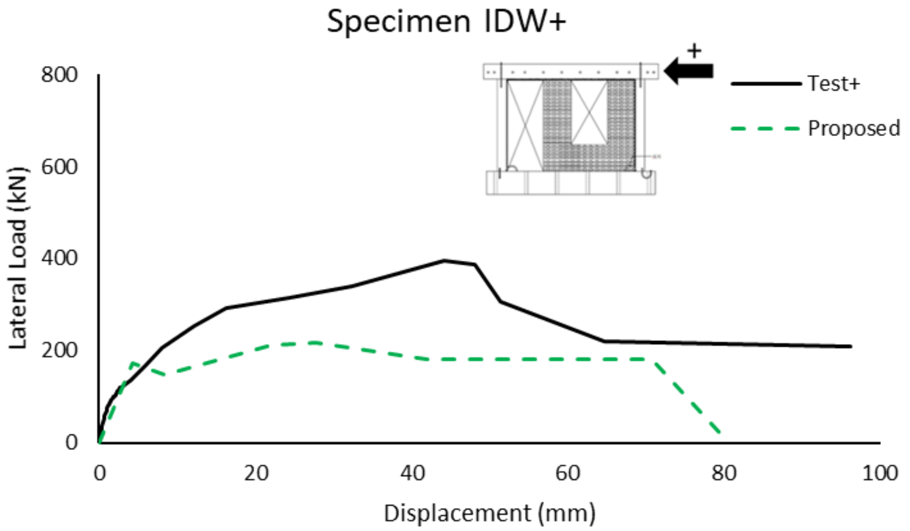

(b) Comparison with test curve

Figure 4-35 Lateral load-deflection curve comparison of Specimen IDW under positive loading

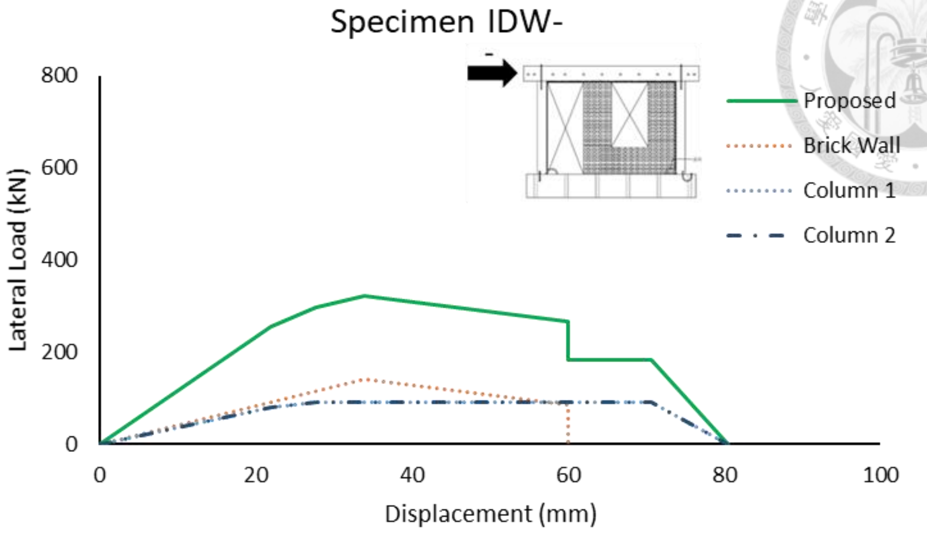

(a) Proposed lateral load-deflection curve

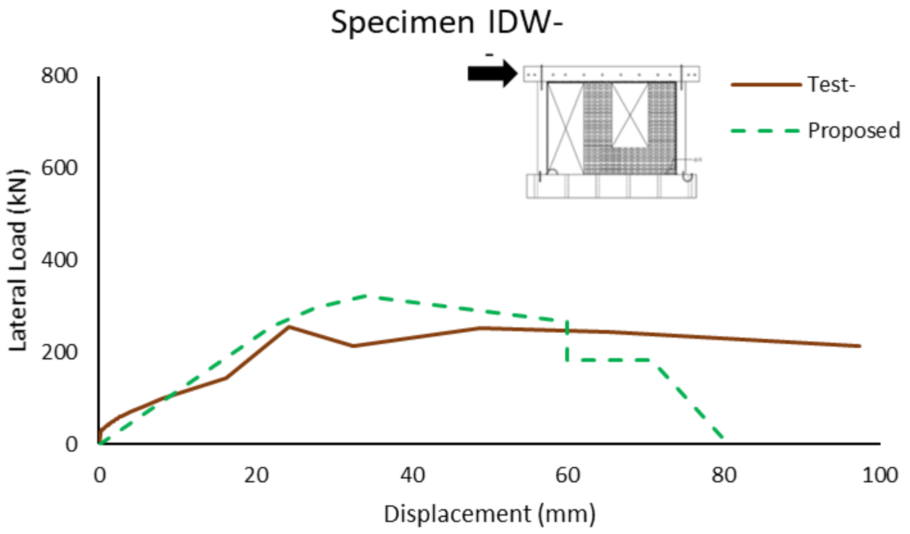

(b) Comparison with test curve

Figure 4-36 Lateral load-deflection curve comparison of Specimen IDW under negative loading

doi:10.6342/NTU202502280

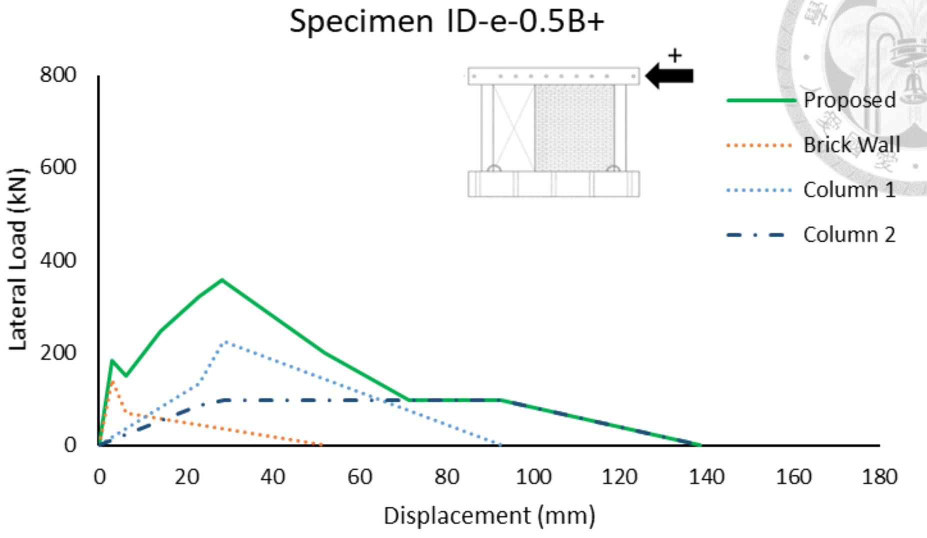

(a) Proposed lateral load-deflection curve

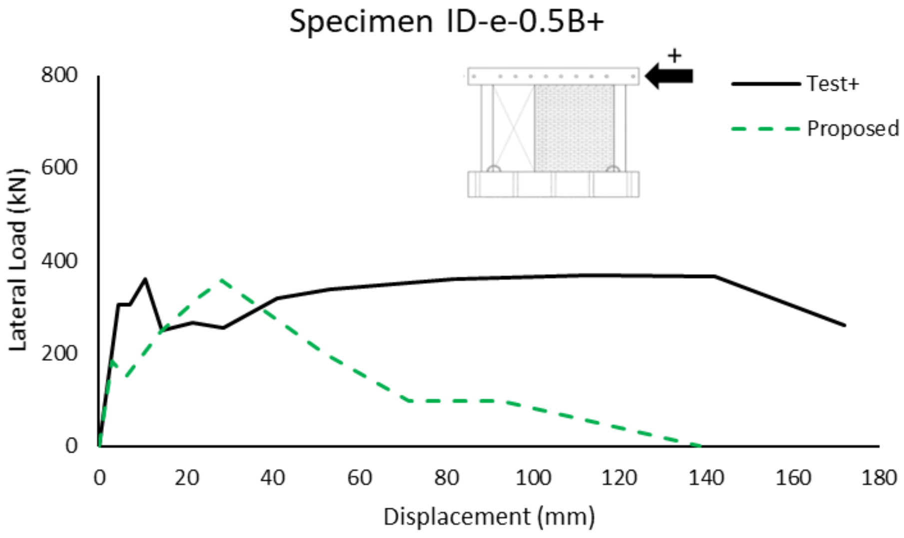

(b) Comparison with test curve

Figure 4-37 Lateral load-deflection curve comparison of Specimen ID-e-0.5B under positive loading

doi:10.6342/NTU202502280

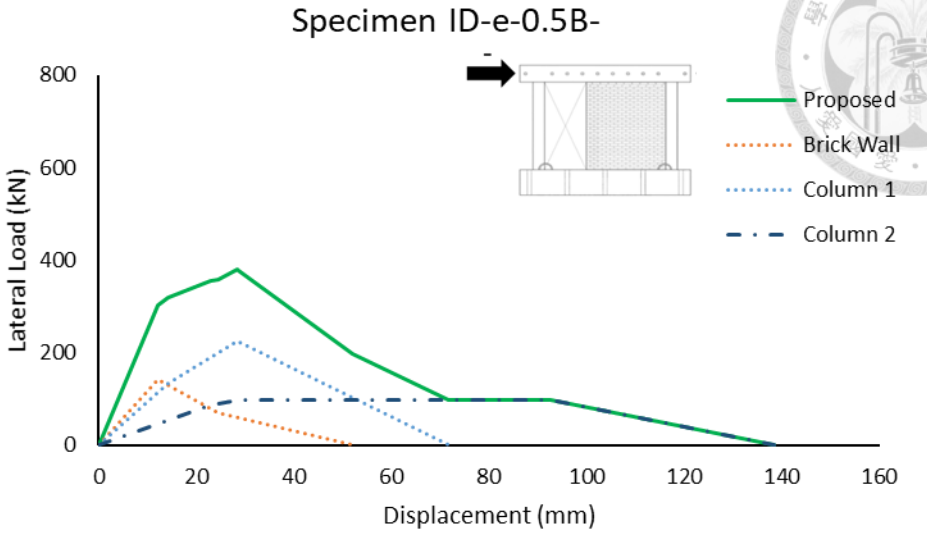

(a) Proposed lateral load-deflection curve

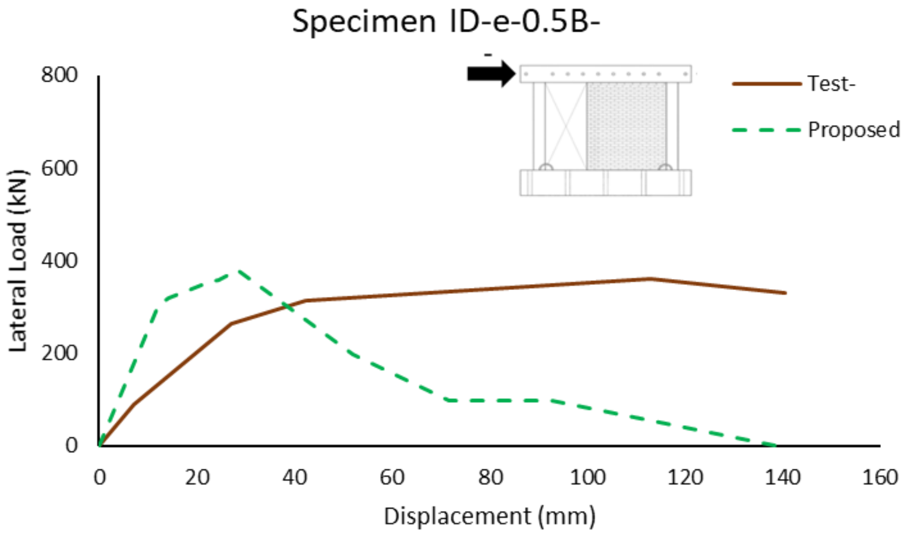

(b) Comparison with test curve

Figure 4-38 Lateral load-deflection curve comparison of Specimen ID-e-0.5B under negative loading

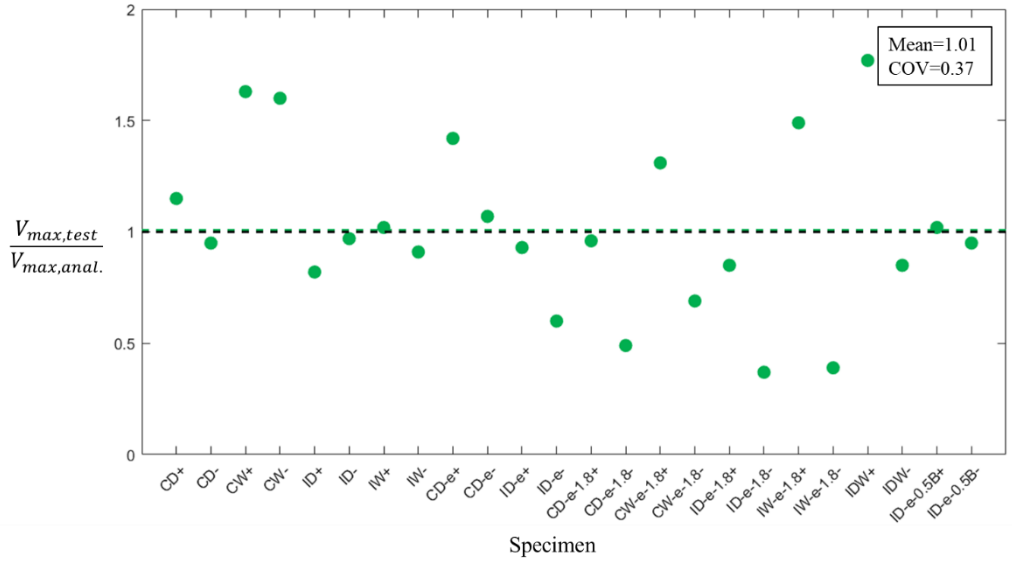

(a) Peak strength comparison

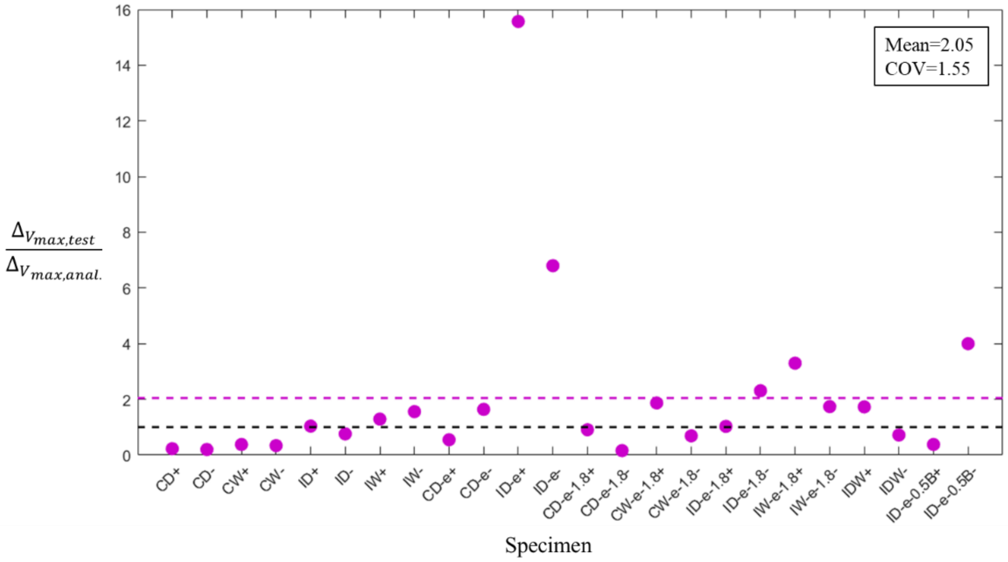

(b) Displacement at peak strength comparison

Figure 4-39 Statistical comparison between test and analytical values of brick infill walls with openings specimens

doi:10.6342/NTU202502280

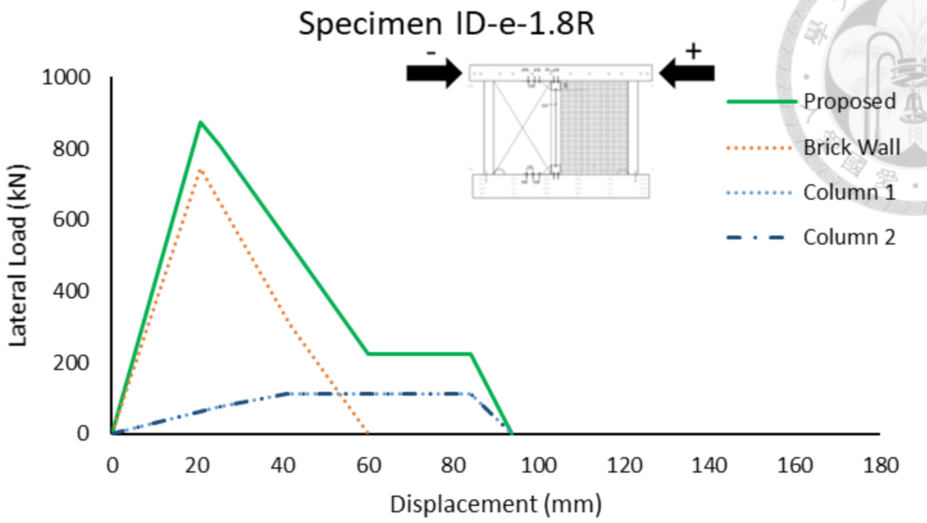

(a) Proposed lateral load-deflection curve

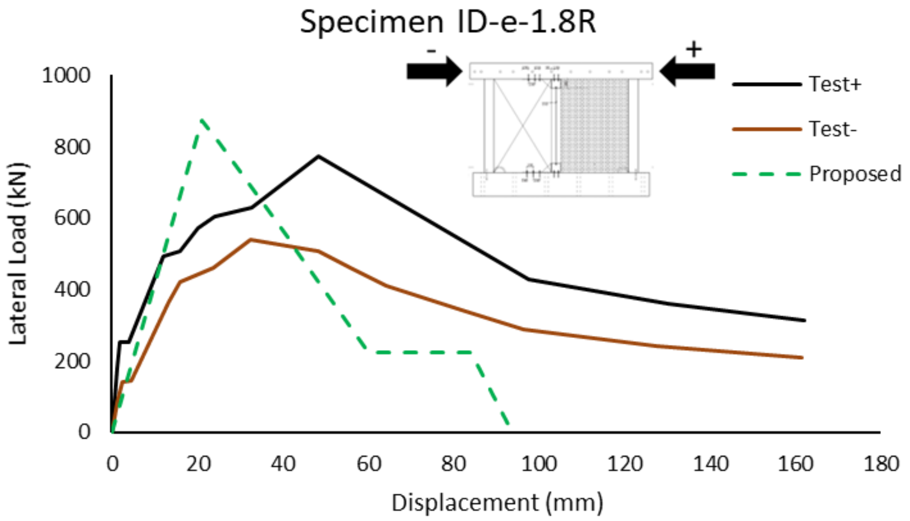

(b) Comparison with test curve

Figure 4-40 Lateral load-deflection curve comparison of Specimen ID-e-1.8R under positive and negative loading

doi:10.6342/NTU202502280

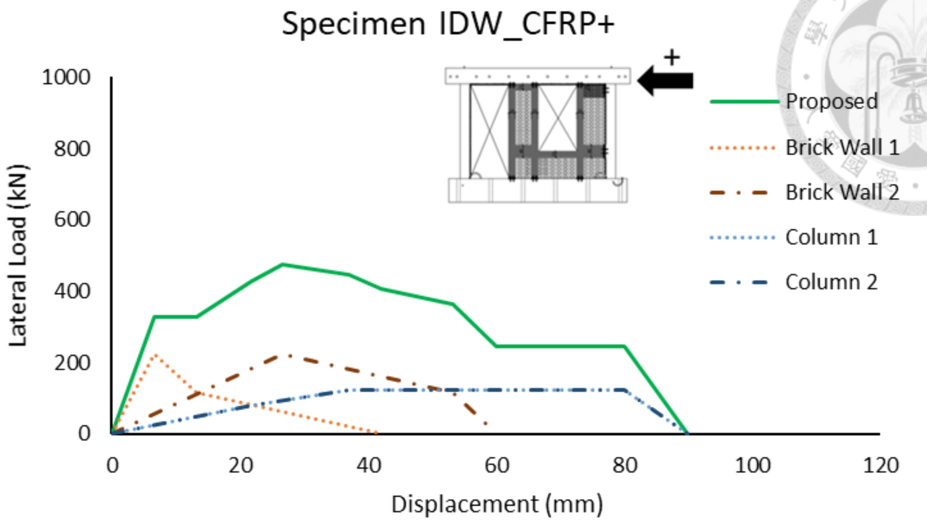

(a) Proposed lateral load-deflection curve

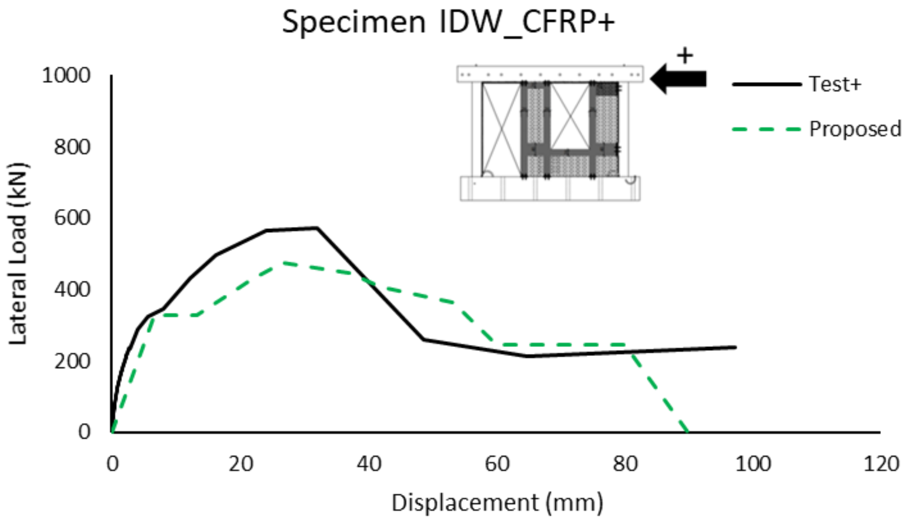

(b) Comparison with test curve

Figure 4-41 Lateral load-deflection curve comparison of Specimen IDW_CFRP under positive loading

doi:10.6342/NTU202502280

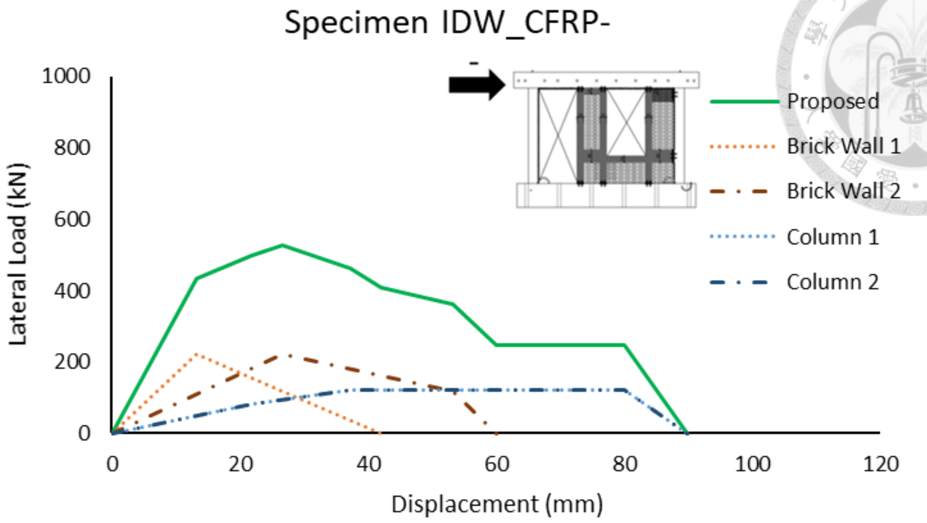

(a) Proposed lateral load-deflection curve

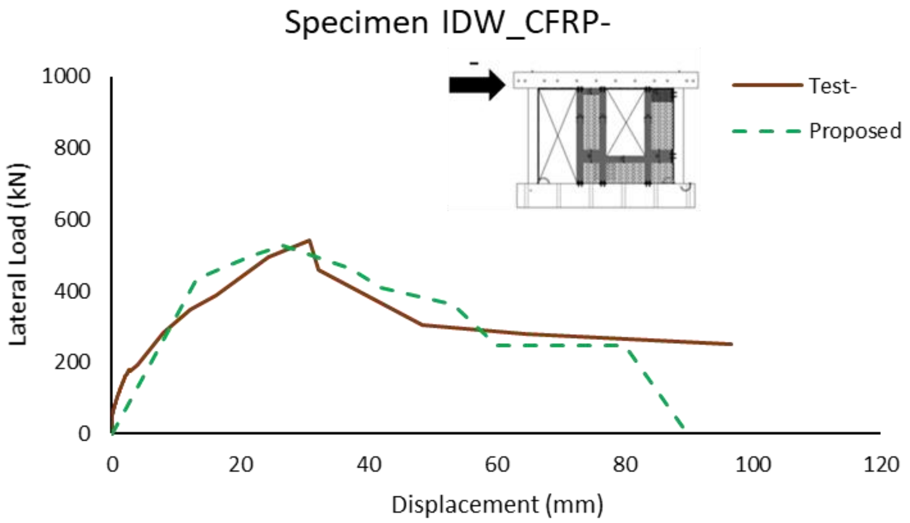

(b) Comparison with test curve

Figure 4-42 Lateral load-deflection curve comparison of Specimen IDW_CFRP under negative loading

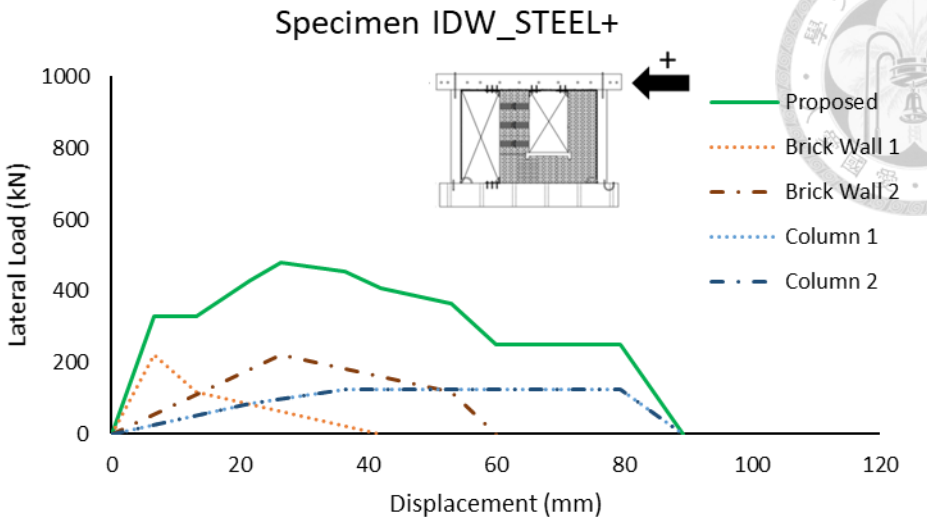

(a) Proposed lateral load-deflection curve

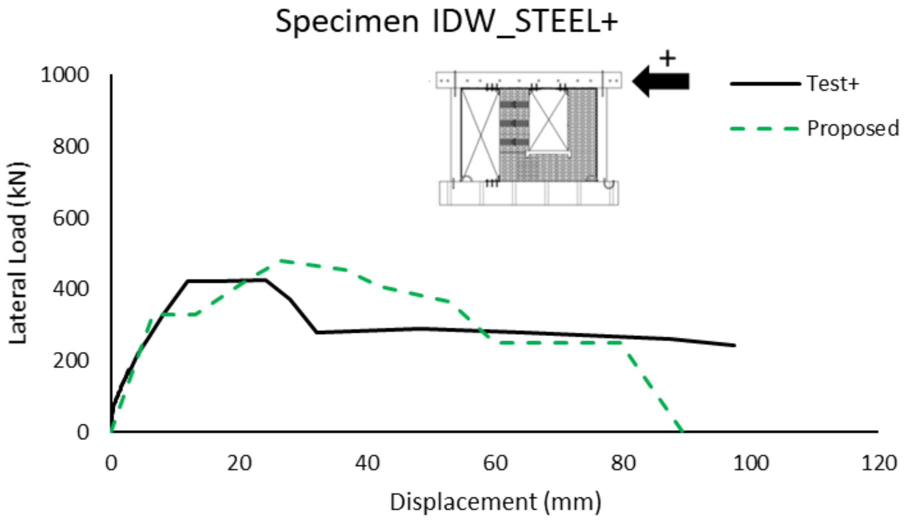

(b) Comparison with test curve

Figure 4-43 Lateral load-deflection curve comparison of Specimen IDW_STEEL under positive loading

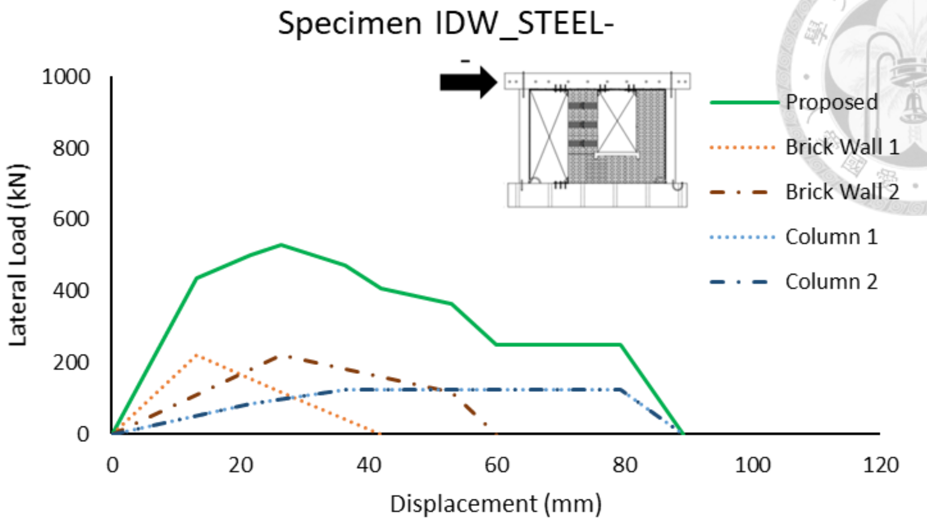

(a) Proposed lateral load-deflection curve

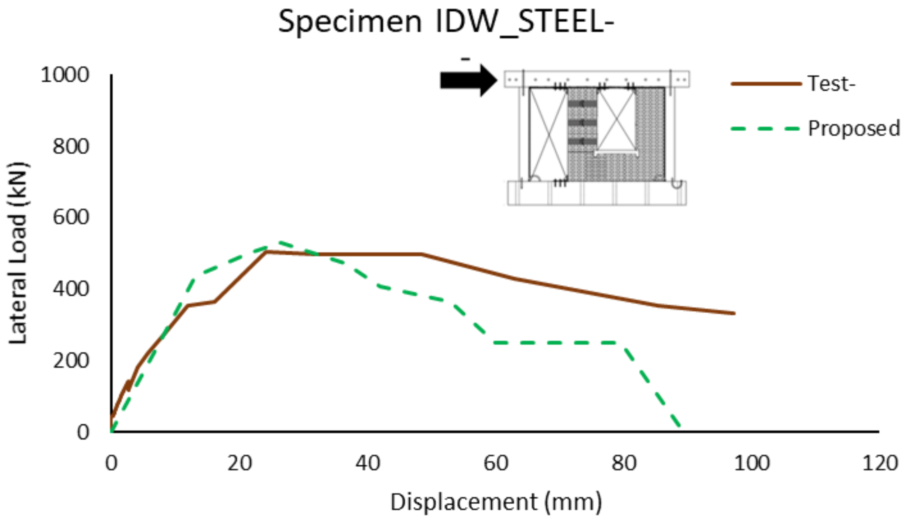

(b) Comparison with test curve

Figure 4-44 Lateral load-deflection curve comparison of Specimen IDW_STEEL under negative loading

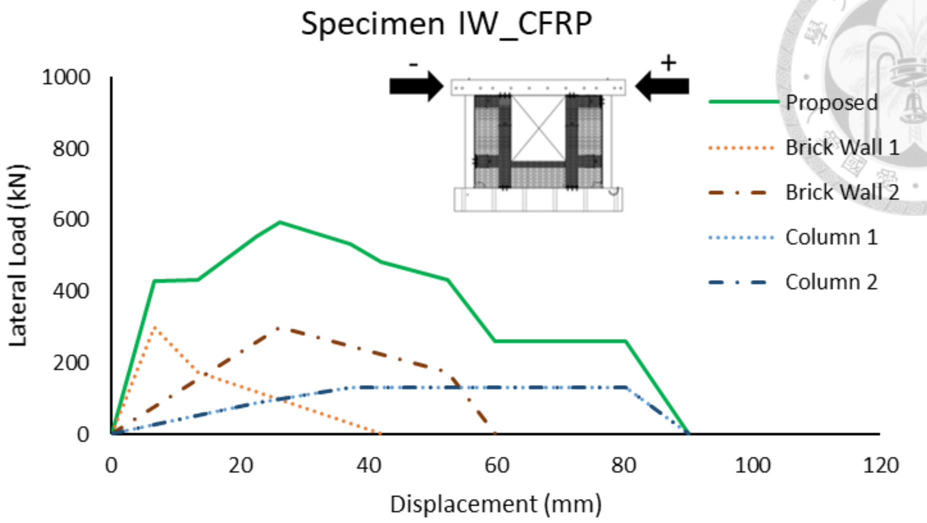

(a) Proposed lateral load-deflection curve

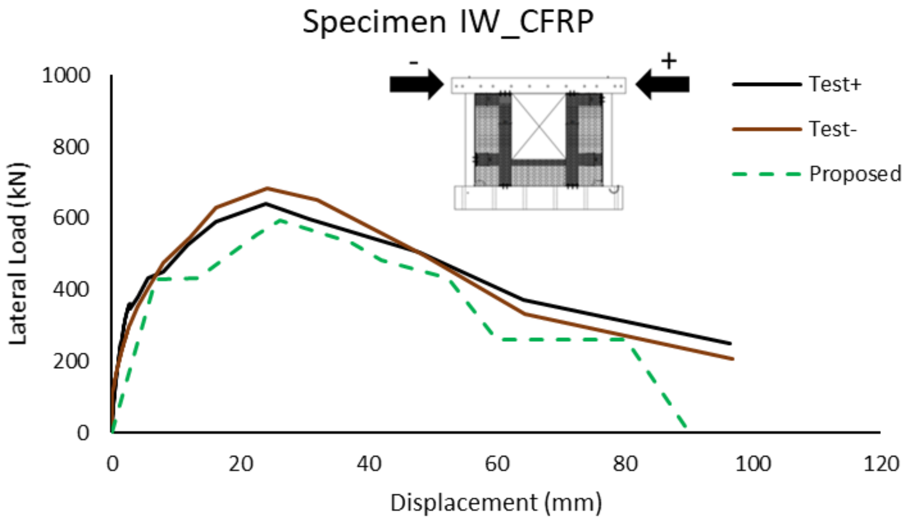

(b) Comparison with test curve

Figure 4-45 Lateral load-deflection curve comparison of Specimen IW_CFRP under positive and negative loading

doi:10.6342/NTU202502280

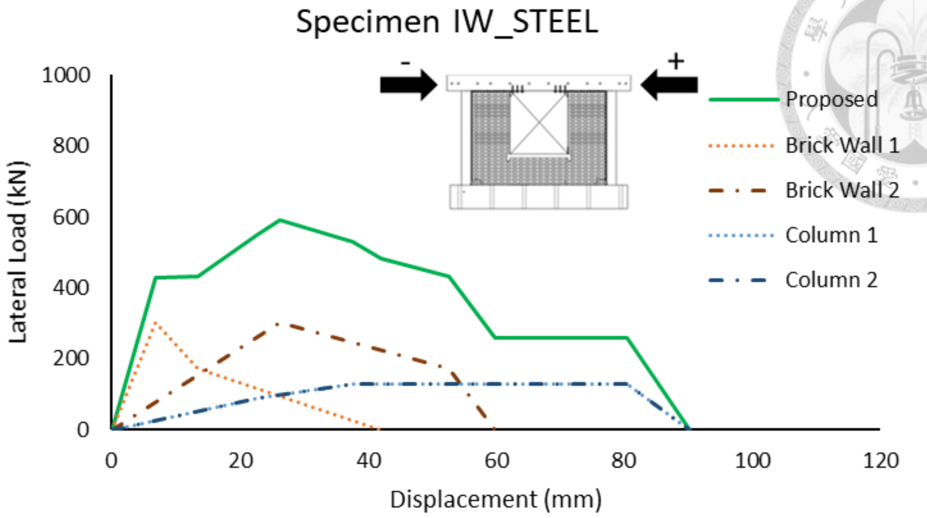

(a) Proposed lateral load-deflection curve

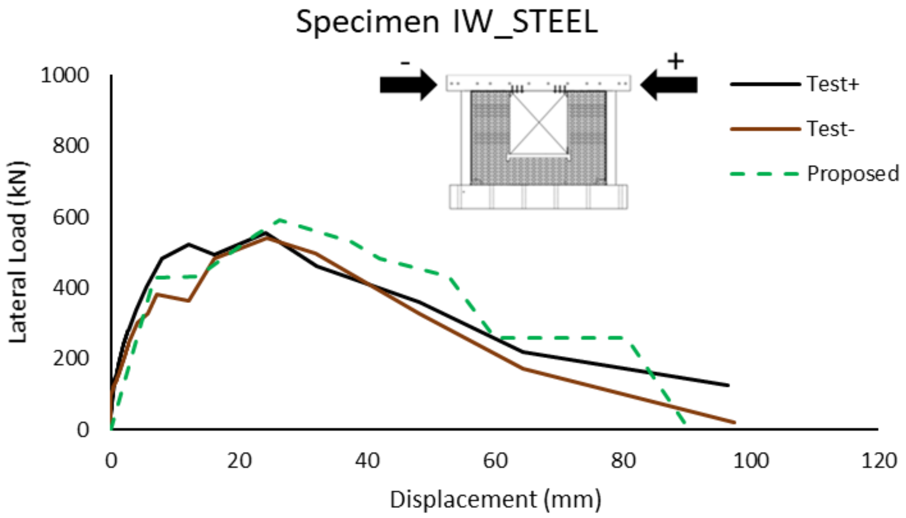

(b) Comparison with test curve

Figure 4-46 Lateral load-deflection curve comparison of Specimen IW_STEEL under positive and negative loading

doi:10.6342/NTU202502280

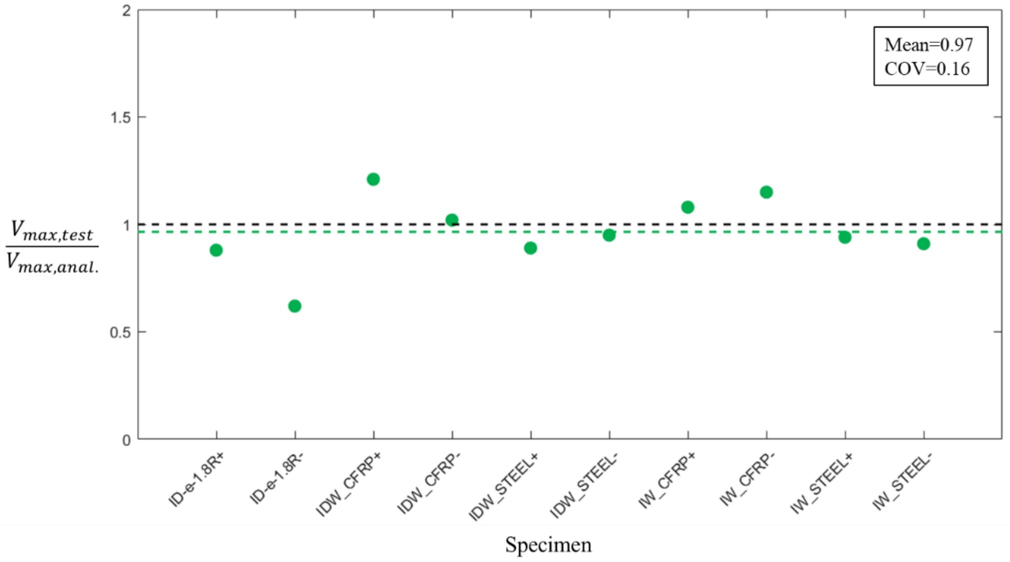

(a) Peak strength comparison

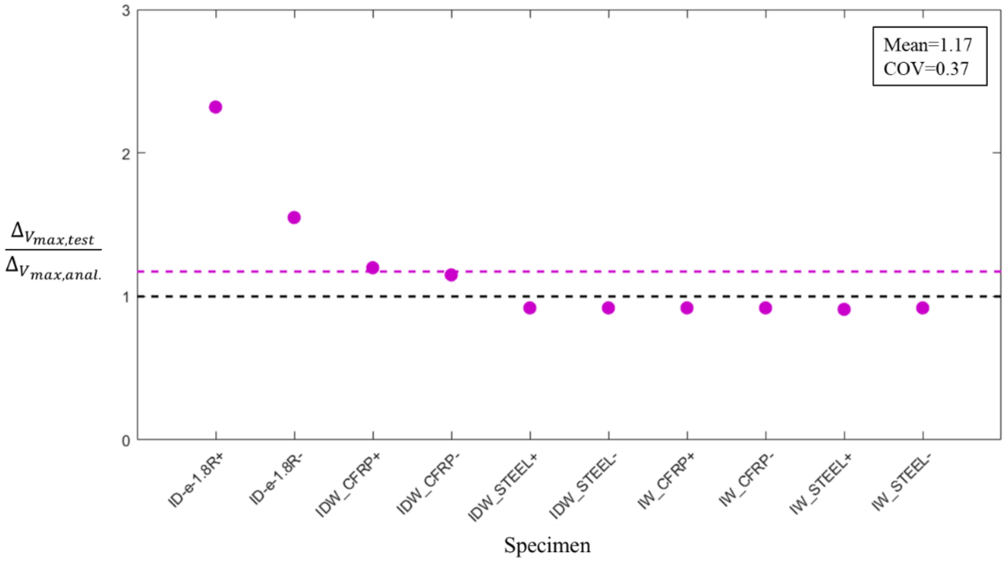

(b) Displacement at peak strength comparison

Figure 4-47 Statistical comparison between test and analytical values of retrofitted brick infill walls with openings specimens

doi:10.6342/NTU202502280

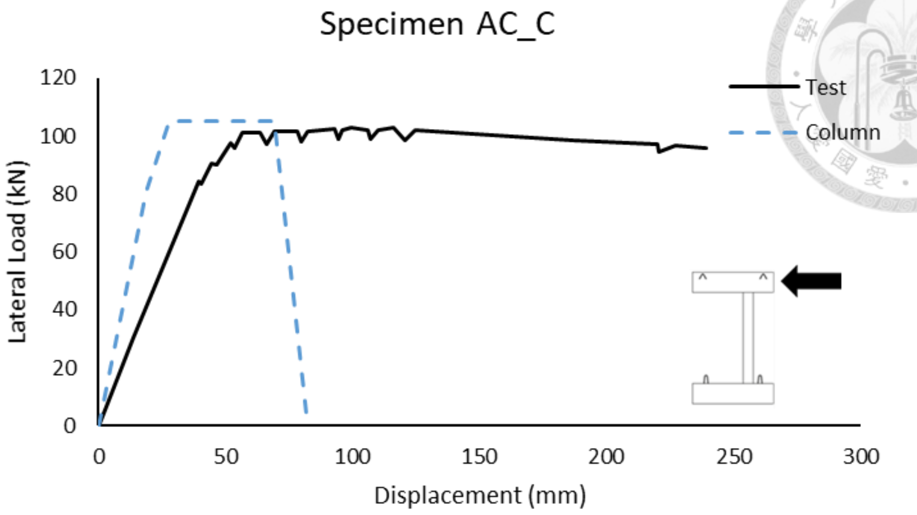

Figure 4-48 Lateral load-deflection curve comparison of Specimen AC_C

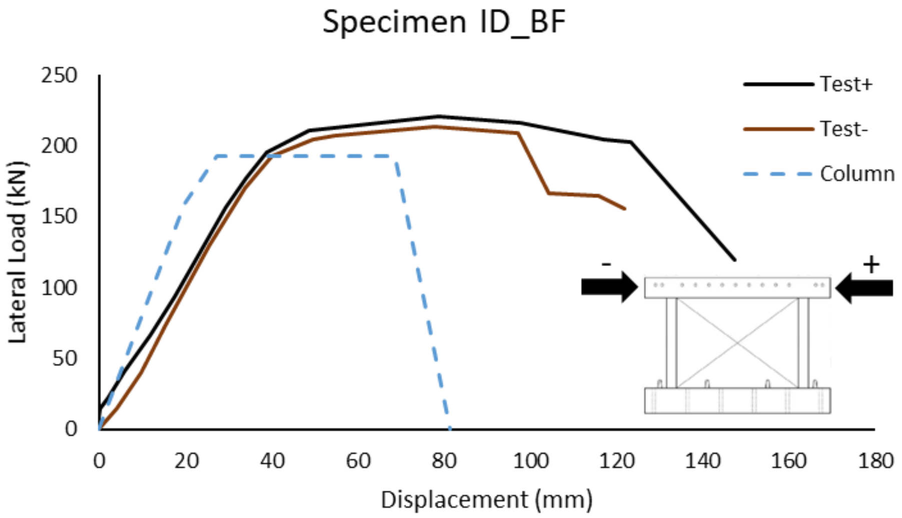

Figure 4-49 Lateral load-deflection curve comparison of Specimen ID_BF under positive and negative loading

doi:10.6342/NTU202502280

APPENDIX A CALCULATION DATA

Table A-1 Brick infill calculation data

Specimen	f'_m (MPa)	N_b (kN)	K_b $\left(\mathrm{kN}/\mathrm{mm}\right)$	V_b (kN)	Δ_b (mm)	V_r (kN)	Δ_u (mm)
Four-sided confined brick infill							
B39-L	12.63*	0	132.87	302.78	2.28	181.67	52.8
B83-L	12.63*	0	88.43	351.75	3.98	92.41	52.8
B39-T	14.96*	0	155.35	470.80	3.03	282.48	52.8
B83-T	14.96*	0	102.64	397.82	3.88	126.71	52.8
CS	15.50	181.91	109.30	754.26	6.90	452.56	60
IS	21.32	212.95	145.63	591.21	4.06	354.72	60
P1	11.20	0	129.38	449.47	3.47	269.68	35.2
P2	13.60	0	154.44	508.80	3.29	305.28	35.2
Three-sided confined brick infill							
A	16.54**	86.10	18.38	197.67	10.76	115.69	54
B	16.54**	68.28	18.41	188.96	10.27	102.62	54
C	18.26**	69.68	5.03	155.03	30.84	93.02	54
AC+	18.26**	62.60	20.16	151.61	7.52	90.97	54
AC-	18.26**	62.60	5.04	151.61	30.09	90.97	54
AL	18.26**	80.60	32.74	200.76	6.13	120.46	54
BC	18.26**	55.41	20.11	148.13	7.37	87.89	54
BS	18.26**	41.89	9.84	101.15	10.28	60.69	54
Brick infill walls with openings							
CD_1	11.58	78.44	21.29	181.97	8.55	109.18	54
CD_2	11.58	78.44	5.32	181.97	34.19	109.18	54
CW_1	11.58	78.96	43.84	182.23	4.16	109.34	36
CW_2	11.58	78.96	5.32	182.23	34.27	109.34	54
ID_1	17.97	104.00	31.56	177.95	5.64	106.77	54
ID_2	17.97	104.00	7.89	177.95	22.56	106.77	54
IW_1	21.32	114.23	76.70	177.80	2.32	106.68	36
IW_2	21.32	114.23	9.30	177.80	19.11	106.68	54
CD-e+	15.50	155.90	87.38	428.46	4.90	257.07	60
CD-e-	15.50	155.90	21.85	428.46	19.61	257.07	60
ID-e+	21.32	186.47	116.42	362.05	3.11	217.23	60
ID-e-	21.32	186.47	29.11	362.05	12.44	217.23	60
CD-e-1.8+	11.42	127.99	47.44	414.46	8.74	248.67	60
CD-e-1.8-	11.42	127.99	11.86	414.46	34.95	248.67	60
CW-e-1.8+	11.42	126.15	76.67	330.07	4.31	198.04	42
CW-e-1.8-	11.42	126.15	11.88	413.52	34.79	248.11	60
ID-e-1.8+	17.87	170.12	70.91	496.91	7.01	298.15	60
ID-e-1.8-	17.87	170.12	17.73	496.91	28.03	298.15	60
IW-e-1.8+	17.87	170.12	114.35	385.48	3.37	231.29	42
IW-e-1.8-	17.87	170.12	17.73	496.91	28.03	298.15	60
IDW+	15.09	32.14	33.48	141.83	4.24	85.10	42

doi:10.6342/NTU202502280

IDW-	15.09	32.14	4.17	141.83	33.98	85.10	60
ID-e-0.5B+	20.43	0.00	46.37	141.82	3.06	70.45	52
ID-e-0.5B-	20.43	0.00	11.59	141.82	12.23	70.45	52
Retrofitted brick infill walls with openings							
ID-e-1.8R	17.87	170.17	35.63	745.26	20.92	306.66	60
IDW_CFRP+_1	15.09	31.84	33.52	222.73	6.64	116.59	42
IDW_CFRP+_2	15.09	31.84	8.36	222.73	26.64	116.59	60
IDW_CFRP-_1	15.09	31.84	16.76	222.73	13.29	116.59	42
IDW_CFRP-_2	15.09	31.84	8.36	222.73	26.64	116.59	60
IDW_STEEL+_1	15.09	31.19	33.62	222.21	6.61	116.08	42
IDW_STEEL+_2	15.09	31.19	8.38	222.21	26.50	116.08	60
IDW_STEEL-_1	15.09	31.19	16.81	222.21	13.22	116.08	42
IDW_STEEL-_2	15.09	31.19	8.38	222.21	26.50	116.08	60
IW_CFRP_1	15.09	79.70	44.37	299.90	6.76	172.54	42
IW_CFRP_2	15.09	79.70	11.42	299.90	26.26	172.54	60
IW_STEEL_1	15.09	80.52	44.30	300.54	6.78	173.18	42
IW_STEEL_2	15.09	80.52	11.40	300.54	26.35	173.18	60

* the value is calculated referring to TMS 402-11 (2011) due to limited information, the calculation is performed in Appendix B.1

** the value is obtained using height-to-thickness correction factors specified in ASTM C1314 (2000), as performed in Appendix B.2

Table A-2 Column calculation data

Specimen	N_c (kN)	M_n (kN − mm)	V_{cr} (kN)	Δ_{cr} (mm)	V_{mn} (kN)	Δ_{mn} (mm)	Δ_s (mm)	Δ_a (mm)
Four-sided confined brick infill								
B39-L	0	144132	80.24	9.55	109.19	18.00	60.54	75.73
B83-L_1	0	148248	84.25	9.15	112.31	17.11	59.65	74.84
B83-L_2	0	110397	69.79	11.06	83.63	17.64	67.35	92.58
B39-T	0	146160	81.89	9.38	110.73	17.66	60.19	75.39
B83-T_1	0	146882	82.69	9.30	111.27	17.47	60.00	75.20
B83-T_2	0	109566	68.72	11.27	83.00	18.04	67.74	92.98
CS	104.20	203024	89.29	21.97	135.35	37.50	80.50	90.29
IS	88.68	190480	88.45	21.77	126.99	35.23	78.22	88.02
P1	0	136266	78.33	4.21	154.85*	12.36*	-*	47.15
P2	0	137031	79.42	4.17	155.72*	12.30*	-*	47.08
Three-sided confined brick infill								
A	240.40	132642	78.04	18.66	98.25	26.97	68.46	81.20
B	193.83	129058	76.54	18.00	95.60	25.93	67.43	80.17
C	259.52	141412	86.10	20.32	104.75	28.06	69.56	82.30
AC	238.80	142163	86.16	19.85	105.31	27.63	69.13	81.86
AL	244.50	147394	88.97	19.34	109.18	27.11	68.60	81.34
BC	206.38	138265	83.66	19.74	102.42	27.54	69.04	81.77
BS	244.12	144008	87.19	19.73	106.67	27.50	69.00	81.74

Brick infill walls with openings								
CD	156.88	124730	76.71	18.69	92.39	25.83	67.33	80.07
CW	156.40	124276	76.31	18.77	92.06	25.97	67.47	80.21
ID	131.46	121532	74.69	18.55	90.02	25.69	67.19	79.92
IW	122.86	121481	75.01	18.27	89.99	25.23	66.73	79.47
CD-e	117.20	194491	89.99	22.14	129.66	35.90	78.89	88.69
ID-e	101.92	193269	89.17	21.94	128.85	35.71	78.70	88.50
CD-e-1.8	131.76	120494	78.16	25.42	80.33	28.96	71.96	81.75
CW-e-1.8	132.61	122947	79.06	25.18	81.96	28.96	71.96	81.75
ID-e-1.8	110.73	118568	76.66	25.20	79.05	28.83	71.82	81.62
IW-e-1.8	110.73	118568	76.66	25.20	79.05	28.83	71.82	81.62
IDW	71.92	136066	80.95	22.00	90.71	27.76	70.75	80.55
ID-e-0.5B_1	0	316685	134.30	14.25	243.60*	28.37*	-*	71.67
ID-e-0.5B_2	0	126013	86.72	23.00	96.93	28.76	92.70	138.53
Retrofitted brick infill walls with openings								
ID-e-1.8R	110.30	168710	76.64	25.19	112.47	41.02	84.02	93.81
IDW_CFRP	72.22	184402	81.62	21.89	122.93	37.13	80.13	89.92
IDW_STEEL	72.87	186668	83.11	21.63	124.45	36.54	79.53	89.33
IW_CFRP	157.39	194391	88.32	22.66	129.59	37.31	80.31	90.10
IW_STEEL	156.58	193114	87.50	22.80	128.74	37.62	80.61	90.41
Column								
AC_C	125.60	142163	80.67	18.59	105.31	27.86	69.36	82.10
ID_BF	235.38	129837	79.65	19.79	96.18	27.22	68.71	81.45

* shear failure mode

APPENDIX B CALCULATION EXAMPLES

B.1. Four-sided Confined Brick Infill – Specimen B39-L

B.1.1. Brick Infill

(1) Axial Load

Due to the limited information on the value of brick prism compressive strength f'_m, the following table from TMS 602-11 (2011) is used to obtain f'_m based on mortar type and solid clay brick compressive strength f_{bc},

Table B-1 Brick prism compressive strength based on mortar type and solid clay brick compressive strength (TMS 602-11, 2011)

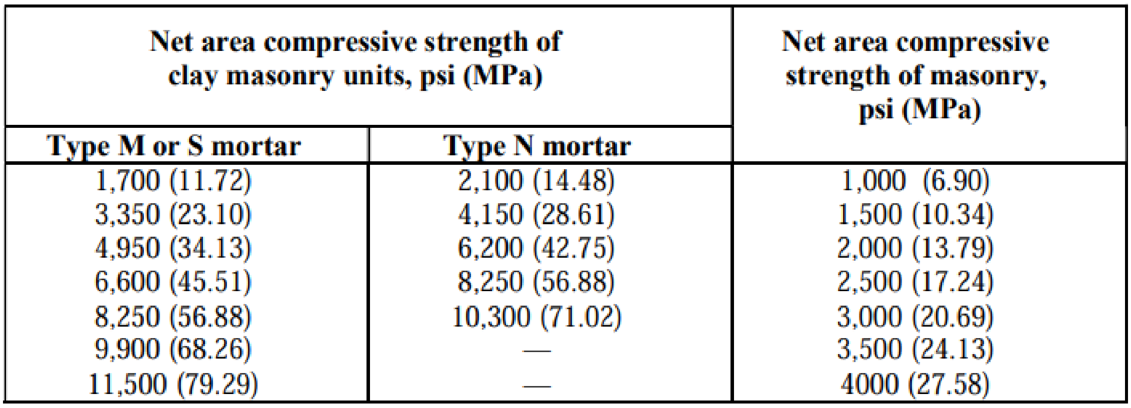

Net area compressive strength of clay masonry units, psi (MPa)		Net area compressive strength of masonry, psi (MPa)
Type M or S mortar	Type N mortar	
1,700 (11.72)	2,100 (14.48)	1,000 (6.90)
3,350 (23.10)	4,150 (28.61)	1,500 (10.34)
4,950 (34.13)	6,200 (42.75)	2,000 (13.79)
6,600 (45.51)	8,250 (56.88)	2,500 (17.24)
8,250 (56.88)	10,300 (71.02)	3,000 (20.69)
9,900 (68.26)	—	3,500 (24.13)
11,500 (79.29)	—	4000 (27.58)

$f_{mc} = 7$ MPa (Type N mortar)

$f_{bc} = 38$ MPa

Through Interpolation, we can obtain

$$f'_m = \frac{13.79 - 10.34}{42.75 - 28.61} \times (38 - 28.61) + 10.34 = 12.63 \text{ MPa}$$

$$E_b = 550 f'_m = 550 \times 12.63 = 6947 \text{ MPa}$$

doi:10.6342/NTU202502280

$$N_b = \frac{E_b A_b}{E_b A_b + 2E_c A_c} \times N_{total}$$

$$= \frac{6947 \times 1360000}{6947 \times 1360000 + 2 \times 23500 \times 140000} \times 0$$

$$= 0$$

(2) Failure Mode Strength

$$\tau_f = 0.0258(f_{mc})^{0.885} + (0.654 + 0.00514 f_{mc}) \frac{N_b}{\ell_b t_b}$$

$$= 0.0258(7)^{0.885} + (0.654 + 0.00514 \times 7) \times \frac{0}{6800 \times 200}$$

$$= 0.14 \text{ MPa}$$

$$f_{mt} = 0.232(f_{mc})^{0.338}$$

$$= 0.232(7)^{0.338}$$

$$= 0.45 \text{ MPa}$$

$$f_{bt} = 0.136 f_{bc}$$

$$= 0.136 \times 38$$

$$= 5.17 \text{ MPa}$$

(3) Stiffness K_b

$$\theta = \tan^{-1}\left(\frac{h_b}{\ell_b}\right) = \tan^{-1}\left(\frac{2640}{6800}\right) = 21.22°$$

$\beta = 1$ (four-sided confined brick infill)

$$K_b = 0.2\left(\frac{E_c I_c}{h_c^4 \sin 2\theta} h_b (E_b t_b)^9\right)^{0.1} \cos^2\theta \times \beta$$

$$= 0.2\left(\frac{23500 \times 1866666667}{(2640)^4 \sin(2 \times 21.22)} \times 2640 \times (6947 \times 200)^9\right)^{0.1} \cos^2(21.22) \times 1$$

$$= 132869 \text{ N/mm} = 132.87 \text{ kN/mm}$$

(4) Peak Strength $\boldsymbol{V_b}$

$$V_b = \tau_f(\ell_b \times t_b) + 0.45 f_{mt}(h_b \times t_b)$$

$$= 0.14(6800 \times 200) + 0.45 \times 0.45(2640 \times 200)$$

$$= 302777 \text{ N} = 302.78 \text{ kN}$$

(5) Peak Displacement $\boldsymbol{\Delta_b}$

$$\Delta_b = \frac{V_b}{K_b} = \frac{302.78}{132.87} = 2.28 \text{ mm}$$

(6) Residual Strength $\boldsymbol{V_r}$

$$V_r = \tau_f(\ell_b \times t_b) \leq 0.6 V_b$$

$$= 0.14(6800 \times 200)$$

$$= 196368 \text{ N} > 0.6 \times 302777 = 181666 \text{ N}$$

$$V_r = 181666 \text{ N} = 181.67 \text{ kN}$$

(7) Ultimate Displacement $\boldsymbol{\Delta_u}$

$$\Delta_u = 0.02 h_b = 0.02 \times 2640 = 52.8 \text{ mm}$$

B.1.2. Column

(1) Axial Load

$$N_c = \frac{E_c A_c}{E_b A_b + 2 E_c A_c} \times N_{total}$$

$$= \frac{23500 \times 140000}{6947 \times 1360000 + 2 \times 23500 \times 140000} \times 0$$

$$= 0$$

doi:10.6342/NTU202502280

(2) Cracking Point $(\boldsymbol{V_{cr}}, \boldsymbol{\Delta_{cr}})$

$$\theta = 65°$$

$$V_{n,c} = K\zeta f_c' A_{str} \cos\theta$$

$$= 1.14 \times 0.52 \times 25 \times 35000 \times \cos(65)$$

$$= 219052 \text{ N}$$

$$V_{n,t} = \frac{A_v f_y d}{s} + \left(\frac{0.5\sqrt{f_c'}}{M/_{Vd}} \sqrt{1 + \frac{N}{0.5\sqrt{f_c'} A_g}} \right) 0.8 A_g$$

$$= \frac{142.66 \times 349 \times 320}{250} + \left(\frac{0.5\sqrt{25}}{4} \sqrt{1 + \frac{0}{0.5\sqrt{25} \times 140000}} \right) 0.8 \times 140000$$

$$= 133729 \text{ N}$$

$$V_n = \min\left(V_{n,c}, V_{n,t}\right)$$

$$= \min(219052, 133729)$$

$$= 133729 \text{ N} = 133.73 \text{ kN}$$

$$V_{cr} = 0.6 V_n$$

$$= 0.6 \times 133.73$$

$$= 80237 \text{ N} = 80.24 \text{ kN}$$

$$\Delta_{cr} = \Delta_{f,cr} + \Delta_{s,cr}$$

$$= \frac{V_{cr} H^3}{12\left(E_c I_{eff}\right)} + \frac{V_{cr} H}{0.4 E_c b d}$$

$$= \frac{80237 \times 2640^3}{12(1.316 \times 10^{13})} + \frac{80237 \times 2640}{0.4 \times 23500 \times 350 \times 320}$$

$$= 9.55 \text{ mm}$$

(3) Strength Point $(\boldsymbol{V_{mn}}, \boldsymbol{\Delta_{mn}})$

$$M_n = 144132438\ \text{N} - \text{mm} = 144132\ \text{kN} - \text{mm}$$

$$V_{mn} = \frac{2M_n}{H}$$

$$= \frac{2 \times 144132438}{2640}$$

$$= 109191\ \text{N} = 109.19\ \text{kN}$$

$$\Delta_{mn} = \Delta_{f,n} + \Delta_{s,n}$$

$$= \frac{V_{mn}H^3}{12\left(E_c I_{eff}\right)} + \frac{V_{mn}L_B}{0.4E_c bd} + 2 \times 0.006 \sin 2\theta \times L_D \times \frac{V_{mn}}{V_n}$$

$$= \frac{109191 \times 2640^3}{12(1.316 \times 10^{13})} + \frac{109191 \times 1267.52}{0.4 \times 23500 \times 350 \times 320} + 2 \times 0.006 \sin(2 \times 65) \times 686.24 \times \frac{109191}{133729}$$

$$= 18\ \text{mm}$$

(4) Post-strength Point $(\boldsymbol{V_{mn}}, \boldsymbol{\Delta_s})$

$$\Delta_s = \Delta_{mn} + a \times H$$

$$= 18 + 0.016 \times 2640$$

$$= 60.54\ \text{mm}$$

(5) Collapse Point $(\boldsymbol{0}, \boldsymbol{\Delta_a})$

$$\Delta_a = \Delta_{mn} + b \times H$$

$$= 18 + 0.022 \times 2640$$

$$= 75.73\ \text{mm}$$

B.1.3. Curves Superposition

The superposed curve for Specimen B39-L is shown in Figure 4-3(a).

B.2. Three-sided Confined Brick Infill – Specimen C

B.2.1. Brick Infill

(1) Axial Load

$f'_m = 19.4$ MPa (brick prism size: 203 mmx205 mmx464 mm)

Due to the different brick prism size between the test and the specified 5-stacked brick prism size specified in ASTM C1314 (2000), as shown in Figure 2-2, the following height-to-thickness correction factors for brick prism compressive strength f'_m specified in ASTM C1314 (2000) is used.

Table B-2 Height-to-thickness correction factors for brick prism compressive strength (ASTM C1314, 2000)

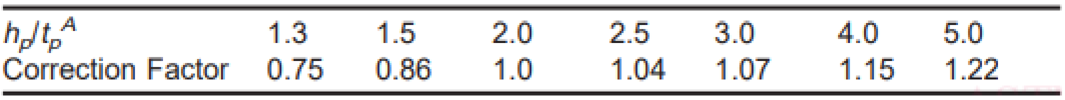

$h_p/t_p{}^A$	1.3	1.5	2.0	2.5	3.0	4.0	5.0
Correction Factor	0.75	0.86	1.0	1.04	1.07	1.15	1.22

For 203 mmx205 mmx464 mm brick prism,

$$\frac{h_p}{t_p} = \frac{464}{203} = 2.29$$

$$\text{Correction Factor 1} = \frac{1.04 - 1}{2.5 - 2} \times (2.29 - 2) + 1 = 1.02$$

For 5-stacked brick prism size,

$$\frac{h_p}{t_p} = \frac{5 \times 53 + 4 \times 10}{95} = 3.21$$

$$\text{Correction Factor 2} = \frac{1.15 - 1.07}{4 - 3} \times (3.21 - 3) + 1.07 = 1.09$$

Corrected brick prism compressive strength f'_m,

$$f'_m = \frac{1.02}{1.09} \times 19.4 = 18.26\ \text{MPa}$$

$$N_b = \frac{E_b A_b}{E_b A_b + E_c A_c} \times N_{total}$$

$$= \frac{10042 \times 180000}{10042 \times 180000 + 26042 \times 120000} \times 329200$$

$$= 69676\ \text{N} = 69.68\ \text{kN}$$

(2) Failure Mode Strength

$$\tau_f = 0.0258(f_{mc})^{0.885} + (0.654 + 0.00514 f_{mc}) \frac{N_b}{\ell_b t_b}$$

$$= 0.0258(13.9)^{0.885} + (0.654 + 0.00514 \times 13.9) \times \frac{69676}{900 \times 200}$$

$$= 0.55\ \text{MPa}$$

$$f_{mt} = 0.232(f_{mc})^{0.338}$$

$$= 0.232(13.9)^{0.338}$$

$$= 0.57\ \text{MPa}$$

$$f_{bt} = 0.136 f_{bc}$$

$$= 0.136 \times 44.5$$

$$= 6.05\ \text{MPa}$$

(3) Stiffness K_b

$$\theta = \tan^{-1}\left(\frac{h_b}{\ell_b}\right) = \tan^{-1}\left(\frac{2700}{900}\right) = 71.57°$$

$\beta = 0.25$ (three-sided confined brick infill when the load strikes the brick wall first)

$$K_b = 0.2\left(\frac{E_c I_c}{h_c^4 \sin 2\theta} h_b (E_b t_b)^9\right)^{0.1} \cos^2\theta \times \beta$$

$$= 0.2\left(\frac{26042 \times 900000000}{(2700)^4 \sin(2 \times 71.57)} \times 2700 \times (10042 \times 200)^9\right)^{0.1} \cos^2(71.57) \times 0.25$$

$$= 5027\ \mathrm{N/mm} = 5.03\ \mathrm{kN/mm}$$

(4) Peak Strength $\boldsymbol{V_b}$

$$V_b = \tau_f\left(\frac{2}{3}\ell_b \times t_b\right) + 0.225 f_{mt}\left(\frac{2}{3}\ell_b \tan\theta_c \times t_b\right) + 0.225\left(\frac{f_{mt}+f_{bt}}{2}\right)\left(h_b' - \frac{2}{3}\ell_b \tan\theta_c\right) \times t_b$$

$$= 0.55 \times \left(\frac{2}{3} \times 900 \times 200\right) + 0.225 \times 0.57 \times \left(\frac{2}{3} \times 900 \times 0.6 \times 200\right) + 0.225\left(\frac{0.57+6.05}{2}\right)\left(900 - \frac{2}{3} \times 900 \times 0.6\right) \times 200$$

$$= 155035\ \mathrm{N} = 155.03\ \mathrm{kN}$$

(5) Peak Displacement $\boldsymbol{\Delta_b}$

$$\Delta_b = \frac{V_b}{K_b} = \frac{155.03}{5.03} = 30.84\ \mathrm{mm}$$

(6) Residual Strength $\boldsymbol{V_r}$

$$V_r = \tau_f(\ell_b \times t_b) \le 0.6 V_b$$

$$= 0.55(900 \times 200)$$

$$= 98240\ \mathrm{N} > 0.6 \times 155035 = 93021\ \mathrm{N}$$

$$V_r = 93021\ \mathrm{N} = 93.02\ \mathrm{kN}$$

(7) Ultimate Displacement $\boldsymbol{\Delta_u}$

$$\Delta_u = 0.02 h_b = 0.02 \times 2700 = 54\ \mathrm{mm}$$

B.2.2. Column

(1) Axial Load

$$N_c = \frac{E_c A_c}{E_b A_b + E_c A_c} \times N_{total}$$

$$= \frac{26042 \times 120000}{10042 \times 180000 + 26042 \times 120000} \times 329200$$

$$= 259524 \text{ N} = 259.52 \text{ kN}$$

(2) Cracking Point $(\boldsymbol{V_{cr}}, \Delta_{cr})$

$$\theta = 65°$$

$$V_{n,c} = K\zeta f_c' A_{str} \cos\theta$$

$$= 1.11 \times 0.52 \times 30.7 \times 37186 \times \cos(65)$$

$$= 277747 \text{ N}$$

$$V_{n,t} = \frac{A_v f_y d}{s} + \left(\frac{0.5\sqrt{f_c'}}{M/_{Vd}}\sqrt{1 + \frac{N}{0.5\sqrt{f_c'}A_g}}\right)0.8A_g$$

$$= \frac{142.66 \times 400 \times 240}{250} + \left(\frac{0.5\sqrt{30.7}}{4}\sqrt{1 + \frac{259524}{0.5\sqrt{30.7} \times 120000}}\right)0.8 \times 120000$$

$$= 143505 \text{ N}$$

$$V_n = \min\left(V_{n,c}, V_{n,t}\right)$$

$$= \min(277747, 143505)$$

$$= 143505 \text{ N} = 143.51 \text{ kN}$$

$$V_{cr} = 0.6V_n$$

$$= 0.6 \times 143505$$

$$= 86103 \text{ N} = 86.10 \text{ kN}$$

$$\Delta_{cr} = \Delta_{f,cr} + \Delta_{s,cr}$$

$$= \frac{V_{cr}H^3}{12\left(E_c I_{eff}\right)} + \frac{V_{cr}H}{0.4E_c bd}$$

doi:10.6342/NTU202502280

$$= \frac{86103 \times 2700^3}{12(7.03 \times 10^{12})} + \frac{86103 \times 2700}{0.4 \times 26042 \times 400 \times 240}$$

$$= 20.32 \text{ mm}$$

(3) Strength Point $(\boldsymbol{V_{mn}}, \boldsymbol{\Delta_{mn}})$

$$M_n = 141412450 \text{ N} - \text{mm} = 141412 \text{ kN} - \text{mm}$$

$$V_{mn} = \frac{2M_n}{H}$$

$$= \frac{2 \times 141412450}{2700}$$

$$= 104750 \text{ N} = 104.75 \text{ kN}$$

$$\Delta_{mn} = \Delta_{f,n} + \Delta_{s,n}$$

$$= \frac{V_{mn}H^3}{12\left(E_c I_{eff}\right)} + \frac{V_{mn}L_B}{0.4E_c bd} + 2 \times 0.006 \sin 2\theta \times L_D \times \frac{V_{mn}}{V_n}$$

$$= \frac{104750 \times 2700^3}{12(7.03 \times 10^{12})} + \frac{104750 \times 1670.64}{0.4 \times 26042 \times 400 \times 240} + 2 \times 0.006 \sin(2 \times 65) \times 514.68 \times \frac{104750}{143505}$$

$$= 28.06 \text{ mm}$$

(4) Post-strength Point $(\boldsymbol{V_{mn}}, \Delta_s)$

$$\Delta_s = \Delta_{mn} + a \times H$$

$$= 28.06 + 0.015 \times 2700$$

$$= 69.56 \text{ mm}$$

(5) Collapse Point $(\mathbf{0}, \boldsymbol{\Delta_a})$

$$\Delta_a = \Delta_{mn} + b \times H$$

$$= 28.06 + 0.02 \times 2700$$

$$= 82.30 \text{ mm}$$

B.2.3. Curves Superposition

The superposed curve for Specimen C is shown in Figure 4-12(a).

doi:10.6342/NTU202502280

B.3. Brick Infill Walls with Openings – Specimen IDW+

B.3.1. Brick Infill

(1) Axial Load

$$N_b = \frac{E_b A_b}{2E_b A_b + 2E_c A_c} \times N_{total}$$

$$= \frac{8300 \times 200000}{2 \times 8300 \times 200000 + 2 \times 24759 \times 150000} \times 208125$$

$$= 32144 \text{ N} = 32.14 \text{ kN}$$

(2) Failure Mode Strength

$$\tau_f = 0.0258(f_{mc})^{0.885} + (0.654 + 0.00514 f_{mc}) \frac{N_b}{\ell_b t_b}$$

$$= 0.0258(25.78)^{0.885} + (0.654 + 0.00514 \times 25.78) \times \frac{32144}{1000 \times 200}$$

$$= 0.58 \text{ MPa}$$

$$f_{mt} = 0.232(f_{mc})^{0.338}$$

$$= 0.232(25.78)^{0.338}$$

$$= 0.70 \text{ MPa}$$

$$f_{bt} = 0.136 f_{bc}$$

$$= 0.136 \times 22.89$$

$$= 3.11 \text{ MPa}$$

(3) Stiffness K_b

$$\theta = \tan^{-1}\left(\frac{h_b}{\ell_b}\right) = \tan^{-1}\left(\frac{2100}{1000}\right) = 64.54°$$

$\beta = 1$ (three-sided confined brick infill when the load strikes the column first)

$$K_b = 0.2\left(\frac{E_c I_c}{h_c^4 \sin 2\theta} h_b (E_b t_b)^9\right)^{0.1} \cos^2\theta \times \beta$$

$$= 0.2\left(\frac{24759 \times 1.125 \times 10^9}{(2100)^4 \sin(2 \times 64.54)} \times 2100 \times (8300 \times 200)^9\right)^{0.1} \cos^2(64.54) \times 1$$

$$= 33475 \text{ N/mm} = 33.48 \text{ kN/mm}$$

(4) Peak Strength V_b

$$V_b = \tau_f\left(\frac{2}{3}\ell_b \times t_b\right) + 0.225 f_{mt}\left(\frac{2}{3}\ell_b \tan\theta_c \times t_b\right) + 0.225\left(\frac{f_{mt}+f_{bt}}{2}\right)\left(h_b' -\right.$$

$$\left.\frac{2}{3}\ell_b \tan\theta_c\right) \times t_b$$

$$= 0.58 \times \left(\frac{2}{3} \times 1000 \times 200\right) + 0.225 \times 0.70 \times \left(\frac{2}{3} \times 1000 \times 0.6 \times 200\right) +$$

$$0.225\left(\frac{0.70+3.11}{2}\right)\left(1000 - \frac{2}{3} \times 1000 \times 0.6\right) \times 200$$

$$= 141829 \text{ N} = 141.83 \text{ kN}$$

(5) Peak Displacement Δ_b

$$\Delta_b = \frac{V_b}{K_b} = \frac{141.83}{33.48} = 4.24 \text{ mm}$$

(6) Residual Strength V_r

$$V_r = \tau_f(\ell_b \times t_b) \leq 0.6 V_b$$

$$= 0.58(1000 \times 200)$$

$$= 116827 \text{ N} > 0.6 \times 141829 = 85098 \text{ N}$$

$$V_r = 85098 \text{ N} = 85.10 \text{ kN}$$

(7) Ultimate Displacement Δ_u

$$\Delta_u = 0.02 h_b = 0.02 \times 2100 = 42 \text{ mm}$$

B.3.2. Column

(1) Axial Load

$$N_c = \frac{E_c A_c}{2E_b A_b + 2E_c A_c} \times N_{total}$$

$$= \frac{24759 \times 150000}{2 \times 8300 \times 200000 + 2 \times 24759 \times 150000} \times 208125$$

$$= 71918 \text{ N} = 71.92 \text{ kN}$$

(2) Cracking Point $(\boldsymbol{V_{cr}}, \Delta_{cr})$

$$\theta = 65°$$

$$V_{n,c} = K\zeta f_c' A_{str} \cos\theta$$

$$= 1.08 \times 0.52 \times 27.75 \times 39703 \times \cos(65)$$

$$= 261495 \text{ N}$$

$$V_{n,t} = \frac{A_v f_y d}{s} + \left(\frac{0.5\sqrt{f_c'}}{M/_{Vd}} \sqrt{1 + \frac{N}{0.5\sqrt{f_c'} A_g}} \right) 0.8 A_g$$

$$= \frac{142.66 \times 357.9 \times 240}{250} + \left(\frac{0.5\sqrt{27.75}}{4} \sqrt{1 + \frac{71918}{0.5\sqrt{27.75} \times 150000}} \right) 0.8$$

$$\times 150000$$

$$= 134924 \text{ N}$$

$$V_n = \min\left(V_{n,c}, V_{n,t}\right)$$

$$= \min(261495, 134924)$$

$$= 134924 \text{ N} = 134.92 \text{ kN}$$

$$V_{cr} = 0.6 V_n$$

$$= 0.6 \times 134924$$

$$= 80955 \text{ N} = 80.95 \text{ kN}$$

$$\Delta_{cr} = \Delta_{f,cr} + \Delta_{s,cr}$$

$$= \frac{V_{cr}H^3}{12\left(E_c I_{eff}\right)} + \frac{V_{cr}H}{0.4E_c bd}$$

$$= \frac{80955 \times 3000^3}{12(8.36 \times 10^{12})} + \frac{80955 \times 3000}{0.4 \times 24759 \times 500 \times 240}$$

$$= 22.00 \text{ mm}$$

(3) Strength Point (V_{mn}, Δ_{mn})

$$M_n = 136065582 \text{ N} - \text{mm} = 136066 \text{ kN} - \text{mm}$$

$$V_{mn} = \frac{2M_n}{H}$$

$$= \frac{2 \times 136065582}{3000}$$

$$= 90710 \text{ N} = 90.71 \text{ kN}$$

$$\Delta_{mn} = \Delta_{f,n} + \Delta_{s,n}$$

$$= \frac{V_{mn}H^3}{12\left(E_c I_{eff}\right)} + \frac{V_{mn}L_B}{0.4E_c bd} + 2 \times 0.006 \sin 2\theta \times L_D \times \frac{V_{mn}}{V_n}$$

$$= \frac{90710 \times 3000^3}{12(8.36 \times 10^{12})} + \frac{90710 \times 1970.64}{0.4 \times 24759 \times 500 \times 240} + 2 \times 0.006 \sin(2 \times 65) \times 514.68 \times \frac{90710}{134924}$$

$$= 27.76 \text{ mm}$$

(4) Post-strength Point (V_{mn}, Δ_s)

$$\Delta_s = \Delta_{mn} + a \times H$$

$$= 27.76 + 0.014 \times 3000$$

$$= 70.75 \text{ mm}$$

doi:10.6342/NTU202502280

(5) Collapse Point $(\mathbf{0}, \Delta_{\boldsymbol{a}})$

$$\Delta_a = \Delta_{mn} + b \times H$$

$$= 27.76 + 0.018 \times 3000$$

$$= 80.55 \text{ mm}$$

B.3.3. Curves Superposition

The superposed curve for Specimen IDW+ is shown in Figure 4-35(a).

doi:10.6342/NTU202502280

B.4. Retrofitted Brick Infill Walls with Openings – Specimen IDW_CFRP+

B.4.1. Brick Infill 1 – Retrofitted Three-sided Confined Brick Infill

(1) Axial Load

$$N_b = \frac{E_{b1}A_{b1}}{E_{b1}A_{b1} + E_{b2}A_{b2} + 2E_cA_c} \times N_{total}$$

$$= \frac{8300 \times 200000}{8300 \times 200000 + 8300 \times 200000 + 2 \times 25096 \times 150000} \times 208125$$

$$= 31845\ \mathrm{N} = 31.84\ \mathrm{kN}$$

(2) Failure Mode Strength

$$\tau_f = 0.0258(f_{mc})^{0.885} + (0.654 + 0.00514 f_{mc}) \frac{N_b}{\ell_b t_b}$$

$$= 0.0258(25.78)^{0.885} + (0.654 + 0.00514 \times 25.78) \times \frac{31845}{1000 \times 200}$$

$$= 0.58\ \mathrm{MPa}$$

$$f_{mt} = 0.232(f_{mc})^{0.338}$$

$$= 0.232(25.78)^{0.338}$$

$$= 0.70\ \mathrm{MPa}$$

$$f_{bt} = 0.136 f_{bc}$$

$$= 0.136 \times 22.89$$

$$= 3.11\ \mathrm{MPa}$$

(3) Stiffness K_b

$$\theta = \tan^{-1}\left(\frac{h_b}{\ell_b}\right) = \tan^{-1}\left(\frac{2100}{1000}\right) = 64.54°$$

$\beta = 1$ (retrofitted three-sided confined brick infill when the load strikes the column first)

doi:10.6342/NTU202502280

$$K_b = 0.2\left(\frac{E_c I_c}{h_c^4 \sin 2\theta} h_b (E_b t_b)^9\right)^{0.1} \cos^2\theta \times \beta$$

$$= 0.2\left(\frac{25096 \times 1.125 \times 10^9}{(2100)^4 \sin(2 \times 64.54)} \times 2100 \times (8300 \times 200)^9\right)^{0.1} \cos^2(64.54) \times 1$$

$$= 33521\ \mathrm{N/mm} = 33.52\ \mathrm{kN/mm}$$

(4) Peak Strength V_b

$$V_b = \tau_f(\ell_b \times t_b) + 0.45 f_{mt}(l_b \tan\theta_c \times t_b) + 0.45\left(\frac{f_{mt} + f_{bt}}{2}\right)(h_b' - \ell_b \tan\theta_c) \times t_b$$

$$= 0.58 \times (1000 \times 200) + 0.45 \times 0.70 \times (1000 \times 0.6 \times 200) +$$

$$0.45\left(\frac{0.70+3.11}{2}\right)(1000 - 1000 \times 0.6) \times 200$$

$$= 222726\ \mathrm{N} = 222.73\ \mathrm{kN}$$

(5) Peak Displacement Δ_b

$$\Delta_b = \frac{V_b}{K_b} = \frac{222.73}{33.52} = 6.64\ \mathrm{mm}$$

(6) Residual Strength V_r

$$V_r = \tau_f(\ell_b \times t_b) \le 0.6 V_b$$

$$= 0.58(1000 \times 200)$$

$$= 116591\ \mathrm{N} > 0.6 \times 222726 = 133635\ \mathrm{N}$$

$$V_r = 116591\ \mathrm{N} = 116.59\ \mathrm{kN}$$

(7) Ultimate Displacement Δ_u

$$\Delta_u = 0.02 h_b = 0.02 \times 2100 = 42\ \mathrm{mm}$$

B.4.2. Brick Infill 2 – Retrofitted Two-sided Confined Brick Infill

(1) Axial Load

$$N_b = \frac{E_{b2}A_{b2}}{E_{b1}A_{b1} + E_{b2}A_{b2} + 2E_cA_c} \times N_{total}$$

$$= \frac{8300 \times 200000}{8300 \times 200000 + 8300 \times 200000 + 2 \times 25096 \times 150000} \times 208125$$

$$= 31845\ \mathrm{N} = 31.84\ \mathrm{kN}$$

(2) Failure Mode Strength

$$\tau_f = 0.0258(f_{mc})^{0.885} + (0.654 + 0.00514 f_{mc}) \frac{N_b}{\ell_b t_b}$$

$$= 0.0258(25.78)^{0.885} + (0.654 + 0.00514 \times 25.78) \times \frac{31845}{1000 \times 200}$$

$$= 0.58\ \mathrm{MPa}$$

$$f_{mt} = 0.232(f_{mc})^{0.338}$$

$$= 0.232(25.78)^{0.338}$$

$$= 0.70\ \mathrm{MPa}$$

$$f_{bt} = 0.136 f_{bc}$$

$$= 0.136 \times 22.89$$

$$= 3.11\ \mathrm{MPa}$$

(3) Stiffness K_b

$$\theta = \tan^{-1}\left(\frac{h_b}{\ell_b}\right) = \tan^{-1}\left(\frac{3000}{1000}\right) = 71.57°$$

$$K_b = 0.1\left(\frac{1}{\sin 2\theta}(E_b t_b)^{10}\right)^{0.1} \cos^2\theta$$

$$= 0.1\left(\frac{1}{\sin(2 \times 71.57)} \times (8300 \times 200)^{10}\right)^{0.1} \cos^2(71.57)$$

doi:10.6342/NTU202502280

$$= 8360\ \mathrm{N/mm} = 8.36\ \mathrm{kN/mm}$$

(4) Peak Strength $\boldsymbol{V_b}$

$$V_b = \tau_f(\ell_b \times t_b) + 0.45 f_{mt}(l_b \tan\theta_c \times t_b) + 0.45\left(\frac{f_{mt} + f_{bt}}{2}\right)(h'_b - \ell_b \tan\theta_c) \times t_b$$

$$= 0.58 \times (1000 \times 200) + 0.45 \times 0.70 \times (1000 \times 0.6 \times 200) +$$

$$0.45\left(\frac{0.70+3.11}{2}\right)(1000 - 1000 \times 0.6) \times 200$$

$$= 222726\ \mathrm{N} = 222.73\ \mathrm{kN}$$

(5) Peak Displacement $\boldsymbol{\Delta_b}$

$$\Delta_b = \frac{V_b}{K_b} = \frac{222.73}{8.36} = 26.64\ \mathrm{mm}$$

(6) Residual Strength $\boldsymbol{V_r}$

$$V_r = \tau_f(\ell_b \times t_b) \leq 0.6 V_b$$

$$= 0.58(1000 \times 200)$$

$$= 116591\ \mathrm{N} > 0.6 \times 222726 = 133635\ \mathrm{N}$$

$$V_r = 116591\ \mathrm{N} = 116.59\ \mathrm{kN}$$

(7) Ultimate Displacement $\boldsymbol{\Delta_u}$

$$\Delta_u = 0.02 h_b = 0.02 \times 3000 = 60\ \mathrm{mm}$$

B.4.3. Column

(1) Axial Load

$$N_c = \frac{E_c A_c}{E_{b1}A_{b1} + E_{b2}A_{b2} + 2E_c A_c} \times N_{total}$$

$$= \frac{25096 \times 150000}{8300 \times 200000 + 8300 \times 200000 + 2 \times 25096 \times 150000} \times 208125$$

$$= 72218\ \text{N} = 72.22\ \text{kN}$$

(2) Cracking Point $(\boldsymbol{V_{cr}}, \Delta_{cr})$

$$\theta = 65°$$

$$V_{n,c} = K\zeta f_c' A_{str} \cos\theta$$

$$= 1.08 \times 0.52 \times 28.51 \times 39653 \times \cos(65)$$

$$= 267673\ \text{N}$$

$$V_{n,t} = \frac{A_v f_y d}{s} + \left(\frac{0.5\sqrt{f_c'}}{{M}/{Vd}} \sqrt{1 + \frac{N}{0.5\sqrt{f_c'} A_g}} \right) 0.8 A_g$$

$$= \frac{142.66 \times 357.9 \times 240}{250} + \left(\frac{0.5\sqrt{28.51}}{4} \sqrt{1 + \frac{72218}{0.5\sqrt{28.51} \times 150000}} \right) 0.8$$

$$\times 150000$$

$$= 136030\ \text{N}$$

$$V_n = \min\left(V_{n,c}, V_{n,t}\right)$$

$$= \min(267673, 136030)$$

$$= 136030\ \text{N} = 136.03\ \text{kN}$$

$$V_{cr} = 0.6 V_n$$

$$= 0.6 \times 136030$$

$$= 81618\ \text{N} = 81.62\ \text{kN}$$

$$\Delta_{cr} = \Delta_{f,cr} + \Delta_{s,cr}$$

$$= \frac{V_{cr} H^3}{12\left(E_c I_{eff}\right)} + \frac{V_{cr} H}{0.4 E_c b d}$$

doi:10.6342/NTU202502280

$$= \frac{81618 \times 3000^3}{12(8.47 \times 10^{12})} + \frac{81618 \times 3000}{0.4 \times 25096 \times 500 \times 240}$$

$$= 21.89 \text{ mm}$$

(3) Strength Point $(\boldsymbol{V_{mn}}, \boldsymbol{\Delta_{mn}})$

$$M_n = 184402243 \text{ N} - \text{mm} = 184402 \text{ kN} - \text{mm}$$

$$V_{mn} = \frac{2M_n}{H}$$

$$= \frac{2 \times 184402}{3000}$$

$$= 122935 \text{ N} = 122.93 \text{ kN}$$

$$\Delta_{mn} = \Delta_{f,n} + \Delta_{s,n}$$

$$= \frac{V_{mn}H^3}{12\left(E_c I_{eff}\right)} + \frac{V_{mn}L_B}{0.4E_c bd} + 2 \times 0.006 \sin 2\theta \times L_D \times \frac{V_{mn}}{V_n}$$

$$= \frac{122935 \times 3000^3}{12(8.47 \times 10^{12})} + \frac{122935 \times 1970.64}{0.4 \times 25096 \times 500 \times 240} + 2 \times 0.006 \sin(2 \times 65) \times 514.68 \times \frac{122935}{136030}$$

$$= 37.13 \text{ mm}$$

(4) Post-strength Point $(\boldsymbol{V_{mn}}, \Delta_{\boldsymbol{s}})$

$$\Delta_s = \Delta_{mn} + a \times H$$

$$= 37.13 + 0.014 \times 3000$$

$$= 80.13 \text{ mm}$$

(5) Collapse Point $(\mathbf{0}, \Delta_{\boldsymbol{a}})$

$$\Delta_a = \Delta_{mn} + b \times H$$

$$= 37.13 + 0.018 \times 3000$$

$$= 89.92 \text{ mm}$$

B.4.4. Curves Superposition

The superposed curve for Specimen IDW_CFRP+ is shown in Figure 4-41(a).

doi:10.6342/NTU202502280